Dipl.-Ing. Corina Klug

Assessment of Passive Vulnerable Road User Protection with Human Body Models

Doctoral Thesis

to achieve the university degree of

"Doktor der technischen Wissenschaften"

submitted to

Graz University of Technology

Faculty of Mechanical Engineering

Vehicle Safety Institute

First Reviewer:

Univ.-Prof. Dipl.-Ing. Dr.techn. Hermann Steffan

Second Reviewer:

Assoc.Prof. Dr. Ciaran Simms

Supervisor:

Assoc.Prof. Dipl.-Ing. Dr.techn. Wolfgang Sinz

Graz, November 2018

I.   AFFIDATIV

I declare that I have authored this thesis independently, that I have not used other than the declared sources/resources, and that I have explicitly indicated all material which has been quoted either literally or by content from the sources used. The text document uploaded to TUGRAZonline is identical to the present doctoral thesis.

1.11.2018

_____
Date

_____
Signature

II. ACKNOWLEDGEMENT

III.   ABSTRACT

Vulnerable Road Users (VRUs) account for about 50% of the road fatalities worldwide. They have to rely heavily on the partner protection of the other road user with which they collide, whereby passenger cars represent the most relevant collision partner. Active safety technologies play increasingly important roles in VRU protection. However, passive protective countermeasures will be still important in the future, as not all accidents will be avoidable. The current state-of-the-art assessment of passive VRU protection of passenger cars is performed using pedestrian subsystem impactors. This method offers high levels of comparability and has guided the design of more "forgiving" car fronts within the last 20 years, but has several drawbacks in terms of its biofidelity.

In the work presented in this thesis, the applicability of Human Body Models (HBMs) for the assessment of passive protective countermeasures that address VRU safety was discussed. In contrast to the state-of-the-art approach, virtual assessment with biofidelic HBMs enables to consider the interaction of the full body with the vehicle. Furthermore, different types of VRUs can be replicated by repositioning the HBM, multiple scenarios can be simulated and human diversity can be considered. The unknown degree of comparability in virtual testing with HBMs and uncertainty in applicable assessment criteria were identified as the biggest challenges, at the starting point of the research described in this thesis. To address these issues, the first harmonised simulation protocol for pedestrian simulations was developed in order to define all the relevant boundary conditions that were identified as part of the sensitivity studies. In the developed reference setup, pedestrian models were impacted with representative generic vehicle models based on newly developed stiffness corridors and median shapes. The simulation results of different institutions using different HBMs and Finite Element (FE) software-packages were analysed and compared. A certification procedure was established which enables to compare the response of a specific HBM using specific settings and a specific FE solver with reference simulations, which led to a significant reduction in the variation among results that are relevant for the Euro NCAP assessment of deployable systems. It was shown that vehicle geometry and stiffness together affect kinematics, which requires the application of highly biofidelic HBMs for reasonable kinematic-based assessment. Strain-based assessment methods were applied in simulated, real-world bicycle accidents for the brain and cortical bones. The potential of HBM simulations to be used for the assessment of VRU protection was demonstrated, as injuries in body regions were correctly predicted with the HBM that cannot be assessed with current state-of-the-art impactors. Further research is needed to improve and validate assessment criteria to exploit the full potential of HBM-based assessment methods. At the current stage, the kinematic-based assessment results can be used as input for physical tests in which injury criteria are evaluated.

The research presented in this thesis was conducted to address some of the challenges of virtual testing with HBMs. Several guidelines were developed that support the harmonised application of HBMs and can be used by members of the scientific community, car manufacturers and representatives of institutions performing assessments. The author hopes that these improved assessment methods will inspire improvements in countermeasures that address VRU safety.

IV. ABBREVIATIONS AND GENERAL DEFINITIONS

AC	Midpoint of centre of right and left *acetabulum*
ACEA	European Automobile Manufacturers' Association
ACL	Anterior Cruciate Ligament
AEB	Autonomous Emergency Breaking
AF05	5th percentile American Female
AIS	Abbreviated Injury Scale
AM50	50th percentile American Male
AM95	95th percentile American Male
aPLI	Advanced pedestrian legform impactor
ATD	Anthropometric Test Device
bic.	bicyclist
ble	Bonner Leading Edge
bleh	Bonnet Leading Edge Height [mm]
BMD	Bone Mineral Density
bmp	Bumper
bnt	Bonnet
BrIC	Brain Injury Criterion
C1-C7	Cervical Vertebrae
CAD	Computer Aided Design
CC	Corpus Callosum
CEDATU	Central Database for In-Depth Accident Study
CFC	Channel Frequency Class
CIREN	Crash Injury Research (Centre of NHTSA)
CL	Vehicle Centerline
CoG	Centre of Gravity
Collision speed	Speed of the vehicle at t0 [km/h]
CORA	Correlation and Analysis
CP	Contact Point
CPU	Central Processing Unit
CSDM	Cumulative Strain Damage Measure
CSDM	Cumulative Strain Damage Measure
CT	Computed Tomography
DAI	Diffuse Axonal Injuries
DYNASAUR	DYNAmic Simulation Analysis of nUmerical Results – open source python based postprocessing software
E	Edge
EEVC	European Enhanced Vehicle-Safety Committee
Euro NCAP	European New Car Assessment Program
FCR	Family Car
FD	Dynamic Friction Coefficient
FE	Finite Element

Fr, Fl	Femoral Epicondyle Right (r) and Left (l)
FS	Static Friction Coefficient
GHBMC	Global Human Body Modelling Consortium
GIDAS	German In-Depth Accident Study
GPV models	Generic Parameterisable Vehicle models
grl	Grill
GV models	Generic Vehicle models
HBM	Human Body Model (Definition on page 13)
HC	Head Centre of Gravity
HIC	Head Injury Criterion
HIT	Head Impact Time [ms]
HIVel	Head Impact Velocity [m/s]
IGLAD	Initiative for the Global Harmonization of Accident Data
IMVITER	IMplementation of VIrtual TEsting in safety Regulations
IP	Intellectual Property
IQR	Interquartile Range
IRC	Injury Risk Curve
KR, KL	Knee Right and Left (center of patella)
LAB	Laboratory of Accidentology and Biomechanics
LCL	Lateral Collateral Ligament
Ld	Leading
M	Midsection
MADYMO	MAthematical DYnamic MOdel
MB	Multibody
MCL	Medial Collateral Ligament
MPI	Message Passing Interface
MPS	Maximum Principal Strain
MPV	Multi-Purpose Vehicles
Mr, Ml	Intermalleolar Tip Right (r) and Left (l)
MRI	Magnetic Resonance Imaging
n	Number of Samples
NASS	National Automotive Sampling System (US In-Depth database)
NCAP	New Car Assessment Program
NDS	Naturalistic Driving Studies
NHTSA	National Highway Traffic Safety Agency (USA)
OR	Odds Ratio (defined in Equation (1) on page 22)
OS	Open Source
PMHS	Post-mortem Human Subject
PS	Principal Strains
Q1, Q3	First Quartile, Third Quartile
R²	Goodness of fit (coefficient of determination)
RAIDS	Road accident in-depth studies
RDS	Roadster
SAE	Society of Automotive Engineers
spl	Spoiler
SSL	Struck side leg

SUV	Sport Utility Vehicle
t0	Time of first contact between vehicle and VRU
T1-T12	Thoracic Vertebrae
TB	Technical Bulletin
TBI	Traumatic Brain Injury
thk	Thickness
THUMS	Total Human Model of Safety
THUMS v4	THUMS version 4
Tr	Tracing
VDC	Vicsous Damping Coefficient
vel	velocity
VRU	Vulnerable Road User (Definition in Chapter 1 on page 1)
WAD	Wrap around distance
WHO	World Health Organisation
yo	year-old
YoR	Year of Registration
α	Rotational acceleration [rad/s²]
a	Acceleration [g]
ε	Strain [-]
σ	Stress [kN/mm²]
v	Velocity [m/s]
v_col	Collision speed [km/h]
ω	Rotational velocity [rad/s]

V.   TABLE OF CONTENTS

1   INTRODUCTION

1.1   Motivation

The term Vulnerable Road Users (VRUs) refers to participants in traffic that are not protected by any mechanical system, including pedestrians, motorcyclists and bicyclists. (ERTRAC Working Group on Road Transport Safety and Security, 2011)

According to the World Health Organisation (WHO), VRUs made up almost half of the 1.25 million traffic fatalities worldwide in the year 2013. (WHO, 2015)

As shown in Figure 1, great regional differences can be observed when comparing the relevance of VRUs to the total traffic fatalities in different countries. While they make up 83% of all traffic fatalities in Thailand, their share is only 12% in Argentina. Austria and most other central European countries are in the mid-range and, therefore, denoted with blue colour, representing countries in which about 50% of the traffic fatalities are associated to the group of VRU. (WHO, 2016)
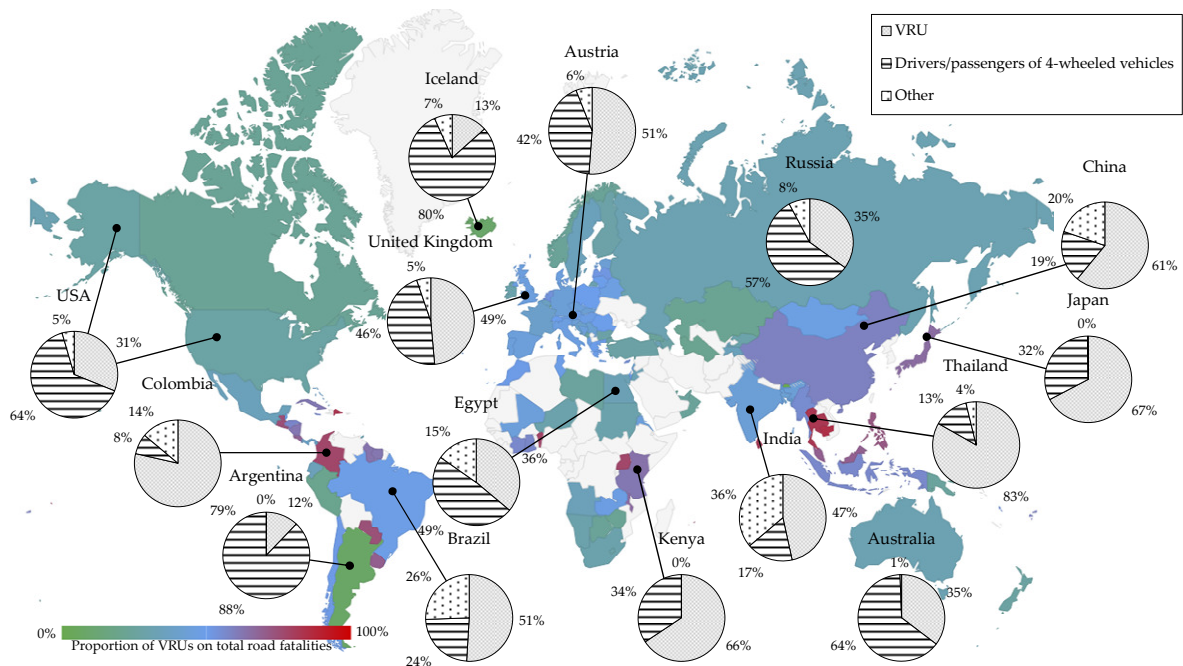
Figure 1: Worldwide proportion of VRUs to total road fatalities in 2013 (based on WHO, 2016)

Figure 2 shows the exemplary, historic development of the number of road fatalities for four European countries since 2000. The different groups of road users are stacked, and the proportion of VRUs to total road fatalities is shown as a red line over a time period of fifteen years. The figures show that, while the number of all road fatalities has decreased from 2000-2015, the proportion of VRUs has tended to increase.

It seems, therefore, that the safety measures introduced since 2000 addressing VRUs have been less effective than those addressing vehicle occupants. This suggests that protection of VRUs needs to be further improved to reduce the number of fatalities. The head, thorax and lower extremities are the most relevant body regions when considering severe or fatal injuries. (Fredriksson and Rosen, 2012; Wisch *et al.,* 2017; Fredriksson and Sui, 2015; Piantini *et al.,* 2017)
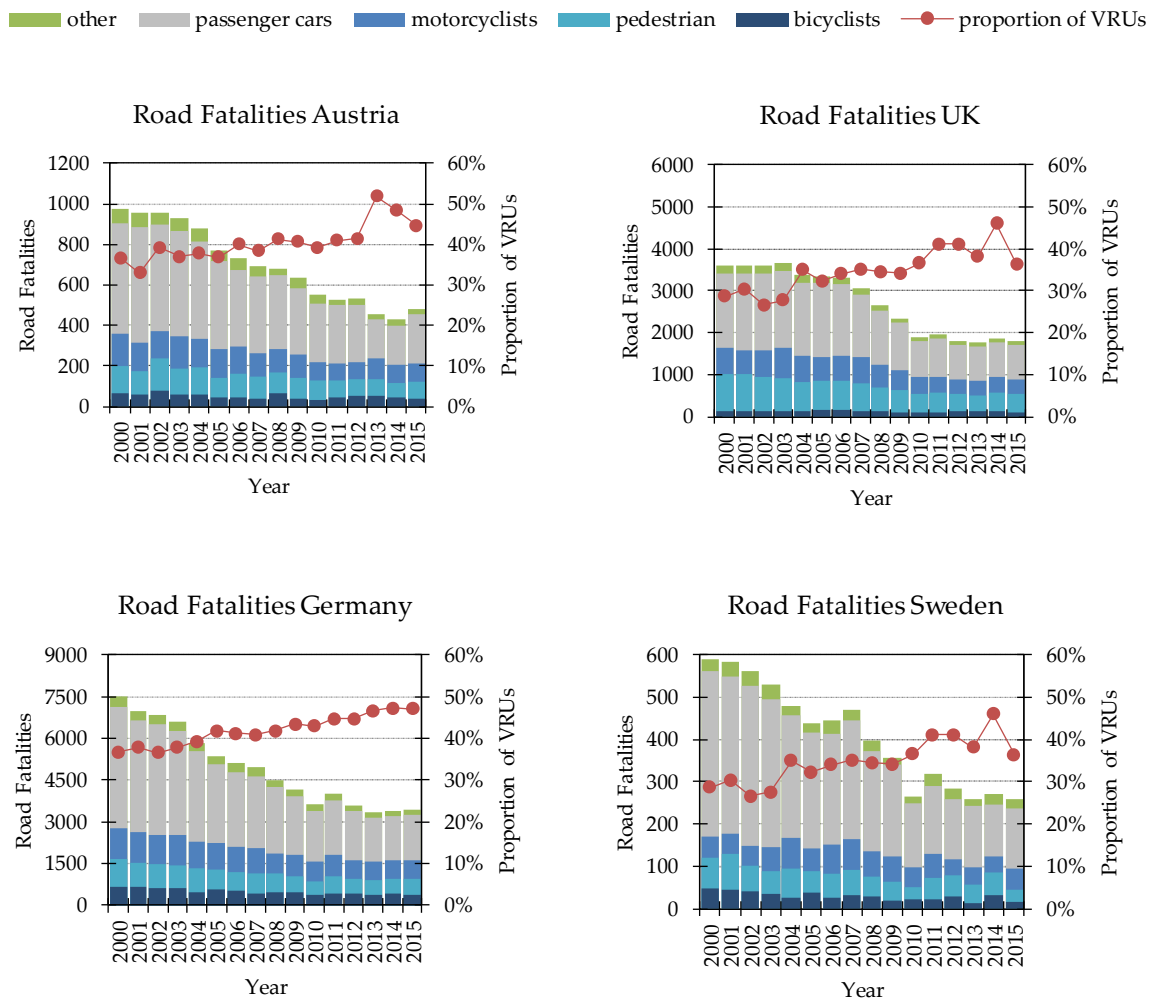
Figure 2: Historical development of Road Fatalities of different Road user groups in Austria, UK, Germany and Sweden from 2000 – 2015 (European Commission, 2016)

In the event of an accident with other road users, VRUs have to rely mainly on the partner protection of the road user with which they collide. Figure 3 shows that passenger cars are the most relevant collision partner for VRUs. Passenger cars were involved in 56% of all police-reported VRU accidents in Austria between 2002-2016. Regarding pedestrian accidents (Figure 4), passenger cars were even involved in 71% of the police-reported accidents.

Other road users involved in VRU accidents

Source: Stastistics Austria 2002-2016
Analysed by: TU Graz (VSI)

Other road users involved in pedestrian accidents

Source: Statistics Austria 2002-2016
Analysed by: TU Graz (VSI)
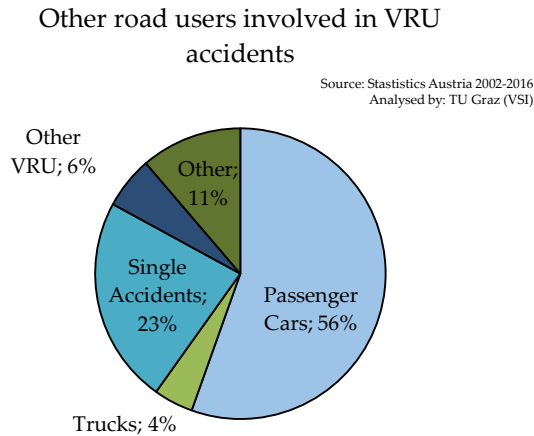
Figure 3: Collision partners in VRU accidents (all accidents reported in Austrian road traffic statistics with at least one VRU involved from 2002-2016; *n* = 64,143)
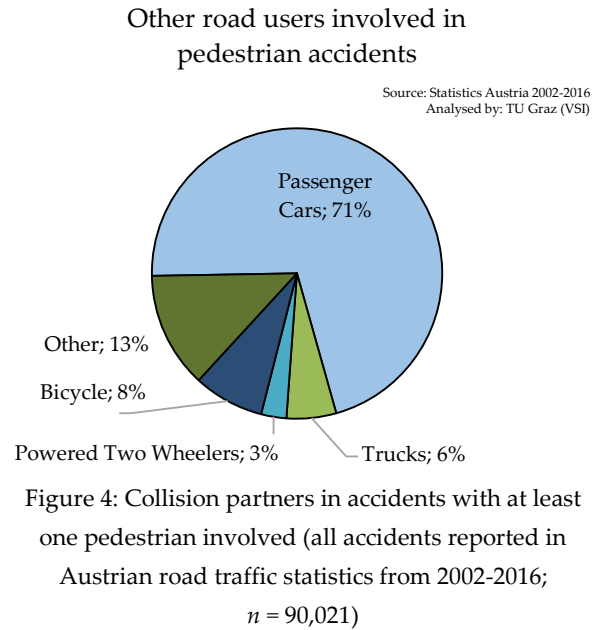
Figure 4: Collision partners in accidents with at least one pedestrian involved (all accidents reported in Austrian road traffic statistics from 2002-2016; *n* = 90,021)

Pedestrian protection regulations for passenger cars came into force in Europe in 2005 (Kühn *et al.*, 2006), and pedestrian protection has been rated by the consumer information programme Euro NCAP (European New Car Assessment Programme) since 1997 (Euro NCAP, 2018). In the USA, the assessment of pedestrian safety is not part of the homologation of passenger cars. According to a report from the National Highway Traffic Safety Agency (NHTSA, 2018b), the number of pedestrians killed in traffic accidents increased by 27% from 2007 (4 699 pedestrian fatalities, which are 11% of total road traffic fatalities) to 2016 (5 987 pedestrian fatalities, corresponding to 16% of total road traffic fatalities).

The assessment of protective measures of passenger cars seems, therefore, to be highly relevant and needs to be further improved to decrease the number of (fatally) injured VRUs, which is the focus of this thesis.

1.2   Problem Statement

To gain better understanding of the problem, the different phases and mechanisms of collisions between VRUs and passenger cars are discussed at first (based on Kühn *et al.*, 2006; Simms and Wood, 2009; Wood *et al.*, 2005):

- *Pre-crash phase:* Within this phase, a conflict situation can be either avoided by the participants or the phase ends just before the contact occurs between the VRU and the other road user.

- *In-crash phase:* This phase covers the time from the first contact between VRU and vehicle (t0) until the VRU comes to rest. The phase can be further subdivided and consists of multiple impacts with different structures:

- *Primary impact with the vehicle:* The phase starts with the first contact between the vehicle and the VRU and usually ends with a head impact. The kinematics in this phase are strongly affected by the vehicle's geometry and the size of the VRU. The kinematics can be separated into three main groups:

  o Forward projection for cases where the bonnet leading edge height (*bleh*) of the vehicle is higher than the Centre of Gravity (CoG) of the VRU. In this case, the VRU remains upright during the impact phase, is projected horizontally and then falls over.

  o Wrap projection for cases where the CoG of the VRU is higher than the *bleh*. This leads to a rotation of the VRU around the bonnet leading edge (ble). The body of the VRU wraps around the vehicle front and bonnet until the VRU's head impacts the bonnet or windscreen.

  o Fender vaults for cases when the VRU is hit by the corner of the vehicle. The offset collision causes the VRU to laterally slide off the vehicle without subsequent impacts with the vehicle.

- *Subsequent impacts with the vehicle:* The VRU can contact the collision partner multiple times on different structures during the in-crash phase. These impacts usually interrupt the free flight phase.

- *Free flight phases*: In this phases, the VRU contacts no other structures.

- *Impact with the environment:* The in-crash phase usually ends with the VRU impacting the ground or part of the infrastructure of the accident scene before he or she finally comes to a rest.

- **Post-crash phase:** During this phase, the accident victim is rescued and transported to the hospital. A proper working rescue chain can affect the outcome of the accident in cases of critical injuries. So-called eCall Systems are able to make an emergency call in the event of the crash and are, therefore, able to save significant time. This phase is not considered in work described in this thesis.

The pre-crash phase is addressed by active safety measures. Accidents can be avoided or mitigated with infrastructure measures or by car systems that help the driver detect the conflict situation, warn, or even take over the reaction (Kühn *et al.*, 2006).

Autonomous emergency braking systems (AEB) are a promising technology to improve the safety of VRUs. The potential of AEB systems depends on system parameters, such as the sensor angle, width and detection algorithms. A proper system design is essential to detect the VRUs early enough to avoid the accident or reduce the impact speed. (Hamdane *et al.*, 2015)

Physical tests for the assessment of AEB systems for VRU protection were introduced by Euro NCAP in 2015, and continuous updates will follow within the next years (Euro NCAP, 2018). As the trajectory of VRUs is difficult to predict, and scenarios highly vary (including sight obstructions that do not allow detection), pedestrian AEB systems will not able to detect all accidents in the

future (Hummel *et al.*, 2011; Chen *et al.*, 2015b; Strandroth *et al.*, 2016; Vertal and Steffan, 2016; Luttenberger *et al.*, 2014; Detwiller and Gabler, 2017).

Therefore, passive safety measures – addressing the mitigation of injuries in the in-crash phase – are still needed. They are in the focus of the research presented this thesis. To analyse the efficiency of passive safety measures, appropriate assessment methods are needed. The following requirements were summarised by the author of this thesis, that are important for an appropriate assessment of passive VRU protection:

- *Biofidelity:* Assessment tools have to behave as human-like as possible. Ideally, the assessment tool replicates kinematics, loads and deformations as they are observed in real-world accidents for the whole in-crash phase. The interaction between the VRU and impacted structure as well as the interactions between body parts have to be replicated. Impact times, velocities, locations and contact forces have to be predicted correctly. Furthermore, biofidelity also means that the assessment tool is capable to replicate injury mechanisms and patterns that are comparable with real-world accidents.

- *Appropriate Assessment Criteria:* In the end, an assessment tool has to generate objective, quantifiable outputs to assess the protective countermeasures. The gained output has to be meaningful, and it has to be assignable to human load limits. The aim is to link the output with the risk of specific injuries. The criteria have to already be applicable during the development process of protective countermeasures as design targets. The injuries predicted using assessment criteria have to be in accordance with injuries from real-world accidents.

- *Comparability:* It is essential for an assessment that results are comparable. The assessment method has to provide results that can be compared between car manufactures or test labs that apply the method to allow a fair comparison of protective countermeasures. When different tools and methods are applicable to the assessment, these need to lead to comparable results. Assessment methods and tools also have to be also reproducible: The procedure has to be clear and robust enough to gain same assessment results when repeated multiple times. The testing procedures have to define relevant boundary conditions that must be complied with. The assessment protocol has to be clear, transparent and verifiable. When the same method is applied several times to assess one impact structure, the results should ideally not deviate from one another. As this is often technically not feasible, tolerances are needed that should be as narrow as possible.

- *Human Variability:* To protect as many VRUs as possible, assessment methods need to reflect the diversity of the population (varying ages, heights, weight, gender). This means that biofidelity has to be present for different anthropometries and, ideally, assessment criteria can be also adjusted to different load limits (e.g. age dependent adjustment of criteria).

- *Variability of Scenarios:* As accident scenarios of VRUs vary greatly, a proper assessment method has to be able to replicate a variety of relevant scenarios. Varying impact directions, velocities and initial postures between the VRU and impact structure have to be replicable in a biofidelic way. The interaction with the impact structure has to be replicated correctly for different initial conditions of VRU impacts. This requirement is also of great importance, because it allows the integrated safety assessment of active and passive safety features, as the active safety system will cause a change in the impact scenario.

1.3 State-of-the-art

The requirements described within the previous section were applied to compare state-of-the-art methods for the assessment of VRU. The advantages and disadvantages of different methods are discussed in the following chapters and summarised in tabular form in Chapter 1.3.8.

1.3.1 Real-World Accident Data

The effects of safety measures can be evaluated retrospectively by means of real-world accident data. Different data sources for real-world accidents are available:

- Macroscopic databases, such as national statistics are not appropriate for this purpose, as detailed information about the accident scenario, injuries and vehicle parameters (e.g. collision speed) are missing. These databases can only be used to analyse general trends and derive representative boundary conditions for an assessment method.

- Video records from on-board cameras of vehicles (e.g. from Naturalistic Driving Studies) or traffic surveillance cameras are also not suitable data sources, as there are no injury data available. Nevertheless, the video analysis can provide valuable input for the development and validation of other assessment methods (e.g. for ground impacts). (Han *et al.*, 2017; Barry and Simms, 2016; Li *et al.*, 2018b)

- Data from in-depth databases include detailed information about the accident scenario as well as the injuries of all participants and are, therefore, generally appropriate for an assessment. Several such databases exist: e.g. the German GIDAS (Brunner *et al.*, 2003), Austrian CEDATU (Tomasch and Steffan, 2006), American NASS (NHTSA, 2018a), UK-wide RAIDS (Department of Transport, 2013) and the international IGLAD (Bakker *et al.*, 2017). Further statements in this chapter refer to these kinds of data sources.

The analysis of real-world accident data from in-depth databases enables to retrospectively evaluate the effects of safety regulations and NCAP ratings on the injuries observed (Zander *et al.*, 2015; Pastor, 2013; Strandroth *et al.*, 2011; Li *et al.*, 2018a). Furthermore, the numbers of specific injuries of specific car categories can be compared. This allows, for example, the analysis of the effects of different car geometries in the field (Li *et al.*, 2017a). Other parameters that can be analysed by means of accident statistics are the effects of age of the VRU and collision speed (Rosén and Sander, 2009; Wisch *et al.*, 2017; Otte *et al.*, 2012; Li *et al.*, 2017a; Piantini *et al.*, 2017).

There is nothing more biofidelic and realistic than real-world accident data. An examination of this data allows the analysis of the outcome of VRU accidents for diverse population groups in a wide variety of scenarios. The number of injuries (of a specific severity) could be used as an assessment criterion as it is an objective, quantifiable output. In any case, this can only be done retrospectively. When new safety measures are introduced, it takes several years until the market penetration is high enough to observe an effect in the accident data. According to the European Automobile Manufacturers' Association (ACEA, 2018), the average age of passenger cars (for European cars) was 11 years in 2017. Therefore, the assessment criteria applicable for this method do not fulfil all requirements, because they cannot be used within the development process as design targets.

Another big challenge is comparability: The composition of the analysed sample can strongly affect the results. The sample sizes in single in-depth accident databases quickly diminish when one asks specific research questions (Klug *et al.*, 2015b; Li *et al.*, 2017a). Therefore, it can be challenging to draw significant conclusions using a single database. This is a problematic issue, as accidents cover a large number of parameters, and filter criteria have to be applied to make meaningful comparisons. One could combine accident databases into one sample, but this is also not straightforward due to differences in data composition between the databases (Klug *et al.*, 2015b). Furthermore, there are many unknown parameters, which have to be derived from the accident reconstructions as best estimates. No harmonised, European, in-depth data collection is ongoing, although there have been some initiatives in the past (Ross *et al.*, 1998; del Pozo de Dios *et al.*, 2013; Lenard *et al.*, 2006).

Nevertheless, real-world accident data are valuable for identifying the most common or most critical injury sources (Mallory *et al.*, 2012; Fredriksson and Rosen, 2012; Klug *et al.*, 2015b; Otte *et al.*, 2012) and accident scenarios (Fredriksson and Rosen, 2012; Li *et al.*, 2016; Lindman *et al.*, 2015). The data from the in-depth accident databases is highly useful for defining boundary conditions for assessment procedures or assessing the biofidelity of assessment methods.

1.3.2 Post-mortem Human Subjects

Tests with Post-Mortem Subjects (PMHS) are the only (ethically justifiable) possibility to physically test humans at high loads under controlled boundary conditions. PMHS tests can be subdivided into three main categories:

- "Full-scale tests", which means the testing of full human bodies,

- "Component tests", which means tests with human body parts (e.g. whole femur bone)

- "Material tests" with small samples of human tissue (e.g. samples of cortical femur bone).

During PMHS tests, the kinematics can be tracked via video analysis. Instruments can be attached to the PMHS, such as with acceleration sensors and strain gauges, to gain additional outputs. Furthermore, injuries can be analysed in autopsies after the tests. (Forman *et al.*, 2015b; Subit *et al.*, 2008; Kerrigan *et al.*, 2012b)

Tests with PMHS offer a high level of biofidelity, but the missing muscle activity can affect the kinematics and injury outcomes (Paas *et al.*, 2012; Kerrigan *et al.*, 2012b). Discrepancies between the frequency of spinal, knee and pelvic injuries in PMHS tests and real-world cases were observed in a study by Kerrigan *et al.* (2012b). Furthermore, the mechanical characteristics of PMHS can be compromised due to preservation techniques (embalming and freezing), which is applied in several tests as the time frame with fresh PMHs is very limited (Paas, 2015; Crandall, 1994; Crandall *et al.*, 2011).

In addition, the discrepancies to the filed data can be also caused by the advanced age and, therefore, often low bone density of the PMHS (Kerrigan *et al.*, 2012b). Most of the PMHS are elderly people (Crandall *et al.*, 2011; Kerrigan *et al.*, 2012b). Therefore, no conclusions for the whole diverse population can be drawn.

Tests with PMHS are not suitable for guiding the design of protective countermeasures and cannot be applied during the development process. Apart from ethical issues, the number of subjects is limited and tests are highly complex and not reproducible. The greatest weakness of PMHS tests is their comparability: It is challenging or even impossible to achieve reproducibility, as every human is different and, even if the same human could be used, it would be challenging to place the PMHS in the same initial posture.

The number of scenarios that can be tested with PMHS is also limited: Most of the tests are conducted with the same initial posture according to SAE J2782 (SAE International, 2010b): The struck side leg (SSL) faces backwards and the arms are positioned in front of the body close to the abdomen with tied wrists to improve comparability (Kam *et al.*, 2005). In a recent study, tests were conducted with a more natural arm position, highlighting the importance of the shoulder and elbow impact (Paas *et al.*, 2015a; Paas *et al.*, 2012). No data on ground impact are available in most of the studies, as catching apparatuses are usually used.

In summary, PMHS tests offer high levels of biofidelity, but because of the lack of comparability, PMHS tests are not a suitable method for the assessment of passive VRU protection. Nevertheless, they can help researchers gain a better understanding of key parameters. Furthermore, PMHS tests are essential for the assessment of the biofidelity of other assessment methods.

Table Appendix A-1 summarises full-scale PMHS tests chronologically. A focus was placed on recent tests (published within the last 20 years) and tests that were used for the validation of other assessment methods explained in Chapter 1.3.3 -1.3.6. To the author's knowledge, no PMHS tests representing motorcyclists are available. Only one PMHS test including bicyclists (Serre *et al.*, 2007) was found during the review of literature. All other studies placed a focus on pedestrians (Ishikawa *et al.*, 1993; Cesari, 1998; Yang *et al.*, 2000; Schroeder *et al.*, 2000; Snedeker *et al.*, 2005; Kerrigan *et al.*, 2005a; Kerrigan *et al.*, 2005b; Crandall *et al.*, 2006; Kerrigan *et al.*, 2007; Masson *et al.*, 2007, Serre *et al.*, 2007; Untaroiu *et al.*, 2007; Kerrigan *et al.*, 2008; Schroeder *et al.*, 2008; Subit *et al.*, 2008; Kerrigan *et al.*, 2009a; Kerrigan *et al.*, 2009b; Kerrigan *et al.*, 2012a; Paas *et al.*, 2012; Paas *et al.*, 2015b; Forman *et al.*, 2015a; Forman *et al.*, 2015b; Song *et al.*, 2017a; Song *et al.*, 2017b).

1.3.3   Anthropometric Test Devices

Anthropometric test devices (ATDs) are mechanical surrogates of the human body used in crash testing and are also often called "crash test dummies". They offer the possibility to measure loads on the body in the event of a crash. In addition to offering biofidelity, they have been designed to be robust and are carried out to obtain reproducible and repeatable results. (Schmitt *et al.*, 2004)

ATDs have been applied for several years for the assessment of occupant protection, but they have only been used for research activities in the field of VRU safety. ATDs representing VRUs have to sustain higher loads than the occupants and allow oblique loading. (Simms and Wood, 2009; Yoganandan *et al.*, 2015; Schmitt *et al.*, 2014)

A Hybrid III pedestrian dummy has been applied in some studies as a motorcyclist (Hering and Derler, 2000), bicyclist (Zander *et al.*, 2013) and pedestrian (Feist *et al.*, 2009). Because the Hybrid III was originally designed as a frontal occupant dummy, however, lateral impacts are likely to lead to damage in the thorax or lower extremities of the dummy. It, therefore, provides insufficient biofidelity for these load cases (Feist *et al.*, 2009).

The Polar pedestrian dummy was developed to replicate kinematics of pedestrians upon impact. A 50th percentile male dummy was built based on the THOR (Test Device for Human Occupant Restraint) dummy with several modifications (Akiyama *et al.*, 1999). Over the years, several adjustments of the Polar dummy were made to improve biofidelity (Akiyama *et al.*, 1999; Akiyama *et al.*, 2001; Kerrigan *et al.*, 2005a; Kerrigan *et al.*, 2009a; Bose *et al.*, 2007; Subit *et al.*, 2006; Asanuma and Takahashi, 2015). Deviations in the head impact velocity, head impact time and associated head injury criteria were reported due to the relatively stiff neck of the dummy (Kerrigan *et al.*, 2005a; Kerrigan *et al.*, 2009a).

The Polar II dummy has been applied for research on VRU airbags (Wallentowitz *et al.*, 2009; Fredriksson *et al.*, 2014), an evaluation of pedestrian subsystem impactors (Zander *et al.*, 2011) and an analysis of bicyclist impact kinematics (van Schijndel *et al.*, 2012). Measurement signals from the sensors installed in the dummy can be used for the assessment. Common injury criteria from occupant ATDs were applied within these studies (based on forces, moments and accelerations). To the author's knowledge, no study is available that compares those outputs with the real-world injury risk of VRUs, and no injury assessment reference values have been made available until now (Fredriksson *et al.*, 2014).

The number of VRU scenarios that can be tested with ATDs is limited. Tests are costly, and the dummy does not allow for arbitrary positioning (Fredriksson *et al.*, 2014). Test setups allowing reproducible and repeatable results are complicated and restrict possible scenarios (e.g. initial velocity of the dummy would lead to more realistic scenarios, but worse repeatability).

As material parameters of the dummy can change over the time, dummies have to be regularly certified to ensure that the response of the dummy fits predefined response corridors to ensure comparability (Mohan *et al.*, 2009).

A Finite Element (FE) model of the Polar II model is available, which allows the virtual application of the dummy in the development process of safety measures (Untaroiu *et al.*, 2010; Fredriksson *et al.*, 2011).

Only a 50th percentile male Polar dummy is available, which means that the diversity of the population cannot be replicated using this assessment method at the current developmental stage.

In summary, the Polar dummy shows reasonable levels of biofidelity with some limitations in terms of reproducing injury mechanisms. The outputs need further validation to be applicable as assessment criteria. Comparable tests can be performed, but require high amounts of invested effort and, therefore, this limits the number of scenarios. Another drawback of the approach is the lacking possibility to replicate diversity.

1.3.4 Subsystem Impactors

As part of homologation and consumer information, subsystem impactors are applied to assess the pedestrian protection of passengers. The impactors are representing different body regions:

- Adult and child headform for the assessment of the protective capabilities of the car bonnet and windshield

- Upper legform impactors for the assessment of the risk of pelvic and femoral injuries caused by the bonnet leading edge or bumper

- Legform impactor to assess the risk of tibia and knee injuries caused by vehicle fronts

Testing with pedestrian subsystem impactors allows comparable, transparent and relatively cheap assessments to be made. Furthermore, the whole area of the impact structure can be assessed.

The assessment criteria are based on the instrumentation of the impactor. Transfer functions are often needed to convert the output of the impactor with limited biofidelity to human load limits (Takahashi *et al.*, 2012). The currently assessed criteria are not able to address all injury mechanisms of real-world injuries (Sanchez-Molina *et al.*, 2012; Feist *et al.*, 2009; Ott *et al.*, 2012). Discrepancies between assessment results and the relative frequencies of injuries in the field were observed in some studies (Lubbe *et al.*, 2011; Snedeker *et al.*, 2003; Li *et al.*, 2018a; Snedeker *et al.*, 2005).

Only impactors for selected body regions are available. No assessment of thoracic injuries can be performed, although this is a relevant region of the body that tends to be seriously injured (Wisch *et al.*, 2017).

The test method has several drawbacks in terms of biofidelity:

- The replication of the interaction between vehicle and VRU is limited for this assessment method. The preloading of the vehicle from other body parts is not replicable (e.g. deformations of the bonnet due to contact with other body parts before the head contact occurs) (Chen, 2017).

- The subsystem impactors are not able to replicate interactions between body parts. The effect of this drawback was shown by comparing these tests with PMHS tests (Kerrigan *et al.*, 2008) and simulations. Activities are ongoing aiming to improve biofidelity of the leg form impactor by adding a simplified upper body mass (Zander *et al.*, 2009; Bovenkerk and Zander, 2009; Isshiki *et al.*, 2016a, 2016b; Isshiki *et al.*, 2017; Isshiki *et al.*, 2018).

- The missing full-body kinematics do not allow for the evaluation of the effect of vehicle geometry and stiffness on the impact velocity, location and angle of other body parts. The wrap-around distance (*WAD*) and head impact time (*HIT*) cannot be assessed with the impactors alone. Subsequent impacts on the car and ground impacts are also not covered with the current procedures and cannot be assessed with isolated impactors alone, as they are strongly affected by the vehicle geometry (Crocetta *et al.*, 2015; Shang *et al.*, 2017).

- The effect of the vehicle geometry on primary impact velocities and impact angles can be only replicated through approximation models (Lubbe *et al.*, 2011; Snedeker *et al.*, 2003; Li *et al.*, 2018a; Snedeker *et al.*, 2005; Hutchinson *et al.*, 2012; Masson *et al.*, 2007).

Such approximation models (extrapolations or lookup tables) are also needed to obtain the boundary conditions for varying scenarios (as it is needed for integrated assessments when collision speed and impact points variable) (Edwards *et al.*, 2015; Wimmer *et al.*, 2015; Ferenczi *et al.*, 2015). These approaches are challenging, as several vehicle parameters affect the impact angles and impact velocities of the body parts.

Subsystem tests are also limited when it comes to diversity: While two different head impactors (adult and child headform, which differ in terms of mass) are available, and head impact points can be varied, the legform impactors only replicate a 50th percentile male. The impactors were developed to replicate pedestrian kinematics and are not directly transferable to other VRUs.

Simulation models of the impactors are available that allow the application for virtual product development. Tests with the physical subsystems can be also used to validate numerical models for the impact structures.

In summary, subsystem testing has led to modifications in the stiffness of the car front and the bonnet which benefit pedestrians (Zander *et al.*, 2015; Li *et al.*, 2018a), but there is a lack in biofidelity and applicability for varying scenario, other road users and consideration of diverse population, which requires improved assessment methods.

1.3.5   Humanoid Multibody Models

Multibody (MB) models consist of rigid bodies that are connected with joints. The joint stiffness characteristics can be calibrated to approximate a biofidelic behaviour of the models. Penetration search algorithms are defined to model the contact stiffness between the rigid bodies. (Simms and Wood, 2009)

The PC-Crash humanoid MB model is commonly used for accident reconstructions (Peng *et al.*, 2012a; Martínez *et al.*, 2016; Otte *et al.*, 2012; Depriester *et al.*, 2005). The multibody model is highly

simplified and is used to predict global kinematics and throw distances, which were validated by a comparison with dummy kinematics (Moser *et al.*, 2000). The biofidelity of this model, is not sufficient for the assessment of protective countermeasures.

MADYMO (Mathematical Dynamic Model) ellipsoid models are frequently applied in studies on VRU accidents (Bourdet *et al.*, 2012; Bourdet *et al.*, 2014; McNally and Whitehead, 2013; Elliott *et al.*, 2012a; Serre *et al.*, 2007; Li *et al.*, 2017b; Peng *et al.*, 2012a; Crocetta *et al.*, 2015; Untaroiu *et al.*, 2009; Peng *et al.*, 2012b). The current MADYMO humanoid model consists of rigid bodies, representing the skeletal system, and 64 ellipsoids, representing the outer surface of the body (Simms and Wood, 2009). The anthropometry is based on the RAMSIS software and represents an average western European male (Simms and Wood, 2009).

According to the MADYMO human model manual (TASS International BV, 2017), the pedestrian is validated to predict global kinematics and impact points on the vehicles. The lower extremities of the ellipsoid model include several "bending/fracture joints" to achieve biofidelic behaviour. Whenever the fracture tolerance (shear force or bending moment) is exceeded, the angular resistance of those joints is set to 0 for the remaining simulation time. The occurrence of fractures in the upper and lower leg during impact can be predicted reasonably well. The manual states that the model can predict the shape and trends of the acceleration for the head, chest and pelvis. (TASS International BV, 2017)

The MADYMO human models can be coupled to FE solvers which enables to use the full FE impact structure together with the multibody model (Leglatin *et al.*, 2006).

The biofidelity of the model has been evaluated in several studies:

- In addition to a variety of validations conducted on the component level, the pedestrian kinematic of the MADYMO ellipsoid pedestrian model was validated by the developers of the models using five PMHS tests published by Ishikawa *et al.* (1993), three tests by Yang *et al.* (2000) and five tests by the EEVC working group (Cesari, 1998). High levels of correlation in terms of kinematics were observed, but high amounts of deviation in terms of accelerations were reported: It was shown that the model could be used to predict a head impact location that approximated those reported in the literature (mean deviation of 5%). The deviation in the time of the maximum head acceleration between the simulations and tests was between 1% and 20% (average deviation of 9%). Maximum accelerations differed by up to 100% (mean deviation of 40% for the head). (van Hoof *et al.*, 2003).
- Elliott *et al.* (2012a) compared the kinematics of MADYMO pedestrian models with more recent, full-scale pedestrian PMHS tests (Subit *et al.*, 2008; Kerrigan *et al.*, 2008; Kerrigan *et al.*, 2009a). Difference in terms of *HIT*s were between -15% and +10%. The head impact velocities differed from those in the PMHS tests by -10% to +36%. For the head impact location, deviations between -13 and +17% were observed. (Elliott *et al.*, 2012a)
- The lack of spine elongation in the MB model was mentioned as a drawback in terms of biofidelity in one study, which may explain the lower location of head impact points (Ishikawa *et al.*, 1993).

- Reasonable correlations among global kinematics was reported when comparing the model positioned on a bicycle with one full-scale PMHS test. (Serre *et al.*, 2007)

Due to their short simulation times and high robustness, MB models can be used to simulate ground impacts (Crocetta *et al.*, 2015) and a variety of scenarios (Li *et al.*, 2016). No validation is available for the free flight phase and the ground impact. MB Models can be easly scaled to varying anthropometries.

In general, MB models are a practical tool that can be used for several applications, as they allow users to run a large number of simulations and are applicable to different road users and anthropometries. The models have significant drawbacks in terms of their biofidelity and validity of output regarding interaction forces and injury predictors. Stiffness effects cannot be replicated in detail. No procedure is currently available to ensure comparability when simulations are performed by different users, on different platforms in different software versions, or with different multibody models.

1.3.6   Human Body Models

Human Body Models (HBMs) are understood to be detailed, finite-element models of the human body. The following definition for a Human Body Model was applied as part of this thesis work, which was developed by the author together with project partners within the CoHerent project and was included in the Euro NCAP Technical Bulletin TB 024 (Euro NCAP, 2017b):

> *"A Human Body Model (HBM) is understood as a virtual geometric and mechanical representation of the human body. The geometry of the model should result in dimensions, masses and moments of inertia per body parts in agreement with standard anthropometry databases. It has to consider the complex human anatomy and consist of a full skeleton composed of all bones (except for the feet, hands, face and ear where simplifications are allowed) and soft tissue. All the bones should be articulated in a realistic manner allowing a biofidelic range of motion for all joints."*

Several Human Body Models have been developed over the years since the first HBM was published in 1994 (Yang *et al.*, 2006). Models are available in varying sizes and with differing degrees of accuracy: The Total Human Model of Safety (THUMS) and the models of the Global Human Body Modelling Consortium (GBHMC) are widespread and commercially available HBMs. They have been applied in several studies on VRU accidents, which are listed in Table Appendix A-2. The models are available in different sizes and postures. For pedestrian simulations, some in-house models are also applied (Kunitomi *et al.*, 2017; Takahashi *et al.*, 2015). Additional to those models, specific models of children, such as PIPER (Giordano *et al.*, 2017) and CHARM-10 (Shen *et al.*, 2016; Shen *et al.*, 2015) or models representing elderly people, such as the CHARM-70 (Hammad *et al.*, 2017; Khandelwal *et al.*, 2017), are available.

The models have to be validated based on their intended use. It has to be evaluated if they are applicable to predict the responses needed to answer the questions of interest. (Cronin, 2011)

HBMs are validated using PMHS tests on the component level and full-scale tests. As validation is not harmonised, no general statement on biofidelity can be made. Details on the validation of the THUMS v4 and GHBMC models can be found in Chapter 2.3.1. Both models show good levels of biofidelity for various validation load cases. It was also shown in some studies that biofidelic HBMs can be used to replicate injury mechanisms from real-world accidents (Coulongeat *et al.*, 2014; Giordano *et al.*, 2017; Golman *et al.*, 2014; Wen *et al.*, 2015).

Human Body Models allow users to simulate full-body kinematics and deformations according to the constitutive properties of the body parts (Simms and Wood, 2009). Compared to other simulation methods, the main benefit of their use is that they can be used to analyse results on the tissue level to predict potential injuries (Cronin, 2011). Instead of using simplified, acceleration-based injury criteria, tissue level injury predictors can be used to analyse the stresses and strains within each element (Yoganandan *et al.*, 2015). Furthermore, HBMs can be morphed to varying ages and Body Mass Indexes (BMIs) to assess the protection of a wider range of the population (Zhang *et al.*, 2017b; Zhang *et al.*, 2017a; Schoell *et al.*, 2015; Huang *et al.*, 2018a; Giordano *et al.*, 2017). The position of body parts can be changed to replicate different road users (Katsuhara *et al.*, 2014; Ito *et al.*, 2014) and different initial postures (Chen *et al.*, 2015a; Li *et al.*, 2015). Furthermore, the virtual assessment with HBMs enables to consider varying scenarios, and the whole in-crash phase can be simulated (Katsuhara *et al.*, 2014; Bastien *et al.*, 2017).

Although HBM simulations are promising for the assessment, several challenges were identified during the literature review:

- A high amount of expertise is needed to apply HBMs and interpret simulation results. The complexity of the models can mask relationships. Results are more difficult to interpret compared to simulations with MB models. (Simms and Wood, 2009)

- No harmonised injury risk assessment is available (Ghosh *et al.*, 2016). There are only a few injury risk curves available (Peres *et al.*, 2016; Forman *et al.*, 2012) that allow probabilistic injury evaluations as assessment criteria. There is a lack of guidelines on how to interpret the results of HBM simulations.

- There is also no procedure available that ensures comparability between the different HBMs, for different users, platforms, FE software packages, or simulation settings. Lack in harmonisation is the biggest challenge for the application of HBMs in safety assessments:

  - The validation of HBMs is not harmonised. PMHS tests from different sources are used, and objective rating methods (Barbat *et al.*, 2013) are rarely applied.

  - Most of the HBMs are replications of one individual whose anthropometry is close to the percentile that shall be modelled (Kitagawa and Yasuki, 2014; Shigeta *et al.*, 2009; Gayzik *et al.*, 2011). Therefore, the detailed anthropometries of HBMs differ.

  - HBMs are available in different codes for different FE software packages. The translation of the models can be very challenging (Fuchs *et al.*, 2014), as element formulations, material laws and contact settings can differ among different FE codes.

- Varying in-house modifications of HBMs are available (Ghosh *et al.*, 2016).

- No clear protocol describing how simulations should be set up is available. Therefore, boundary conditions can vary considerably (Klug *et al.*, 2017; Klug *et al.*, 2016).

- No positioning protocol specific for HBMs is available. Angles are specified for dummies (SAE International, 2010a), but there is no clear method that can be applied to measure the angles in HBMs (Eggers *et al.*, 2012).

In summary, the application of HBMs is promising for the assessment of VRU assessment, but comparability is unknown and progress in the interpretation of results and harmonisation must be made.

1.3.7   Mixed Approaches

Mixed approaches can be used to combine the benefits of single assessment methods. In this chapter, some examples of mixed approaches are discussed. They are not included in the summary, as they cannot be generalised. Depending on the assessment focus, different combinations are beneficial.

Combination of virtual full-body simulation and physical assessment with subsystems:

For the assessment of deployable systems such as active pop-up bonnets, the timing and impact location of the head are essential information. Such systems have been developed to increase the clearance between the bonnet and underlying structures and, therefore, improve head protection. The system must detect the pedestrian and fully deploy rapidly enough before the head contacts the bonnet. Furthermore, evidence has to be provided that the bonnet and the support structures are stiff enough, so that the additional clearance has not already been significantly compromised due to the body load prior to the head impact.

These parameters cannot be assessed using the subsystem impactors. Therefore, input from simulations is needed: A hybrid approach has been adapted by Euro NCAP for the assessment of deployable systems, which covers virtual simulations with pedestrian models, and physical tests with pedestrian subsystem impactors. The simulations with the pedestrian models are carried out to derive inputs for the subsequent physical tests with headform impactors. The virtual tests cover multiple collision speeds and pedestrian statures: First, the head impact location (*WAD*) and Head Impact Time (*HIT*) for several pedestrian sizes are determined to assess whether the system can be fully deployed by the time of head impact for the most critical pedestrian stature. Based on these results, the bonnet is impacted with the head impactors in their deployed or undeployed state (location dependent) in the physical test. Second, the pedestrian size that is hardest for the sensor system to detect can be determined by means of performing simulations as an alternative to physical tests and to select appropriate test tools. Finally, the bonnet deflection due to the bonnet loading is derived from the simulations with pedestrian models to prove that the head protection is not compromised by a collapse of the bonnet. (Euro NCAP, 2016)

Based on the simulation results, physical tests are performed when the active bonnet is in its deployed, undeployed, or dynamic status. Conventional headform impactors (as explained in Chapter 1.3.4) are used, and the linear accelerations are applied to derive the Head Injury Criterion (*HIC*) values upon which the final scores are based. (Euro NCAP, 2016)

The simulations have to be carried out at varying collision speeds with several sizes of the pedestrian models (6yo, 5th, 50th, 95th). Until 2018, all pedestrian models listed in Technical Bulletin 13 (Euro NCAP, 2015b) could be applied for the virtual part of the assessment. (Euro NCAP, 2016).

Such a list does not cover the effects of altering simulation settings and is hard to maintain as HBMs are continuously revised. Furthermore, the protocol does not include all details for the HBM simulations (e.g. open arm and torso posture, open contact settings), although the effects of these boundary conditions have been shown in several studies (Tang *et al.*, 2016; Chen *et al.*, 2015a; Paas *et al.*, 2015c; Watanabe *et al.*, 2011; Kam *et al.*, 2005; Elliott *et al.*, 2012b; Kerrigan *et al.*, 2009a).

Overall, the described hybrid approach for the assessment of deployable systems can be taken to combine some of the advantages of virtual testing with HBMs and physical tests with subsystems. The boundary conditions for the tests are derived from full-body simulations, and the physical tests allow to carry out comparable assessments of the *HIC*. On the other hand, the procedure has still some drawbacks: The comparability of the simulations with HBMs is unknown, and the *HIC* cannot be used to replicate all head injury mechanisms (Sanchez-Molina *et al.*, 2012; Feist *et al.*, 2009).

Conversion Models

The use of conversion models enables to convert kinematic results into injury predictors on the tissue level. Body regions of HBMs can be isolated to analyse their responses when exposed to external loads. The external loads are usually measured in physical tests and then applied to the FE model (Bourdet *et al.*, 2016; Klug *et al.*, 2015a; Roseveare *et al.*, 2016; Hansen *et al.*, 2013; Siegkas and Ghajari, 2017). Alternatively, a simulation with simplified HBMs or multibody models can be also used as input (Bourdet *et al.*, 2013; Huang *et al.*, 2018b).

This approach allows an analysis of sophisticated injury predictors combined with comparable tests or fast simulations to be made. As a drawback, boundary conditions have to be simplified and, therefore, the biofidelity is lower compared to in full-body simulations.

A high number of generic simulations can also be performed in advance with isolated, detailed FE models to generate lookup tables or statistical prediction models to allow their immediate evaluation (Takhounts *et al.*, 2013; Ji and Zhao, 2015). This can be used to save simulation time, allow decisions to be made rapidly, or ensure that comparable assessment criteria are used. On the other hand, the generalisation of loads leads to lower accuracy in terms of injury prediction and has limited validity (Zhao *et al.*, 2017).

Conversion models can be applied for the assessment of protective equipment for VRUs, such as helmets, as they can be used to improve the significance of the assessment criteria, unlike a mere analysis of pure linear accelerations (Bourdet *et al.*, 2016; Klug *et al.*, 2015a; Roseveare *et al.*, 2016;

Hansen *et al.*, 2013; Deck *et al.*, 2017). As a drawback, they highly depend on the design of experiments of the underlying data points and are only applicable within predefined boundaries.

Combination of Humanoid Multibody Models and FE Human Body Models

The "Virthuman" model is a mix of a multibody and FE models and has been applied for the simulation of VRU impacts. It allows faster simulations to be carried out, but its biofidelity and applicable assessment criteria are limited. (Hynčík *et al.*, 2017)

1.3.8 Summary

In Table 1, all state-of-the-art approaches for the assessment of passive VRU protection are compared. It summarises the advantages and disadvantages discussed in the previous sections of this chapter. The individual grades reflect the personal conclusions of the author based on the review of literature. For the overall rating, the unweighted mean value of all grades was calculated using the following definitions:

- Poor conformity with requirements: 5
- Sufficient conformity with requirements: 4
- Satisfying conformity with requirements: 3
- Good conformity with requirements: 2
- Very good conformity with requirements: 1

Table 1: Comparison of state-of-the-art assessment methods

	Real-world Accidents	PMHS	ATDs	Subsystems	MB models	HBMs
Biofidelity	1	2	3	4	3	2
Assessment Criteria	5	3	3	3	4	3
Comparability	5	5	2	1	4	4
Human Variability	2	3	5	4	1	1
Variability of Scenarios	2	4	3	4	1	1
Mean	3.0	3.4	3.2	3.2	2.6	2.2

The table shows that the two virtual assessment methods using either multibody models or HBMs can most effectively be used to fulfil the defined requirements. Assessments based on real-world accidents, PMHS and ATD have some benefits compared to other methods, but each of these show poor conformity with the requirements in at least one criterion. The current state of the art – testing with subsystems – partly fulfils all requirements.

Virtual testing with HBMs has the best overall grade as it offers a higher level of biofidelity and improved assessment criteria compared to multibody models. If the comparability of HBMs and the objectivity of assessment criteria can be improved, the approach has the potential to be the most applicable method for the assessment of VRU protection. As one method may not effectively fulfil all criteria, the use combinations of methods seems to be beneficial.

1.4 Objective

The overriding aim of the research described in this thesis is to improve VRU protection and reduce the number of fatal and severely injured VRUs.

Pedestrian protection is currently assessed using isolated impactors that represent selected body parts, which is a highly simplified way of considering the complex VRU kinematics. Furthermore, only selected scenarios, types of VRUs and anthropometries are addressed by the state-of-the-art assessment. Virtual testing enables researchers to address these drawbacks, requiring biofidelic virtual models of the VRU. HBMs are detailed numeric replications of the human body and, therefore, promise high levels of biofidelity.

The goal of the work described in this thesis was to answer the following research question:

Are Human Body Models appropriate tools for the assessment of passive VRU safety?

The term HBM is hereby understood as explained in 1.3.6. and refers to validated models that show a high level of biofidelity for load cases that are representative for the assessment focus. The research presented focuses on state-of-the-art HBMs and their potential and limitations are discussed.

The HBMs can be used for assessing kinematics or strains. Suitable assessment criteria have to be defined and comparability has to be ensured to make HBMs applicable for the assessment of passive VRU safety. Therefore, the main research question was further subdivided into three more specific questions:

1. *Are assessment results comparable among different state-of-the-art HBMs and among different institutions performing HBM simulations?*
2. *Are Human Body Models useful for kinematic-based assessments of passive VRU safety?*
3. *Are strain-based assessment criteria derived from simulations with state-of-the-art HBMs appropriate for the assessment of passive VRU safety?*

Possible approaches that can be taken to integrate the HBM in safety assessments are shown throughout the research presented in this thesis to address the research questions.

1.5 Problem Solving Approach and Structure of the Thesis

In the work presented in this thesis, different approaches are shown and discussed that can enable the application of HBMs for the comparable, virtual assessment of VRU protection.

Figure 5 shows the designed assessment methods, which combine several approaches depending on the assessment focus. The HBM can be either used as part of a mixed approach or as a stand-alone method.
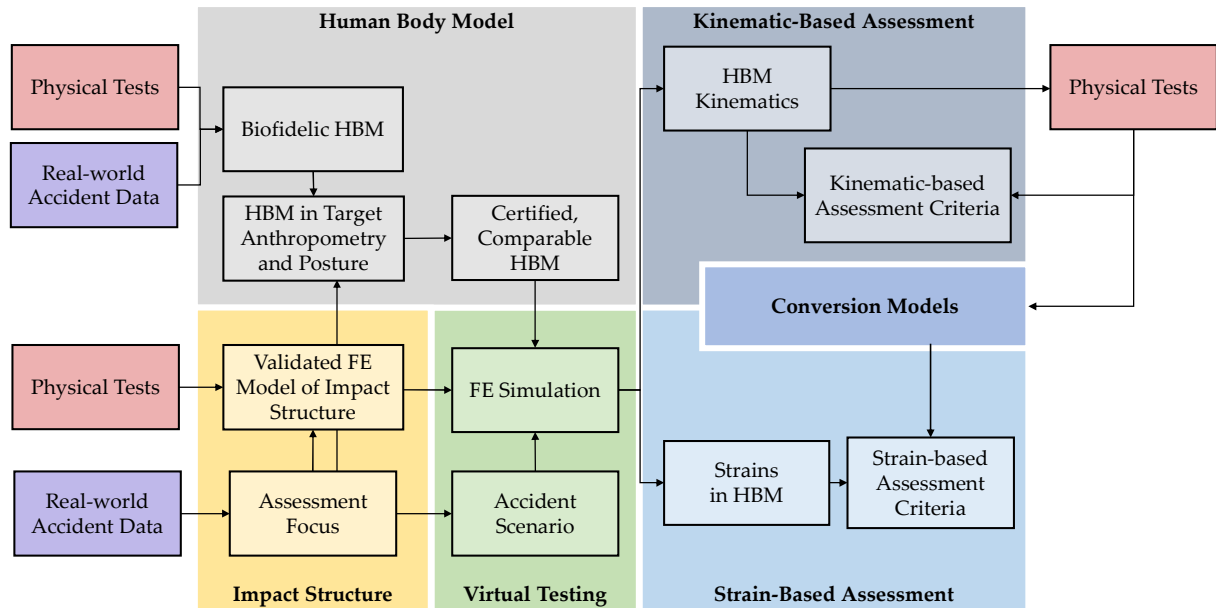
Figure 5: Designed assessment methods

The procedure consists of the following steps, which are explained in detail in later chapters in the thesis:

- **Impact structures** are structures that are impacted by the VRU. The type of impact structures analysed depends on the assessment focus, which can be derived from an analysis of real-world accidents. Examples of impact structures are deployable bonnets, "forgiving" car fronts and helmets. FE models of the impact structures have to be validated by carrying out physical tests to ensure the consistency of behaviour between numeric models and real-world structures. Examples of generic representative impact structures and the definition of boundary conditions for simulations based on real-world accident data are shown in Chapter 3.

- **Human Body Models** have to provide evidence that they are biofidelic before they can be used for safety assessments. They have to be validated with physical tests with humans (ideally PMHS and volunteers) in load cases close to the assessment focus. Their biofidelity has to be appropriate for the intended application. Based on the assessment focus, appropriate anthropometries and postures of the HBM are applied. The finalised models have to be certified to prove their comparability with reference simulations in the specific simulation environment (solver version, control settings, platform) that is used for the virtual testing. Such a certification procedure is developed in Chapter 4.

- **Virtual testing:** The FE model of the impact structure can be virtually tested with the HBM in predefined scenarios. Based on the assessment focus, accident scenarios are selected. Those scenarios can be the output of an upstream assessment of active systems. Based on the scenario, the initial boundary conditions for the simulation are set. No chapter on virtual testing is included in this thesis, as an assessment of a specific protective countermeasure was not carried out. Instead, a focus was placed on the methods associated with the virtual testing, which can be applied for the assessment of any impact structure addressing VRU protection.

- **Kinematic-based assessment:** For this approach, kinematic data such as impact velocities, impact times, impact locations, or accelerations are applied as results from the HBM simulations. The results can either be directly used as kinematic criteria or as input for physical tests and conversion models. The application of HBMs for kinematic-based assessment criteria are discussed in Chapter 5 of this thesis.

- **Strain-based assessment:** For this approach, deformations within the tissue of the HBM resulting from the simulations are applied as assessment criteria. Strain-based injury predictors can be used to indicate injuries and compare protective countermeasures. Strain-based assessment methods are discussed in Chapter 6 of this thesis.

- **Conversion models** allow users to predict strain-based assessment criteria from kinematic data. This can be done by applying the kinematics on FE models (e.g. isolated heads) or by using statistical prediction models. They allow users to draw initial, rapid conclusions and can be used as kinds of filters to reduce the number of simulations. Furthermore, they can be used to improve the comparability of strain-based assessments. No chapter on conversion models was included in the present thesis.

- Conversion models were applied by the author of this thesis, and the results appear in two publications on the assessment of bicycle helmets (Klug *et al.*, 2015a; Feist and Klug, 2016), which is not the focus of the present work.

The developed problem-solving approach was applied throughout the work presented in this thesis either for pedestrians or bicyclists as examples. The presented findings are transferable to all kind of Vulnerable Road Users.

1.6   Significance of the Study

The research presented in this thesis was conducted in an effort to improve the assessment methods, which should help decrease the significant number of fatal and severely injured VRUs. As about half of the road fatalities belong to this group of road users worldwide, this is of substantial interest to members of society.

The findings, methods and tools described in this thesis contribute to a better understanding of VRU impact kinematics, injury mechanisms and assessment methods in several ways:

- The newly developed generic vehicle models, median geometries, stiffness corridors and can be used by researchers for further studies on VRU impacts to improve replication of modern vehicles when performing sensitivity studies, accident reconstructions or for the development of new pedestrian bucks for PMHS test.
- The first certification procedure and detailed simulation protocol specifically for HBMs was developed. The procedure enables users to compare the kinematic response resulting from simulations with a specific pedestrian model using a specific FE solver and specific simulation settings with reference simulations to evaluate comparability. The protocol allows researchers, car manufacturers, regulatory bodies and consumer information organisations to make fair and reasonable comparisons among HBM simulations, which enables them to integrate the HBM in their assessment procedures. The developed protocol can be also applied by researchers developing HBMs to check the robustness of their models, compare translated models in different codes and check the compliance with new solver versions or settings.
- The deviations of kinematic results between a set of numerical pedestrian models in different codes were compared for the first time with deviations resulting from varying boundary conditions with one specific HBM. Those results are essential for the development of proper virtual testing protocols. Recommendations derived from the findings of this study were already implemented by Euro NCAP in January 2018 for the kinematic-based assessment of deployable systems with the updated pedestrian testing protocols and, therefore, had already contributed to the new state of the art.
- To the best knowledge of the author, the first comparison of full body strain-based assessment with a detailed HBM was performed for real-world bicycle accidents. The results show the potential and limitations of strain-based assessment addressing bicyclist safety and can be used by researcher to improve strain-based assessment methods.

2   METHOD

In this chapter, data sources, tools, basic assumptions and principal methodologies that are applied throughout the thesis are explained.

2.1   Accident Analysis

Three different data sources were applied for the analysis of real-world accidents: The Austrian road accident statistics, the Austrian in-depth accident database CEDATU and the international in-depth accident database IGLAD.

The Austrian road accident statistics from "Statistik Austria" include all statistics for all accidents recorded by the Austrian police. Accidents from 2002-2016 were included for the analysis as part of this research work. The data represents the most representative applied data source, as the whole population of accidents reported by the Police is included. The accidents are classified in nine main groups (e.g. pedestrian accident) and several further specifications (e.g. collision with pedestrian while turning to the right with same moving direction) are included, which are described in detail in the available documentation (Statistik Austria, 2000).

Injury severities are classified into "light", "severe" and "fatal" (Statistik Austria, 2010). Based on the Austrian penal code (StGB § 84, 2016), severe injuries are defined as injuries that lead to more than 24 days of health impairment. This classification is based on the estimates made by the law enforcement authorities or the hospital injury report. If the accident victim dies within 30 days of the accident as a result of the incident, it is classified as "fatal" (Statistik Austria, 2010). Before 2011, injury severity could be also classified as "unknown" (Statistik Austria, 2010). Unknown injuries were recoded as "severe" in the presented analysis. Since 2011, this category is no longer present, and the data processing is fully automated, which means that data before 2011 and after 2012 should not be directly compared with each other (Statistik Austria, 2017).

The data from "Statistik Austria" were used in this thesis as examples of European road traffic statistics to analyse collision partners and accident scenarios for different injury severities. The Odds Ratio (OR) was used to compare the odds of fatal injuries for different accident scenarios as described in Equation (1), referring to the numbers explained in Table 2.

Table 2: Methodology used for the calculation of the Odds Ratio

	Scenario A	Scenario B
Number of fatal accidents	n_{F_A}	n_{F_B}
Number of non-fatal accidents	n_{NF_A}	n_{NF_B}

$$OR = \frac{n_{F_A}}{n_{NF_A}} * \frac{n_{NF_B}}{n_{F_B}}$$

(1)

As discussed in chapter 1.3.1, so-called in-depth databases are the only appropriate data source that can be used for a detailed analysis: The in-depth database CEDATU (Vehicle Safety Institute, 2018; Tomasch and Steffan, 2006) currently covers about 3000 cases. Parameters in the database are derived retrospectively from the available documentation for each case, such as police reports, witness statements, photo documentation, autopsy reports and injury reports from the hospital. All accidents in the database were reconstructed using the software PC-Crash to gain additional data, such as pre-crash trajectories, collision speeds and impact locations. (Tomasch and Steffan, 2006)

To get a more international picture, the international, in-depth database IGLAD (Bakker *et al.*, 2017) was applied. IGLAD includes selected cases from the CEDATU and comparable international databases (collection of cases from Germany, Spain, Czech Republic, Italy, Australia, India, USA, France, Sweden, Austria and China) (Bakker *et al.*, 2017). Accidents that occurred between 2007 and 2015 were considered for the IGLAD analysis presented in this thesis.

In the in-depth databases, the Abbreviated Injury Scale (AIS) is used to classify injuries and compare injury severities. Each reported injury is coded based on a coding lexicon. The AIS severity ranges from one for minor injuries to six for maximal injuries and is based on the assessment of threat to life (non-linearly scaled). The MAIS level describes the maximum AIS injury severity, either throughout the whole body or for one body region. (Schmitt *et al.*, 2014; Yoganandan *et al.,* 2015)

2.2   Finite Element Simulations

For crash simulations, the problems are highly dynamic, short and include complex contact situations. Furthermore, a non-linear FE solver is needed for biological tissues and to model the plasticity of materials in crashes (Yoganandan *et al.*, 2015; Crisfield and Borst, 2012; Belytschko *et al.*, 2013). For these transient non-linear analyses, explicit time integration is applied (Nasdala, 2010; Cronin, 2011; Yang, 2018).

A variety of FE software packages is available. These differ greatly in their application purposes and implemented keywords. For crash-simulations, LS-DYNA®, by the Livermore Software Technology Corporation, Virtual Performance Solutions (VPS, before PAMCRASH), by the ESI group, RADIOSS™, by Altair and Abaqus, by Dassault Systèmes® are most commonly used by car manufacturers, suppliers and academic community.

As part of the current research, the explicit solver of the commercial FE simulation software LS-DYNA was applied. The MPI (Message Passing Interface) version allows parallel computing on multiple CPUs (Yang, 2018). Simulations were performed on the High-performance computing (HPC) cluster of TU Graz on a Linux RHEL 5.4 platform with the double precision version R7.1.1 of LS-DYNA (Revision 88920).

LS-DYNA includes numerous predefined keywords that are associated with predefined element formulations, material models, boundary conditions and outputs. LS-DYNA derives the partial differential equations from those keywords and solves them at each time step. (Wu and Gu, 2012)

The keywords are summarised in structured input files for the LS-DYNA simulations (text files). These were created for the presented work using the pre-processing software Visual Crash DYNA (ESI Group) or directly in a text editor.

Figure 6 shows the main points in the process of applying an FE software package. The Finite Element (FE) models consist of discretised geometries with different element formulations grouped in parts. Material Models are associated to each part. The interaction between elements and nodes is described with contacts. External loads and boundary conditions can be defined. As results from the simulations, predefined outputs are gained, such as animated results, nodal outputs, stresses, strains, or interface forces. (Cronin, 2011)

Each of these items are explained in detail in the following chapters.
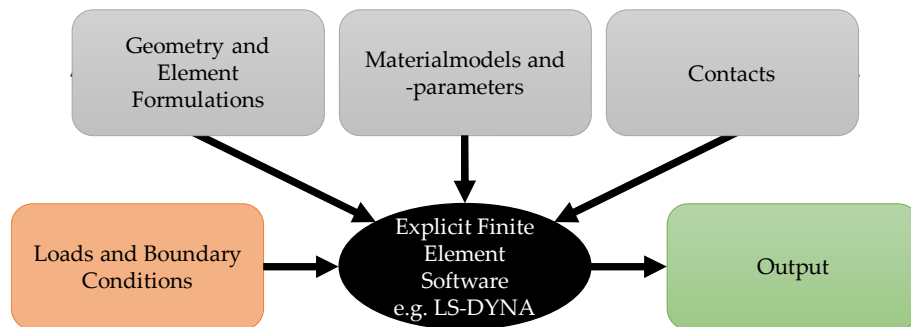
Figure 6: Process for Application of FEM (adapted from Cronin (2011))

2.2.1 Geometry and Element Formulations

The geometry of a FE model has to be discretised with one-dimensional, two-dimensional, or three-dimensional elements:

- To model muscles, springs, or ligaments, one-dimensional beam elements are frequently used. (Cronin, 2011)

- To model thin-walled structures (e.g. cortical bones, metal sheets, membranes) two-dimensional shell elements are applied as they need fewer computational resources than three-dimensional, solid elements. (Cronin, 2011)

- Solid hexahedral or tetrahedral elements are required to model larger volumes, such as foams, organs, brain tissue, or trabecular (spongy) bones. Tetrahedral elements allow the application of automatic meshing algorithms and are, therefore, used for complex geometries or parts have to be re-meshed frequently (e.g. flesh around joints). As a drawback, tetrahedral elements tend to show volumetric locking and, therefore, their behaviour is too stiff. Therefore, hexahedral should be preferably used. (Cronin, 2011; Erhart, 2011)

To reduce computational costs and increase robustness, single integration points or reduced integration element formulations are implemented. These simplifications can lead to "hourglassing", which means that non-physical oscillations with no stress in the element occur.

With specific hourglass models, viscous damping or stiffness control can be added to avoid this numerical issue. (Cronin, 2011; Erhart, 2011)

It was controlled throughout all simulations described in this thesis, that the added "hourglass energy", remains smaller than 10% of the total system energy based on the recommendations of the IMVITER project (García *et al.*, 2012).

For explicit time integration schemes, the Courant condition (Courant *et al.*, 1967) describes the critical time step Δt_c. It is calculated based on Equation (2) in which L_C is the characteristic length. Therefore, the element size is essential for the time step, which can be used for the simulations. The detailed definition of the characteristic length is based on the element form. Detailed definitions can be found in the LS-DYNA theory manual. Equation (3) describes the wave propagation velocity c based of the Young's modulus E, the Poisson's ratio v and the specific mass density ρ. (John O. Hallquist, 2006; Cronin, 2011)

$$\Delta t_c = \frac{L_C}{c} \tag{2}$$

$$c = \sqrt{\frac{E * (1 - v)}{\rho(1 - 2v) * (1 + v)}} \tag{3}$$

In the simulations described in this thesis, a minimum time step was defined for the simulations using the keyword *CONTROL_TIMESTEP (e.g. 4E-4 ms for THUMS simulations). This enables to run simulations with a constant time step and keep single elements from determining Δt_c, which might be smaller than the one applicable to the majority of elements. This is possible because LS-DYNA scales the mass of the single elements that fall below the defined minimum time step. When applying this approach, the added mass has to be checked to avoid implausible results. (Livermore Software Technology Corporation, 2014b)

In the presented simulations, the total artificial mass increase was checked to make sure that it was smaller than 3% of the original total mass (based on recommendations from the IMVITER project (García *et al.*, 2012).

2.2.2   Material Models

Constitutive equations describe the material behaviour and relate stress to deformations (Belytschko *et al.*, 2013). The simplest version of a material model and corresponding constitutive equation is Hooke's law, representing an isotropic linear elastic material. For impact structures and HBMs, more complex material models are needed, such as strain rate dependency, anisotropy, non-linearity and failure, which need to be frequently considered. (Cronin, 2011).

About 300 different material models are implemented in LS-DYNA. The constitutive equations of the material models are described in the LS-DYNA manuals (John O. Hallquist, 2006; Livermore Software Technology Corporation, 2014b, 2014a):

For each type of material, the user can define a set of parameters to adapt the generic material model to the one that should be replicated. For the isotropic, linear-elastic material, *MAT_ELASTIC appropriate mass density, Young's modulus and Poisson's ratio can be defined in the material card in the input file. In more complex material models, a huge number of parameters can be defined to address multiple properties, such as anisotropy, viscoelasticity, non-linearity, or strain-rate dependency, based on the underlying constitutive equations. Some material models also allow users to directly include force-deflection or stress-strain curves obtained from experimental tests. LS-DYNA derives the needed input parameters from those curves together with additional input (e.g. sample dimensions and strain rate) via approximations made during the initialisation process (e.g. for *MAT_OGDEN_RUBBER or *MAT_FU_CHANG_FOAM).

A variety of failure criteria are also implemented in several material models. Elements can either be deleted when these are reached or lose their stiffness.

Throughout the work described in this thesis, material models of the HBMs were not altered from their original status and are, therefore, not further addressed here.

Material parameters used for the generic impact structure are described in Appendix-B: The isotropic, elasto-plastic material (*MAT_PIECEWISE_LINEAR_PLASTICITY) and the foam material for highly compressible foams with low densities (*MAT_FU_CHANG_FOAM) were applied. Stress vs. strain curves were used as input for this material model to define loading and unloading characteristics.

2.2.3 Contacts

A variety of contact types are implemented in LS-DYNA, which can be used when creating the model setup:

For standard contacts, the keyword *CONTACT_AUTOMATIC_SURFACE_TO_SURFACE is most frequently used in LS-DYNA. It allows sliding with closure and separation. Slave and master surfaces are selected automatically within LS-DYNA from the part IDs defined by the user. As soon as the slave nodes penetrate the master segment, a force is applied to the node proportional to the amount of penetration (spring-like behaviour). Three main formulations that define the contact stiffness are available for the contacts: standard penalty formulation, soft constraint penalty formulation and segment-based penalty formulation. (John O. Hallquist, 2006)

For *standard penalty formulation* contacts, the contact stiffness k_i is derived from a scale factor f_{si}, the bulk modulus K_i, the face arae of the element A_i that is penetrated and the volume V_i as in Equation (4). For very soft materials, this formulation can lead to undesired soft behaviour and excessive penetration. (John O. Hallquist, 2006)

$$k_{penalty} = \frac{f_{si} K_i A_i^2}{V_i} \tag{4}$$

The *soft constraint formulation* tends to be more robust for such applications, as it uses an additional stiffness based on the Courant stability criterion as shown in Equation (5). A scale factor

f_{soft} can be defined. The parameter m^* is a function of the mass of slave and master nodes and Δt_c is the initial solution timestep, which is adjusted to the current time step, if it increases during the calculation. Both contact stiffnesses ($k_{penalty}$ and k_{soft}) are computed at each time step, and the higher value is applied. (John O. Hallquist, 2006)

$$k_{soft}(\text{t}) = 0.5 \cdot f_{soft} \cdot m^* \cdot \left(\frac{1}{\Delta t_c(t)}\right) \tag{5}$$

For the *segment-based penalty formulation*, the mass of the contacting segments (m_1 and m_2) is used instead of the nodal mass m^*. The stiffness is adjusted with a combination of scale factors, summarized with f_s as shown in Equation (6). In contrast to the "soft constraint formulation", the timestep Δt_c is only updated if it increases more than 5%. (John O. Hallquist, 2006)

$$k_{soft\_seg}(\text{t}) = 0.5 \cdot f_s \cdot \left(\frac{m_1 m_2}{m_1 + m_2}\right) \cdot \left(\frac{1}{\Delta t_c(t)}\right) \tag{6}$$

LS-Dyna also offers the possibility to model a large degree of penetration (comparable to multibody solvers) for generic structural behaviour between a deformable and a rigid surface by using the keyword *CONTACT_RIGID_BODY_ONE_WAY_TO_RIGID_BODY. Force or pressure can be defined as a function of penetration. An additional curve for unloading can be also defined. (John O. Hallquist, 2006)

This approach is useful to easily parameterise structural behaviour. Therefore, it was applied to model the Generic Parameterisable Vehicle models (GPV) for the real-world accident reconstructions presented in Chapter 6.

2.2.4   Loads and Boundary Conditions

A variety of keywords for the definition of initial conditions, such as velocities, accelerations, or constraints, can be defined. Furthermore, the coordinates of nodes can be transformed to bring them into the desired initial position.

Throughout the work described in this thesis, the coordinate system of the vehicle and the global coordinate system is defined as shown in Figure 7:

- *x-direction* is the driving direction of the vehicle (longitudinal axis) and $x = 0$ at the foremost point of the vehicle at t0

- *y-direction* is the vehicle lateral axis with $y = 0$ at the vehicle centreline

- *z-direction* is parallel to the vehicle height axis, facing upward with $z = 0$ at the ground level
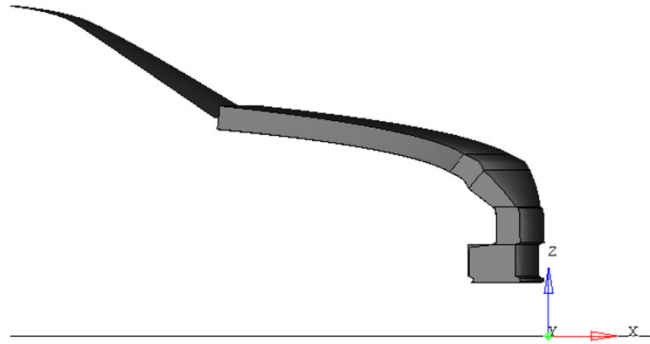
Figure 7: Coordinate system of the vehicle as applied in this thesis

To define initial velocities, the keyword *INITIAL_VELOCITY_GENERATION was used together with sets defining the nodes or parts to which the velocity should be applied. Gravitation was considered by applying an acceleration field in the z-direction with *LOAD_BODY_Z throughout all presented simulations. A rigid wall was modelled as the ground level at $z = 0$. The position of the HBM relative to the impact structure was defined with an *INCLUDE_TRANSFORM keyword and by defining an appropriate offset with *DEFINE_TRANSFORMATION. The keyword *INCLUDE_TRANSORM was also used to adjust the unit system of THUMS from *mm, s, t* into *mm, ms, kg*, which was the baseline unit system used in all simulations.

2.2.5   Output

LS-DYNA provides quantitative and animated results as output. The desired output has to be defined by the user with *DATABASE keywords.

Animated results are prepared as binary files and can be visualised by using special postprocessing software. A time interval of 2 ms was chosen to export animations. Animations were checked for contact issues by making sure that no sticky nodes or intersections were visible.

Time histories of nodes, elements, contact forces, energies and section forces were specified as quantitative output. Output is provided from multiprocessor simulations in binary files. These *binout* files were analysed using the postprocessing software Hyperview (Altair) or DYNASAUR (further explained in Chapter 2.3.3).

To gain output for node histories, sensora have to be specified. Additional nodes were created for this purpose and connected with the surrounding structure by interpolation constraints (Keyword *CONSTRAINED_INTERPOLATION in LS-DYNA). This means that the motion of the single node that is used as a sensor depends on the average motion of a set of master (independent) nodes of the surrounding structure. This approach is recommended for HBM simulations (Golman *et al.*, 2015), as the response of a single node from a deformable structure would not lead to meaningful results. The keyword used does not change the behaviour of the slave nodes, which would be the case when using other approaches like *CONSTRAINED_NODAL_RIGIDBODY.

The parameter IACCOP was set to 1 in *CONTROL_OTUPUT, so that the accelerations were smoothed (averaged between output intervals) before being sent to the *nodout* file.

Outputs from *matsum* and *glstat* files were used to check mass scaling and energy balance. For the evaluation of contact forces, *rcfroc* files were used. The following quality criteria were checked for all simulations, based on the recommendations of the IMVITER project (García *et al.*, 2012):

- Hourglass energies were lower than 10% of the total energy

- Total energy remained constant within a 15% tolerance range

- Contact energy at the simulation start was less than 1% of the total energy

- Artificial mass increase remained less than 3%

The strain tensors that LS-DYNA provides as output are based on the integration of the strain rate tensor. For shell elements, the strain tensor is integrated at each integration point, so that the results contain at least two strain tensors (based on the number of specified integration points, additional results can be available).

2.3   Applied Human Body Models

As part of the research described in this thesis, the LS-DYNA versions of two different Human Body Models were applied:

- The Total Human Model of Safety (THUMS) Version 4

- The Global Human Body Model Consortium-owned GHBMC simplified pedestrian (PS) model

Both models are commercially available and also offer academic licensing. The HBMs were applied and were not further developed as part of the work presented in this thesis. Both models can be termed as "state-of-the-art models", although they have several significant differences. They have been developed over many years. Their biofidelity has been continuously improved, and several papers on the development, validation and applications of the models are available.

THUMS

The Toyota Motor Corporation and Toyota Central R&D Labs, Inc have jointly developed THUMS models since 1997 in an attempt to understand injury mechanisms in car crashes. The models have undergone several significant revisions. The level of detail in the model has significantly increased over the years. (JSOL Corporation, 2018)

Version 4 of THUMS was released in 2009 and is the most detailed HBM of the model family. The HBM replicates human anatomy in a high level of detail and includes detailed models of internal organs and the brain. It is available in pedestrian and occupant postures in four different sizes (6yo child, 5th percentile female, 50th percentile male, 95th percentile male). (JSOL Corporation, 2018)

The geometry data for these models were derived by the developers from scans of living human subjects which were close to the particular percentile. For the model representing the

anthropometry of an American 50th percentile male (AM50), scans of a 39-yo male with 173 cm body height and 77 kg bodyweight were used. (Kitagawa and Yasuki, 2014; Shigeta *et al.*, 2009)

The AM50 pedestrian model was applied for the research described in this thesis. The model consists of around two million elements, each with a size of 3-5 mm (Kitagawa and Yasuki, 2014; Watanabe *et al.*, 2011). The mesh fulfils several conventional quality criteria (Kitagawa and Yasuki, 2014; Watanabe *et al.*, 2011).

All simulations with the THUMS v4 models presented in this thesis were performed with a timestep of 4E-4 ms and default control settings of the model. The fracture mode of the bones was deactivated in all simulations.

GHBMC Models

The Global Human Body Models Consortium (GHBMC) was formed in 2006 and consists of car manufacturers and suppliers working together with research institutes and government agencies. The models were developed at multiple universities worldwide as well as software developers and other consortia around the globe. (GHBMC, 2016)

The geometry of the AM50 model was derived by the developers of the models from medical images of a 26-year old male with 175 cm body height and 78.6 kg body weight. A highly detailed CAD geometry was developed using a multi-modality protocol(Gayzik *et al.*, 2011), collecting a total of 72 scans (MRI and CT). MRI scans were also acquired with the volunteer in an upright position, and the outer surfaces were recorded with a 3D laser scanner. The scans of the individual were used as a template. The segmented data were compared and augmented with data from over 75 literature sources on the average morphology of the human body. (Untaroiu *et al.*, 2015; Gayzik *et al.*, 2011)

The simplified pedestrian (PS) GHBMC model is based on the GHBMC model in the occupant posture. The developers attempted to develop a biofidelic pedestrian HBM with low computational costs (Untaroiu *et al.*, 2015; Gayzik *et al.*, 2011).

Several modifications of the occupant model were performed by the GHBMC developers:

- The bones of the occupant GHBMC model were reoriented to match the CAD data of a standing human. A special focus was placed on the knee and ankle joint, which are modelled with a high level of detail. (Untaroiu *et al.*, 2015)
- The lumbar spine was improved compared to the occupant model: Ligaments were added as beams to the rigid lumbar vertebras connected with joints. The properties were optimised to meet the results of PMHS component tests (Rohlmann *et al.*, 2001) as closely as possible. (Untaroiu *et al.*, 2015)
- To reduce computational costs, the models of organs and the brain were replaced by the developers with representative, added masses on nodes and a homogenised filling structure model. This modification does not affect the global response of the HBM, but limited the applicable assessment criteria. (Untaroiu *et al.*, 2015)

The AM50 PS GHBMC model was morphed to the anthropometry of a 95th percentile American Male (Pak and Untaroiu, 2016) and 5th percentile female for additional models. Furthermore, the AF05 model was morphed and modified to fit the anthropometry of a six-year-old (6yo) child (Meng *et al.*, 2017). Within the 6yo model, the material properties of the lower extremities were adjusted to meet those of a child (Meng *et al.*, 2017).

All simulations with the GHBMC models presented in this thesis were performed with a time step of 3.6E-4 ms and the default control settings of the model. The default settings for bone and ligament fracture were active in all simulations. The PS models representing an AM50 and a 6yo child were applied.

2.3.1 Biofidelity

Both HBMs were validated with a number of component level and full-scale tests by the developers of the models. In most of the studies, responses are compared qualitatively.

Objective biofidelity assessments enables a quantitative comparison of the level of biofidelity to be made. The CORA (CORrelation and Analysis) method can be used to compare two curves resulting in one number describing the correlation of those curves objectively (Gehre *et al.*, 2009). CORA was further improved by the ISO working group for virtual testing (TC22/SC10/SC12/WG4) and published as an ISO objective rating method (Barbat *et al.*, 2013). The total rating is calculated from three different scores: one describing the phase shift error, one, the magnitude error and one, the slope error. An ISO rating > 0.94 indicates excellent and a score ≤ 0.58, a poor correlation (Barbat *et al.*, 2013).

The biofidelity of THUMS v4 model was validated with more than 27 validation cases, covering full-scale and component-level PMHS tests by the developers of the model. Four full-scale pedestrian load cases were also used to validate the model. The response of the THUMS v4 model for impacts at 40 km/h was compared with the PMHS tests published by Subit *et al.* (2008) and Schroeder et al. (2008), replicating impacts with a SUV, Sedan, Mini Van and Mini Car (For details on the PMHS tests, see Table Appendix A-1). Trajectories, final coordinates and injuries were compared and showed good correlation. (Kitagawa and Yasuki, 2014)

Poulard *et al.* (2016) replicated two PMHS tests with a mid-sized sedan, which had been performed by Subit et al. (2008) using a personalised version of the THUMS v4.01 pedestrian model. They showed that, if HBM was morphed to the anthropometry of two PMHS (matching knee and pelvis heights), very similar *HIT* (± 1 ms; i.e. less than 1%), *WAD* (± 30 mm; i.e. less than 2%) and Head Impact Velocities (+0.4m/s, i.e. less than 3%) were achieved to those in the PMHS tests (Poulard *et al.*, 2016).

An objective rating was applied in three different recent studies to compare the PMHS and THUMS v4 kinematics upon pedestrian impacts:

Paas *et al.* (2015c) compared the response of THUMS v4 with 6 degree-of-freedom kinematics recorded in PMHS tests with natural arm posture. A general good correlation of THUMS was reported for in-plane (x-z) motions. Poor scores were reported for displacements in y-direction,

which were generally small in the experiments. The best overall correlation and highest CORA scores were achieved when the height of the pelvis was aligned with the PMHS (average CORA score of 0.5 compared to 0.25 for the baseline simulations). It was also shown that the CORA score was unexpected high for one case, although the visual comparison showed fundamental differences between the simulation and PMHS test. (Paas *et al.*, 2015c)

Wu et al. (2017) compared the response of THUMS v4.01 with recent PMHS tests performed at the University of Virginia Centre for Applied Biomechanics (Forman *et al.*, 2015a; Forman *et al.*, 2015b). Good ISO scores (0.56-0.98) were reached for the trajectories in the driving direction (x) and vertical (z) direction of the car for all targets and tests, as well as for the head velocity (0.71-.093). Poor ISO ratings were observed for the lateral displacements relative to the car / sagittal plane of the pedestrian (0.008-0.55) as well as for some of the accelerations, angular velocities and contact forces. Limitations of the FE pedestrian buck model were mentioned as one possible reason for discrepancies. Furthermore, only a basic morphing approach was used. The hip heights were not aligned between HBM and PMHS. Head impact times differed up to 7 ms (5%) between HBM and PMHS. In the case with the closest match between hip heights, the difference in terms of *HIT* was smallest (3 ms = 2%). The authors of this study concluded that objective rating methods should not be used as the sole criterion for rating the biofidelity of a model, and that a certain degree of caution has to be taken when applying such methods, as results can be sensitive to the general shape of the response due to its type and settings, such as the choice of the interval of the signal. (Wu *et al.*, 2017)

Chen *et al.* (2018) morphed the pedestrian model to meet the anthropometric specifications of two obese PMHS. When the model was personalised, it reproduced high CORA scores for trajectories (CORA score = 0.927 ± 0.092), velocities (0.975 ± 0.027), accelerations (0.862 ± 0.072) and strains (0.707 ± 0.143). (Chen *et al.*, 2018).

For the GHBMC model, fewer publications are available, as the model is relatively new. Some validation cases have been performed specifically with the simplified pedestrian model in addition to those published for the occupant model. The overall kinematics upon pedestrian impacts were compared with the full-scale PMHS tests published by Kerrigan *et al.* (2007) for impacts with a mid-sized family car at 40 km/h. The model was not morphed to the PMHS of varying sizes, but showed the best correlation of the trajectories with the test in which the height of the greater trochanter of the PMHS was close to that in the model. Discrepancies in the injury prediction were observed for ligament rupture. (Untaroiu *et al.*, 2015)

All validation load cases relevant for VRU load cases are summarised in Table 3. Information for THUMS v4 was taken from Watanabe *et al.*, 2011; Kitagawa and Yasuki, 2014; Kimpara *et al.*, 2006; Paas *et al.*, 2015c; Wu *et al.*, 2017; Poulard *et al.*, 2016. The validation of the GHBMC PS model is described in Untaroiu *et al.*, 2015; Mao *et al.*, 2013; Untaroiu *et al.*, 2018; Untaroiu *et al.*, 2013. As the lower extremity model was used from the detailed occupant model, additional validation cases were taken from Untaroiu *et al.*, 2013.

Table 3: Validation of the GHBMC PS and THUMS v4 pedestrian models

	THUMS v4		GHBMC PS	
	PMHS tests	**Validation of**	**PMHS tests**	**Validation of**
Lateral head impact	Yoganandan *et al.*, 2004	Force-time histories and peak force of contact surface	Yoganandan *et al.*, 1995	Maximum force and fracture pattern (published for occupant model)
Lateral Chest Impact	Viano, 1989 Shaw *et al.*, 2006	Chest force-deflection, number of rib fractures	Viano, 1989	Impact force-time histories (full-scale impacts)
Lateral Pelvis Impact	Guillemot *et al.*, 1997	Force-time response of isolated pelvis	Viano, 1989	Impact force-time histories (full-scale impacts)
Lateral Shoulder Impact	Ono *et al.*, 2005	Displacement vs. time from volunteer tests	Viano, 1989	Impact force-time histories (full-scale impacts)
Lumbar spine	Demetropoulos *et al.*, 1998	Flexion and extension moment vs. angle Forces-displacement characteristics	Rohlmann *et al.*, 2001	Flexion, extension and bending angle
Knee bending	Bose *et al.*, 2004	Moment vs. bending angle	Bose *et al.*, 2008	Moment vs. bending angle; MCL and ACL rupture
Full-scale PMHS tests	Schroeder *et al.*, 2008	Trajectories and injuries	Kerrigan *et al.*, 2007	Trajectories and injuries
	Subit *et al.*, 2008	Trajectories and injuries, *HIT*, *WAD*		
	Forman *et al.*, 2015a	Time-dependent head kinematics, ISO scores		
	Paas *et al.*, 2015b	Time-dependent kinematics, *HIT*, *WAD*, CORA scores		
	Chen *et al.*, 2018	Time dependent kinematics, CORA scores		
Femur bending	Yamada and Evans, 1970	Force–displacement of isolated femoral bone	Funk *et al.*, 2004	Force–displacement and force level at fracture
Lower leg bending	Schreiber *et al.*, 1998	Force–displacement of tibia bone with flesh	Untaroiu *et al.*, 2008a	Bending moment vs. axial force
Lateral knee impact	Kajzer *et al.*, 1997	Tibia acceleration vs. time	Information not available for simplified pedestrian model	
Head-Neck Drop	Nightingale *et al.*, 1997	Contact forces vs. time	Information not available for simplified pedestrian model	
Head-Neck Bending	Stemper *et al.*, 2004	Head angulation and retraction relative to T1		
Intracranial pressure	Nahum *et al.*, 1977	Pressure vs. time at four locations for frontal impact	Not applicable, as brain was simplified	
Brain Displacement	Hardy *et al.*, 2001; Kleiven and Hardy, 2002	x vs. z motion of 10 targets	Not applicable, as brain was simplified	

Based on the available literature which described the biofidelity of the THUMS v4 and GHBMC PS model, both models were found to be appropriate for application within the presented work to answer the research questions.

2.3.2 Positioning

To bring THUMS into the desired initial posture, simulations were performed. The displacement of selected anatomic landmarks was prescribed to move the HBM until the target posture was achieved. The displacement-time functions were derived with internal tools developed by Dr. Florian Feist. The tools allow a preview of the final posture with a highly simplified model that includes the main joints of the HBM. Appropriate displacements were derived from user-specified joint rotations. For the positioning of the bicyclist, a simple visualisation in Microsoft Excel is available. A higher degree of freedom was needed for the pedestrian, so visualisation was implemented in the Pre-Processor Visual-Crash Dyna by using the integrated Dummy Positioning tool. The derived displacements were included as parameters in the prepared simulation input files to prescribe the motion (using the keyword *BOUNDARY_PRESRIBED_MOTION). Nothing in the HBM was modified for the simulations to allow anatomic correct movements of the human joint. After 100 ms simulation time, the model achieved its final posture. The coordinates of all nodes in the final frame of the animated results were exported with the post-processor Hyperview (Altair). From these data, the coordinates of the nodes from the original HBM were replaced with the exported coordinates. The mesh quality was finally checked before running the main simulations with the adjusted HBM posture.

This method avoids biomechanically implausible movements. Ligaments and the flesh around the joint are deformed, and intersections between bones are avoided due to the defined contacts within the HBM. As a drawback, this method is time consuming and does not allow 100% precise positioning, as too many boundary conditions would lead to an excessive amount of overdetermination, which causes bones to deform during the positioning simulations.

Angles and heights were measured to compare the initial postures using a measurement protocol that was developed as part of this research work. The measures were based on clearly described reference points and were, therefore, comparable between different HBMs. The definitions of the reference axis and the specification of the reference points is provided in the tables and figures in Appendix C.

2.3.3 Postprocessing

As conventional postprocessing tools were found to be not robust and flexible enough for the postprocessing of HBM results, a postprocessing tool called "DYNASAUR" (Schachner *et al.*, 2018; Klug *et al.*, 2018c) was developed by the author of this thesis together with Peter Luttenberger, Martin Schachner, Jakub Micorek and Robert Greimel. DYNASAUR was published as open source software under the GNU GPL v3 license and can be downloaded from Gitlab (Schachner *et al.*, 2018).

The tool was written in Python. It is able to handle big data and probabilistic and deterministic injury predictors to be easily implemented to quantify HBM results. Binary output files (binout) from LS-DYNA are used for the evaluations. The input reader transforms the default stresses and strains provided by the element history file into the principal directions and prepares an efficient data structure. Four different modules for the further postprocessing were implemented in DYNASAUR: "CSDM", "Universal", "Rib fracture" and "Cross section". The first three modules of DYNASAUR v1.0 were applied as part of the research presented in this thesis with the following settings and background:

Module CSDM: The module allows the calculation of the percentage of volume of a body part that exceeds a specified threshold. The Cumulative Strain Damage Measure (CSDM) is frequently applied as a strain-based brain injury predictor in finite element head models (Takhounts *et al.*, 2003; Kimpara and Iwamoto, 2012; Katsuhara *et al.*, 2014). The percentage of the brain's volume that exceeds a pre-defined strain is calculated. As reported in the literature (Watanabe *et al.*, 2011), a principal strain (PS) of 0.25 was chosen as strain limit. The original volume of each element of the brain was exported using LS-PrePost (v4.5) and provided as an input file (*volume.key*).

Module Rib Fracture: The module includes a probabilistic rib fracture prediction model published by Forman et al. (2012). The maximum Principal Strains for each element of the cortical rib bones are evaluated to assess the risk of a fracture. The step-function published by Forman et al. (2012) was used to evaluate the risk of fracture for each rib for specific ages based on the maximum strain observed for one rib. The risk of fractures of single ribs is then in the end summarized to assess the risk of a specific number of rib fractures using the probabilistic equation provided by Forman et al. (2012).

Module Universal: The module allows the analysis of stresses and strains on body parts in detail using a variety of user-defined settings. The following general settings were used for the presented analysis:

- Principal strains were analysed

- The strain outputs of different integration points of shell elements were averaged

- Tension and compression were not distinguished

- 95th and 99th percentile principal strains (PS) were calculated, as shown in Figure 8
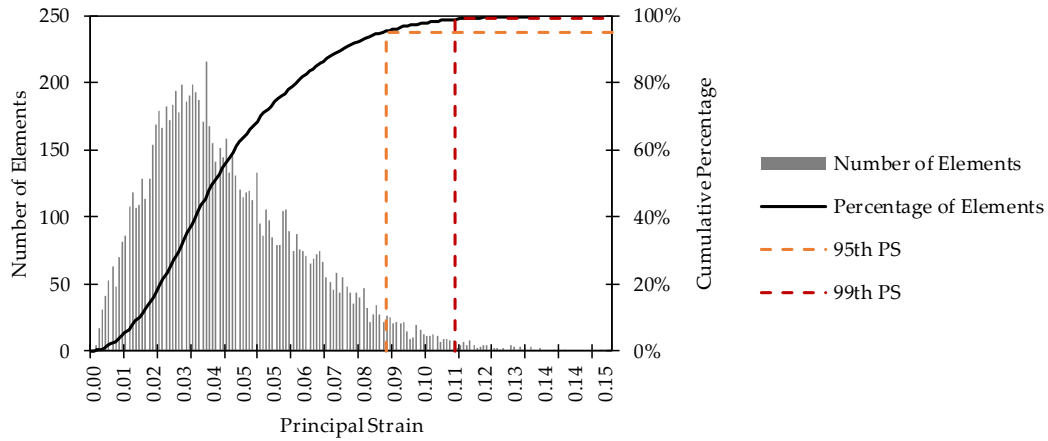
Figure 8: Definitions of 95th and 99th percentile strains

2.4 Assessment Criteria

To identify appropriate assessment criteria, relevant body regions were identified in a first step. Based on these findings, applicable criteria were collected based on the available literature, and objective definitions are provided below.

2.4.1 Relevant Body Regions

The relevance of different body regions was analysed based on IGLAD data and compared to findings reported in the literature.
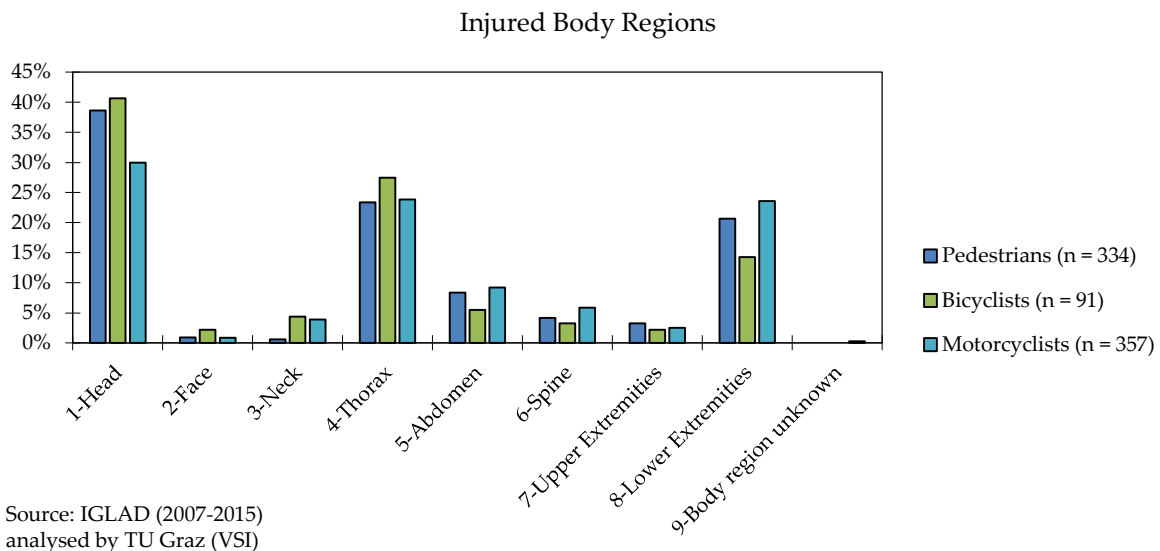
Source: IGLAD (2007-2015)
analysed by TU Graz (VSI)

Figure 9: Injured AIS 3+ body regions of VRUs in cases from IGLAD (2007-2015)

As shown in Figure 9, the results of the IGLAD analysis indicate that the three most relevant body regions for serious injuries (AIS 3+) for all groups of VRUs is the head followed by the thorax and

lower extremities. These findings are in accordance with those from other studies based on the analysis of the GIDAS database (Fredriksson and Rosen, 2012; Wisch *et al.*, 2017; Fredriksson and Sui, 2015; Piantini *et al.*, 2017).

2.4.2 Kinematic-Based Assessment Criteria

The kinematic assessment placed a focus on the head, as it was shown in the previous section that this is the most relevant body region for VRUs regarding severe injuries.

The head impact time (*HIT*) is defined as the time from the first increase in the bumper contact force (*C*) until the first increase in the contact force between the head and vehicle (*H*), as shown in Figure 10 and described in Equation (7)

$$HIT \ [ms] = H - C \tag{7}$$

H is defined as the time at which the contact force between head and vehicle starts to increase (first time when the contact force deviates from zero). The acceleration measured within the head CoG, was also used to double-check the result, as shown in Figure 10. To determine *C*, only the contact between the lower extremities and bumper was considered (as this is also used as a trigger for active bonnets). A first contact between upper extremities and bumper was ignored.
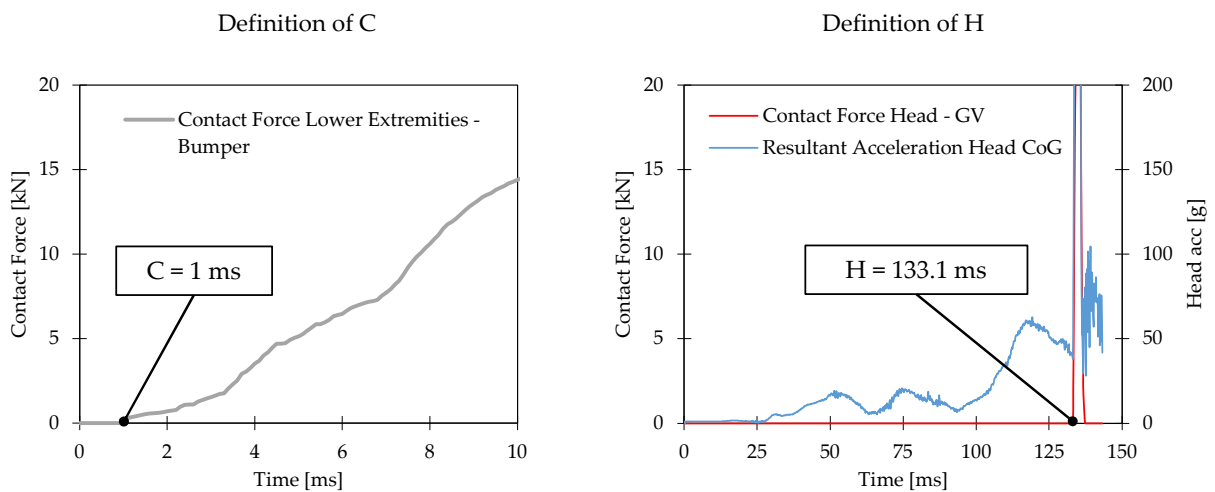
Figure 10: Example for calculation of *HIT* based on *H* and *C*

The Head Impact Velocity (*HIVel*) was defined as the value of the resultant velocity of the head of the pedestrian relative to that of the vehicle 0.1 ms before the head impact. The velocity of the vehicle in x-direction was subtracted from the global head velocity in x-direction before the resultant velocity was calculated.

In addition to these global kinematic assessment criteria, kinematic injury criteria based on nodal histories were applied to assess the head injury risk from the simulation results provided in Chapter 6. Calculations were carried out in the software DIAdem by National Instruments using the following injury criteria and risk curves:

In legislative and consumer information testing related to transport safety, the head injury criterion (*HIC*) is commonly used to quantify the risk of injury to the head. The *HIC*, established by Versace (Versace, 1971) is based on the resultant head acceleration a_{res} [g] and the impact duration $(t_2 - t_1)$ as shown in Equation (8). The maximum *HIC* value of varied time windows with a maximum duration of 15 ms is provided as *HIC15*. A CFC (Channel Frequency Class) 1000 filter was applied on the acceleration signals in the three directions, before the resultant acceleration was derived, that was used for the calculation of *HIC*.

$$HIC = (t_2 - t_1) \cdot max\left[\frac{1}{(t_2 - t_1)}\int_{t_1}^{t_2} a_{res}(t)dt\right]^{2.5} \tag{8}$$

Equation (9) was used to derive the risk of an AIS 4+ head injury based on *HIC* (Prasad and Mertz, 1985; Mueller *et al.*, 2015; Mertz *et al.*, 1996).

$$p(AIS4+) = Normal\left(\frac{HIC - 1434}{430}\right) \tag{9}$$

To analyse the AIS 3+ head injury risk, Equation (10), based on the American Regulation FMVSS 201 (1999), was applied (Mueller *et al.*, 2015):

$$p(AIS3+) = \frac{1}{1 + e^{3.39 + \frac{200}{HIC} - 0.00372 * HIC}} \tag{10}$$

As the *HIC* omits rotational loads, the Brain Injury Criterion (*BRIC*), was introduced in 2011 to predict brain injuries (Takhounts *et al.*, 2011) and later, in 2013 (Takhounts *et al.*, 2013), it was revised and abbreviated as *BrIC*. The criterion was found to correlate with the response (MPS) of the simulated injury monitor (SIMon) and the Global Human Body Models Consortium (GHBMC) head model and can, therefore, be referred to as the "Conversion Model". As shown in Equation (11), the *BrIC* is a function of the ratio of the maximum rotational velocities (ω_{max}) and critical values for each (local) direction of head rotation. (Takhounts *et al.*, 2013)

$$BrIC = \sqrt{\left(\frac{\omega_{max\_x}}{\omega_{cr\_x}}\right)^2 + \left(\frac{\omega_{max\_y}}{\omega_{cr\_y}}\right)^2 + \left(\frac{\omega_{max\_z}}{\omega_{cr\_z}}\right)^2} \tag{11}$$

The 'new' *BrIC* as described in (11) was applied in this work using the critical values published by Takhounts *et al.* (2013): $\omega_{cr_x} = 66{,}25\frac{rad}{s}$; $\omega_{cr_y} = 56{,}45\ rad/s$; $\omega_{cr_z} = 42{,}87\ rad/s$.

The unfiltered rotational velocities of the head CoG were applied from the node history file.

A local coordinate system was included in the head CoG of the HBM using a x-y plane parallel to the Frankfort Plane. The x-direction was defined parallel to the line from the midpoint of the left and right external *auditory meatus* to the midpoint of the lowest points of the left and right *orbit*. The y-axis was defined parallel to the line reaching from the previously constructed starting point to the upper margin of the right external *auditory meatus*.

The risk of an AIS 4+ risk is described with Equation (12). A BrIC of 1 was defined by Takhounts *et al.* (2013) as corresponding to a CSDM = 0.425, which signifies a 30% probability of AIS 4+.

$$p(AIS4) \ = \ 1 - e^{-\left(\frac{BrIC}{1.204}\right)^{2.84}} \tag{12}$$

The original risk curve was scaled by Takhounts *et al.* (2013) using data from animal tests to gain risk curves for other injury severities. Equation (13) was used to derive the risk of an AIS 3 brain injury based on BrIC.

$$p(AIS3) \ = \ 1 - e^{-\left(\frac{BrIC}{0.987}\right)^{2.84}} \tag{13}$$

2.4.3   Strain-Based Assessment Criteria

HBMs offer the possibility to analyse not only kinematic-assessment criteria, but also deformations of the human body as injury predictors and, therefore, so-called strain-based assessment criteria.

The postprocessing software DYNASAUR (explained in 2.3.3) was adjusted to THUMS v4 by modifying the definition file (*dynasaur.def*) and preparing a *volume.key* file that included the volume of each element of the parts for which the CSDM calculation is intended.

The limits listed in Table 4 reported in the literature were used as strain-based injury predictors in this work.

Table 4: Strain-based assessment criteria

Injury	Injury Predictor	Threshold	Source	Model used in source
Cortical bone fracture	PS	0.015	Wu *et al.*, 2017	THUMS v4
Brain DAI	CSDM (0.25)	54%	Watanabe *et al.*, 2011	THUMS v4
Brain tissue damage	PS	0.3	Watanabe *et al.*, 2011	THUMS v4
Number of rib fractures	PS	Step function	Forman *et al.*, 2012	Modified THUMS v3

2.5   Generic Impact Structures

Impact structures are understood as anything that is impacted by the VRU. This means that impact structures include all kinds of vehicles, the environment as well as personal protective equipment. The author was also involved in published studies (Klug *et al.*, 2015a; Feist and Klug, 2016) on the application of Human Body Models for the assessment of helmets, but these results were not included in the present thesis. The current thesis includes the results of studies on passenger cars as impact structures instead, as they are the most relevant collision partner (see Chapter 1.1).

As it is aimed to discuss the applicability of HBMs for the assessment of passive VRU protection in general, generic vehicle models were applied instead of a single serial vehicle model.

The use of generic vehicle models gave the author the freedom to publish all results obtained and freely modify the vehicles. This is not the case for FE vehicles of serial cars, as they belong to car manufactures, are covered by Non-Disclosure Agreements and are usually encrypted.

Furthermore, the application of a single serial car would have limited the general applicability of the presented work.

The ideas and modelling approaches for the applied generic vehicle models were developed by Dr. Florian Feist (Feist, 2016).

Two different approaches were used throughout the work described within this thesis. These are explained in more detail in Chapters 4.1.2 and 6.1.1. In the Chapters 3-5, Generic Vehicle (GV) models were used that are easy transferable to other codes and representative for the European fleet. In Chapter 6, a Generic Parameterisable Vehicle Model (GPV) was applied that enables to replicate specific cars of real-world accidents.

2.5.1 Parametrisation of Vehicle Geometry

The geometry of the vehicle was parameterised with Bezier curves and a total set of 120 parameters: The vehicle midsection was subdivided into ten curves as shown in Figure 11. The start- and end-points and corresponding slope of the tangents were defined for every single curve. The start-point is abbreviated with Ld (leading) and the end-point, with Tr (Tracing curve). The curvature in the y-direction (top-view) was described by using four additional parameters that are shown on the bottom of Figure 11 for each start- and end-point of the curves of the midsection. This resulted in a total of 120 parameters for the whole 3D vehicle front. The coordinates of the edge in y-direction were named with E and those of the Midsection, with M. The origin of the vehicle coordinate system was defined such that the most frontal point of the vehicle, the ground level and the vehicle midsection defined the origin. The direction of the axes are shown in Figure 11. (Feist, 2016)
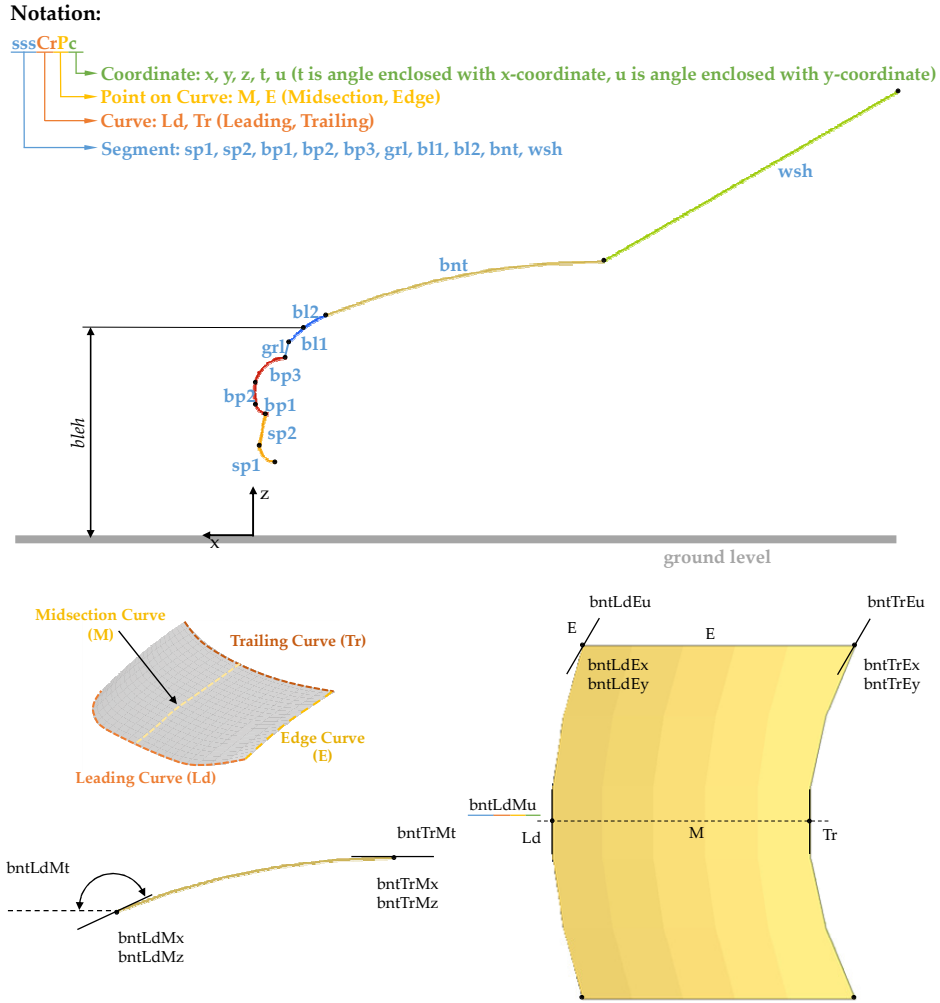
Figure 11: Parameters describing the geometry of the car fronts (Feist, 2016)

2.5.2   Definition of Vehicle Stiffness

The force-deflection characteristics of the impact structures was defined based on simulations with a rigid cylindrical impactor.

In total, eight different impactor locations were chosen as specified in Table 5. An appropriate offset in the impact direction was applied for the initial posture to avoid initial penetrations for the individual shapes and position the impactor as close as possible to the outer surface of the impact structure. The abbreviations in Table 5, which specify the impact location in the x-z plane, refer to the parameters of the Bezier curves as named in Figure 11.

Table 5: Impactor simulations defining force-deflection characteristics of impact structures

Load Case ID	Impact Location			Impact Direction (around y-axis)
	(x)	(y)	(z)	
1	sp1LdMx	0	sp1LdMz	45°
2	sp1LdEx	sp1LdEy	sp1LdMz	45°
3	0	0	$\frac{bp2LdMz+bp2TrMz}{2}$	90°
4	$-\frac{bp2LdEx+bp2TrEx}{2}$	$\frac{bp2LdEy+bp2TrEy}{2}$	$\frac{bp2LdMz+bp2TrMz}{2}$	90°
5	bl2LdMx	0	bl2LdMz = bleh	-50°
6	bl2LdEx	bl2LdEy	bl2LdMz = bleh	-50°
7	$-\frac{bntLdMx+bntTrMx}{2}$	0	$\frac{bntLdMz+bntTrMz}{2}$	$\frac{bntLdMt+bntTrMt}{2}$
8	$-\frac{bntLdEx+bntTeEx}{2}$	bl2LdEy	$\frac{bntLdMz+bntTrMz}{2}$	$\frac{bntLdMt+bntTrMt}{2}$

A rigid impactor was used that had a mass of 5.95 kg, diameter of 120 mm and length of 400 mm. The impactor was modelled as a rigid structure to minimise code-specific effects, as impactor simulations were performed with four different FE software packages (LS-Dyna, Abaqus, Radioss and VPS).

An initial velocity of 11.11 m/s was defined for the impactor in the impact direction. All other degrees of freedom were locked. The motion of the impactor was not prescribed. The simulations were run until the impactor returned to the initial position after the unloading phase. An automatic surface-to-surface contact between the vehicle and impactor was defined with a segment-based penalty formulation. A coefficient of friction of 0.3 was assumed.

The acceleration and displacement of the CoG of the impactor (from nodal history output of FE software) were used to derive force-deflection curves for each impact location.

3   IMPACT STRUCTURE

In this chapter, the requirements for a representative impact structure for VRU accidents are derived that were needed to address the research questions posed in this thesis.

Parts of the presented work were published within the IRCOBI 2017 conference proceedings (Klug *et al.*, 2017).

3.1   Method

For the development of a generic impact structure, the boundary conditions, such as representative accident scenarios, vehicle geometry and stiffness, were captured and used as input for the following chapters.

3.1.1   Representative Boundary Conditions

How real-world accident data should be applied together with the assessment focus to define appropriate representative boundary conditions for the virtual assessment is shown here in an exemplary fashion.

To define the exemplary requirements, representative accident scenarios for pedestrians were derived that were based on analyses of the IGLAD Database and Austrian national statistics. As the aim of this work was not to assess a specific safety measure, the present analyses were performed very generally. The analyses were run for the pedestrian data, as the analytical results were needed as input for the studies described in Chapters 4 and 5, which place a focus on this group of VRUs.

The following parameters were analysed:

- Relevance of the impact structure
- Relevant accident scenarios
- Relevant collision speeds

3.1.2   Representative Vehicle Geometry

The geometries of nineteen current European passenger cars were analysed in detail and classified to derive generic, representative, 3D vehicle geometries.

The vehicle shapes of modern, representative (frequently sold) passenger cars of different European car makes were provided by ACEA and anonymised. Table 6 gives an overview of the sample of passenger cars used, which consists of modern vehicles (the oldest vehicle shape was introduced in 2009).

Table 6: Applied sample of passenger cars used for deriving generic shapes and stiffness corridors

ID	Vehicle type	Shape introduced in	Used for stiffness corridors	Year of Euro NCAP rating	Pedestrian rating
1	FCR	2011	yes	2011	78%
2	FCR	2014	yes	2014	77%
3	FCR	2009	yes	2009	39%
4	FCR	2012	no	-	-
5	FCR	2014	no	-	-
6	FCR	2012	no	-	-
7	MPV	2010	yes	2010	49%
8	MPV	2015	yes	2015	71%
9	MPV	2011	yes	2011	53%
10	MPV	2012	no	-	-
11	MPV	2013	no	-	-
12	RDS	2015	yes	2013	91%
13	RDS	2015	yes	2014	82%
14	SUV	2015	yes	2015	82%
15	SUV	2013	yes	not available	-
16	SUV	2017	yes	2017	73%
17	SUV	2011	no	-	-
18	SUV	2012	no	-	-
19	SUV	2011	no	-	-

The geometry of all available vehicles was parameterised based on the method described in Chapter 2.5, using 3D outer shapes or pictures with vehicle dimensions. The most frontal point and the ground level were used as the origin points of the coordinate system and aligned for all analyses.

The outer shapes of the vehicles were all overlaid and grouped into four different categories that showed comparable geometries: Sport Utility Vehicle (SUV), Family Car/Sedan (FCR), Roadster (RDS) and Multi-purpose Vehicles combined with Superminis (MPV). The sample used to derive the median consisted of six vehicles for FCR and SUV, five, for MPV and two, for RDS.

The median values for each of the 120 parameters were derived for each vehicle category, resulting in representative, 3D, median vehicle shapes for four different vehicle categories. Representative Stiffness

Impact simulations with eleven full FE vehicle models at eight different impact locations were performed by the car manufacturers by applying the method described in Chapter 2.5. Full FE vehicle models of serial vehicles were used that were extensively validated to predict the responses of pedestrian protection testing.

In total, eleven vehicle models from five different car manufacturers were used to derive the stiffness corridors. In Table 6, the sample of vehicles is described by showing the year in which the vehicle was tested by Euro NCAP and the vehicle's pedestrian rating.

Force-Displacement curves were derived from accelerations and displacements of the centre of the impactor for each load case. Displacements were discretised (2.5-mm steps) and separated into loading and unloading curves (based on the maximum deflection) for each load case and vehicle. The median, maximum and minimum force values were derived for each discretised displacement over all vehicles and within grouped vehicle categories (FCR, SUV, MPV and RDS).

3.2 Results

3.2.1 Representative Boundary Conditions

Boundary conditions from real-world accidents were analysed to find the most representative ones, which were subsequently used as input for the studies described in the following Chapters (4 and 5).

Relevance of the Impact Structure

As shown in Figure 12, passenger cars are highly relevant to pedestrian accidents regardless of the considered injury severity. They were involved in nearly 80% of accidents in which light or severe injuries were reported. With respect to pedestrian accidents that resulted in fatal injuries, trucks had a greater relevance than for the other injury severities. They were involved in more than 20% of the fatal accidents. Nonetheless, passenger cars were still identified as being the most relevant collision partner and were involved in 66% of the fatal cases.
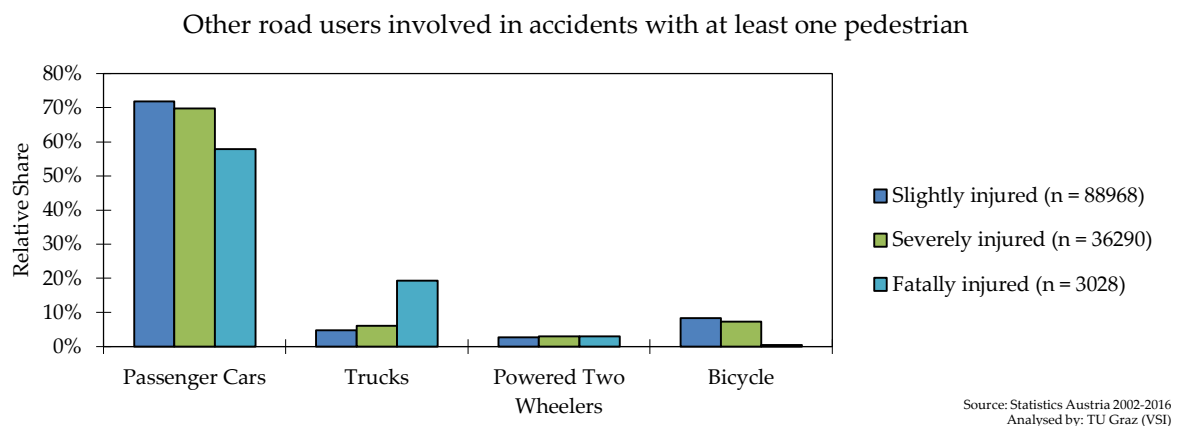
Figure 12: Relevance of other road users involved in pedestrian accidents based on Austrian road traffic statistics from 2002-2016

Figure 13 shows that the vehicle front of passenger cars is the most relevant impact area of the vehicle. The vehicle front was deformed in 92% of the fatal and 82% of the total number of pedestrian accidents available in the IGLAD data sample. Based on these analysed data points, the vehicle front of passenger cars can be classified as a highly relevant impact structure.
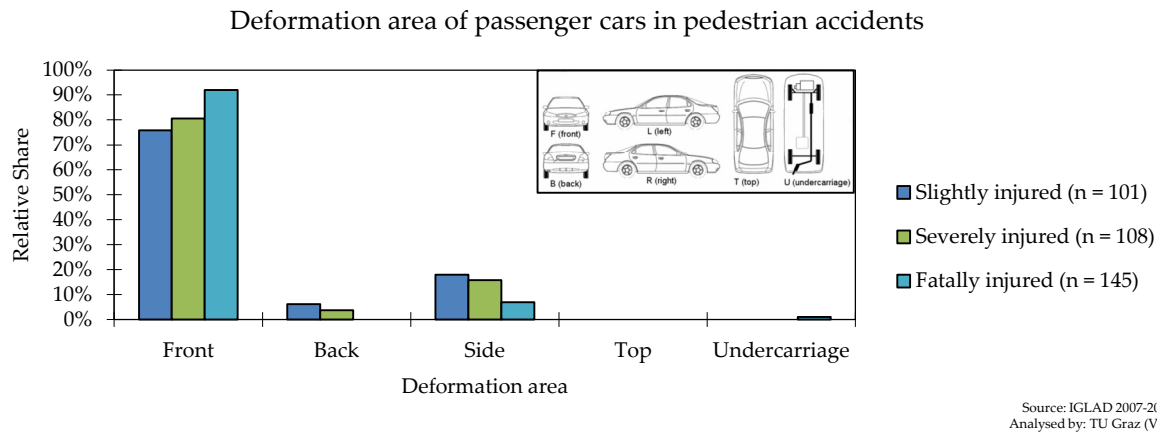
Figure 13: Deformation areas of passenger cars upon the first collision with pedestrians based on IGLAD data from 2007-2015

Relevant Accident Scenarios

To analyse the accident scenarios between pedestrian and passenger cars, the scenarios were grouped according to the direction of movement of the pedestrian and vehicle. For the two scenarios "pedestrian crossing from left" and "pedestrian crossing from right", all scenarios in which the vehicle went straight before impacting a pedestrian that came from the left or right side were summarised. As the impact direction is more oblique in accidents that involve turning vehicles, these scenarios were separated and no distinction was made between whether the pedestrian came from right or left side. Furthermore, accidents where pedestrians were walking in the same or opposite direction were analysed separately. All remaining accident scenarios were classified as "other". Figure 14 summarises the results. The numbers in the legend refer to the original accident scenario classification for the Austrian road traffic statistics (Statistik Austria, 2010). It was observed that the two categories in which the pedestrians were crossing the street while the passenger car was driving straight ahead were the most common scenarios. While the "pedestrian crossing from right" was identified as the most relevant category across all accidents, the "pedestrian crossing from left" was the most common among fatal accidents. This indicates that the odds of being fatally injured in this scenario is higher compared to the other side (Odds Ratio = 1.5). The same trend was identified within the IGLAD data sample: While pedestrian crossing from the left accounted for 35% of the total and 41% of the fatal accidents, 39% of the total and 35% of the total accidents were assigned to the category scenario with the pedestrian crossing from the right (OR = 1.7).

Pedestrian accident scenarios for impacts with passenger cars
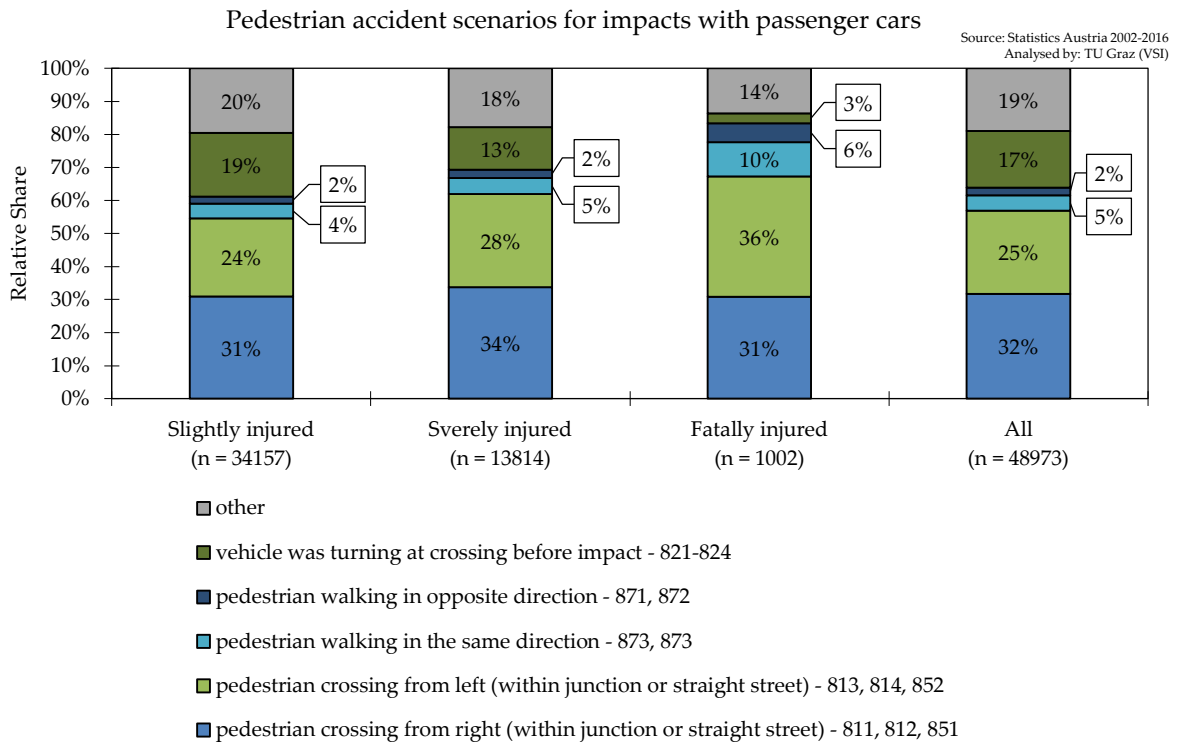
Figure 14: Accident scenarios involving pedestrians and passenger cars based on Austrian road traffic statistics from 2002-2016

Relevant Collision Speeds

93.13% of the accidents from the analysed Statistics Austria sample occurred in the inner city, 6.54% occurred on rural roads and 0.33%, on highways. When analysing fatal accidents, the accidents on rural roads were identified as more relevant. They accounted for 34.6% of the accidents (62.3% inner city). The odds for being fatally injured are clearly higher (OR=8.3) when the accident involving a pedestrian happens outside of a city. This is associated with the collision speed. While the speed limit is 50 km/h inside cities in Austria, it is 100 km/h on rural roads (if unrestricted).

In the unbiased IGLAD dataset, the mean collision speed of passenger cars was 34 km/h for all pedestrian accidents (Median Values is 30 km/h). Figure 15 shows the cumulative distribution of the collision speed for accidents involving at least one pedestrian. In 51% of all pedestrian accidents, the collision speed was less than 30 km/h. In 19% of the pedestrian accidents, the collision speed was higher than 50 km/h. When considering only accidents with AIS 3+ injuries, the collision speeds were higher. The mean collision speed for these cases was 41.6 km/h (Median = 40.0 km/h). The speed was lower than 30 km/h in 25% of the cases and higher than 50 km/h in 35% of the cases.

Collision speeds of passenger cars in accidents involving pedestrians
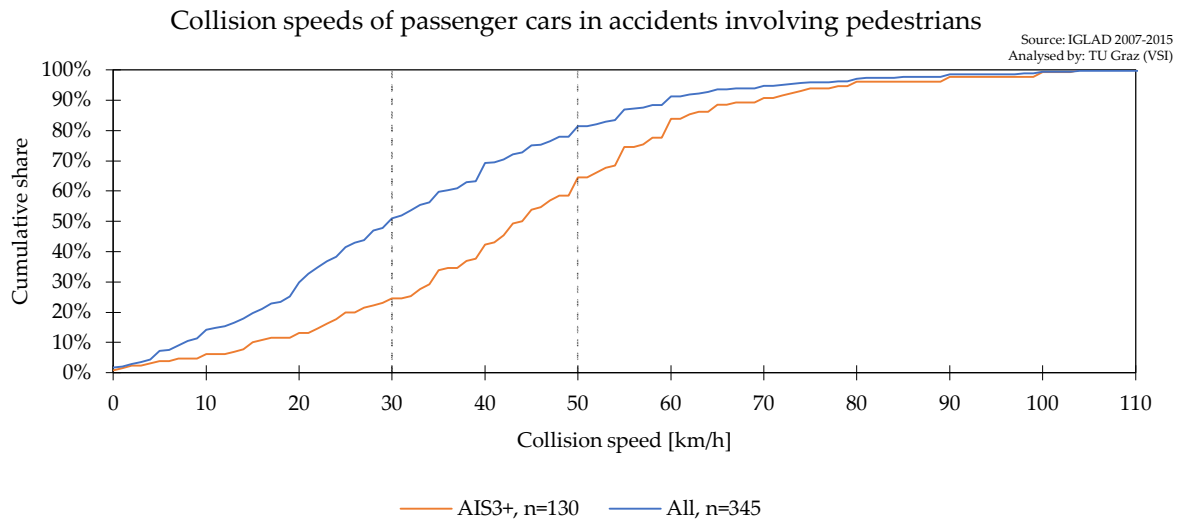
Figure 15: Collision speed of passenger cars upon the first collision with pedestrians based on IGLAD data from 2007-2015 (n = 345) for all accidents and accidents with AIS 3+ injuries

3.2.2   Representative Vehicle Geometry

The derived median midsections for each vehicle category compared with the original shapes are shown in Figure 16. All FCRs of the analysed sample showed very similar geometries. For the SUV and MPV categories, one smaller car compared to the others was included in the dataset, while the rest were again very similar. The RDS geometry is based on two different vehicle geometries which showed differences in terms of *bleh* and bonnet length. The mean parameters for each vehicle category are listed in Table Appendix B-1.

The four median midsections of each category are compared in Figure 17. Clear differences in among the categories are visible, indicating that the selected classification was appropriate to cover the fleet. The higher MPVs are represented by the SUV shape and the lower ones by the FCR shape. The median RDS and FCR midsections seemed to be most comparable when comparing the height, angle and length of the bonnet. On the other hand, the spoiler region of the RDS starts lower compared to the FCR, and significant differences in terms of the bonnet stiffness also were noted in the later analysis, so these two categories were kept separated.

Figure 18 shows the four finalised 3D median geometries of the four categories that were established and used as baseline for developing the generic vehicle models.
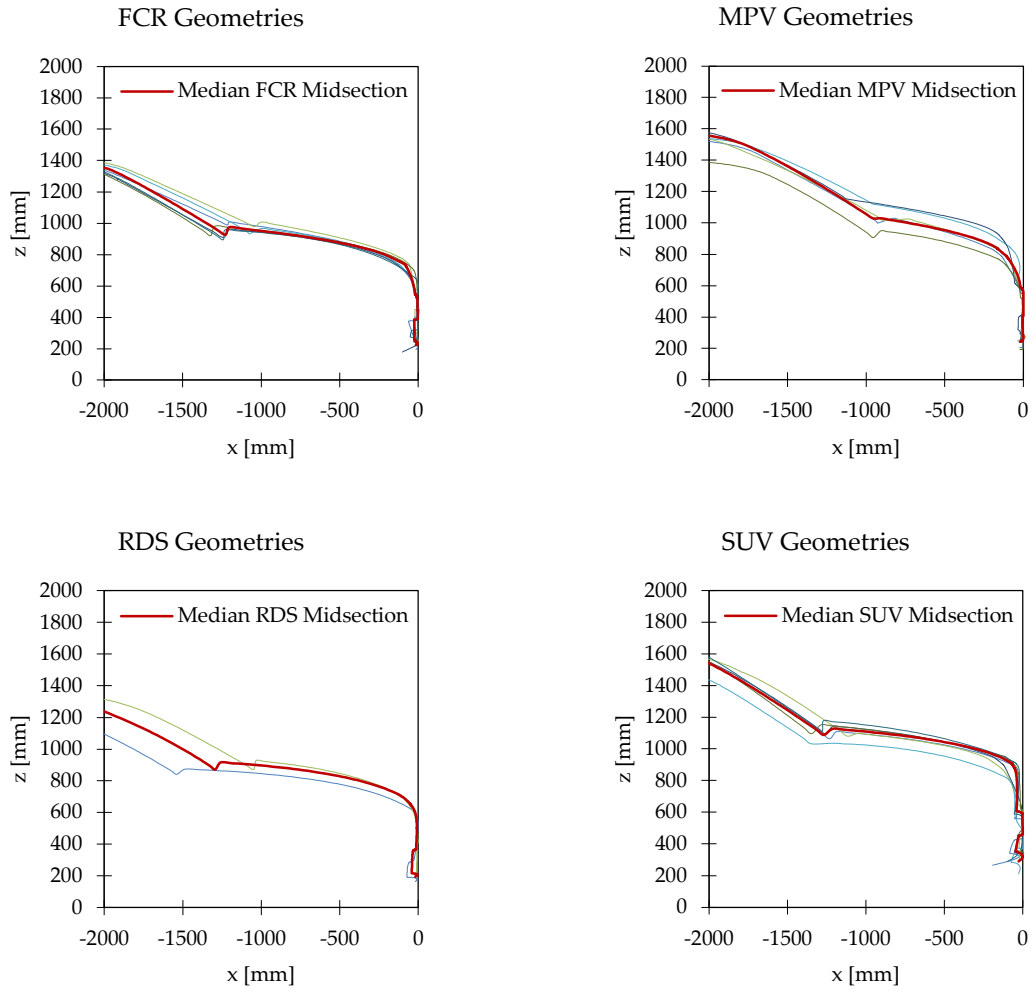
Figure 16: Comparison of derived median midsections versus vehicle shapes of current European fleet
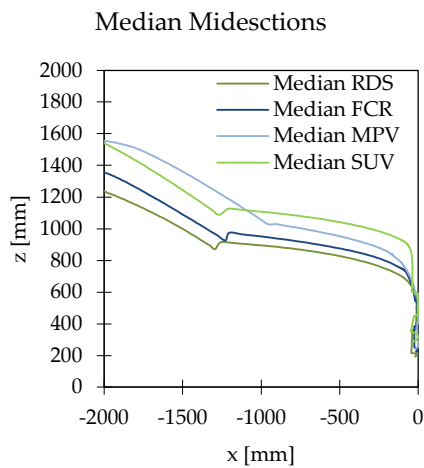
Figure 17: Comparison of midsections of the median vehicle midsections of the categories FCR, MPV, RDS and SUV
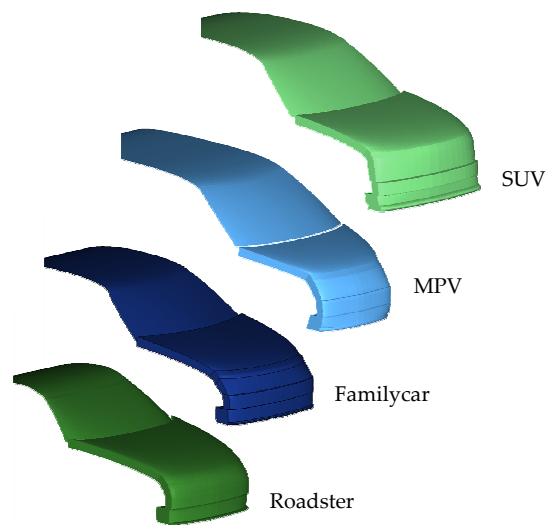
Figure 18: Median 3D Vehicle Shapes of the categories RDS, FCR, MPV and SUV

3.2.3   Representative Vehicle Stiffness

The responses of all impacted vehicles for the impactor simulation 3 (bumper impacted at vehicle centreline = CL) within the loading phase are shown in Figure 19. The vehicles were grouped into the four categories defined for deriving the median geometries. The responses of three vehicles per category were available, except for RDS, where only the results of two vehicles were provided. Figure 20 shows the responses of the cars in the category FCR compared to the derived median for this category. In Figure 21, the same is shown for the SUV, which shows a higher span of the derived force-deflection characteristics.
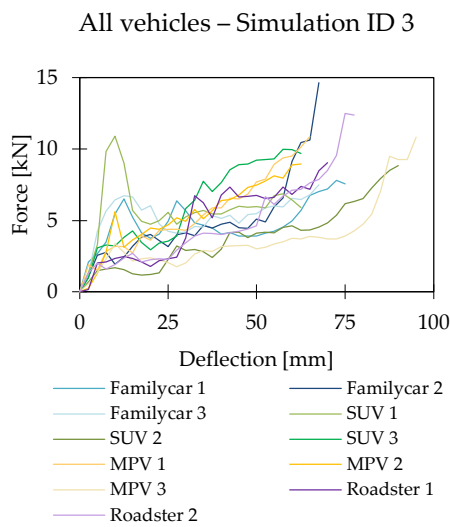
Figure 19: Force deflection characteristic of single vehicles for impact simulations at the bumper CL
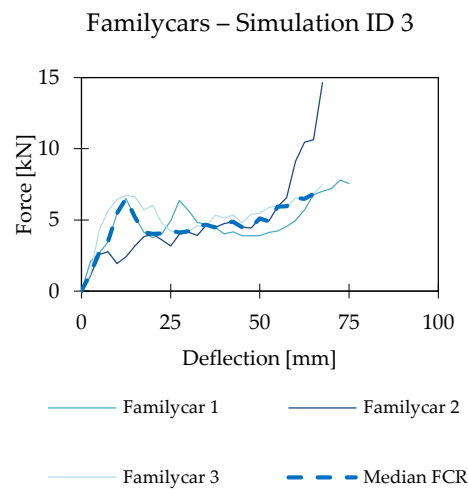
Figure 20: Force deflection characteristic of single vehicles and median of the category FCR for impact simulations at the bumper CL
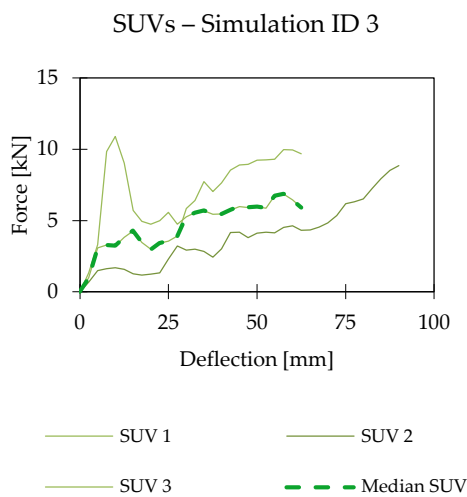
Figure 21: Force deflection characteristic of single vehicles and median of the category SUV for impact simulations at the bumper CL
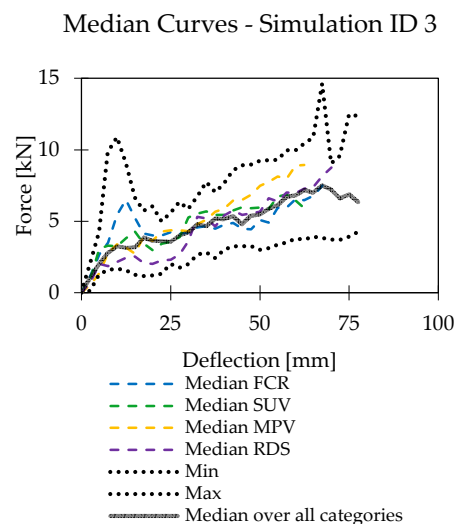
Figure 22: Median force-deflection characteristic for impact at the bumper centreline for single vehicle categories and over all categories

The median curves for each vehicle category are compared in Figure 22. It was observed that the variation between the median values for each vehicle category was smaller than the variation

within one category. Therefore, the median force-deflection curve was derived over all vehicle categories. Corridors were defined from the minimum force to the maximum force for each deflection from the responses of all full FE vehicles.

A significant difference between vehicle categories was observed for the impact at the bonnet (Simulation ID 7 and 8). As shown in Figure 23 and Figure 24, roadsters showed less clearance in the bonnet impacts. The maximum deflection was, therefore, much smaller than for the other vehicles. The median maximal deflection was 68 mm for the vehicles of the category RDS, while it was 99 mm for the other vehicles.
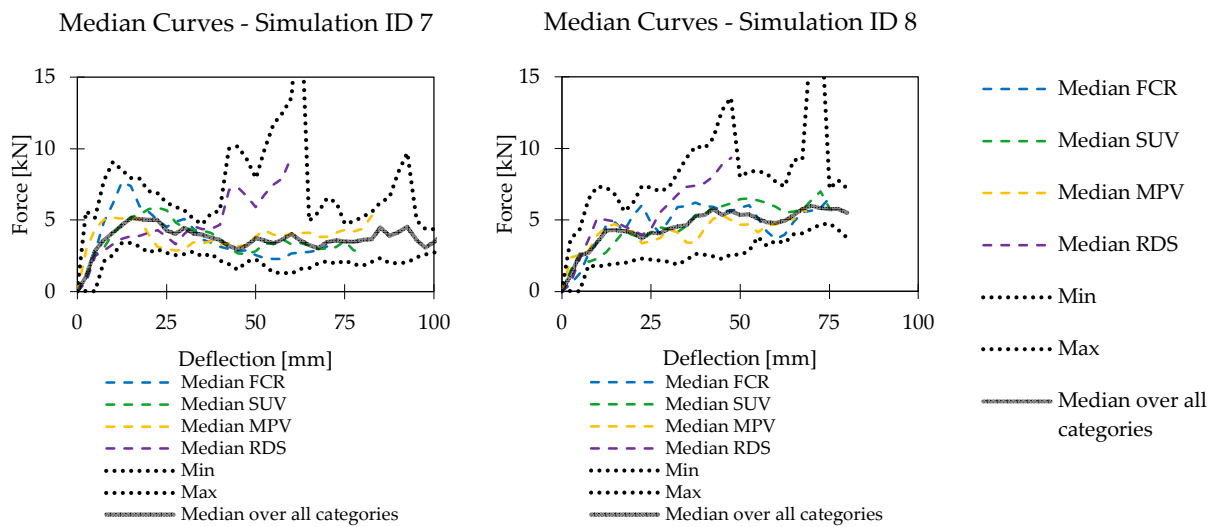
Figure 23: Median force-deflection characteristic for impact at the bonnet centreline for single vehicle categories and over all categories

Figure 24: Median force-deflection characteristic for impact at the bonnet in the y-offset position for single vehicle categories and over all categories

The final corridors and median characteristics for loading and unloading at all impact locations are shown in Figure 25. For the simulations in the offset position (2, 4, 6 and 8), high forces at low deflections were observed for single vehicles, leading to a wider corridor for the loading phase compared to those for the impacts at the vehicle centreline (1, 3, 5 and 7).
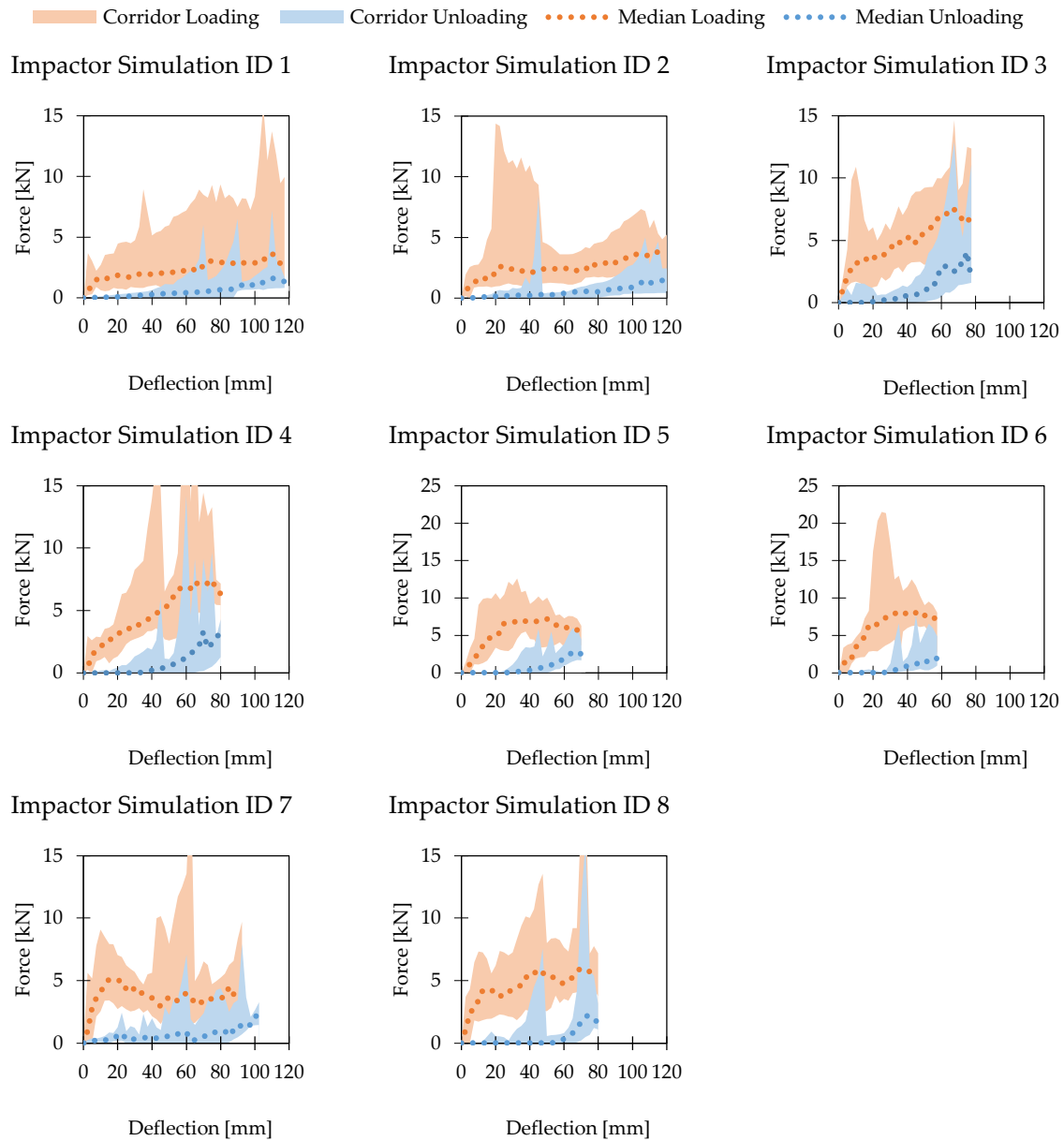
Figure 25: Stiffness corridors and median force-deflection characteristics for four different impact locations

3.3   Discussion

3.3.1   Representative Boundary Conditions

The presented results show exemplary how boundary conditions for virtual testing can be derived from real-world accident data. This is not new as such, and similar analyses were published in the past (Fredriksson and Rosen, 2012; Otte *et al.*, 2012; Lenard *et al.*, 2014; Lindman *et al.*, 2011). Representative accident scenarios are likely to change in the near future due to new vehicle types, active safety systems, such as AEB systems or autonomous emergency steering (Luttenberger *et al.*, 2014; Svensson *et al.*, 2014; Detwiller and Gabler, 2017; Strandroth *et al.*, 2016). Therefore, it is important that scenarios applied in virtual testing get regularly updated based on updated analysis of real-world accident data.

Based on the presented analysis, representative pedestrian accident scenarios were defined that were needed as prerequisite for the Chapter 4 and 5.

The current analysis of accident scenarios and involved road users was performed based on Austrian National Statistics. Regional differences can lead to differing results when performing the same analysis in other countries. The IGLAD dataset consists of differing international databases and includes a limited sample of data with an unknown basic population. No weighting of the data was performed although samples of IGLAD can be biased due to the selection criteria (Bakker *et al.*, 2017). The analysis of the collision speed was cross-checked with the literature: Fredriksson and Rosen (2012) performed an analysis of pedestrian accidents with passenger cars based on GIDAS. For all cases with AIS 3+ injuries of the VRU, the mean collision speed was 44 km/h. Therefore, although the IGLAD dataset was unbiased, the result obtained was very similar (42 km/h).

3.3.2   Representative Vehicle Geometry

The derived median geometries were compared with vehicles applied in PMHS tests to analyse whether the available PMHS tests are representative for current European vehicles.

As the review of the literature indicated that the height the pedestrian relative to the bonnet leading edge is one of the key factors for the pedestrian kinematic (Kerrigan *et al.*, 2007; Kerrigan *et al.*, 2012a; Paas *et al.*, 2015b), the *bleh* of the current analysis was compared to the PMHS tests from the literature, as summarised in Kerrigan *et al.* (2012b). Figure 26 shows that the *bleh* of the family car used in the PMHS tests published by Snedeker *et al.* (2005) is very close to the derived median value. The most comparable *bleh* for the category MPVs was the small city car used by Subit *et al.* (2008). The SUV used by Schroeder is representative for the European fleet in terms of *bleh*, while the one used by Crandall *et al.* (2006) and Kerrigan *et al.* (2012a, 2005b and 2008) has a significantly higher *bleh*. No PMHS tests of vehicles that could be associated with the category roadster are available. The *bleh* of the FCRs used within the study of Ishikawa *et al.* (1993) was close to the median *bleh* of RDS derived in the current analysis, but the vehicle shapes are not comparable, as current vehicles are more smooth and rounded than they were in the reported PMHS tests.
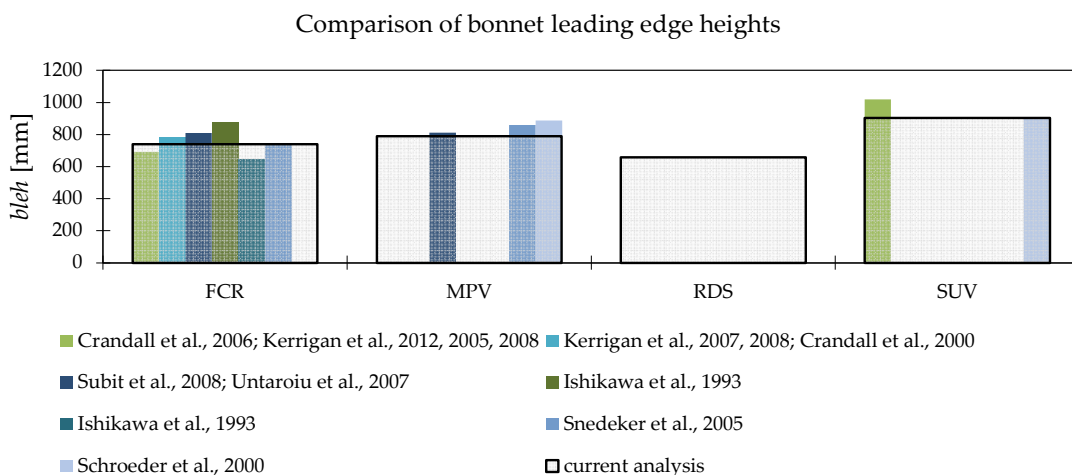
Figure 26: Comparison of bonnet leading edge heights of vehicles used in PMHS tests with derived median values of the current study (based on Kerrigan *et al.*, 2012b)

The derived median midsection of the vehicle category FCR was also compared with the latest generation of pedestrian bucks used within PMHS tests (Song *et al.*, 2017a; Forman *et al.*, 2015b; Forman *et al.*, 2015a).

Comparison of SAE Buck and Median FCR   Comparison of LAB Buck and Median FCR
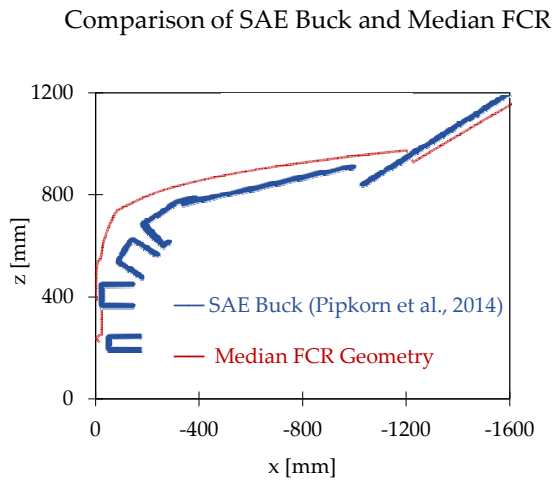
Figure 27: Geometric comparison of midsection of the median FCR with the SAE Buck (based on Pipkorn *et al.*, 2014)
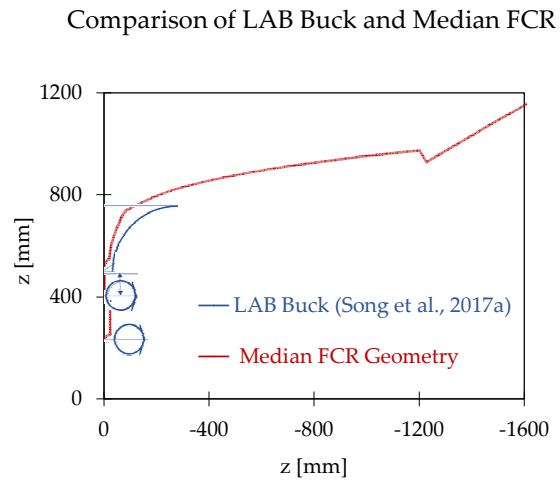
Figure 28: Geometric comparison of the midsection of a median FCR with a simplified pedestrian buck used by LAB in PMHS tests (based on Song *et al.*, 2017a)

As shown in Figure 27, significant differences to the SAE buck introduced by Pipkorn *et al.* (2014) could be observed. The *bleh* of the SAE buck is lower, and the length of the bonnet is shorter than the geometry derived in the current analysis. Furthermore, the lateral distances between the spoiler and bumper as well as the bumper and bonnet leading edge are higher in the SAE buck. This discrepancy is caused by the fact that the SAE buck geometry was developed to meet the geometric corridors for small FCRs as developed as part of the APROSYS project, which was finalized nearly ten years ago (Hardy, 2009). On the one hand, vehicle geometries have changed in the meantime, and, on the other hand, the geometry used in the current analysis represented a median of large and small FCRs. The simplified pedestrian front used by Song *et al.* (2017a) was more similar to the median geometry (Figure 27). For future PMHS tests, bucks with a higher *bleh* should be established, as they would be more representative for current passenger cars.

3.3.3   Representative Vehicle Stiffness

The median stiffness was also compared with characteristics described in the literature. The Force-Deflection characteristics of pedestrian bucks (Pipkorn *et al.*, 2014) and stiffness corridors published by Martinez *et al.* (2007) were compared to those obtained as a result of the analyses conducted in this study for the bonnet leading edge (Figure 29) and the bumper (Figure 30).

The ble stiffness derived in the current study shows a higher degree of stiffness compared to the stiffness derived by Martinez *et al.* (2007) and of the SAE Buck (Pipkorn *et al.*, 2014).

The derived bumper stiffness agrees with the characteristics of the numeric buck developed for the a-PLI studies (Isshiki *et al.*, 2014). The SAE buck, again, tends to be softer than the corridors of the

current study. The stiffness derived by Martinez is softer at the beginning, but tends to be near the upper boundary of the corridor at higher deflection.

The SAE buck touches the minimum line for ble and bumper and, therefore, seems to represent only the softer vehicles.

The difference observed in our dataset to the dataset of Martinez *et al.* (2007) can be partly explained by the different approaches taken. The Euro NCAP results were used in the latter study to derive the stiffnesses and, therefore, the masses of the impactor and the degrees of freedom differed from those in the current study. The approach chosen in the current study has the benefit of better controlled boundary conditions compared to physical tests with impactors.

Another explanation for the stiffer ble could be that the stiffness in this area has not improved due to pedestrian safety regulations and ratings. When reviewing the Euro NCAP results of current vehicles from the Euro NCAP website, it seemed that the bonnet leading edge was not the development focus of all car manufacturers. Within the applied data set of vehicles that were used to derive the stiffness corridors, only four of the eleven impacted cars received a "good" (= green) rating of the ble. One vehicle showed "marginal," and the majority of vehicles showed "poor" pedestrian protection in the area of the ble.
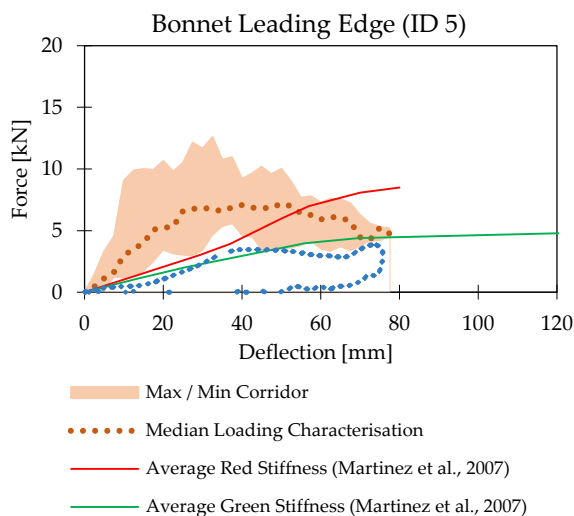
Figure 29: Comparison of derived stiffness corridors for the bonnet leading edge with those cited in other studies
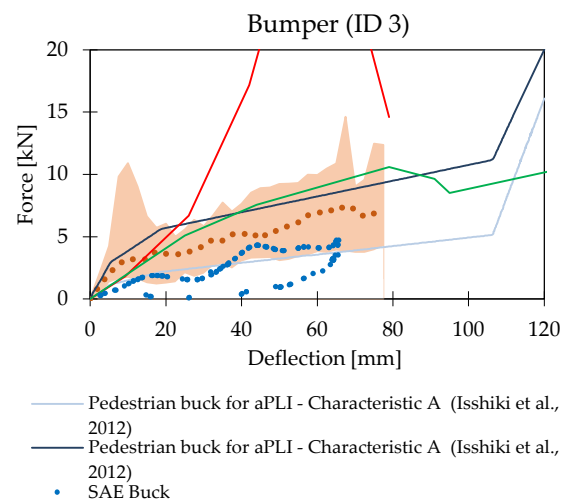
Figure 30: Comparison of derived stiffness corridors for the bumper with those cited in other studies

One limitation of the developed stiffness corridors was the selected impactor configuration. To keep the loading conditions harmonised, the impactor angle and initial velocity were not varied during the simulations although differing vehicle geometries can lead to different impact conditions during the full-body simulations.

An impactor angle of 45 degrees was chosen for the spoiler impact. This angle is representative for the later stage of the pedestrian impact when the legs are moving upwards (after 20 ms for the

struck side leg and after 40 ms for the non-struck side leg as shown in Figure 31). The first impact, where the leg is in a vertical position, was not replicated with impactor tests in this study.

| 10 ms | 20 ms | 30 ms | 40 ms | 50 ms |
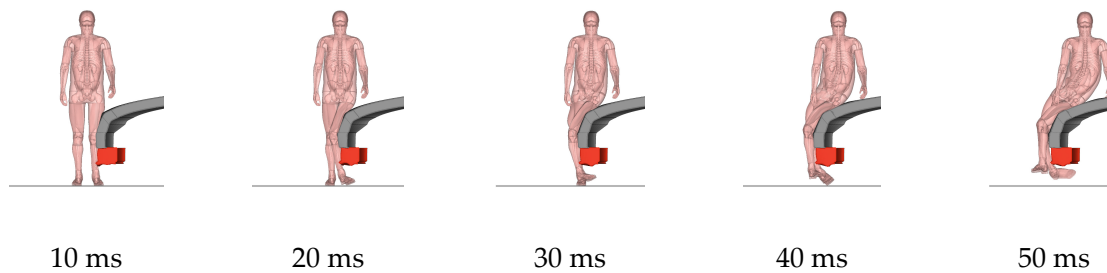
Figure 31: Leg impact kinematics and spoiler deformations for FCR impact at 40 km/h simulated with the THUMS AM50 model (pictures show the GV cross-section at $y = 310$ for better visualisation of the deformations)

Furthermore, the maximum displacement of the impactor was not prescribed. Therefore, theoretically, the impactor could lead to less intrusion than the HBM simulations. This was double-checked after the first generation of generic vehicle models was developed as well as during simulations with full FE serial vehicles. No higher deformations were observed during those simulations prior to the head impact. Therefore, the applied kinetic energy of the impactor was assumed to be sufficient to replicate the deformations as they were observed in the HBM simulations.

The chosen approach was found to be appropriate for deriving stiffness characteristics and allowing the development of a representative impact structure that led to realistic kinematics.

3.4   Summary

In this chapter, the following prerequisites for the subsequent chapters were derived:

- Boundary conditions for representative pedestrian accident scenarios were derived based on the analysis of real-world accident data: Simulations should be performed representing a pedestrian crossing the street from the left while a passenger car drives straight ahead with a speed of 30-50 km/h.
- The selected approach for the parametrisation of the vehicle geometry was appropriate to derive representative vehicle shapes. Four median shapes were established representing Family cars, Roadsters, SUVs and Multipurpose Vans.
- Representative stiffnesses and vehicle shapes were derived that can be considered to develop generic impact structures representative for contemporary passenger cars. Large variations in the stiffness within the selected vehicle categories were observed, which is why stiffness corridors were eventually established over all categories.

4   HUMAN BODY MODELS

It was shown in Chapter 2.3.1 that the biofidelity of the HBMs was evaluated within several studies (Kitagawa and Yasuki, 2014; Watanabe *et al.*, 2011; Combest, 2016; Untaroiu *et al.*, 2015; Wu *et al.*, 2017). The data sources used for the validations varied between HBMs. Previous studies have also reported challenges when attempting to translate the HBMs to different codes and highlighted the importance of harmonising the HBMs for virtual testing (Fuchs *et al.*, 2014; Ghosh *et al.*, 2016). Studies have shown that the HBM has to be adapted to the anthropometry of the PMHS so that reasonable comparisons can be made (Chen *et al.*, 2018; Poulard *et al.*, 2016; Paas *et al.*, 2015c) and that scaling PMHS data to an average size is not straightforward (Untaroiu *et al.*, 2008b; Yanaoka *et al.*, 2016; Kerrigan *et al.*, 2007). Furthermore, no PMHS data are available for several load cases (e.g. impacts with roadsters, varying velocities, or children). Unknown comparability among simulation results was identified as one of the biggest weaknesses of virtual assessment with HBMs in Chapter 1.3.8.

In the current chapter, the comparability among simulation results from different HBMs and among simulations performed by different institutions is analysed. Possibilities to improve comparability are described.

Requirements for the HBM and the simulation setup were developed for the kinematic-based pedestrian assessment of deployable systems (explained in Chapter 1.3.7). To address other assessment foci, additional or alternative requirements, but similar approaches to derive those requirements, will have to be applied.

The findings of the work presented in this chapter were published and presented at several conferences (Klug *et al.*, 2017; Klug *et al.*, 2016; Klug *et al.*, 2018a). The author had the main responsibility for the study and performed all analyses independently. The developed certification procedure has been adopted by Euro NCAP as of Jan 2018 and was published in Technical Bulletin 024 (Euro NCAP, 2017b).

4.1   Method

The Euro NCAP assessment of deployable systems (i.e. active bonnets) represents the first application of Human Body Models within a consumer information safety rating. As explained in Chapter 1.3.7, the list of applicable pedestrian models defined within Technical Bulletin (TB) 13 (Euro NCAP, 2015b) has several drawbacks. Furthermore, several boundary conditions were only prescribed in broad terms in the initial version of the Euro NCAP pedestrian testing protocol, that was in force at the starting point of this study (Euro NCAP, 2016).

The question was raised as to whether all these listed models applied by different users within the boundaries allowed in the protocol would predict similar outcomes and lead to the same rating of the deployable system performance. The spread in terms of *HIT*s was of special interest, as there were dossiers submitted to Euro NCAP in which the predicted *HIT* of the simulations was equal

to the system deployment time, indicating that small differences in *HIT* can already significantly affect the outcome of the assessment.

A procedure was developed as part of this research work, which allows an objective comparison of results from pedestrian simulations independent of the HBM and FE code. A harmonised method for simulations with HBMs was developed which included all relevant boundary conditions and attempted to improve the comparability of simulation results.

Finally, certification requirements were developed that ensure that different HBMs or a single HBM implemented in different FE software packages or run with different solver versions leads to comparable assessment results with a tolerable spread.

A certification procedure that is applicable for different HBMs in varying codes was defined, consisting of the following requisites:

- Establishment of generic vehicle models that are representative of contemporary passenger cars

- Definition of harmonised initial posture of pedestrian models

- Definition of harmonised simulation setup

- Definition of harmonised output

- Definition of requirements for certification procedure (corridors and tolerances)

4.1.1 Pedestrian Models

Two Human Body Models were used a baseline to define a harmonised pedestrian simulation setup and develop a protocol for pedestrian simulations to ensure that the procedure is applicable for different HBMs.

The 50th percentile male Total Human Model of Safety (THUMS) v4.02 and the simplified pedestrian model v1-4 of the Global Human Body Model Consortium (GHBMC) (both in LS-DYNA) were used to develop the harmonised pedestrian simulation setup. Both models were used, as their biofidelity has been thoroughly documented in several papers, which is shown in Chapter 2.3.1.

As part of a sensitivity study, boundary conditions which affect the HBM kinematics were identified, as they have to be carefully considered and consistent to enable a fair comparison to be made between pedestrian simulation results.

After the procedure was set, the protocol was disseminated among members of the HBM community. This was done to make sure that all definitions were clear and could be followed by a variety of users. On the other hand, this step was also needed to make sure that the procedure was applicable in all codes to various pedestrian models.

Several institutions around the world applied the protocol and provided their results: Audi AG, BMW Group, Daimler AG, ESI Group, HongIk University, Jaguar Land Rover, Honda R&D, Japan Automobile Manufacturers Association (JAMA) and Japan Automobile Research Institute (JARI),

Nissan Motor Company, TASS International, Subaru Corporation, Wake Forest University. All the contents of the presented work, except the data provided by data providers, are solely at the author's own discretion. The results from the following pedestrian models (HBMs and multibody humanoid models) were included in the final dataset (random order):

- GHBMC simplified pedestrian model:
  - VPS version without fracture mode (two different institutions)
  - RADIOSS version without fracture mode
  - LS-DYNA with fracture mode (v1.4.5 and v1.4.3)
- THUMS:
  - THUMS v4.02 in LS-DYNA without fracture mode (two different institutions)
  - THUMS v4 in VPS without fracture mode
  - THUMS TUC in LS-DYNA without fracture mode
  - THUMS -D in LS-DYNA without fracture mode
  - THUMS v3 in Abaqus without fracture mode
- JAMA Pedestrian Model (HBM) in VPS with and without fracture mode
- Honda HBM in VPS without fracture mode
- MADYMO pedestrian models (multibody humanoid model) coupled with LS-DYNA (two different institutions)
- JLR humanoid FE model in LS-DYNA
- ESI PED 50 humanoid FE model in VPS

The provided results were anonymised and named as Model 01-Model 18. All of the above listed models were included in the list of Euro NCAP TB013 and were, therefore, applicable for Euro NCAP assessment of deployable systems until December 2017.

4.1.2 Representative Generic Vehicle Models

As an impact structure, generic vehicle models were applied that were easily transferrable to other codes and, therefore, applicable for comparison of HBMs in different codes (LS-Dyna, VPS, Radioss and Abaqus). The modelling approach and structure of the models are explained in Appendix B. (Feist, 2016)

The parameters of the material model for each of the deformable areas (spoiler, bumper, grill, bonnet lead and bonnet) were calibrated using the software LS-OPT version 5.2 to achieve the closest possible correlation with the target median force-deflection curve derived in Chapter 3.2.3. The optimisation was performed using the curve-mapping algorithm (instead of the least squares method). Details of the algorithm are described within the LS-Opt Manual (Stander *et al.*, 2015).

The windshield was modelled rigidly, as simulation results were only analysed up to the point of head impact.

The LS-DYNA version of the models was translated into the other FE codes by the FE code houses (ESI Group, Altair and Dassault Systèmes).

4.1.3   Harmonised Initial Posture of Pedestrian Models

To analyse, if further definitions of the initial posture of the pedestrian model (compared to the 2016 version of the Euro NCAP protocol) are needed and to define proper requirements, a sensitivity study was conducted: The effects of small variations in the initial posture of the HBM on the kinematics in pedestrian simulations were analysed. THUMS was repositioned by carrying out pre-simulations. The GHBMC model was geometrically repositioned by its distributor, Elemance (USA) to match the THUMS postures as closely as possible.

To comply with the 2016 Euro NCAP pedestrian testing protocol (Euro NCAP, 2016), the following conditions were used as starting points and were fulfilled for all postures:

- the heel-to-heel distance was 310 ± 10 mm

- the head centre of gravity (CoG) was aligned with the vehicle centreline

- the struck-side leg was facing backwards

For the baseline postures 1, 2 and 3, the legs were positioned according to the SAE specifications for pedestrian dummies (SAE International, 2010b) and remained unchanged for these postures. The three defined arm postures (1, 2 and 3) represented the SAE specifications for pedestrian dummies (SAE International, 2010b), the position of the pedestrian target used for the AEB testing (Euro NCAP, 2015a) and a natural gait posture (Untaroiu *et al.*, 2009; Perry, 1992) representing the 40% gait cycle. The THUMS v4 and GHBMC PS models are shown in the three initial postures in Figure 32 and Figure 33, respectively. In Posture 2, the wrists are close to each other in front of the body, which represents the usual posture used within PMHS tests. In contrast to the PMHS tests, the wrists were not tied together. The main difference between postures 2 and 3 is the elbow angle. For the AEB target, the elbow is extended, while it is bent in the natural walking Posture 3.
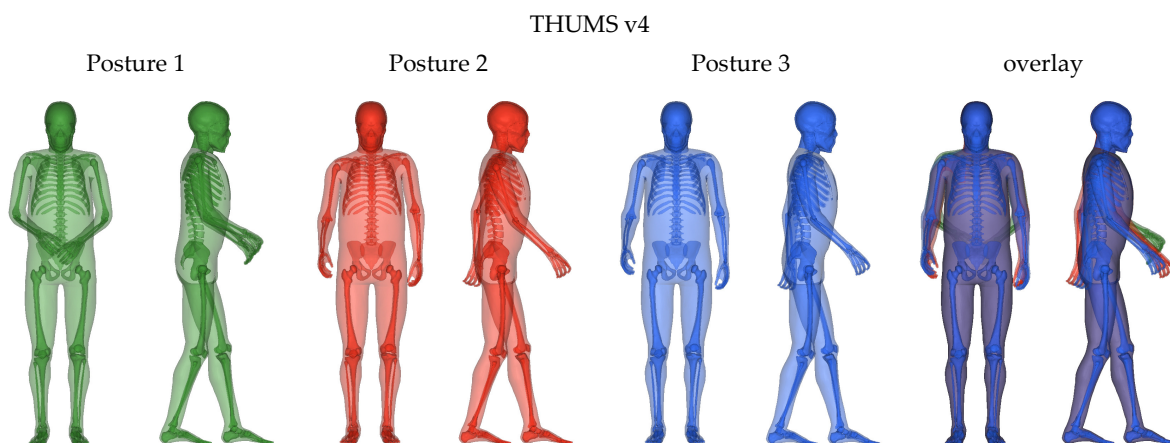
Figure 32: Applied variations in arm posture within THUMS v4

GHBMC

Posture 1	Posture 2	Posture 3	overlay
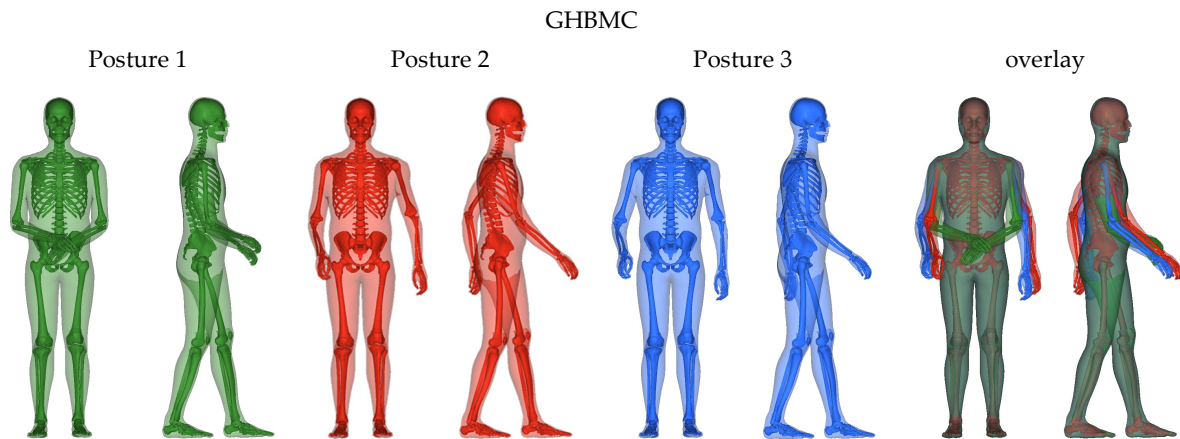
Figure 33: Applied variations in arm posture within GHBMC PS Model

THUMS was positioned into eight additional postures. The torso angle, leg angle, shoe angle and the head angle were slightly varied to analyse the sensitivity at each angle. All initial postures are specified in Table Appendix C-2. The angles were measured based on anatomic landmarks, taking into account the recommended landmarks for anatomic axis definitions from the international society of biomechanics (Wu *et al.*, 2002; Wu *et al.*, 2005) and according to the developed measurement protocol explained in Appendix C.

The sensitivity study was carried out using the generic family car model with a collision speed of 40 km/h. To test whether the conclusions could be transferred to other load cases, selected variations were simulated using the generic SUV model.

4.1.4 Harmonised Simulation Setup

In the 2016 Euro NCAP protocol, only the coefficient of friction between the HBM and the ground was specified as 0.3. The contact settings with the vehicle and initialisation of simulations were not prescribed.

To analyse if further specifications are needed, variations of the contact between the vehicle and the HBMs were made: For the baseline simulations, a surface-to-surface contact with segment-based penalty formulation (SOFT = 2, DEPTH = 13), a coefficient of friction (static FS and dynamic FD) of 0.3 and a viscous damping coefficient (VDC) of 20% were defined.

The following variations were performed:

- change in the damping coefficient (VDC = 0),
- variation of the coefficient of friction (FS and FD = 0.2-0.5)
- change in the standard penalty formulation (SOFT = 0, DEPTH = 2)

Furthermore, the effects of pre-simulations were analysed. The impact with the family car at 40 km/h was simulated with and without pre-simulations for the GHBMC and THUMS models in order to establish the equilibrium and ground force. The skin of the pedestrian models was switched to rigid, and gravity was applied until the contact force with the ground equalled the

weight force of the HBM. The coefficient of friction between the HBM and the ground (0.3-0.9) was also varied.

In all simulations, the initial velocity was applied to the vehicle, and the pedestrian was at rest prior to the contact with the vehicle. Simulations were performed at three different collision speeds: 30, 40 and 50 km/h to cover a range representative for real-world accidents and common lower and upper thresholds of deployable systems.

4.1.5 Harmonised Output

For the evaluation of trajectories, sensors were implemented in the HBMs at selected reference points:

- the head centre of gravity (HC),

- the centre (average of all nodal coordinates) of the vertebral body of C7 and T12,

- the midpoint of the left and right centre of the *acetabulum* (AC)

- the *inter-malleolar* point on the right (MR) and left leg (ML) and the centre of the right (KR) and left patella (KL).
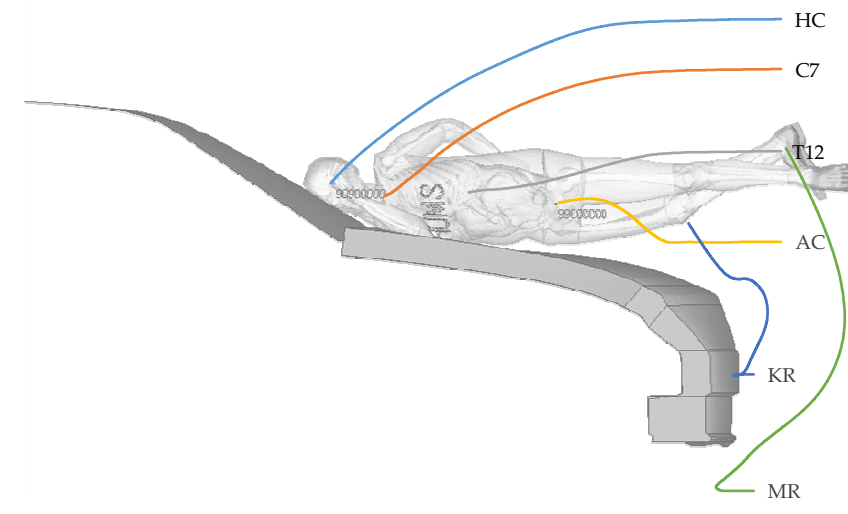
Figure 34: Exemplary trajectories of sensors for kinematic tracking of impact with the generic FCR model and a collision speed of 30 km/h

As shown in Figure 34, the selected sensor locations allowed the full-body kinematics to be tracked. The figure shows the trajectory of each reference point for an exemplary load case and a screenshot of the HBM posture at the time of head impact.

A detailed description of the reference point sensor locations can be found in the Appendix C, allowing comparable sensor positioning in multiple HBMs. The sensors were connected with the structure using the keyword *CONSTRAINED_INTERPOLATE in LS-DYNA. In the other FE software packages, keywords with the same algorithm were identified and are provided in Table Appendix C-4.

For the evaluation of the trajectories, the x displacement of the vehicle was subtracted from the x coordinates of the sensors (stationary vehicle view in local vehicle coordinate system according to Figure 7). Contact forces and node histories were outputted every 0.1 ms. Unfiltered curves were used.

HIT was defined as described in Chapter 2.4.2. The contact forces were separated by body region and contact surface. For the comparison between the models, the resultant total contact force between HBM and GV was used. The times of all contact forces were offset with the value C (time of first contact = 0), as defined in Chapter 2.4.2.

All results performed by external institutions were provided using predefined templates that included the following time histories (every 0.1 ms) for each load case:

- Contact Forces: HBM – GV, Head – GV, arms – GV, right leg – GV, HBM – bumper, HBM – bonnet

- Coordinates: x- and z-coordinate of sensors located at HC, C7, T12, T8, AC, KR, MR, KL, ML

- Resultant acceleration and velocity of head CoG

- Energies: total hourglass energy, internal energy, total energy, contact energy, elastic contact energy

- Artificial added mass

- Time step

A quality check was performed on all submitted results, ensuring that the quality criteria defined in Chapter 2.2.5 had been fulfilled.

4.1.6 Certification Procedure

The idea of the certification procedure is that simulations performed by a specific user with a specific HBM using a specific FE solver and specific control settings can be compared to a set of reference simulations. This shall help to ensure comparability of kinematic-based simulation results. For the final assessment simulations only the vehicle model is exchanged (using the detailed serial FE vehicle model instead of the generic vehicle model).

The aim of the study was to define corridors and tolerances for a certification procedure based on consistent reference results from state-of-the-art HBMs. The previously defined twelve load cases using the four GV models at three different collision speeds were applied as reference.

Eighteen output dossiers gained from simulations with different models at different institutions and in different FE software packages were grouped into "consistent" and "inconsistent" results based on qualitative comparison of the curves and the results of the statistical analyses.

To compare the *HIT*s, boxplots were used to identify outliers. Outliers were defined as points beyond the 1.5 interquartile ranges ($IQR = Q3 - Q1$) from the median value (shown as a whisker in the diagrams). Reference values and tolerances for head impact times were derived.

Based on the consistent results, corridors were derived for trajectories for the locations of HC, T12 and AC. These reference points were selected as they were most relevant for the assessment of deployable systems for which the head and thorax kinematics were important. The median, minimum and maximum value for each coordinate were derived from all consistent results every 0.1 ms.

Additionally, corridors for the total resultant contact force between HBM and GV were defined based on the minimum and maximum value of the consistent results (again every 0.1 ms).

4.2 Results

4.2.1 Representative Generic Vehicle Models

The responses from the impactor simulations against the calibrated generic FCR models are compared with the derived stiffness corridors from Chapter 3.2.3 in Figure 35. Figure 36 shows the performed impactor simulation at the vehicle midsection with the generic FCR model. The simulation IDs refer to the impact locations as defined in Chapter 2.5.2. A good correlation of the force-deflection characteristics of the GV models and the median curves was achieved. Loading and unloading curves of the GV FCR model remains within the corridors.

The responses of all load cases for the calibrated GV models in all FE codes and the final parameters are included in Appendix-B. The same material properties were applied to all vehicle shapes.
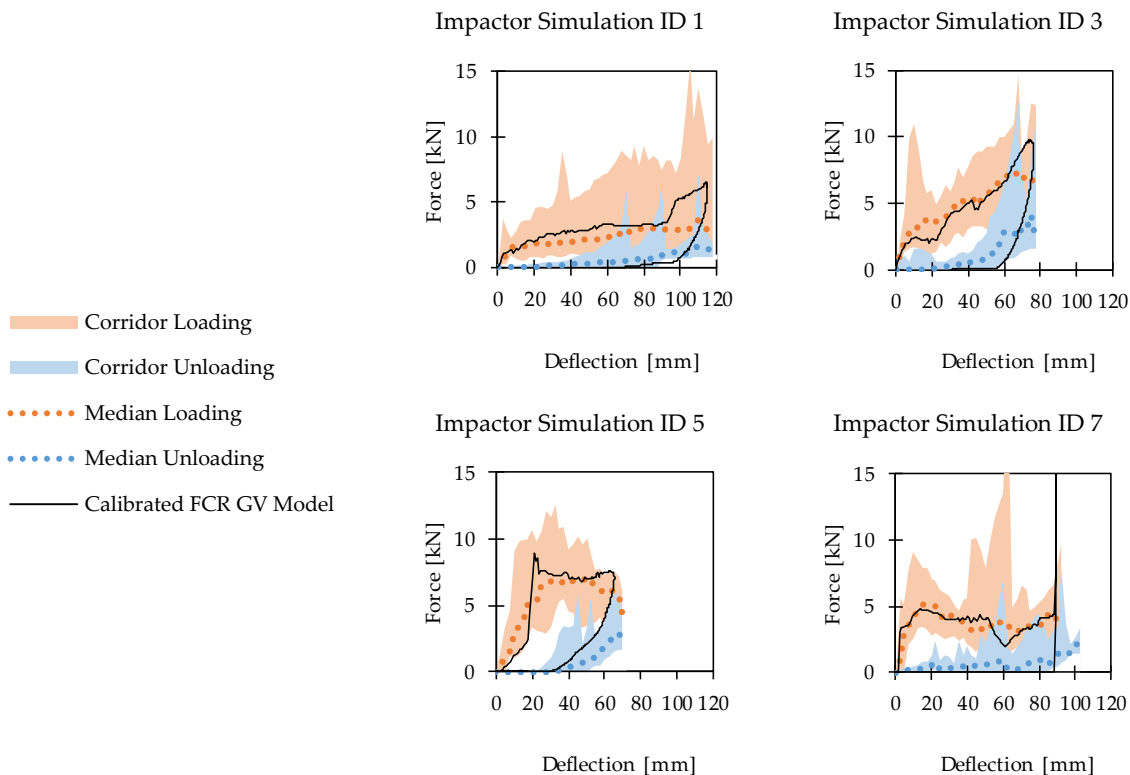
Figure 35: Responses of the calibrated FCR GV Model compared to the developed corridors and median responses for loading and unloading from impactor simulations

Impact Simulation   1   3   5   7

Figure 36: Four impact locations at the vehicle centreline used to gain representative stiffnesses by applying a rigid cylindrical impactor

4.2.2   Harmonised Initial Posture of Pedestrian Models

Figure 37 shows the repositioned THUMS in all analysed postures. The variations in the arm postures for GHBMC are shown in Figure 38. For Postures 1, 2 and 3, only the posture of the arms was varied. Posture 4 has slightly changed arms and legs. Postures 5, 6, 10 and 11 show a variation in the torso and/or neck angle and, therefore, varying head positions (HC). For Posture 7 and 8, the shoe sole angle and height of HC was modified from Posture 2 and 3, respectively. Posture 9 shows the same leg posture as Posture 4, but a modified elbow angle.

The maximum difference in the *HIT* due to a variation in the initial posture of THUMS was 3.7 ms, which is a relative deviation of 2.6% compared to the mean *HIT* (Figure 39). For GHBMC, the resulting *HIT*s related to the modified arm postures are shown in Figure 41. A difference up to 5.2 ms was observed (3.7%). Arm Posture 1 (SAE posture) led to the highest *HIT*, and arm Posture 2 (Pedestrian AEB target) to the smallest *HIT* for both HBMs.

Figure 37: THUMS postures
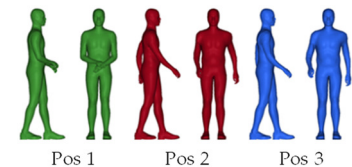
Figure 38: GHBMC postures
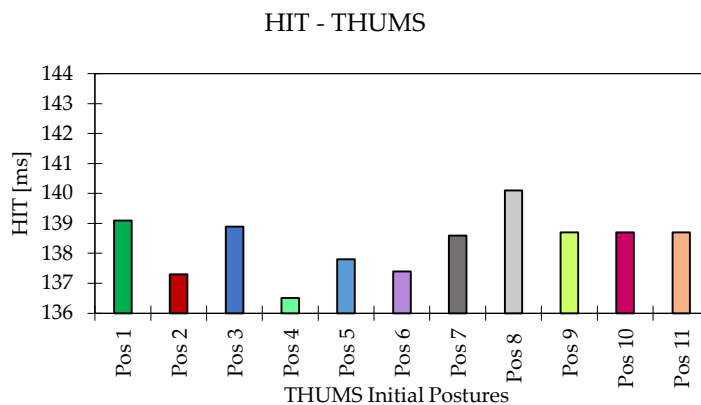
Figure 39: Influence of initial posture of THUMS on *HIT*
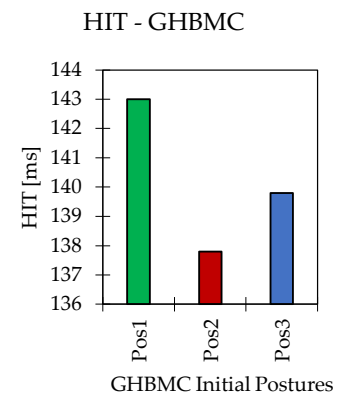
Figure 40: Influence of initial posture of GHBMC on *HIT*

The following sensitivities were observed within the THUMS simulations (summarised in Figure 41):

- Within the baseline postures 1, 2 and 3 in which only the arm posture was varied, a variation in head contact time of up to 1.8 ms was observed.

- For Posture 7 and 8, the sole angle was modified from that in Posture 2 and 3, respectively, which resulted in a higher position of the *acetabulum* and the head. The initial position of HC and AC was 15 mm higher, which led to a 1.3 ms higher head contact time for arm Posture 2 and 1.2 ms for arm Posture 3 (corresponds to a relative deviation of 1%).

- Changing the position of HC in the x (+52 mm) and z-directions (-15 mm) without changing the height of AC in Posture 11 led to a difference in the *HIT* of 1.4 ms (~1%) compared to the baseline Posture 2.

- A smaller variation (11 mm in the x- and 3 mm in the z-direction in posture 5) caused a 0.7 ms smaller *HIT* (~0.5%). A variation of 5 mm in the x-direction did not lead to differences in *HIT* (Posture 6 compared to Posture 3)

- A modification in the torso angle (C7x increased by 38 mm) resulted in a 13 mm smaller z-position of HC and an unchanged HCx, but did not cause a difference in *HIT* (Posture 10 compared to Posture 11).

- In Posture 4, the elbow was stretched more than in Posture 9, which cause a 1.5% smaller *HIT* (ΔHIT = 2.1 ms)

- A modification only in the leg posture and HCx led to virtually no difference in *HIT* (ΔHIT of Posture 9 and Posture 3 is only 0.2 ms).
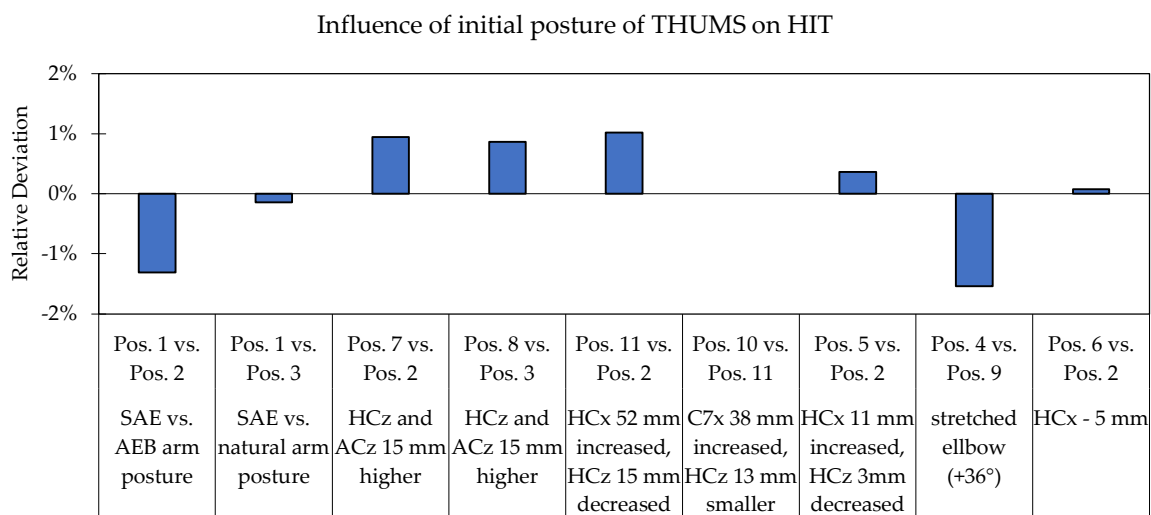
Figure 41: Pairwise comparison of *HIT* for variations in the initial posture of THUMS (simulations with FCR at 40 km/h)

No great differences in the trajectories were observed due to modifications in the initial posture of the HBMs as shown in Figure 42. Differences in the second peak of the contact forces (at about 30 ms) were found when the posture of the legs was modified (Figure 43).

Trajectories
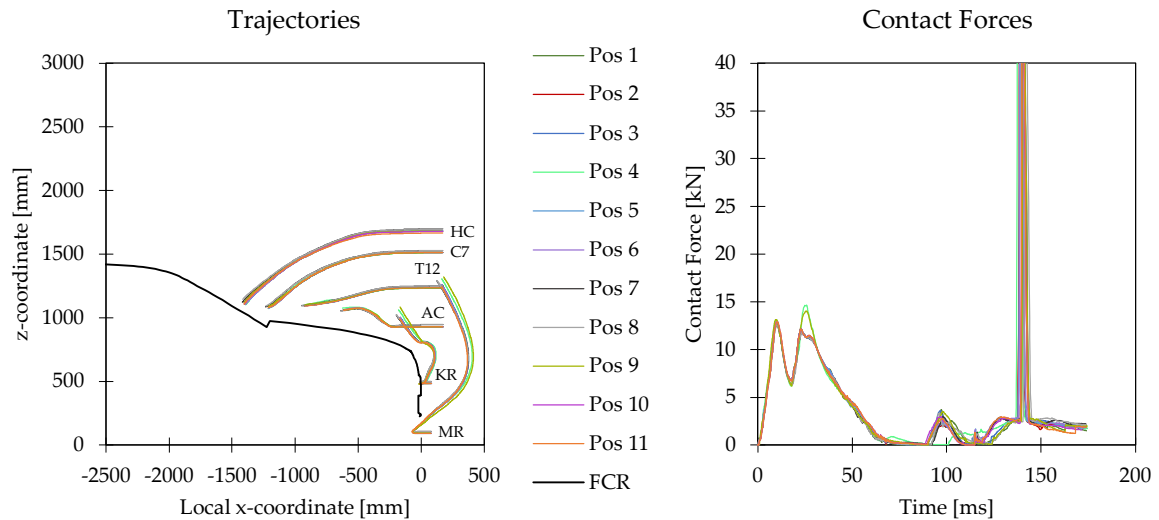
Contact Forces

Figure 42: Influence of initial posture of THUMS on trajectories (impact with generic family car model at 40 km/h)

Figure 43: Influence of initial posture of THUMS on total contact forces (impact with generic family car model at 40 km/h)

The postures of the arms had a negligible effect on the trajectories of both HBMs, which is shown in Figure 44. The contact forces show some differences as soon as the elbow contacted the bonnet of the vehicle (Figure 45). The observed contact force between the right arm of THUMS and the bonnet was only 2 kN for Posture 2, while it was 3.7 kN for Posture 3 and 3.5 kN for Posture 1.

Trajectories
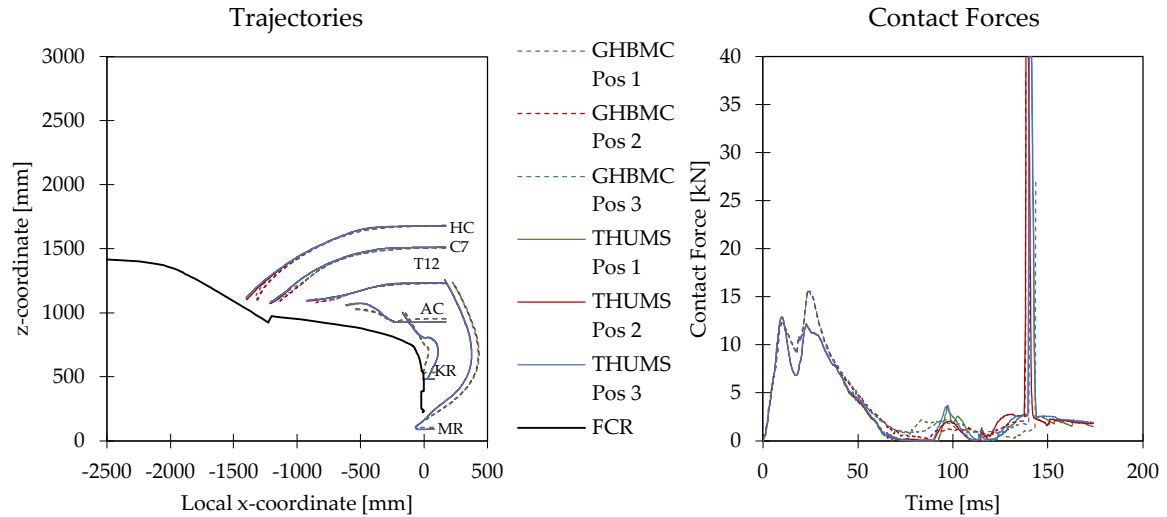
Contact Forces

Figure 44: Influence of initial arm posture on trajectories for THUMS and GHBMC (impact with generic FCR model at 40 km/h)

Figure 45: Influence of initial arm posture on total contact forces for THUMS and GHBMC (impact with generic FCR model at 40 km/h)

No influence in the initial arm posture on the trajectories was observed for the THUMS simulations with the generic SUV model at 40 km/h either, which is shown in Figure 46. For the SUV impact, the contact forces also remained less affected, which is shown in Figure 47. Posture 2 again resulted in the smallest *HIT* (-1.4 ms, which is a relative difference of 1%), while the other two postures also resulted in the same *HIT*.
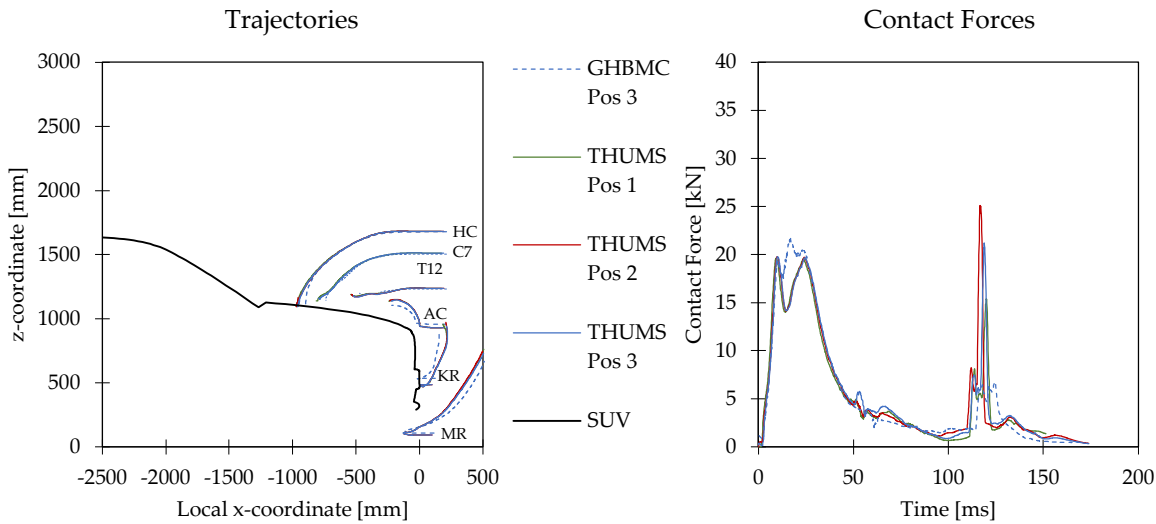
Figure 46: Influence of initial arm posture on trajectories for the impact with the generic SUV model at 40 km/h

Figure 47: Influence of initial arm posture on total contact forces for the impact with the generic SUV model at 40 km/h

As the differences between the two models were smallest for Posture 3, and the posture represents a natural walking posture (Untaroiu *et al.*, 2009), it was used as baseline for all subsequent simulations. Figure 48 shows THUMS and GFigHBMC in Posture 3. In the right figures, the two models are overlaid, showing that the postures match very well.
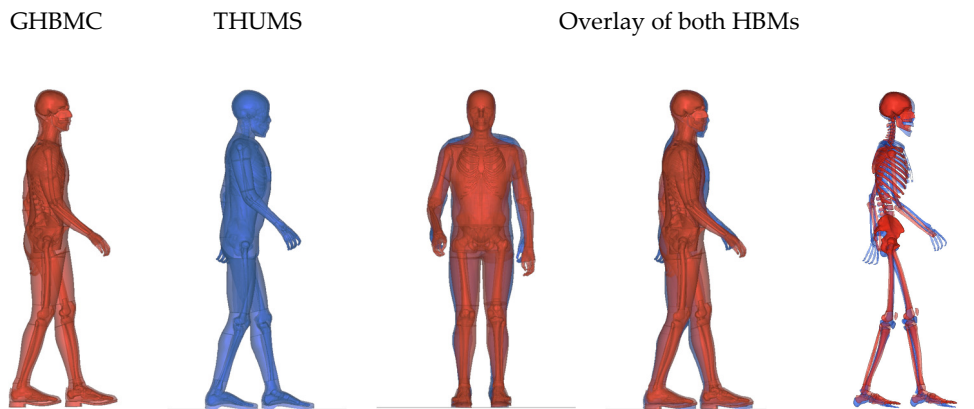
Figure 48: Geometrical comparison of THUMS (blue) and GHBMC (red) AM50 model in Posture 3

With respect to the simulations carried out externally, users were asked to position their models as close as possible to Posture 3 of the THUMS and GHBMC. The measures from Table Appendix C-2 of Posture 3 were provided as reference. A reference skeleton (provided by LAB without IP restrictions) was positioned according to Posture 3 as shown in Figure 49 and provided as a reference for qualitative comparisons. Pictures of overlays with the skeleton were also requested additionally to the measured values to prove that measures had been taken comparable. Figure 50 shows an overlay of THUMS and GHBMC model in Posture 3 with the reference skeleton. Based

on the results of the sensitivity study, it was recommended to start with positioning the centre of *acetabuli* at the correct height and then align the rest. Due to anthropometric differences, the postures cannot be replicated exactly, therefore, appropriate tolerances were defined, taking the results of the sensitivity study into account. The final specifications for the reference posture are provided in Table Appendix C-3. Special attention was taken regarding the height of the *acetabulum*, the head CoG and the angles of the right arm as they turned out to be the most critical factors for the comparability of the results.

Figure 49: Reference skeleton in final selected reference posture

Figure 50: Overlay of THUMS (blue) and GHBMC (red) skeleton with reference skeleton (grey) for final selected reference posture

4.2.3   Harmonised Simulation Setup

No effects on trajectories, contact forces, or *HIT* were observed due to pre-simulations for initialisation of the HBM. The friction between the ground and the shoes also did not affect the results. All curves were congruent and, therefore, are not provided.

The trajectories and head contact time were found to be sensitive to the contact setting, which is shown in Figure 51. Changing the contact formulation from a segment-based penalty formulation to a default penalty formulation (explained in Chapter 2.2.3) led to a higher head impact point (58 mm difference in the x-z plane) and a 2.3 ms higher head contact time. The standard penalty formulation led partly to penetrations of the HBM outer surface into the interface layer of the GV. Therefore, the segment-based penalty formulation is preferable. Increasing the friction between the vehicle and the pedestrian led to a decrease in *HIT* (Figure 52) and a lower end-point of the head trajectory (Figure 51). A modification of the damping coefficient VDC had no effect on *HIT* or the trajectories.

Trajectories

HIT – Contact Parameters
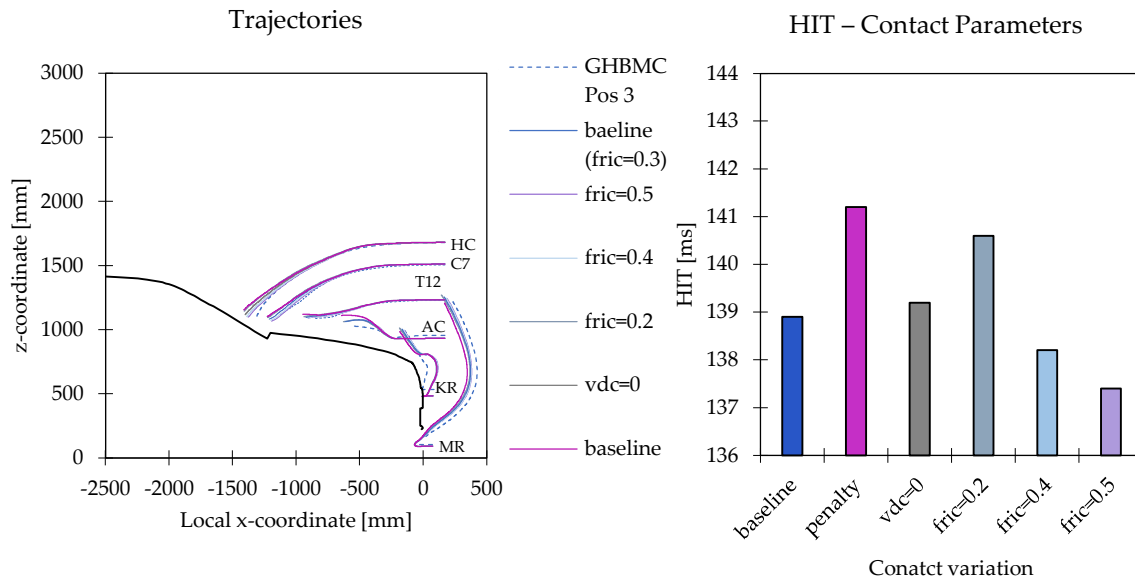
Figure 51: Sensitivity of trajectories to modifications of contact options with THUMS for impact with generic family car model at 40 km/h

Figure 52: Sensitivity of HIT to modifications of contact options with THUMS for impact with generic family car model at 40 km/h

Based on the results of the sensitivity study, the following boundary conditions were fixed for the subsequent simulations:

- The segment-based contact algorithm was used

- The coefficient of friction between the vehicle and the HBM was fixed at 0.3

- No pre-simulations were performed

All details of the finalised simulation protocol were included in the Euro NCAP TB 024 (Euro NCAP, 2017b) and the 2017 version of the pedestrian testing protocol (Euro NCAP, 2017a).

4.2.4   Harmonised Output

The developed simulation protocol was applied to compare the responses of THUMS and GHBMC for twelve reference load cases (FCR, MPV, SUV and RDS impacts with collision speeds of 30, 40 and 50 km/h). It was feasible to apply the developed procedure to the two HBMs: All load cases led to plausible results, and no obviously unrealistic behaviour of the HBMs or the GV models was observed. Furthermore, all quality criteria defined in Chapter 2.2.5 were fulfilled.

Contact forces, *HIT* and trajectories of the two models were compared from all twelve load cases:

The maximum difference of *HIT* was 3.5 ms, which was observed upon the impact with the SUV at 40 km/h. The average difference in *HIT* was 1.9 ms (in 7 of the 12 load cases, the difference was smaller than 2 ms). The best correlation in terms of *HIT* was observed for the impacts with the family car (mean $\Delta HIT = 1$ ms).

Figure 53 summarises the relative deviation in terms of *HIT* values of THUMS compared to GHBMC for all load cases. The maximum deviation was 2.6%, which was observed for the SUV impact at 40 km/h. THUMS was showing a lower *HIT* compared to GHBMC in this load case. In five load cases, the deviation was less than 1% and exceeded 2% in three configurations.

Difference in HIT values between THUMS v4 and GHBMC PS
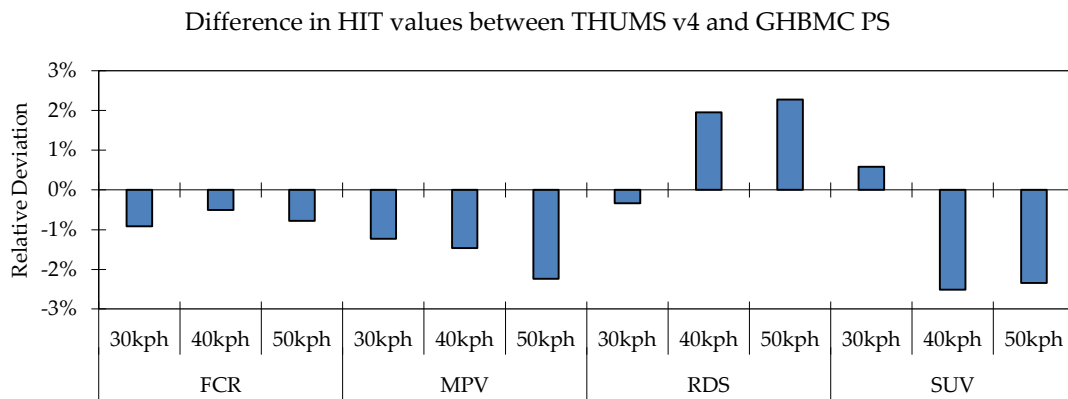
Figure 53: Differences in terms of *HIT*s from simulations with AM50 THUMS v4 and GHBMC PS models in LS-DYNA (shown as relative deviations of THUMC compared to GHBMC)

Figure 54 shows the trajectories and contact forces for the three collision speeds with the FCR model. The differences in terms of the response trajectories between the two models lessened with higher impact velocities.

The contact forces of the two models were very similar for all impact cases. Only minor differences in the first peak (leg impact) between the two models were found. Some differences were observed for the second peak and the unloading (hip impact at the bonnet leading edge). Some differences in the timing and magnitude of the contact force induced by the arm contact with the bonnet were also noted here (small peak after 60 ms).

The results of all load cases are shown in Appendix D. The largest difference in terms of trajectories was observed for the impact with the roadster at 30 km/h. The distance between the locations of HC of the two models was 143 mm at the time of head impact, which corresponds to a path length of 4%. The difference in *HIT* was 0.6 ms for this load case, which was the smallest value observed in all compared simulations.

The knee trajectories showed the biggest differences between the two models. Differences were already observed for the initial posture due to anthropometric reasons. The femur is 25 mm longer in the GHBMC than in the THUMS pedestrian model.
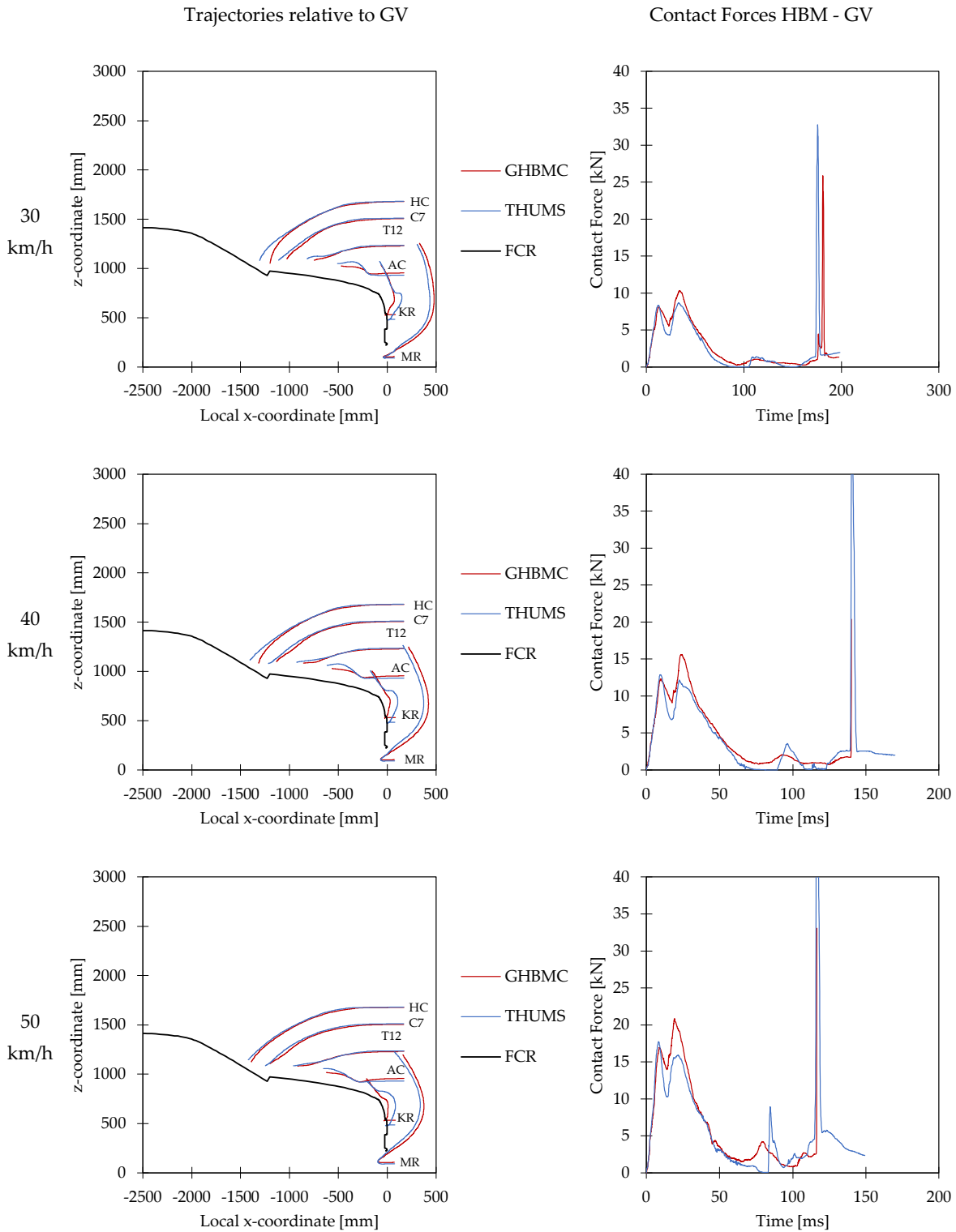
Figure 54: Contact forces and trajectories of THUMS and GHBMC AM50 model in LS-DYNA for impacts with
generic FCR model

For the certification procedure, the number of analysed sensors was reduced: Due to the
anthropometric differences and because the kinematics of the lower extremities have little
importance for the assessment of deployable systems, no requirements for these are specified in
the next chapter. Furthermore, C7 and HC showed highly similar trends.

4.2.5 Certification Procedure

Eighteen different dossiers of results were available for the subsequent analysis, named Model 1-Model 18. For Model 5, no results of the impacts with 30 km/h were provided. For all other Models, the dossier was complete and included all twelve load cases. In the first step, outliers were identified and removed from the dataset. Corridors for the trajectories, displacements and contact forces were specified based on consistent results. Furthermore, reference values and tolerances for *HIT*s were defined for the final certification procedure.

Head Impact Time

The head impact times resulting from the eighteen different pedestrian simulations with varying models and in four different codes are shown in Figure 55. Boxplots were created to identify outliers in the datasets. The boxes show the 1st quartile (*Q1*), median value and 3rd quartile (*Q3*). The whiskers represent the lowest value within the 1.5 *IQR*. The cross indicates the mean value for each load case. As the distributions were not symmetric, the median value together with quartiles were found to be more useful than the mean value with standard deviation.

Six outlying results were identified and are shown as circles in the figure: Results from Pedestrian Models 2, 5, 6, 11, 12 and 15 did not fall within the 1.5 *IQR* for at least one load case.
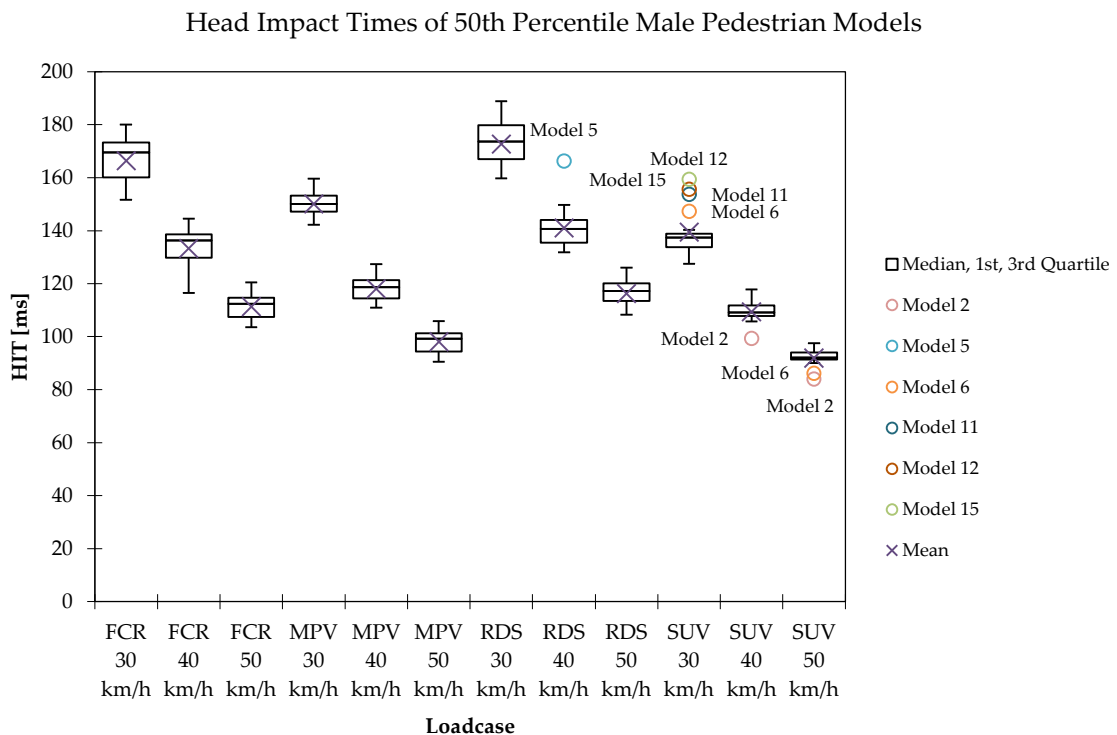
Figure 55: Boxplots of *HITs* from eighteen different pedestrian simulations for impacts with FCR, MPV, RDS and SUV at 20, 40 and 50 km/h with outliers marked with circles

In the next step, the outliers were excluded from the dataset. The median value from the remaining data was calculated as reference value. The relative deviation of each result from the reference

value per load case was calculated as a percentage and plotted in Figure 56. All datasets with outlying behaviour were marked as unfilled circles and the remaining, consistent datasets that were also used to derive the median / reference value are shown as filled circles. A maximum span of 24% variation of *HIT* compared to the reference value was observed in the dataset for all provided results. The greatest deviations were observed for the RDS impact at 40 km/h and the SUV impact at 30 km/h. Pedestrian model 2 showed smaller *HIT*s than the consistent model in most of the load cases. For the other outlier models, no clear trend could be detected. While they tended to have smaller *HIT*s for family cars, higher *HIT*s were observed for the SUV impacts at 30 and 40 km/h.
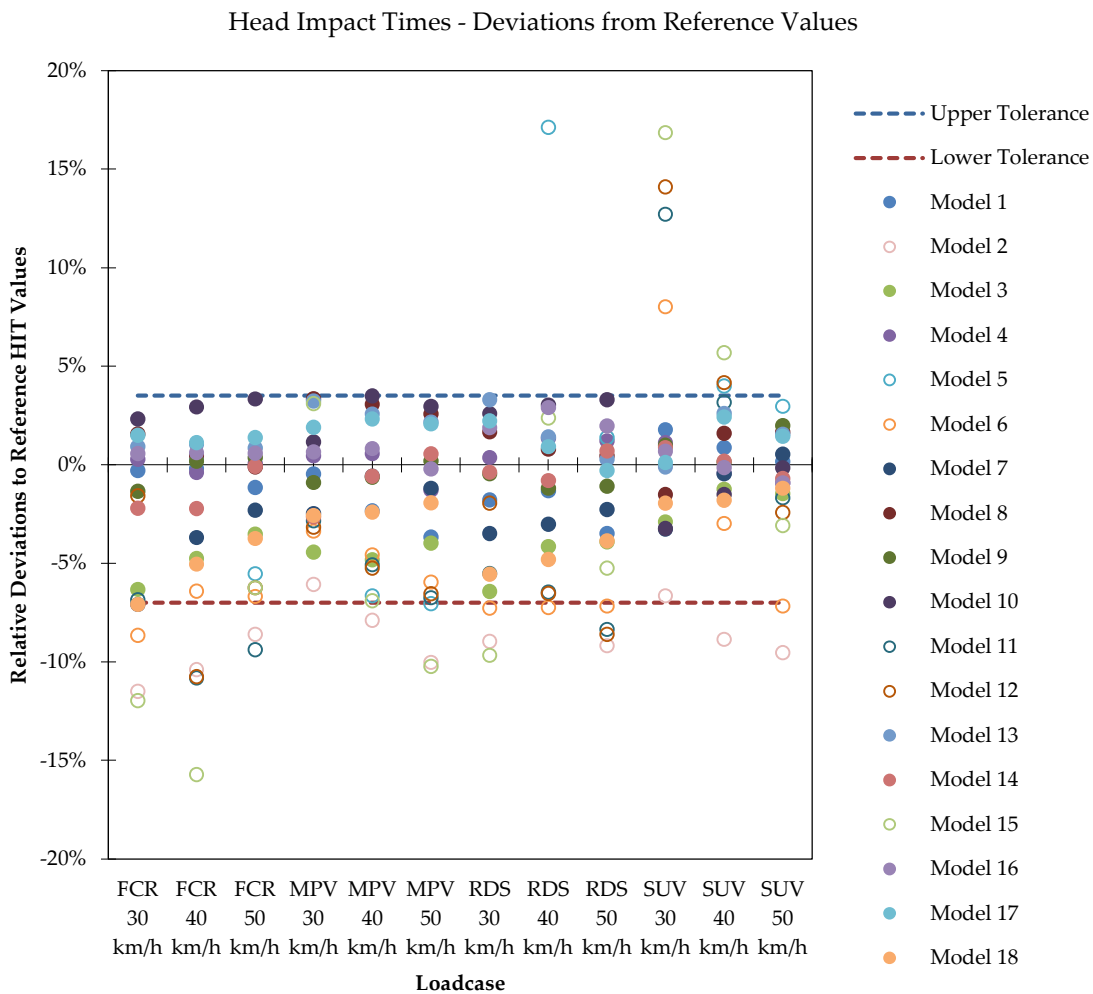
Figure 56: Deviation from reference *HIT* values of the eighteen different datasets in percent for all twelve load cases (FCR, MPV, SUV, RDS at 30, 40 and 50 km/h)

The maximum and minimum relative deviations within the consistent datasets from the reference value were +3.5% (Model 10 at impact with MPV at 40 km/h) and -7% (Model 18 for impact with FCR at 30 km/h), respectively. These values were chosen as upper and lower allowed tolerance values for the certification procedure. The reference values together with the derived upper and lower boundaries for the certification procedure are summarised in Table 7.

Table 7: Reference *HIT* values and upper and lower boundaries for the certification procedure

HIT [ms]	FCR			MPV			RDS			SUV		
	30 km/h	40 km/h	50 km/h	30 km/h	40 km/h	50 km/h	30 km/h	40 km/h	50 km/h	30 km/h	40 km/h	50 km/h
Reference Value	172.3	138.1	114.3	151.5	120.4	100.8	176.9	142.1	119.3	136.5	109.0	92.9
Maximum Value	178.4	143.0	118.4	156.9	124.7	104.4	183.1	147.1	123.5	141.3	112.9	96.2
Minimum Value	160.2	128.4	106.2	140.8	111.9	93.7	164.5	132.1	110.9	126.9	101.3	86.3

Trajectories

When analysing the trajectories, it was observed that models 2 and 15 were also outliers in terms of the initial location of the head CoG. They are shown in red in Figure 57 and Figure 58. The initial posture of the head CoG was significantly lower than that of the other models (1635 mm and 1638 mm, respectively, while the median value was 1680 mm and 1.5 *IQR* was 10 mm). They were even beyond the 95% interval of the mean value ± 2 times the standard deviation (1644-1714 mm).

The head CoG of model 14 was initially located at 1714 mm and, therefore, higher than the median value ±1.5 *IQR*, but fell within the 95% interval. As it showed no outlying behaviour in terms of its *HIT*, it was maintained in the data sample.

To define the corridors, several approaches were taken. As a first approach, the method described in the SAE norm J2868 (SAE International, 2010a) was applied, defining the corridor as a percentage of the path length based median reference trajectories. In this approach, the path length at each time step is derived from the median x and z coordinates for each reference point as a first step. A tolerance of +10% and -5% of the path length is added to the median trajectory, resulting in the corridors shown in Figure 57. As the corridor for the head trajectory was much wider than required, the method was rejected.

FCR 40 km/h
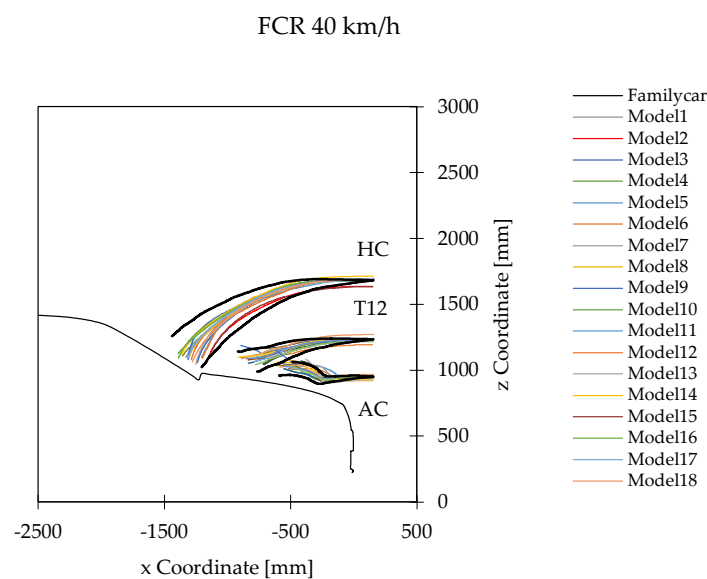
Figure 57: Corridors derived with SAE J2868 approach based on path length for z as a function of the x trajectory relative to the vehicle coordinate system for the FCR impact at 40 km/h

Next, the minimum and maximum values for each time step were derived in the x and z-directions ($x_{min/max}$ and $z_{min/max}$). All models that displayed outlying behaviour in terms of their *HIT*s were sorted out prior to creating the corridor. The corridors shown in Figure 58 are exemplary for the 40 km/h impact with the FCR and were derived by connecting the coordinates $[x_{min}(t_n) \quad z_{min}(t_n)]$ for the ascending trajectories and $[x_{min}(t_n) \quad z_{max}(t_n)]$ for the descending trajectories, as shown in Figure 59. The thick black line in Figure 58 shows the corresponding corridor that was created. Each colour represents the results for one pedestrian model.

FCR 40 km/h
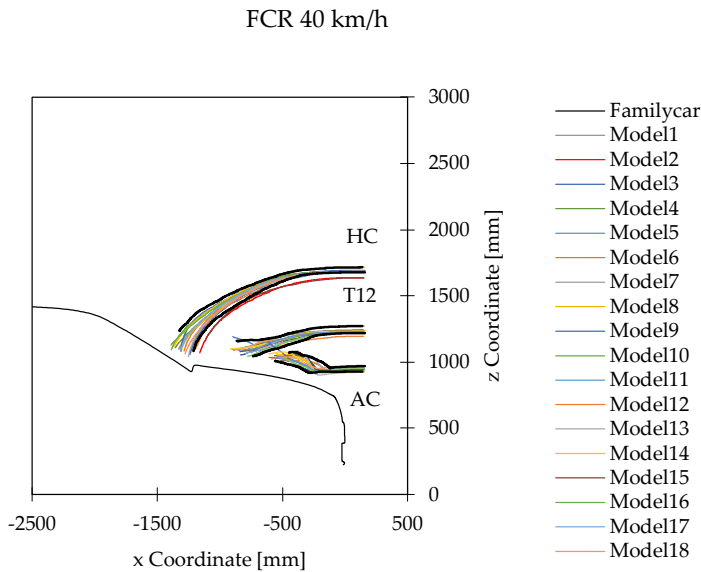
Figure 58: Corridors (black line) for trajectories for z as a function of the x trajectory relative to the vehicle coordinate system for the FCR impact at 40 km/h
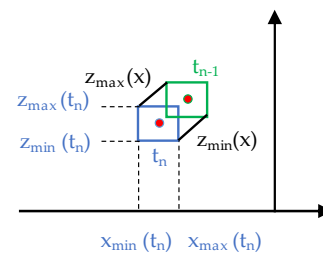
Figure 59: Relationship between time-dependent and x-trajectory-dependent corridors

As timing is essential for the assessment of the deployable systems, a time dependent approach was finally chosen. This means that the coordinate of the analysed reference point (shown as a red point in Figure 59) has to lie within a box that stretched from x_{min} to x_{max} and z_{min} to z_{max} (shown as blue and green boxes in Figure 59 for two different time steps) at each time step. The resulting corridors for z and x as a function of time are shown in Figure 60-Figure 65. The corridors are shown as black dashed lines in the figures.
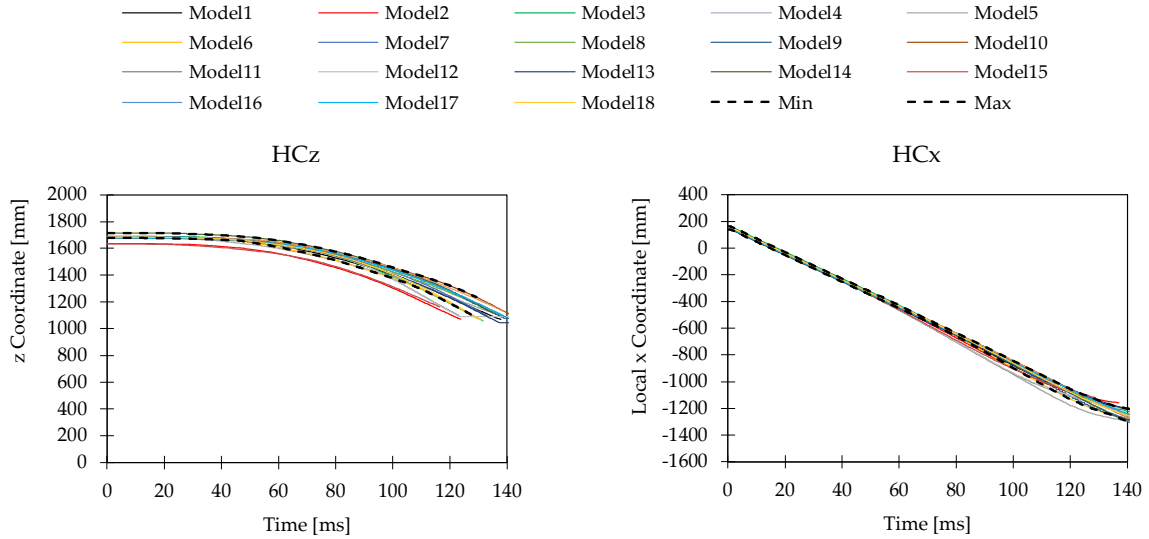
Figure 60: Corridor for the z trajectory as a function of time (black dashed line) for Head CoG for FCR 40 km/h load case

Figure 61: Corridor for the x trajectory as a function of time (black dashed line) for Head CoG for FCR 40 km/h load case
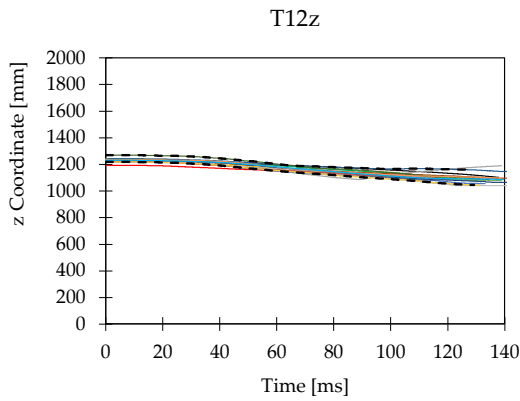
Figure 62: Corridor for the z trajectory as a function of time (black dashed line) for T12 for FCR 40 km/h load case
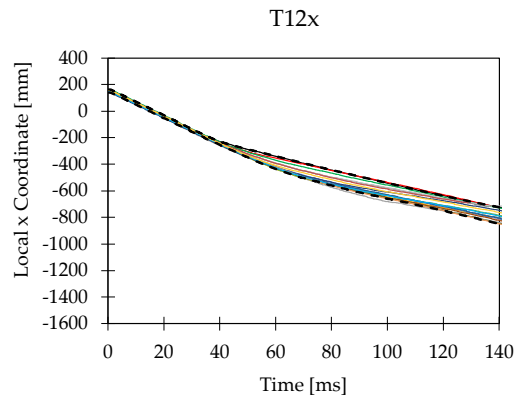
Figure 63: Corridor for the x trajectory as a function of time (black dashed line) for T12 for FCR 40 km/h load case
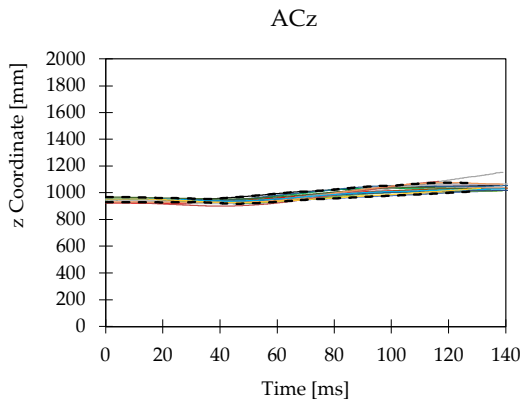
Figure 64: Corridor for the z trajectory as a function of time (black dashed line) for centre of *acetabuli* for FCR 40 km/h load case
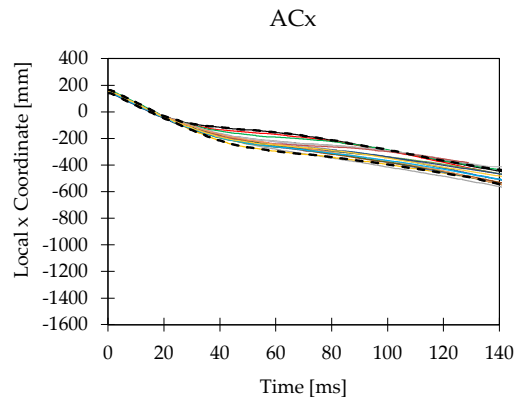
Figure 65: Corridor for the x trajectory as a function of time (black dashed line) for centre of *acetabuli* for FCR 40 km/h load case

As shown in Figure 60, Models 11 and 12 (already defined as outliers because of their *HIT*s – shown in grey) fell outside the z corridor towards the end of the simulation. The responses of the other fourteen pedestrian models remained inside the corridors.

The corridors of all load cases can be found in Appendix-E.

Contact Forces

Figure 66 shows the resultant total contact force observed between the pedestrian and GV using the varying HBMs and varying codes, for the 40 km/h impact with the generic FCR model. All results for which *HIT*s or trajectories showed outlying behaviour *HIT* are drawn in grey. Additionally, the red and orange lines (Models 1 and 3) were also removed, as they showed significantly higher first peaks compared to those in the other models. The corridors, shown as black dashed lines, represent the minimum and maximum values of the contact forces of the remaining consistent models as derived at each time step.

The final corridors for all load cases are shown in Appendix-E.
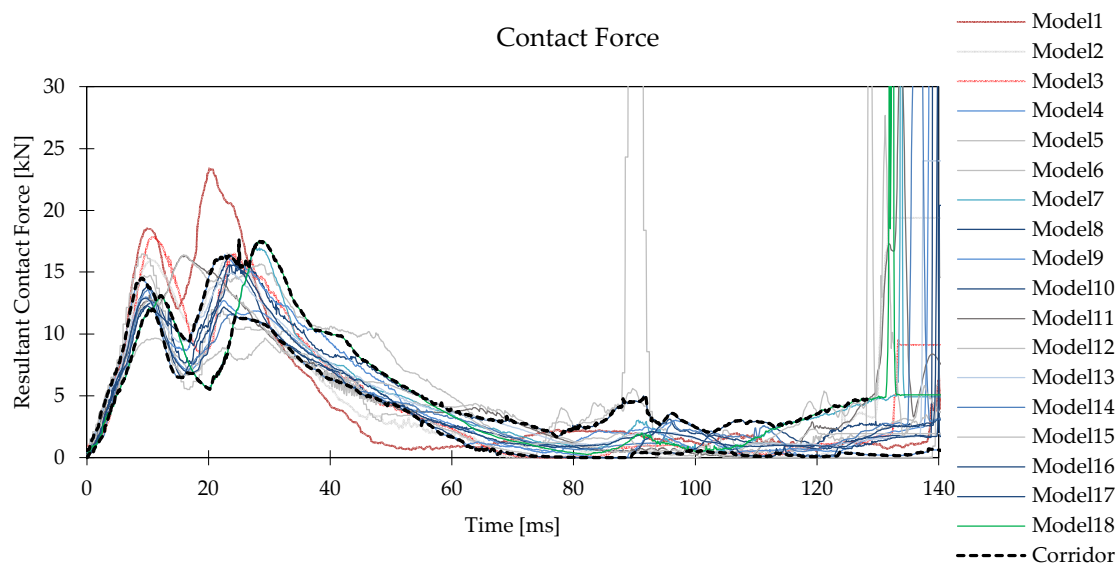
Figure 66: Total resultant contact forces between vehicle and pedestrian models for all submitted results and the derived corridors for a 40 km/h impact with an FCR

4.3 Discussion

4.3.1   Representative Generic Vehicle Models

To avoid inconsistencies from being produced by the GV models when comparing pedestrian models, the impactor simulations should be repeated whenever the FE solver version, platform, or control settings (e.g. time step) are changed.

The material parameters were optimised for the FCR model, which then showed the closest behaviour to the median curves. As the models had to be translated and recalibrated in the other FE codes, it was decided to keep the material parameters consistent for the different shapes. With regard to the other vehicle categories, the responses still fell inside the corridors, but deviations to the median values were observed. The stiffness of the ble of the SUV approached the maximum corridor more closely than the median (Figure Appendix B-6). It was more important in the current study to ascertain that the GV models behaved in a way that was comparable than that the response represented the median characteristic. For this reason, the observed deviation was reasonable. When the GV models were translated, it was found that differences were observed even in those simple models, resulting from inconsistent definitions within the different FE software packages (e.g. element formulations or constitutive laws).

The chosen modelling approach was found to be appropriate for the analyses of global kinematics. No analyses of compliance with current regulations were performed using the developed GV models. Therefore, they should be used for kinematic analyses only at the current developmental stage.

For a discussion of the stiffness corridors and the median geometry, refer to Chapters 3.3.2 and 3.3.3.

4.3.2 Harmonised Initial Postures in Pedestrian Models

Several studies have indicated that the initial pedestrian stance affects the impact kinematics (Chen *et al.*, 2015a; Li *et al.*, 2015; Elliott *et al.*, 2012b; Soni *et al.*, 2013a). In the real world, a variety of impact scenarios and pre-crash reactions of the pedestrian (Soni *et al.*, 2013b) can occur. Nevertheless, the posture has to be harmonised to make comparable assessments. Therefore, it was important to properly define the initial posture(s) to enable comparable virtual testing. In the future, it would be beneficial to perform assessment simulations in various predefined initial postures to cover more real-world scenarios.

All postures used in this study were replications of a midstance. This is in accordance with authors who proposed using the midstance because it is most representative for pedestrian collisions (Kam *et al.*, 2005) and tends to be the "worst case" posture (Soni *et al.*, 2013a).

The struck-side leg faced backwards in all simulations, as this was already defined in the Euro NCAP pedestrian protocol (Euro NCAP, 2016). According to Elliott *et al.* (2012b), this stance represents the "worst case", as head-impact velocities and *WAD* are smaller for impacts with the struck-side leg facing forward. This is because this stance tends to cause more lateral displacement of the pedestrian.

The posture of the arms was completely open in the Euro NCAP pedestrian-testing protocol until 2017. Therefore, the initial posture of the arms varied greatly in the simulations performed by the car manufacturers reported to Euro NCAP. Some studies are available that show that the posture of the arms affects the torso and head kinematics (Schroeder *et al.*, 2000; Brun-Cassan *et al.*, 1984; Crandall *et al.*, 2005; Coley *et al.*, 2001; Paas *et al.*, 2015b). No fully straight arm posture was included

in the present study, which might have caused the arm to get stuck between the HBM and the vehicle. The arm posture mainly affected the *HIT* and had little effect on trajectories and contact forces. *HIT*s were smaller with a stretched elbow than with a bent one. The complete stretched elbow used in Posture 4 was not able to support the torso, which was the case in all postures where the elbow was initially bent. The kinematics are shown in Figure 67. Posture 9 represents the baseline posture for this comparison and is shown in yellow, while Posture 4, with a stretched elbow, is shown in green. The green elbow remains stretched out and, unlike the yellow one, does not impact the bonnet. The missing arm support leads to smaller *HIT*s.

t0   75 ms   100 ms
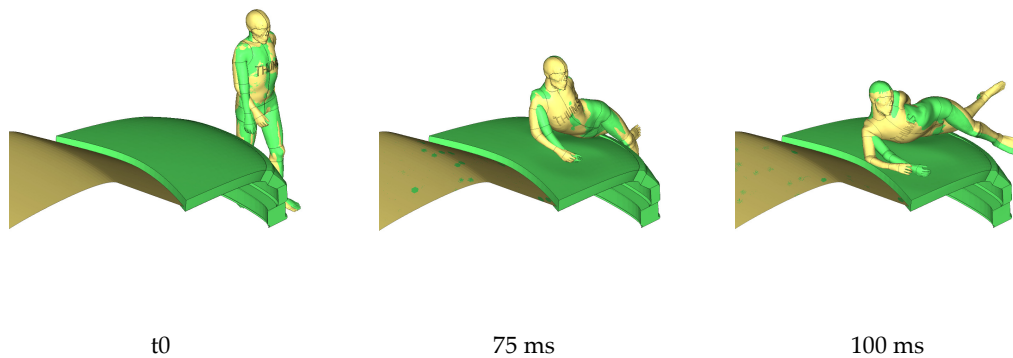
Figure 67: Comparison of arm kinematics of stretched versus bent elbow in THUMS simulations using a generic FCR model at 40 km/h

In Figure 68, the differences in arm support are shown for the GHBMC model. The angles of the humerus for the simulations with GHBMC clearly differed with initial Postures 1, 2 and 3. Posture 1 led to more support and, therefore, slower head velocities in the z-direction, as shown in Figure 69. This led to the significant higher *HIT*s for Posture 1 in the GHBMC simulations.
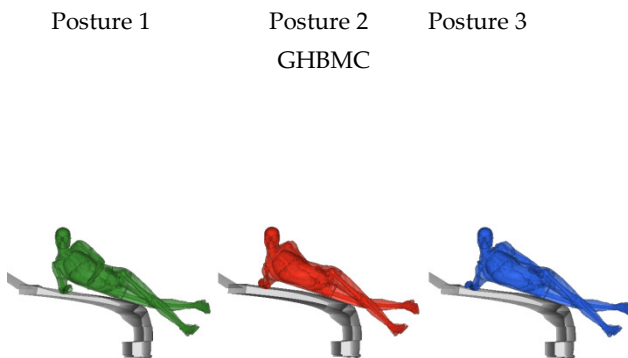
Figure 68: Support of humerus for Posture 1 (green), 2 (red) and 3 (blue) at 100 ms in GHBMC simulations (FCR with 40 km/h)
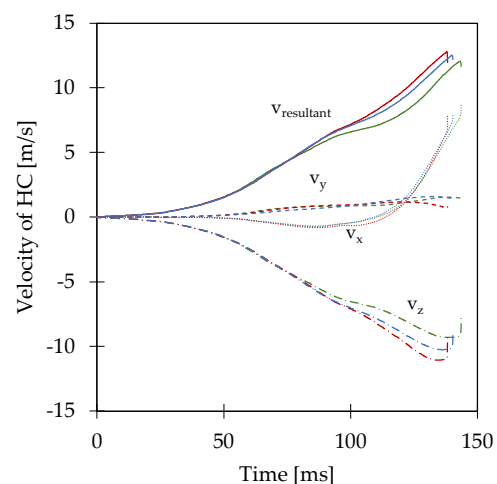
Figure 69: Head velocities of GHBMC with three different arm postures in global coordinate system (FCR impact with 40 km/h)

For the SUV impact, the different arm postures led to fewer differences, and no deviations in terms of contact forces were observed. Due to the higher ble, the upper body kinematics differed in the SUV impact from the FCR impact. The arm was observed to slide away over the bonnet and did not provide as much support as in the FCR impact due to the vehicle shape. Figure 70 shows the arm posture at 72 ms when the arm begins to slide away, resulting from the initial arm postures 1, 2 and 3. Figure 71 shows an overlay of the arm kinematics from 68 – 80 ms (after t0).

| Posture 1 | Posture 2 | Posture 3 |
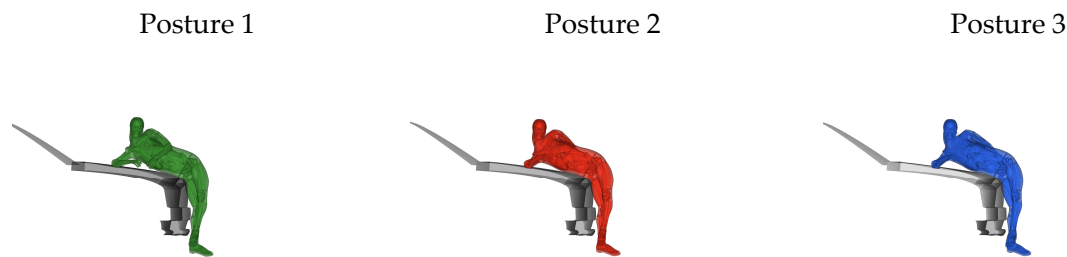
Figure 70: Arm posture of THUMS at 72 ms for impacts with the generic SUV model at 40 km/h and three different initial arm postures

| 68 ms | 72 ms | 76 ms | 80 ms |
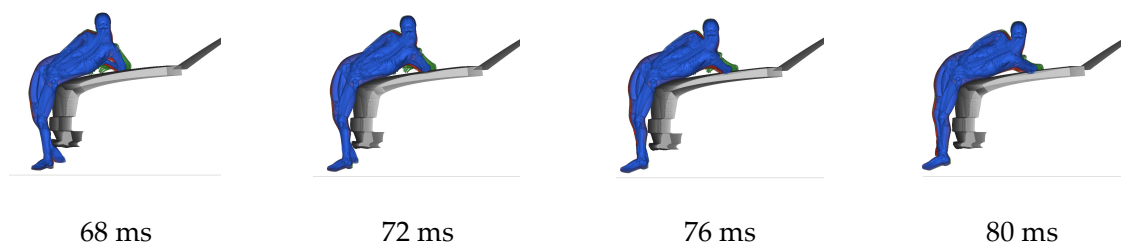
Figure 71: Overlay of arm kinematics for impacts at 40 km/ with the generic SUV model simulated with THUMS and three different initial arm postures (green = Posture 1, red = Posture 2 and blue = Posture 3)

As the arm posture affected the *HIT*, the initial posture has to be defined properly to run comparable simulations and should be as close as possible between different HBMs. An accident analysis of GIDAS data indicated that the shoulder and elbow impacts are associated with severe injuries (Paas *et al.*, 2012). These findings highlight the importance of applying a realistic arm posture in which the wrists are not tied together. Arm Posture 3, which was selected as a harmonised baseline posture is, therefore, a good choice.

It was shown that the kinematics were sensitive to the height of the *acetabulum* centres, which is in accordance with the findings of Kerrigan *et al.* (2009a) and Paas *et al.* (2015c). As the shoe angle and contact with the ground did not affect the results, it was considered preferable to align the height of the AC rather than ensuring ground contact in cases when one of the two options has to be chosen due to anthropometric reasons. Therefore, the findings indicate that the hip height should be aligned as a starting point for the positioning of the HBM.

As the geometries of HBMs represent individuals, anthropometric differences were observed (e.g. differences in neck lengths or femur lengths between THUMS and GHBMC). To further improve the comparability of the results, detailed reference anthropometries would be needed to which the HBMs could be morphed.

4.3.3 Harmonised Simulation Setup

The results of the sensitivity study showed that the friction between the HBM and the vehicle influenced the kinematics. A higher coefficient of friction led to a smaller *HIT* and to a lower head impact point. To make simulations comparable, it was necessary to fix the contact settings.

In the literature, coefficients of friction of up to 0.5 are found (Paas *et al.*, 2015c; Chen *et al.*, 2015a). The friction observed in real-life scenarios depends on the clothes worn by the pedestrian and the vehicle surface. To carry out the procedure, however, the friction has to be harmonised. For this reason, a coefficient of friction of 0.3 was used, which is in agreement with that reported in several other studies (Simms and Wood, 2006; Crocetta *et al.*, 2015; Mizuno and Ishikawa, 2001; Li *et al.*, 2015; Fahlstedt *et al.*, 2016a; Elliott *et al.*, 2012a).

It was observed that changing the penalty formulation caused greater differences in *HIT* than using another HBM. Therefore, consistent contact formulations have to be applied when using other codes, which can be controlled by applying the procedure developed in this study.

Although the results of the current analyses indicated that pre-simulations for initialisation of the HBM were not needed as they did not change the global head impact kinematics, this cannot be generalised. For studies in which a focus is placed on injury mechanisms (e.g. knee ligament rupture), it might be important to consider the (pre-)loading due to the body weight, although it was found to be negligible for the presented analysis of the current study.

It is clear that boundary conditions are varying in real-world accident scenarios and are not all covered by the proposed harmonized setup. However, harmonization is needed to allow fair and reasonable comparison in order to perform an assessment. In the future, a variety of harmonized scenarios might be needed that include a variety of impact scenarios and pedestrian anthropometries to make use of the benefits that accompany virtual testing with HBMs.

Because the boundary conditions affected the simulation results strongly, they should be kept consistent throughout the process. Ideally, the contact settings (in especially the formulation) should be kept consistent to those applied in the validation of the HBM with full-scale tests. Therefore, it would be beneficial if the exact contact and control settings applied during the validation of the models should be provided within the manuals of the HBMs.

4.3.4 Harmonised Output

To see if the time of the head impact had been determined correctly, a cross-check with the head acceleration in the resultant and z-directions was performed. Whenever the maximum resultant head acceleration was observed before the derived time *H* of head contact, a manual check was performed by examining the animated results. In some cases, this discrepancy was caused by the

fact that a direct contact between the head and GV was avoided, as the arm was located between head and GV, leading to high accelerations in the head, but no measured contact force between the head and GV. In these cases, the applied definition led to very high or even no identifiable *HIT*.

Three approaches could be applied to deal with this issue:

1. The time *H* could be defined as the time when the head contacts the arms and at the same time the arms contact the vehicle
2. The time *H* could be defined as the time of maximum head acceleration
3. The contact between arms and head could be disabled in such cases.

Approach 1 leads to significantly lower *HIT*s compared to those obtained in simulations with no contact between arms and head and, therefore, leads to less comparable results. Approach 2 can lead to misleading results, as multiple peaks in the head accelerations were observed in some simulations. When the head of the HBM contacts the shoulder, this can lead to even higher acceleration than if it contacts the bonnet. For these reasons, approach 3 was chosen as it allowed an automatic analysis of *HIT* to be performed and the most comparable results to be obtained.

To cover the body kinematics that were relevant for the chosen assessment focus, the trajectories for the head CoG (HC), centre of T12 and the centre of *acetabuli* (AC) were considered as the final reference points and corridors were defined for those: The location of the head is obviously important for the assessment of deployable system because the wrap-around distance and HIT are important outputs for the assessment simulations. AC and T12 enable to analys the kinematics of the hip and the torso, which are important for the evaluation of the deflection due to the body load and for avoiding implausible full-body kinematics. The reference point AC tends to be close to the CoG of the full-body, and the CoG of the torso is located between AC and T12.

Furthermore, T12 and AC together were shown to be indicators that could effectively be used to identify the time when the curvature of the spine started to change its direction. The spine kinematics could be separated into two phases as shown in Figure 72. In the first phase, the pelvis moved away from the head and the upper torso as it was accelerated by the vehicle impact, while the upper torso and head remained in place due to their inertia. The spine posture at 66 ms showed the maximum spine curvature for this load case (FCR impact at 40 km/h) as the pedestrian wrapped around the vehicle. The head and upper torso then were pulled downwards and the spine was straightened, before its curvature changed into the other direction prior to the head impact at 140 ms. This is clearly visible when examining the figures that had fixed pelvises on the bottom of Figure 72: In phase 1, T12 is located on the left side of AC, while it is located on the right side in phase 2. The observed kinematics are in accordance with movement patterns seen in PMHS tests (Subit *et al.*, 2008).

Phase 1   **Phase 2**   **Head Impact**

Full-body kinematics (initial position in the background) in the global coordinate system

Spine kinematics relative to fixed pelvis coordinate system

| 42 ms | 66ms | 118 ms | 140 ms |
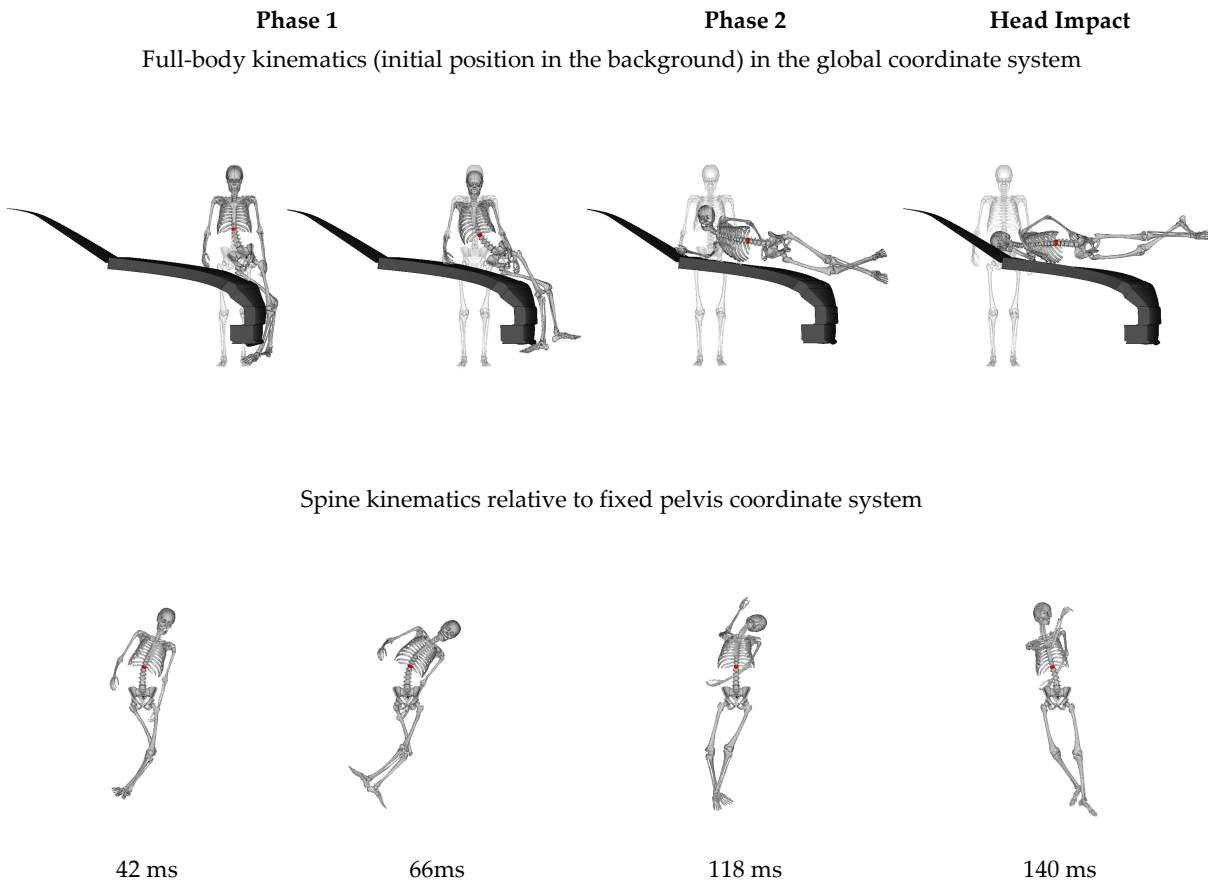
Figure 72: Kinematics of the spine for an impact with the generic FCR model at 40 km/h relative to the global and a local pelvis coordinate system (T12 shown in red)

The trajectories of the lower extremities were not relevant for the assessment of active bonnets and, therefore, were not included.

4.3.5   Certification Procedure

Although GHBMC PS and THUMS AM50 pedestrian models are validated using differing PMHS tests and do not have the exact same geometry, the kinematic responses seen were very similar. This was not true for some of the other pedestrian models. It was possible to identify outliers with inconsistent behaviour compared to the majority of results, and these will have to be revised to pass the certification.

Models that showed outlying behaviour for *HIT* also showed outlying behaviour for the trajectories, indicating that the chosen approach, which began with the identification of outliers based on *HIT*s, was appropriate. Two additional outliers were identified for the contact forces that showed comparable behaviour to the other results in the previous analyses. When examining the details, it was observed that discrepancies seem to come from specific output definitions of the contact forces in one FE software package.

The presented certification procedure does not replace the validation of the HBM in terms of biofidelity. The certification proceeds the validation and allows an HBM in a specific environment to be used as a "virtual test device" for a specific assessment focus (in this case, the kinematic-based assessment of deployable systems). When performing any revisions of the Human Body Models, validations also have to be repeated as well. While the HBM has to be morphed to the anthropometry of the PMHS to perform a proper validation, reference anthropometries are needed for assessment purposes.

Certification procedures are important prerequisites for virtual testing, as they enable users to determine whether the response of a specific virtual test device in a specific environment answers a specific question and provides a comparable response. Within the certification procedure the response of the model is compared to reference simulations using the harmonized setup, target posture and harmonized anthropometry that should be also used for the final assessment simulations.

The certification procedure has been developed to provide evidence that the pedestrian model leads to comparable results within specified tolerance levels when it is applied in a harmonized setup (that is very similar to the setup that is used for the subsequent assessment). This is required to ensure that the variations of results fall within an acceptable range. An alternative approach could also be taken to solve this issue: A virtual testing lab performs assessment simulations with the same pedestrian model in the same code for all kind of cars. Still, once more than one test lab is performing the simulations, or more than one code is used, comparability would be unknown without a certification procedure.

The developed procedure allows users and evaluators to identify user errors when setting up the simulations and find compatibility problems with FE solver versions. Furthermore, the certification can be used to check the sensitivity of the HBM when control settings have to be changed to comply with the full FE vehicles. The certification procedure can help to increase the awareness that small changes can imply significant effects on the HBM simulation results and, therefore, precautions are needed. It can be also used by HBM developers to check robustness of their models.

The certification procedure introduced in this thesis is only applicable to kinematic-based assessments. The comparability of injury metrics, and especially strain-based injury metrics, is not addressed at the current stage. First of all, the kinematics and validations have to be harmonized. Once this has been achieved, similar methods could be applied to compare strain-based assessment results for varying models with different setups and codes.

The corridors and tolerances were defined using current state-of-the-art HBMs. No active pedestrian models were covered. The corridors and tolerances are based on biofidelic models, but should not be understood as biofidelity corridor. The corridors will need to be revised when significant changes in the state of the art of HBMs occur and biofidelity significantly further improves compared to the current status (e.g. due to newly available test data).

Figure 73 shows the deviations among the *HIT* resulting from different variations for one exemplary load case, the family car impact at 40 km/h, as this is the only load case where results

for all variations were available: Due to the harmonised simulation protocol, it was possible to narrow down the differences between two models in one FE code and on one platform in terms of *HIT* from 4.7% to 1.2% for this load case. A total variation of 2.75% was observed from the results received with the two models THUMS v4 and GHBMC PS when including the external simulations performed in different codes by different institution.

Without a certification procedure, the models that were listed within TB013 were showing a variation of up to 18% within the FCR 40 km/h load case. Using the current version of the certification procedure results in a decrease in these differences by allowing a maximum of 10.5% variation.

An unsymmetrical corridor was defined: A greater amount of negative deviation was accepted, because it represents the worst case for the assessment of the deployable system, while a too high *HIT* was unacceptable. It should be aimed to find a way to narrow down the corridors in the future when harmonisation in the HBMs is progressing.
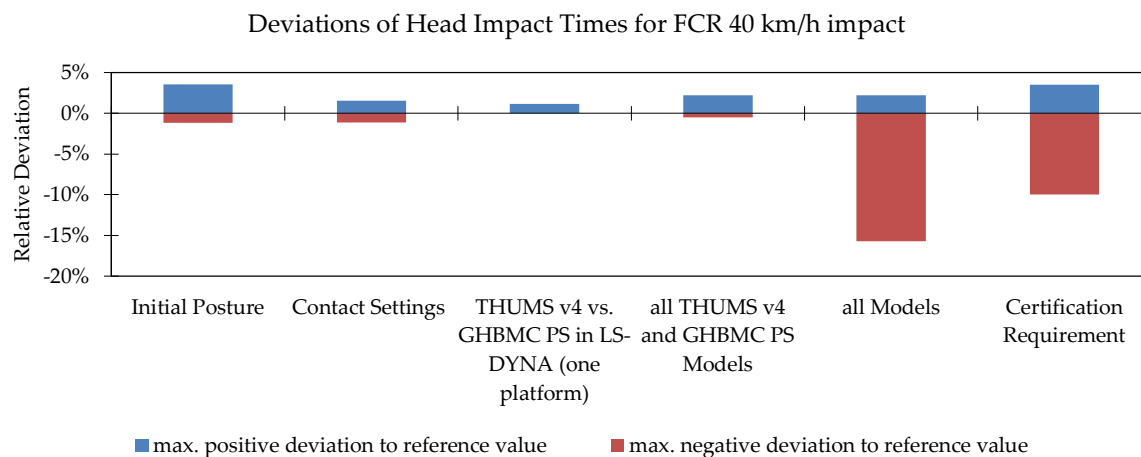
Figure 73: Relative deviations of *HITs* to reference *HIT* (138.1 ms) for the 40 km/h impact with generic FCR models

Examining the maximum differences observed throughout all load cases and all eighteen sets of analysed results, the benefit of the certification procedure becomes even more obvious. As shown in Figure 74, the sum of the absolute maximum deviations observed throughout all simulations made up a total of 33% (maximum of 24% within one load case). Due to the certification requirements, this is more than halved to a maximum of 10.5%. The critical positive deviation compared to the reference value, which led to higher *HIT*s, decreased from 17% to 3.5%. The results of the THUMS and GHBMC PS models – in all codes – did not need the full tolerance. Their results fell within a 6.5% range throughout all load cases.

Maximum deviations of Head Impact Times throughout all load cases
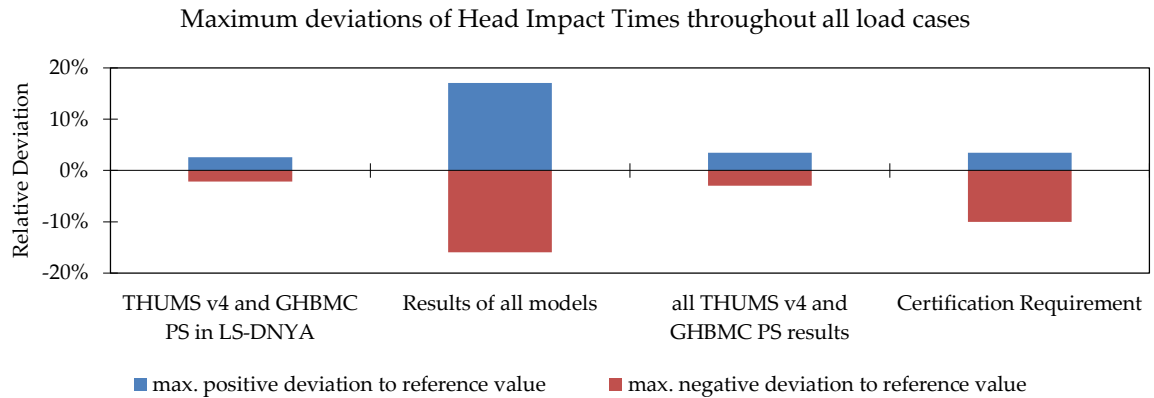
Figure 74: Relative deviations of *HITs* to reference *HITs* throughout all twelve load cases

4.4 Summary

In this chapter, the following results were obtained:

- The use of different initial boundary conditions, which complied with the Euro NCAP pedestrian testing protocol prior to January 2018, led to remarkable differences in the kinematic-based assessment results. The deviations were even higher than the differences observed between two models in one code once the setup had been harmonized.

- Based on the results of sensitivity studies carried out to identify key boundary conditions, a simulation protocol was developed that allows the HBM user and evaluators to make an objective, standardised comparison of the kinematic responses for various HBMs in multiple codes for the first time.

- When applying the standardised procedure, simulations with THUMS v4.02 and GHBMC PS v1.4.3 led to highly comparable kinematics, indicating that these are appropriate for a comparable kinematic-based assessment of deployable systems.

- Other models were identified that did not show comparable responses. Clear outliers were identified when comparing *HITs*, trajectories and contact forces. Corridors and tolerances of the remaining reference simulations were derived. The variation in *HITs* was significantly reduced from 24% to 10.5% when outlying results were sorted out.

- The study highlights the importance of certification procedures for virtual testing. The developed procedure enables users to compare HBMs with tolerable corridors from reference simulations and, therefore, significantly improve the comparability of the results.

5   KINEMATIC-BASED ASSESSMENT

In this chapter, a study is described that tested whether HBMs are appropriate for kinematic-based assessments. Specifically, the effect of the impact structure on the kinematic assessment results for pedestrian accidents was analysed. The plausibility of trends is discussed, and these are cross-checked with observations from PMHS tests reported in the literature.

5.1   Method

The steps described in Chapter 4 were used as prerequisites, meaning that the pedestrian models were certified according to the described procedure, and the harmonised setup using the established GV models was applied.

In addition to the head impact time (*HIT*), which was also discussed in the previous chapter, head impact velocities (*HIVel*) relative to the vehicle were analysed, as these can significantly affect the head injury risk (Hutchinson *et al.*, 2012). The outputs were defined as described in Chapter 2.4.22.3.3.

5.1.1   Effect of Collision Speed

The effects of the collision speed of the vehicle prior to impact on *HIT* and *HIVel* was analysed for impacts at 30, 40 and 50 km/h using the GV models introduced in Chapter 4.2.1. Simulations were performed using two different pedestrian models with the same size (AM50), namely, THUMS v4.02 and the GHBMC PS model v1.4.3. in LS-Dyna. Furthermore, simulations with the simplified GHBMC model with the size of the 6-yo child were performed to analyse the effects of collision velocities on pedestrians of different sizes. All models were used in the harmonised pedestrian Posture 3 as described in Appendix C.

5.1.2   Effect of Vehicle Shape

Both, the collision speed and the vehicle shape, were varied. The four different median vehicle shapes of the category FCR, MPV, RDS and SUV were used to analyse the effect of the vehicle geometry for each of the three different speeds. The effects of *bleh* on *HIT* and *HIVel* with the three different collision speeds and the three different pedestrian models were investigated. The simulations were performed again using the THUMS v4.02 AM50 model and the two sizes of the simplified GHBMC models (AM50 and the 6yo child).

5.1.3   Effect of Vehicle Stiffness

To analyse the effect of vehicle stiffness on the head impact kinematics, the stiffness of the GV models was varied. The slope of the primary stiffness gradient (see parameters in Appendix B), therefore, was increased by a factor of 10 to achieve significant differences. These led to altered force displacement characteristics from those observed in the impactor simulations, which are

shown in Figure 75–Figure 80. The impactor locations were chosen based on the definitions described in Chapter 2.5.2. The solid black line shows the characteristics with modified material parameters while the dashed line represents the baseline simulations (with the original parameters described in Appendix B). As the altered foam characteristic had only a small effect on the impactor simulation 1 (Figure 75), the thickness of the interface layer of the spoiler was also varied and increased from 1.6 mm to 2.6 mm, resulting in the response shown in Figure 76. The abbreviations in the figure captions (shown in brackets) were used in the presented results to distinguish among the different characteristics. Simulations were performed using the THUMS v4.02 AM50 model and the generic FCR model.
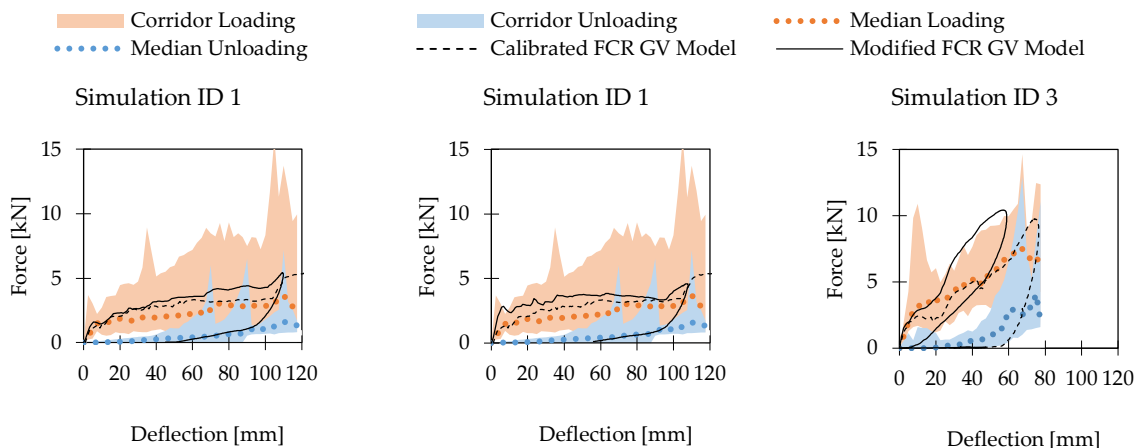
Figure 75: Response of impactor simulation 1 with increased spoiler foam stiffness (stiff spl)

Figure 76: Response of impactor simulation 1 with increased spoiler interface layer thickness (spl thk)

Figure 77: Response of impactor simulation 3 with increased bumper foam stiffness (stiff bmp)
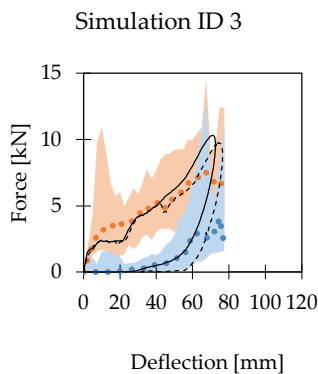
Figure 78: Response of impactor simulation 3 with increased grill foam stiffness (stiff grl)
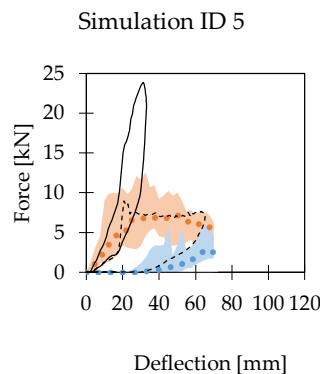
Figure 79: Response of impactor simulation 5 with increased bonnet leading edge foam stiffness (stiff ble)
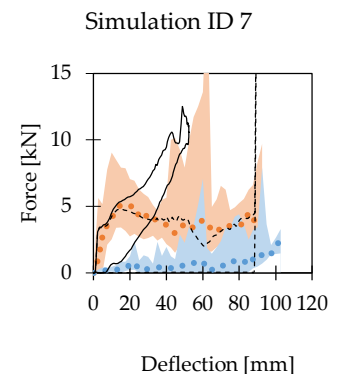
Figure 80: Response of impactor simulation 7 with increased bonnet foam stiffness (stiff bnt)

5.2 Results

5.2.1 Effect of Collision Speed

As shown in Figure 81–Figure 84, higher collision speeds generally led to smaller *HIT*s. This trend was observed for all four considered vehicle shapes. The resulting *HIT*s of the two certified AM50 models were nearly congruent. The smaller pedestrian showed significantly smaller *HIT*s in all load cases. No normal termination was achieved with the 6-yo model for the RDS collision at 50 km/h. Because an attempt was made to leave the HBM unchanged, no results of this load case were included in the present analysis, which is why only two data points appear for the 6-yo in Figure 83. The dependency between *HIT* and collision speed is not fully linear – a kink at 40 km/h is observed for all load cases.

In Figure 85, the results of the four previous figures are overlaid, showing that the highest *HIT* of the child (impact at 30 km/h with the Roadster, i.e., smallest *bleh*) is still smaller than the minimum *HIT* seen in the AM50 models (impact with SUV, i.e., vehicle with highest *bleh* at 50 km/h). It also shows that the results of the FCR and roadster model have smaller differences than those for the other models.
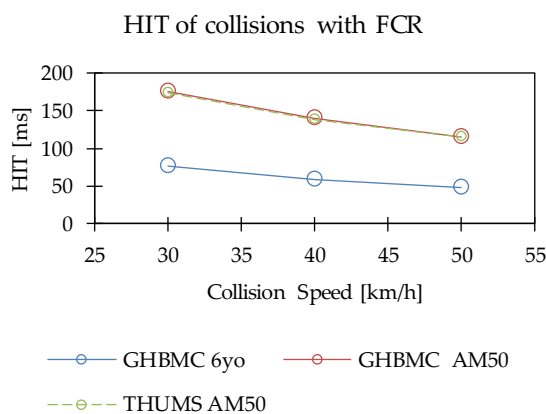
Figure 81: Head impact time as a function of collision speed for impacts with the generic FCR model
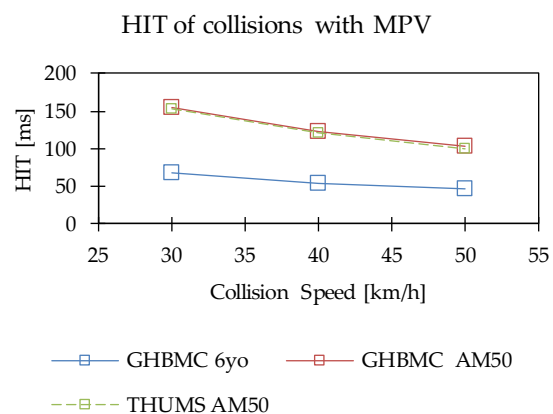
Figure 82: Head impact time as a function of collision speed for impacts with the generic MPV model
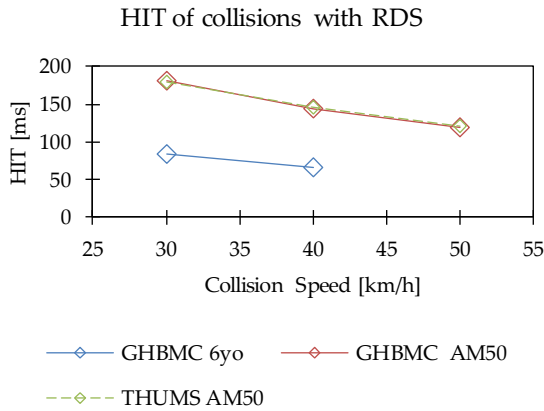
Figure 83: Head impact time as a function of collision speed for impacts with the generic RDS model
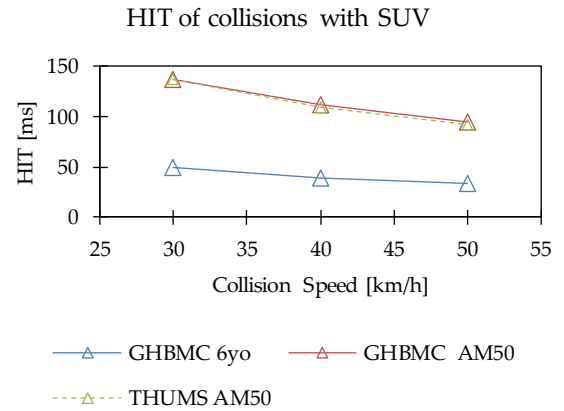
Figure 84: Head impact time as a function of collision speed for impacts with the generic SUV model
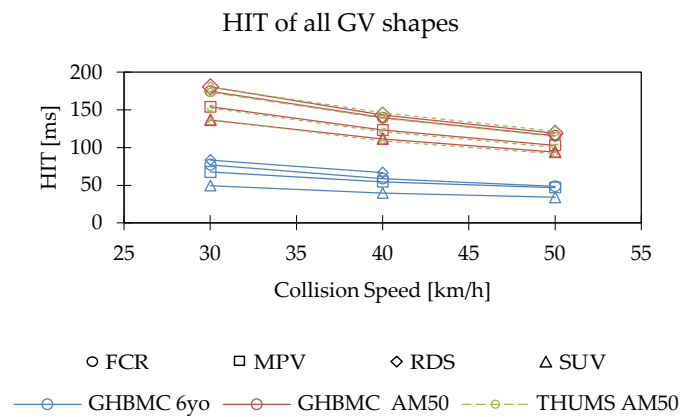
Figure 85: Head impact time as a function of collision speed for the generic FCR, MPV, RDS and SUV models

Figure 86–Figure 89 show the relationship between the *HIVel* and collision speed for each vehicle shape. Higher collision speeds led to higher head impact velocities. The black dashed line in the figures represents the equality of the collision speed and *HIVel*. In all simulations with THUMS, the *HIVel* was higher that the collision speed. The simulations with the AM50 GHBMC model showed lower *HIVel* than the collision speed for the SUV impacts. The head impact velocities of the child model were lower than those seen with the AM50 models for all load cases. A kink at 40 km/h can be observed for all three pedestrian models in the SUV load case.
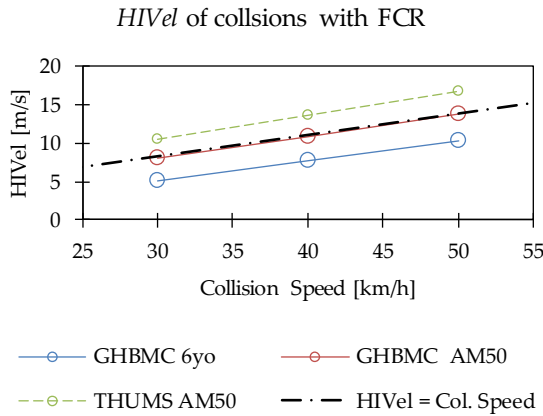
Figure 86: Head impact velocity as a function of collision speed for impacts with the generic FCR model
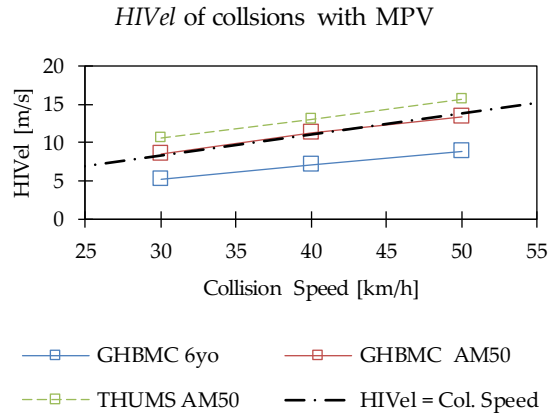
Figure 87: Head impact velocity as a function of collision speed for impacts with the generic MPV model
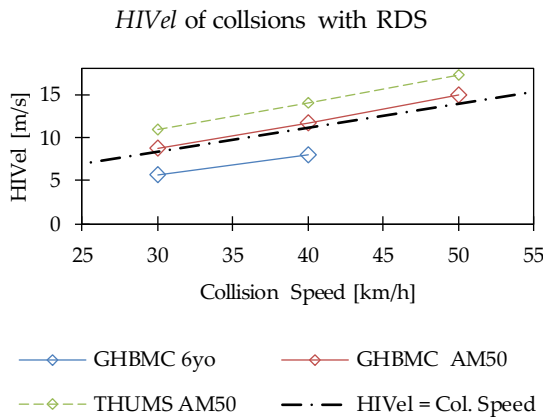
Figure 88: Head impact velocity as a function of collision speed for impacts with the generic RDS model
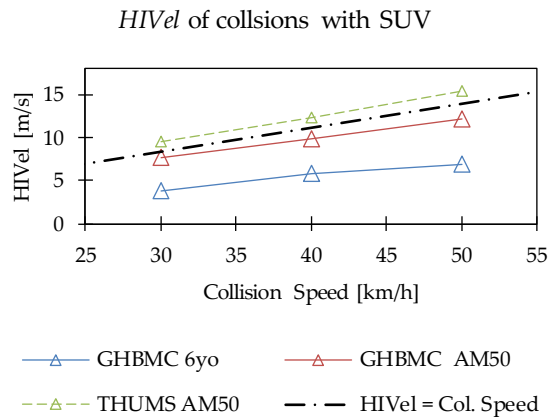
Figure 89: Head impact velocity as a function of collision speed for impacts with the generic SUV model

5.2.2 Effect of Vehicle Shape

As had already been shown in the previous analysis, the vehicle shape affects the kinematic assessment results along with the pedestrian size and collision speed, so the geometry was further investigated. The bonnet leading edge height (*bleh*) was chosen as parameter to describe differences in terms of the shape, as other authors had reported that this is an important shape parameter (Li *et al.*, 2017b; Pal *et al.*, 2013).

Figure 90 shows the effect of the *bleh* on the *HIT* at varying collision speeds in the three pedestrian models. The bigger and thicker the cross is, the higher the collision speed. The results of AM50 models THUMS and GHBMC overlap. One trend line per velocity could be drawn, but the dependency was not linear. While only a small difference was noted in terms of *HIT* between the RDS with the smallest *bleh* (*bleh* = 657 mm) and the FCR (*bleh* = 740 mm), a bigger difference between FCR and MPV was observed for all collision speeds, although the heights of their ble differ

less (49 mm compared to a difference of 63 mm). Vehicles with higher *bleh* and higher collision speeds had smaller *HIT*s. The same trend was observed for the 6yo-child model, but all *HIT*s were significantly smaller.

A similar trend was observed for *HIVel* (Figure 91), but higher differences between results from simulations with the AM50 THUMS and GHBMC models were observed.
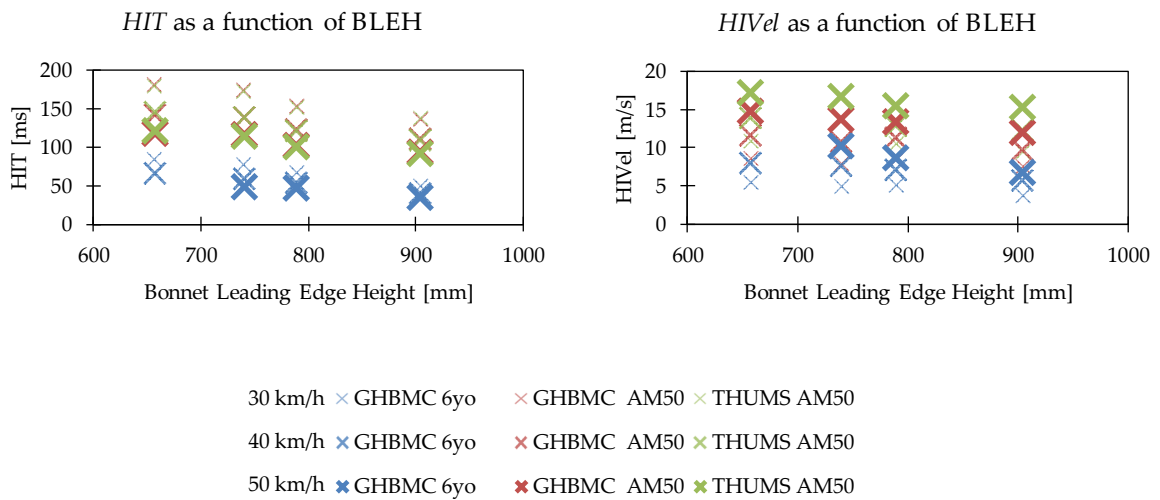
Figure 90: Head impact time as a function of *bleh* at 30, 40 and 50 km/h with the GV models

Figure 91: Head impact velocity as a function of *bleh* for impacts at 30, 40 and 50 km/h with the GV models

5.2.3 Effect of Vehicle Stiffness

The absolute *HIT* values for all stiffness variations is shown in Figure 92. In Figure 94, the differing *HIT* values are shown as relative deviations to the *HIT* of the baseline simulation of the FCR impact at 40 km/h. Figure 93 and Figure 95 show the same analysis for the resultant head impact velocities relative to the vehicle. If the stiffness of all contact areas was increased, the head contacted the vehicle 4.2 ms (3%) later than in the baseline simulations and showed a 7.7% lower *HIVel* (12.5 m/s instead of 13.6 m/s). This seems to be mainly caused by the stiffer ble, which shows similar trends, but with smaller changes (3.3 ms higher *HIT* and -5.8% *HIVel*). When only the bumper was stiffer, the opposite trend was observed: The *HIT* was smaller and *HIVel* higher than in the baseline simulations, but the differences were smaller than 1% for both kinematic measures.

HIT of FCR collisions with stiffness variation

HIVel of FCR collisions with stiffness variation
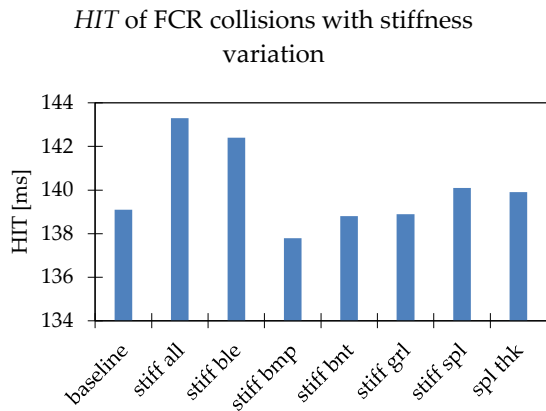
Figure 92: *HITs* for varying vehicle stiffnesses (FCR impact at 40 km/h with the THUMS AM50 model)
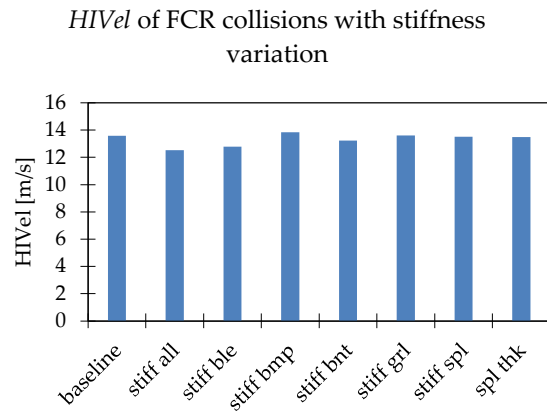
Figure 93: *HIVel* for varying vehicle stiffnesses (FCR impact at 40 km/h with the THUMS AM50 model)

HIT of FCR collisions with stiffness variation - relative deviation

HIVel of FCR collisions with stiffness variation - relative deviation
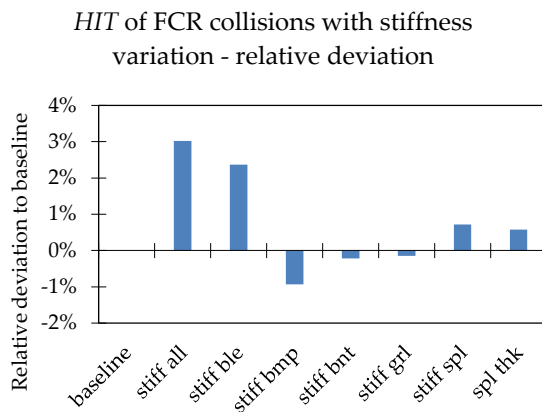
Figure 94: Relative deviation of *HITs* compared to baseline simulation for varying vehicle stiffnesses (FCR impact at 40 km/h)
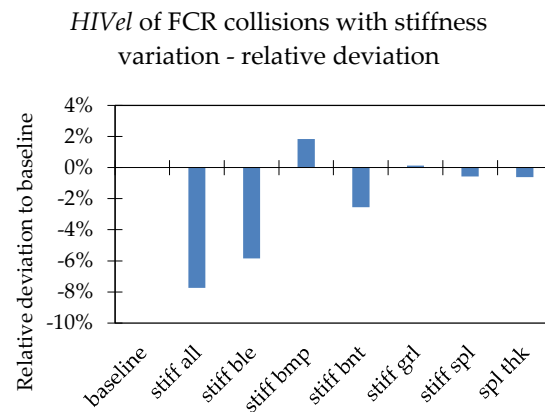
Figure 95: Relative deviation of *HIVel* compared to baseline simulation for varying vehicle stiffnesses (FCR impact at 40 km/h)

5.3   Discussion

In this study, it was possible to show that vehicle shape, stiffness and pedestrian size affected the results of the kinematic assessment. In the following subchapters, the plausibility of the presented results is discussed by comparing the findings of the studies included in this thesis to results from PMHS tests, and a simple analytic approach.

5.3.1   Effect of Collision Speed

Head impact time, location and velocity were affected by the collision speed of the impact structure. These findings are in accordance with those of the PMHS test, where it was observed that higher speed led to higher *WAD* and smaller *HIT* (Yang *et al.*, 2000). The peak resultant head velocity of the AM50 models tend to be higher than the collision speeds, a finding that was also observed in PMHS tests (Forman *et al.*, 2015b; Paas *et al.*, 2015b).

In the load case with the highest deviation between collision speed and *HIVel*, the *HIVel* was 24% higher than the collision speed (RDS impact at 50 km/h). The impact velocity in current state-of-the-art pedestrian subsystem tests is always 40 km/h. Slightly higher impact speed can, therefore, significantly increase the head injury risk, as the clearance between the bonnet and stiff structures underneath the bonnet is designed to meet the test requirements (Hutchinson *et al.*, 2012).

Collsion speed: 30 km/h, 40 km/h, 50 km/h
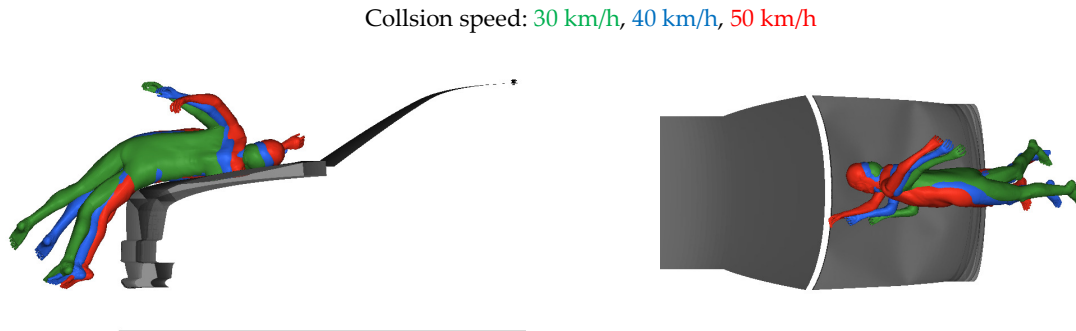
Figure 96: Head impact location from simulations with generic SUV model at 30, 40 and 50 km/h shown in green, blue and red, respectively

The higher the collision speed, the higher the observed wrap around distance. *WAD* tends to be higher than the initial height of the head in all cases: *WAD* for 30 km/h was 1784 mm and for 50 km/h, 1904 mm. The different head impact locations are shown in Figure 96. This effect has also been reported from PMHS tests (Yang *et al.*, 2000).

The *WAD* is higher than the initial height as the pedestrian tends to slide on the bonnet and the feet are not on ground level when the head impact occurs, which is again in accordance with PMHS tests (Kerrigan *et al.*, 2005b; Subit *et al.*, 2008; Kerrigan *et al.*, 2009a).

Furthermore, elongation of the spine can be observed: The spine length can increase during the impact (Ishikawa et al., 1993; Kerrigan et al., 2005a; Paas et al., 2012), which causes higher *WAD* than the stature. To investigate this effect in more detail, the spines in the simulations with the three different collision speeds were overlaid in Figure 97.

Collsion speed: 30 km/h, 40 km/h, 50 km/h

anterior   posterior   lateral
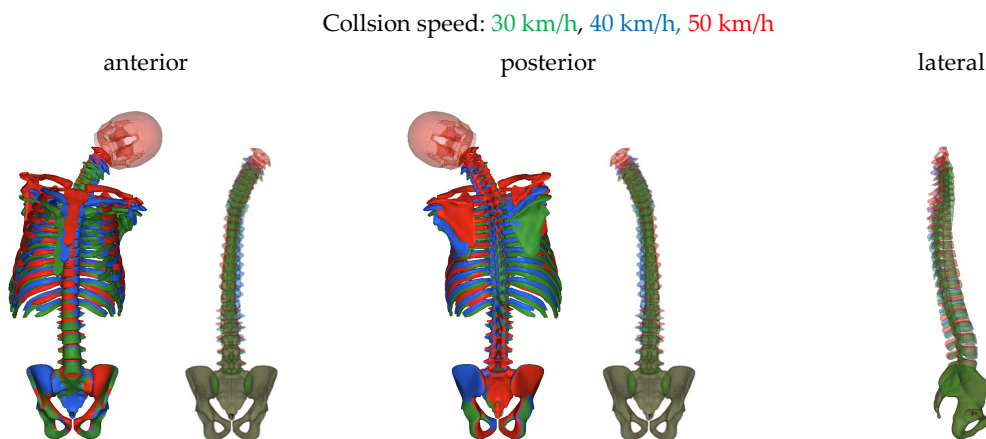
Figure 97: Spine kinematics in impacts with the generic SUV model at 30, 40 and 50 km/h

The beginning of phase 2, as it was described in Chapter 4.3.4, was selected for all three simulations. At this time, the spine is being straightened and stretched before the thoracic and lumbar spine curvature changes its direction. The maximum stretch of the spine can be expected at this time, and curvatures are most easily comparable for different simulations. The location of the *acetabuli* of the pelvic bone was frozen for the visualisation. Only the cortical bones of the thorax and the spine are visualised in Figure 97. A clear difference in the location of C1 is visible. The distance between the centres of C1 of the simulation with 50 km/h and the one with 30 km/h was 44 mm in the coronal plane.

The pedestrian model was stationary before the impact in all simulations shown. In the real world, the pedestrian is likely move and react in different ways. They might accelerate, freeze, back up, or keep walking (Soni *et al.*, 2013b). To evaluate the effect of the initial speed of the pedestrian, two simulations were performed in which an initial velocity was applied in the THUMS models. The mean velocity of adult male pedestrians from the IGLAD dataset (covering data from 2007-2015) was applied, which was 5.1 km/h. Impacts were simulated with the generic FCR and SUV model at 40 km/h. The *HIT* remained unaffected by the initial velocity of the pedestrian. A difference of 0.1 ms was observed for the FCR impact. Head impact velocities also only differed by 1%. The same trend also showed up in the SUV simulations. The *HIT* remained unaffected (-0.1 ms), and only a marginally smaller *HIVel* (< 1%) was observed.

Figure 98 and Figure 99 show that leg kinematics differed from the baseline simulations and that the head impact locations were different. The blue pedestrian shows the baseline simulations, and the green one, those with applied initial velocity for THUMS. Therefore, depending on the assessment focus, the initial velocity of the pedestrian should be considered.
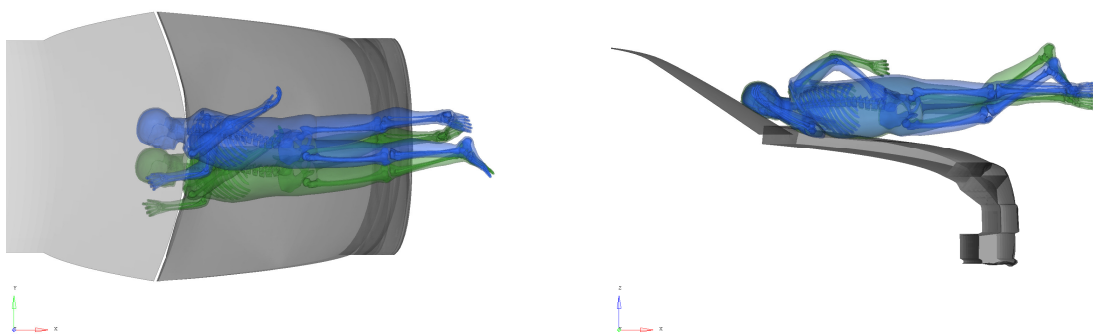
Figure 98: Position of HBM at time of head impact for simulations with (green) and without (blue) initial velocity of the pedestrian for impact with the generic FCR model with a 40 km/h collision speed
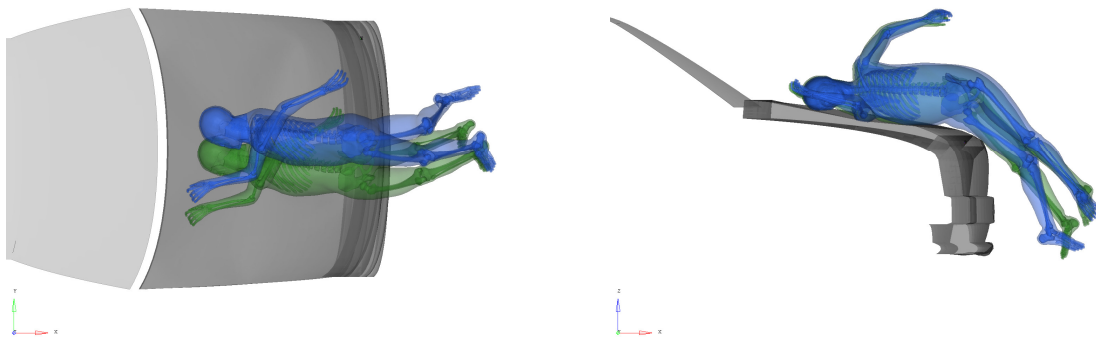
Figure 99: Position of HBM at time of head impact for simulations with (green) and without (blue) initial velocity of the pedestrian for impacts with the generic SUV model with a 40 km/h collision speed

5.3.2   Effect of Vehicle Shape

The material parameters of each segment were kept constant for all vehicle models, which allowed a reasonable comparison regarding the effect of the vehicle geometry to be made. However, the body parts can come contact with other contact areas when different vehicle geometries are present, which also affects the contact forces. A pure analysis of the vehicle geometry would be only possible with homogenous stiffness defection throughout the whole vehicle front, which is not representative for a real serial car.

It was observed that the height of the ble highly affects the head impact kinematics (*HIT* and *HIVel*). This is in accordance with the findings from PMHS tests, in which the height of the hip of the pedestrian relative to the *bleh* was described as one of the key factors affecting kinematics (Kerrigan *et al.*, 2007).

A clear linear trend was visible for *HIVel* and *HIT* as a function of *bleh* with the 6yo child model. The reason for this might be that the child's head always impacts the bonnet of the vehicle. The adult models impact the windshield in some cases. This causes a different orientation of the spine relative to the head at the time of impact and different interaction between the HBM and car. This difference was also observed in tests with smaller and taller PMHS (Subit *et al.*, 2008).

The vehicle geometry also affects the ground impact, which was not considered in the current study, but has been shown in PMHS tests (Snedeker *et al.*, 2005) and with multibody simulations (Crocetta *et al.*, 2015).

5.3.3   Effect of Vehicle Stiffness

The vehicle stiffnesses affected the head impact kinematics significantly. The increased stiffness of the *bleh* led to the highest variation in the results when only one contact area was modified. The force-deflection response of the impactor was also the most strongly affected by the modified foam stiffness for this area.

The effect of the vehicle stiffness highlights the challenge faced when attempting to correctly predict head impact kinematics without applying FE models. Biofidelic interaction and

deformations of the impact structure and the pedestrian have to be replicated correctly to gain correct results.

Due to the higher degree of ble stiffness, the HBM shown in red in Figure 100 experienced more rebound, and there was a bigger gap between the HBM flesh and the ble compared to that in the blue baseline simulation. The left-hand figure shows that, while the head of the two models is on the same position, the hip of the blue model is closer to the vehicle. Therefore, the tensile forces increased more rapidly in the baseline (blue) simulation, causing the head and upper torso to be pulled downwards earlier, leading to an earlier *HIT*, lower head impact point and higher *HIVel* than found in the simulation with the stiff bonnet leading edge. The same trend was visible for the simulation with the stiffness modifications in all areas, but it was even more significant. In the simulations with the stiffer bumper, the head was pulled downwards slightly earlier, leading to smaller *HIT* and lower *HIVel*.

82 ms   116 ms   146 ms
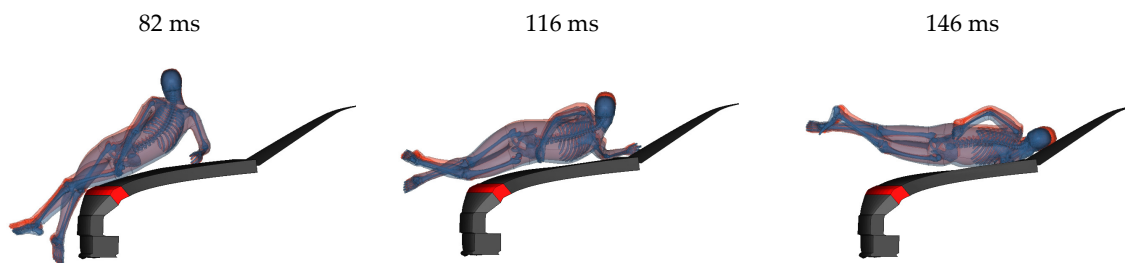
Figure 100: Comparison of kinematics of the THUMS v4 AM50 pedestrian model for baseline simulation (blue) and simulation with stiffer ble (red) of the generic FCR model with a 40 km/h collision speed

To check the effect of increased stiffness with another vehicle geometry, one simulation with the generic SUV model with increased stiffness was performed (stiff all). A different trend was observed for this vehicle shape: The *HIT* decreased by 4.7% due to the greater stiffness of the foam. Figure 101 shows a comparison of the kinematics of the baseline simulation and the simulation with increased stiffness in red. The simulation with higher stiffness (shown in red) leads to the earlier *HIT* as for this load case, so it is shown in the foreground. The higher stiffness in this load case led again to more rebound, but the hip was directly impacted by the ble. Therefore, the higher rebound led to a higher and earlier deformation of the spine, as well as an earlier downwards movement of the head.

46 ms   76 ms   107 ms
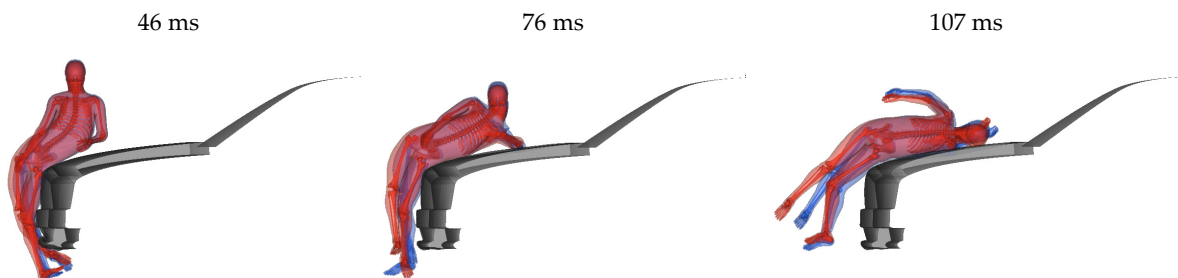
Figure 101: Comparison of kinematics of the THUMS v4 AM50 pedestrian model for baseline simulation (blue) and simulation with increased stiffness (red) of the generic SUV model with a 40 km/h collision speed

The kinematics seemed to be strongly affected by the forces induced from the spine, which, in turn, were affected by the location of the pelvis relative to the head during the impact. The hip kinematics, on the other hand, were strongly affected by the stiffness and geometry.

This indicates the complexity of the interaction between the pedestrian and impact structure, which clearly requires an assessment that considers the full-body kinematics with a highly biofidelic pedestrian model.

5.3.4   Analytical Approximation

To gain a better understanding of the observed trends described in this chapter, an analytical approximation was used to describe the interactions between the impact structure and the pedestrian.

Simms and Wood (2009) provided several approaches for analytical or numerical solutions of pedestrian impact kinematics. In the simplest approach, they considered the pedestrian as a rigid segment and assumed that the vertical impulse was negligible.

Based on the assumptions described by Simms and Wood (2009) and standard mechanical relationships (Gross *et al.*, 2005), a basic analytical model was established to calculate the trajectory of the head CoG of the pedestrian. This model was developed to gain a better understanding of the relationships within the kinematic-based assessment and determine whether the observed trends from the HBM simulations were physically reasonable.
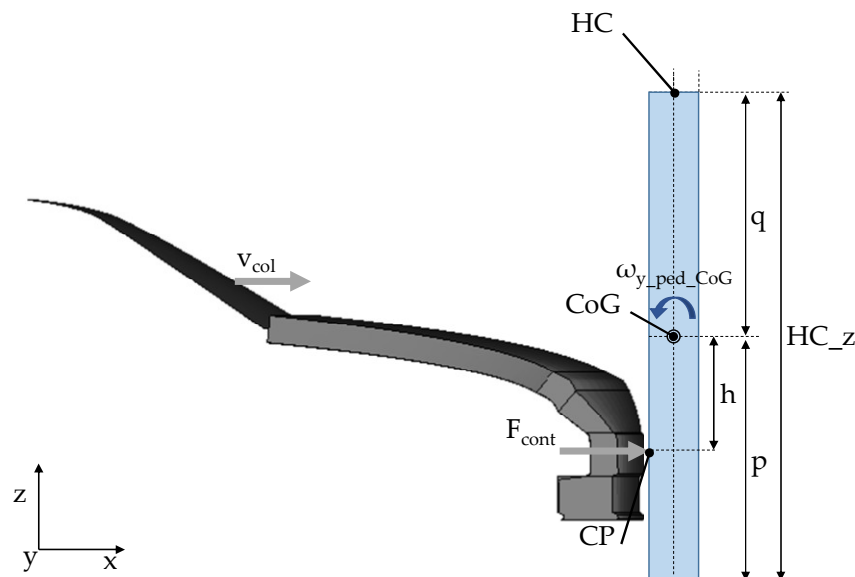
Figure 102: Simplified analytical model for pedestrian impacts (based on Simms and Wood, 2009, p. 128)

The definitions of the variables are shown in Figure 102. The width of the pedestrian in the x-direction was not considered, i.e., the pedestrian was assumed to be a rigid, thin bar (shown in blue). All variables referring to the vehicle are named with $_{veh}$, and those referring to the pedestrian are named $_{ped}$. For the pedestrian, kinematics were analysed at the CoG ($_{CoG}$), the

contact point ($_{CP}$) and the head ($_{HC}$). The components of the vectors in all equations shown correspond to the x-, y- and z-directions.

Equation (14) describes the momentum of the vehicle. The collision speed of the vehicle just prior to the impact was named v_{col} and represents the x-component (first line) of the vector $\overrightarrow{v_{veh}}(t_{0-})$. The y- and z-components of the vehicle speed $\overrightarrow{v_{veh}}$ are equal to zero prior (t_{0-}) and after (t_{0+}) the collision with the pedestrian.

$$m_{veh} * \left(\overrightarrow{v_{veh}}(t_{0+}) - \overrightarrow{v_{veh}}(t_{0-}) \right) = -\hat{F}_{cont} \tag{14}$$

Due to the conservation of momentum, Equation (14) must be equal to the momentum of the pedestrian, described with Equation (15). All velocities of the pedestrian prior to the impact were assumed to be 0 (Equation (16)).

$$m_{ped} * \left(\overrightarrow{v_{ped\_CoG}}(t_{0+}) - \overrightarrow{v_{ped\_CoG}}(t_{0-}) \right) = \hat{F}_{cont} \tag{15}$$

$$\overrightarrow{v_{ped\_CoG}}(t_{0-}) = \overrightarrow{v_{ped\_CP}}(t_{0-}) = \begin{bmatrix} 0 \\ 0 \\ 0 \end{bmatrix} \tag{16}$$

Equation (17) describes the angular momentum around the pedestrian CoG. The distance between the contact point and the pedestrian CoG is described with the vector $\overrightarrow{r_{CP}}$. At t_0 the z-component of $\overrightarrow{r_{CP}}$ is equal to h and all other components are zero. The rotational velocity of the pedestrian $\overrightarrow{\omega_{ped_{CoG}}}$ was zero prior to the impact. After the impact, a pure rotation around the y-axis was assumed, which means that the x- and z- component of $\overrightarrow{\omega_{ped_{CoG}}}(t_{0+})$ were assumed to be zero.

$$\theta_{ped} * \left(\overrightarrow{\omega_{ped_{CoG}}}(t_{0+}) - \overrightarrow{\omega_{ped_{CoG}}}(t_{0-}) \right) = \overrightarrow{r_{CP}}(t_0) \times \hat{F}_{cont} \tag{17}$$

The coefficient of restitution k describes the character of the collision. It was assumed that the collision occurs only in the x-direction. Equation (18) describes the relationship between the linear x-velocity of the pedestrian and the vehicle at the contact point (CP).

$$k = -\frac{v_{veh\_x}(t_{0+}) - v_{ped\_CP\_x}(t_{0+})}{v_{veh\_x}(t_{0-}) - v_{ped\_CP\_x}(t_{0-})} \tag{18}$$

Equation (19) describes the kinematic relationship between the linear and rotational velocities of the pedestrian CoG and CP.

$$\overrightarrow{v_{ped\_CP}}(t_{0+}) = \overrightarrow{v_{ped\_CoG}}(t_{0+}) - \overrightarrow{r_{CP}}(t_{0+}) \times \overrightarrow{\omega_{ped_{CoG}}}(t_{0+}) \tag{19}$$

Due to gravitation, the z-velocity of the pedestrian after the impact is described with Equation (20). The z-acceleration due to gravitation was considered with the constant $g = 9.81 \ m/s^2$.

$$v_{ped_{CoG\_z}}(t_{0+}) = -g * t \tag{20}$$

Equations (14) to (20) result in the Equations (21)-(24), describing the velocities of pedestrian and vehicle after the collision.

$$\overrightarrow{v_{ped\_CoG}}(t_{0+}) = \begin{bmatrix} \dfrac{\frac{m_{veh}}{m_{ped}} * v_{col} * (k+1)}{\left(1 + \frac{m_{veh}}{m_{ped}} + \frac{h^2}{\theta_{ped}} * m_{veh}\right)} \\ 0 \\ -g * t \end{bmatrix} \tag{21}$$

$$\overrightarrow{v_{veh}}(t_{0+}) = \begin{bmatrix} \dfrac{-m_{ped} * v_{ped\_CoG\_x}(t_{0+})}{m_{veh}} + v_{col} \\ 0 \\ 0 \end{bmatrix} = \begin{bmatrix} \dfrac{-v_{col} * (k+1)}{\left(1 + \frac{m_{veh}}{m_{ped}} + \frac{h^2}{\theta_{ped}} * m_{veh}\right)} + v_{col} \\ 0 \\ 0 \end{bmatrix} \tag{22}$$

$$\overrightarrow{v_{ped\_CP}}(t_{0+}) = \begin{bmatrix} k * v_{col} + v_{veh\_x}(t_{0+}) \\ 0 \\ -g * t \end{bmatrix} = \begin{bmatrix} \dfrac{-v_{col} * (k+1)}{\left(1 + \frac{m_{veh}}{m_{ped}} + \frac{h^2}{\theta_{ped}} * m_{veh}\right)} + v_{col} * (k+1) \\ 0 \\ -g * t \end{bmatrix} \tag{23}$$

$$\overrightarrow{\omega_{ped_{CoG}}}(t_{0+}) = \begin{bmatrix} 0 \\ \dfrac{v_{ped_{CP_x}}(t_{0+}) - v_{ped_{CoG_x}}(t_{0+})}{h} \\ 0 \end{bmatrix} = $$
$$\begin{bmatrix} 0 \\ \dfrac{v_{col} * (k+1)}{h} - \dfrac{(m_{ped} + m_{veh})}{h} * \dfrac{v_{col} * (k+1)}{\left(m_{ped} + m_{veh} + \frac{h^2}{\theta_{ped}} * m_{veh*}m_{ped}\right)} \\ 0 \end{bmatrix} \tag{24}$$

Based on the assumption that after the impact (t_1) only gravitation affects the pedestrian, the location of the head CoG can be calculated as shown in Equations (25) and (26).

$$x_{ped\_CoG}(t_1) = v_{x\_ped\_CoG}(t_{0+}) * t_1 \tag{25}$$

$$z_{ped\_CoG}(t_1) = p - g * \frac{t_1^2}{2} \tag{26}$$

With the distance q between the head (HC) and the CoG the pedestrian, and by assuming that the pedestrian was one rigid body, the trajectory of the head can be calculated using Equations (27) and (28).

$$x_{ped\_Head}(t_1) = x_{ped\_COG}(t_1) - q * \sin(\omega_{y_{ped}}(t_{0+}) * t_1) \tag{27}$$

$$z_{ped\_Head}(t_1) = z_{ped\_COG}(t_1) - q * \cos(\omega_{y_{ped}}(t_{0+}) * t_1) \tag{28}$$

The response of the analytical model was compared with the results of the HBM simulations against the generic FCR model with a collision speed of 40 km/h in Figure 103 and Figure 104. The location of the head trajectory (HC) in the analytical model was selected as consistent to the HBM. The moment of inertia θ and h, the location of the pedestrian CoG relative to the contact point and the ground (p) were measured in the THUMS v4.02 AM50 model in the reference posture. with the pre-processing software Visual-Crash Dyna 13.0. The end-point of the bumper was used as contact point $(p = 0.5\ m)$, as this approach led to the most similar trajectories compared to the

THUMS simulations. Furthermore, purely plastic impact ($k = 0$) showed the best correlation with the HBM simulations and is shown in the diagrams.
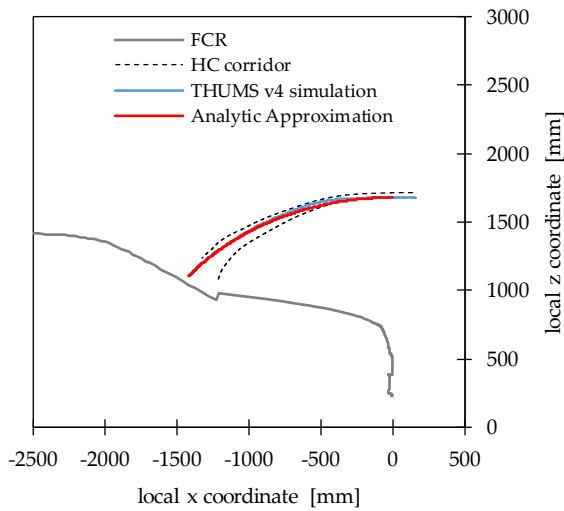
Figure 103: Trajectory based on an analytic approximation compared with corridor from HBM simulations for impact with FCR vehicle shape at 40 km/h
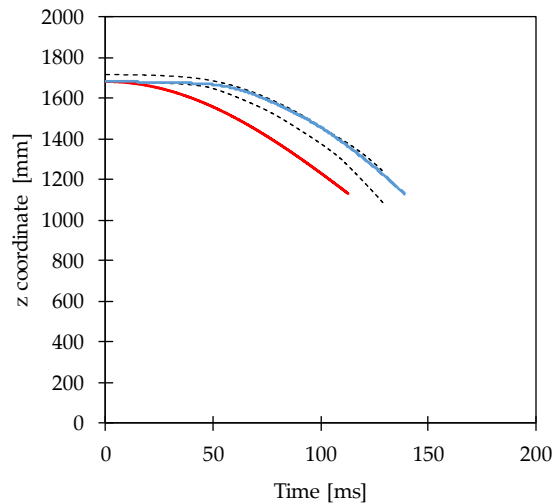
Figure 104: Z coordinate as a function of time based on an analytic approximation compared with corridor from HBM simulations for impact with FCR vehicle shape at 40 km/h

Although the analytical model was highly simplified, highly similar head trajectories of z as a function of x were observed in Figure 103. In contrast, the time histories of z, shown in Figure 104, differed significantly and, therefore, so did the head impact times. Using the analytical approximation *HIT* was 113 ms, while it was 138 ms in the THUMS simulations. These findings highlight the fact that a validation based on trajectories alone is not sufficient. Time histories also have to be considered, as these are much more challenging and influential in a kinematic-based assessment.

With the analytical approximation, sensitivities can be analysed and compared with the simulation results. The equations show why the collision speed, pedestrian CoG height, pedestrian inertia and contact locations (i.e. vehicle shape) all affect the head trajectory and *HIT*.

When the coefficient of restitution was increased, the *HIT* decreased and a lower head impact location was observed. Changing the collision speed had only a minor effect on the z-x trajectory relative to the vehicle in the analytical approximation, which is shown in Figure 105. However, in accordance to the the results of the HBM simulations, the head velocities and, therefore, the displacement of the z coordinate as a function of time were affected. Comparable trends are observed between HBM simulations and the analytical approximation, which is shown in Figure 106.
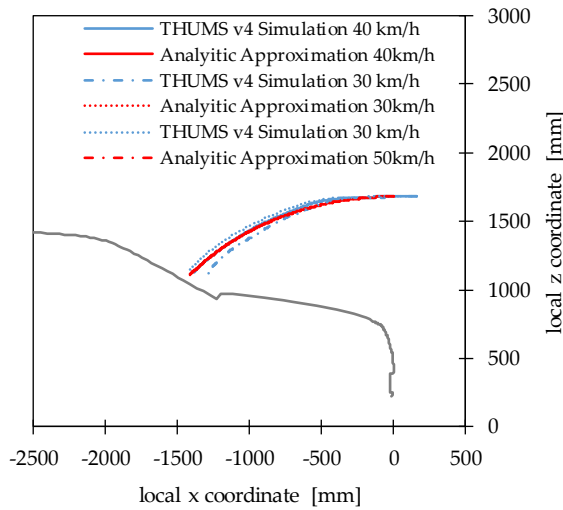
Figure 105: Trajectory based on an analytic approximation compared with HBM simulations for impact with FCR vehicle shape at 30, 40 and 50 km/h
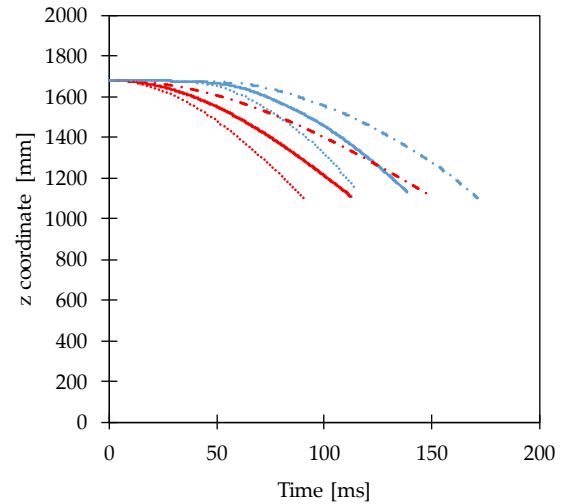
Figure 106: Z coordinate as a function of time based on an analytic approximation compared with HBM simulations for impact with FCR vehicle shape at 30, 40 and 50 km/h

Furthermore, the location of the contact point (CP) was varied. A higher contact point led to a lower head impact location. Figure 107 shows that poor correlations between the analytical model and the THUMS simulations were observed when the highest point of the bumper was applied as contact point for the SUV shape ($h = 0.43$ m). When increasing the height of the contact point to 0.8 m ($h = 0.23$ m), which is located between bumper and bonnet leading edge, the best correlation was achieved for this load case. However, the significant higher contact point results in a slower downwards movement of the head, which is not in line with the simulation results. A single contact point seems to replicate the complex contact conditions in a way that is insufficient for the SUV, where a large area of the vehicle comes into contact with the HBM.
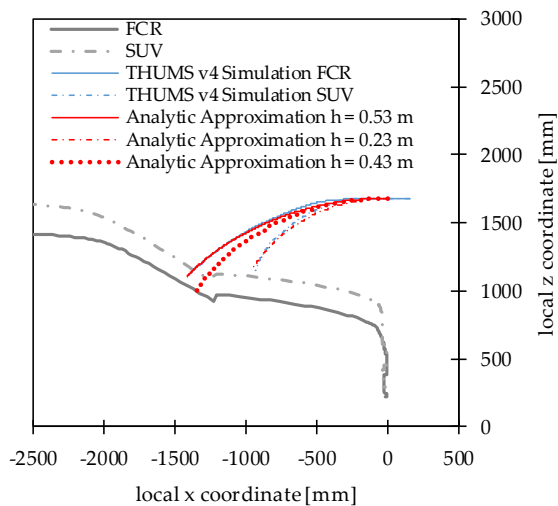
Figure 107: Trajectory based on an analytic approximation compared with HBM simulations for impact with FCR and SUV vehicle shape at 40 km/h
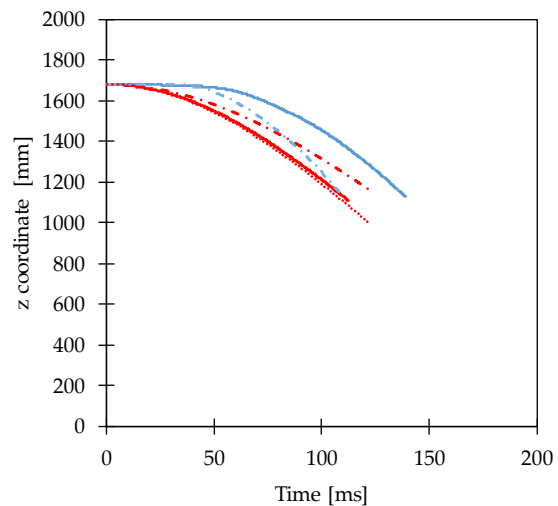
Figure 108: Z coordinate as a function of time based on an analytic approximation compared with HBM simulations for impact with FCR and SUV vehicle shape at 40 km/h

5.3.5 Kinematic-Based Assessment Criteria

In this study, *HIT* and *HIVel* were chosen as exemplary criteria for a kinematic-based assessment. Those criteria are not directly linked to human load limits or injury risk prediction. Therefore, they are not appropriate for a stand-alone evaluation of the protective effect of an impact structure. Both measures could be used in a hybrid approach as input for tests with subsystem impactors. Due to the simplifications within the GV models, no accelerations were evaluated. Because the windshield was rigid, no meaningful evaluation of kinematic injury criteria can be performed.

It was shown that *HIT*, which was used as requirement for the certification procedure of HBMs in Chapter 4, was very similar between the two applied models. In contrast, differences were observed for *HIVel*, which was not evaluated as part of the certification procedure. This highlights the fact that the certification procedure has to be adapted if it is intended to evaluate additional assessment criteria.

5.4 Summary

The findings of the study described in current chapter lead to the following conclusions:

- The kinematic-based assessment results of two different certified HBMs were very similar for all twelve load cases.
- The pedestrian stature, vehicle shape (especially *bleh*), collision speed and vehicle stiffness together affected the head impact time and head impact velocity.
- The head impact velocity can be higher or lower than the collision speed, depending on the pedestrian stature, vehicle shape and stiffness.
- The complexity of the interaction between the pedestrian and vehicle front was discussed in this study. Changes in stiffness and vehicle shape mutually affected one another. This finding highlights the need to use high-biofidelic HBMs and to consider the entire body and vehicle for passive safety assessments.
- The applied kinematic assessment criteria cannot be directly associated with human load limits, but the performed kinematic-based assessment can be used as input for physical tests.
- The trends in the kinematic-based results were found to be plausible, as they were in line with trends that have been reported in the literature and can be explained with a simple analytic model.

6 STRAIN-BASED ASSESSMENT

In the study described in this chapter, it was investigated, if real-world injuries of VRUs can be predicted when applying strain-based assessment criteria.

While this has been already analysed within some studies focusing on pedestrians by comparison with PMHS tests (Wu *et al.*, 2017; Watanabe *et al.*, 2011) and real-world injuries (Coulongeat *et al.*, 2014), no studies on the predictive capabilities of HBMs for bicyclists have been carried out to the author's knowledge. Therefore, real-world bicycle accidents were simulated with one HBM to compare the simulated outcome with the real-world injuries. It was analysed, if strain-based assessment with HBMs is useful for the assessment of countermeasures that address bicyclists.

Parts of this chapter were published at the IRCOBI 2018 (Klug *et al.*, 2018b). All shown simulations and analysis were performed by the author of the thesis, who also had the main responsibility for the study.

6.1 Method

Four representative real-world accidents from CEDATU were selected for the simulations with a detailed HBM. The initial boundary conditions were taken from the available accident reconstruction included in CEDATU and applied in the FE simulations. The accidents were replicated in LS-DYNA simulations using THUMS v4 to model the bicyclist, simplified FE bicycle models and a generic parameterisable vehicle model. Based on the results, a strain-based assessment was performed for each case, and the injuries indicated by the assessment were compared with the real-world injuries.

6.1.1 Real-world Cases

Four real-world cases from CEDATU were selected that fulfilled the following criteria and represented different accident scenarios:
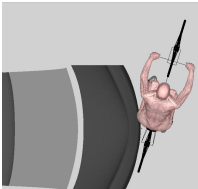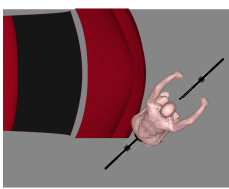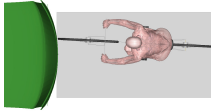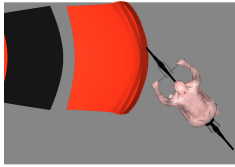
- Bicyclist was impacted by the front of a passenger car

- Height and weight of the bicyclist were within the range of the AM50 THUMS model (178 cm, 77 kg) ±10%

- Bicyclist was younger than 75 years at the time of the accident

- Documentation of injuries for the bicyclist were available

- Pictures of the damages to the car and bicycle were available

The initial conditions for the four selected real-world accidents are summarised in Table 8. They were taken from the available PC-Crash accident reconstructions at t0. In the available reconstructions, a multibody bicyclist model was used to achieve similar final positions and impact points on the vehicle as described in the documentation taken at the real-world accident scene.

The accidents were named according to the scenario they represented. In the first three cases, the bicyclist (bic.) was fatally injured. In the fourth case, the bicyclist sustained only minor injuries. Details of the documented injuries of the real-world cases are provided in the results section of this chapter.

The orientation of the bicycle is defined as counter-clockwise, such that 0° would mean that the bicycle and car were moving in the same direction. The x and y offsets were measured between the origin of the vehicle coordinate system (as defined in 2.2.4) and the centre of the chain wheel of the bicycle. The saddle height was measured relative to the ground. A crank angle of 0° was defined as the posture where the right leg is straight (6 o'clock), and 90° means that the right pedal was on the most rearward point (9 o'clock).

Table 8: Overview of reconstructed real-world accidents

	Crossing bic.	Left-turning bic.	Oncoming bic.	Slightly injured bic.
Car model	Renault Megane (YoR 1998)	Renault Espace (YoR 1993)	Skoda Fabia (YoR 2000)	Mazda 2 (YoR 2009)
Bicycle frame type	Trapeze Frame	Trapeze Frame	Swan's Neck Frame	Diamond Frame
Velocity of car at t0	60 km/h	70 km/h	28 km/h	10 km/h; 0.47 rad/s
Start of car braking	Before t0 (6.5 m/s²)	t0 (7.6 m/s²)	t0 (7 m/s²)	800 ms after t0
Velocity of bicycle at t0	15 km/h	15 km/h	17 km/h	25 km/h
Orientation of bicycle relative to the car	73°	43°	177°	131°
x and y location of bicycle crank relative to car CSYS	x = 208 mm, y = 288 mm	x = 239 mm, y = -487 mm	x = 927 mm, y = 138 mm	x = 552 mm, y = -348 mm
Bicyclist	Female, 65-yo, anthropometry unkn.; in reconstruction: 175 cm and 80 kg	Male, 59-yo, 179 cm; "strong and well boned"	Male, 73-yo, 171 cm, 82 kg	Female, 41-yo, anthropometry unkn.; in reconstruction: 172 cm and 80 kg
Crank angle	0°	0°	90°	0°
Saddle height	855 mm	840 mm	1000 mm	975 mm
Impact configuration				

In two of the cases, the anthropometry of the bicyclist was not documented and therefore unknown (unkn.). The anthropometry of the bicyclist that was used in the available PC-Crash accident reconstructions was similar to the anthropometry of the AM50 and therefore it was found to be reasonable to use the THUMS AM50 model for all simulations.

6.1.2   Bicycle Model

The applied simplified bicycle model was developed as part of research published in a bachelor's thesis (Hainisch, 2015). The frame and handlebar of the bicycle were modelled with beams. Shell elements were used to model the tire and rim. The spokes were modelled with beams and connected with discrete element to the rims to model pre-stressing of the spokes. They were preloaded with 2 kN and transferred only tensile forces. An inner pressure of 3.4 bar was simulated for the tires. The deformation behaviour of the wheel was compared to that described in experiments published by Watson (2010): The saddle was fixed and the rear wheel was impacted with a plate fixed on a pendulum. The impact velocity was 2.5 m/s, and the energy input was 1.46 kJ. Figure 109 shows the deformed wheel. Similar deformations of the spokes and the rim were observed as in the pictures provided by Watson (2010).
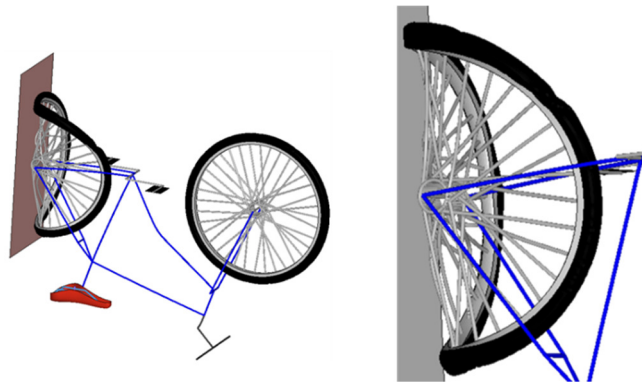
Figure 109: Simulation of the bicycle tests reported by Watson (2010)

The same frame type as in the real-world accident was used, and the saddle height was adjusted as in the accident reconstructions. Three different frame types were applied, which are shown in Figure 110: swan's neck, diamond and trapeze frames. The frame of the swan's neck was modelled with parameters of steel, while it was assumed that the diamond and trapeze frames were made of aluminium.

6.1.3   Model of the Bicyclists

The THUMS AM50 v4.01 was used as an HBM to replicate the bicyclist. The model was positioned on a simplified parameterisable bicycle model through pre-simulations, as explained in Chapter 2.3.2. Pre-strains through seating simulations were not considered in the main simulations. Figure 110 shows the three different initial postures that were applied to simulate the accidents. The leg posture was aligned with the leg posture described in the accident reconstructions in PC-Crash.
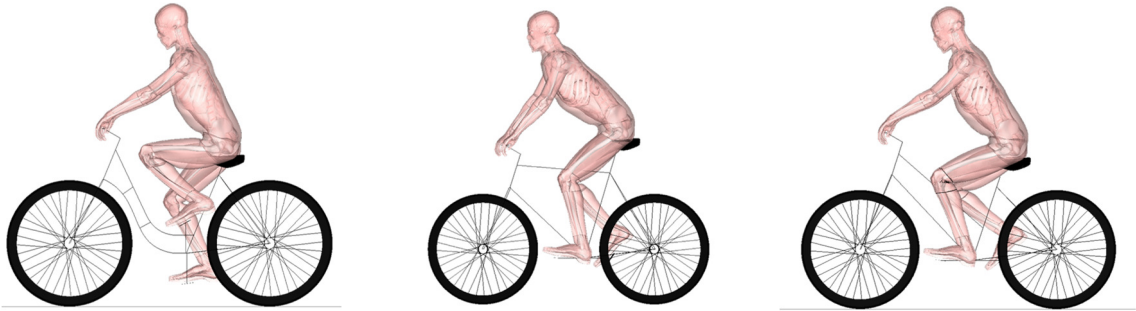
Figure 110: THUMS AM50 model positioned on three different kinds of bicycle frames (swan's neck, diamond and trapeze frames)

The initial boundary conditions from the accident reconstruction were applied, and the bicyclist model was impacted with a parameterisable generic car front described in the following chapter.

6.1.4   Generic Parameterisable Vehicle Models

As no full FE vehicle models of the cars that were involved in the accidents were available, Generic Parameterisable Vehicle (GPV) models were applied to replicate the cars from the real-world accidents. The models have been established in previous projects and showed comparable kinematics and accelerations as simulations with full FE vehicle models (Feist and Klug, 2017).

The parameters controlling the geometry of the vehicle front were selected to replicate the cars from the real-world accidents. Pictures of the vehicle together with the vehicle database of PC-crash were used as source for the original geometries. As the geometry of the Renault Espace is very similar to that of the Renault Megane Scenic, the same GPV model was used for these two cases (shown in Figure 111).
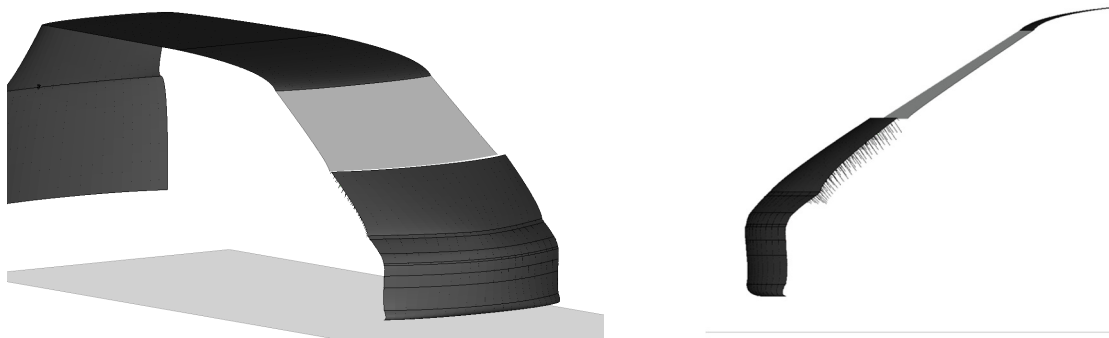
Figure 111: Generic parameterisable vehicle model of the two Renaults involved in the real-world bicycle accidents

The windshield of the GPV models was modelled as deformable with two layers: PVB and glass. The PVB was modelled as Ogden material and fitted by four terms to curves published by Timmel *et al.* (2007). The glass was modelled with non-local failure as described by Pyttel *et al.* (2011). The frame of the windshield was modelled as rigid. The bonnet of the GPV model was modelled to

mimic steel. Within the calibration of the GPV models, the thickness of the bonnet was used as parameter to adjust the stiffness. The bonnet was supported by 1D elements to allow to simulate a hard stop.

The stiffness of the GPV front was modelled with a large penetration contact and calibrated to the target force-deflection characteristics. The large penetration contact was used to define the contact force as a function of penetration for the surfaces representing the spoiler, bumper, grill and bonnet leading edge. The corridors of current cars introduced in Chapter 3.2.3 were again applied as reference. As the two Renaults were not developed to meet pedestrian safety requirements (the year of registration was before 1998 for both cars), the maximum of the stiffness corridors was used as target curve for all contact areas. The responses of the calibrated GPV model, representing the two Renault MPVs, are shown in Figure 112. The Simulation IDs refer to the impact location with the rigid cylindrical impactor introduced in Chapter 2.5.2.
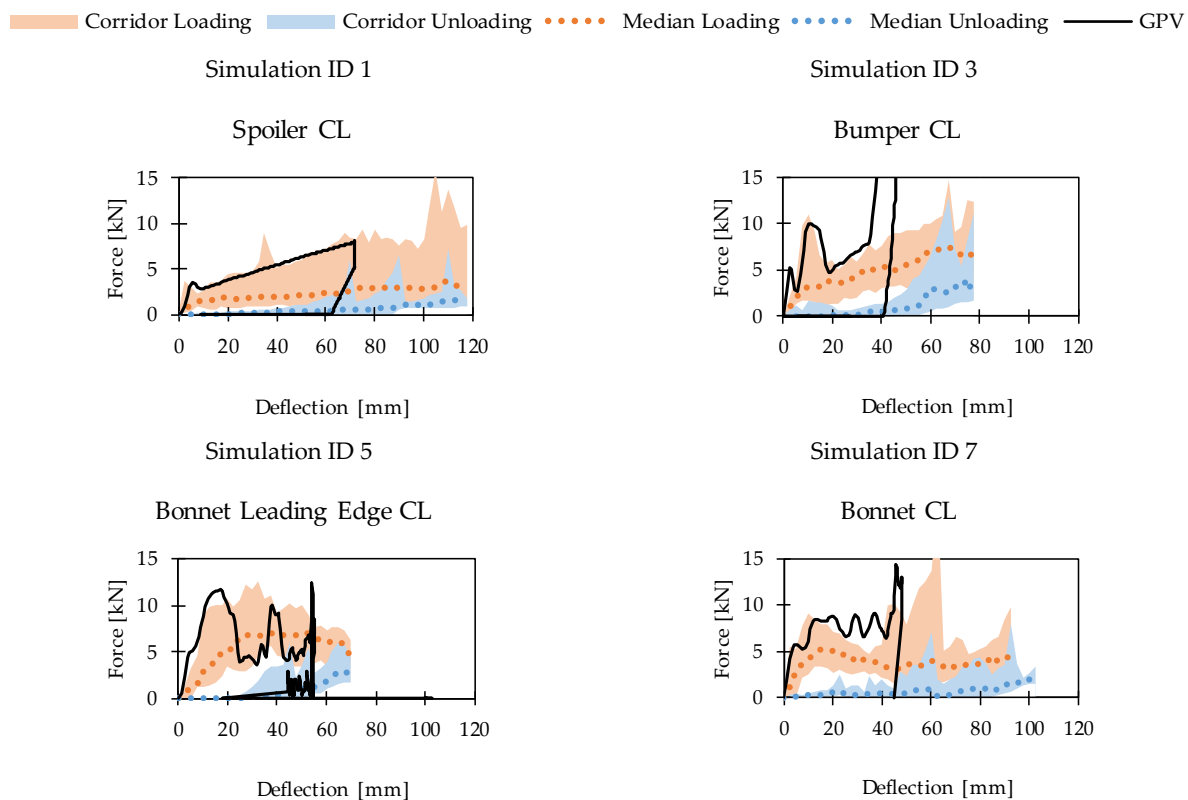
Figure 112: Response of calibrated GPV model representing the Renault MPVs from the real-world accidents

In the Euro NCAP rating of the Skoda Fabia (Euro NCAP, 2000), a soft bonnet and very stiff car front were reported. Therefore, the bonnet was calibrated to fit the median characteristics derived in Chapter 3.2.3, while the upper boundary of the stiffness corridor was used as target curve for the other contact areas. The responses of the impactor simulations for the GPV model calibrated to the Skoda Fabia are shown in Figure Appendix B-7.

The Mazda 2 received only two stars in the Euro NCAP pedestrian safety rating due to its mixed performance (Euro NCAP, 2007). Therefore, the same target curves as for the Skoda Fabia were

applied. The response of the GPV model calibrated to the Mazda 2 can be found in Figure Appendix B-8.

A coefficient of fiction of 0.3 was assumed for all external contacts (bicycle – car, HBM – car and HBM – bicycle).

6.1.5   Strain-Based Assessment Criteria

The strains of the HBM were evaluated using the developed postprocessing tool "DYNASAUR" explained in Chapter 2.3.3. DYNASAUR was used to calculate Maximum Principal Strains (MPS), 95th percentile and 99th percentile principal strains (PS) as well as the Cumulative Strain Damage Measure (CSDM) from the element history within the binary output file.

Element histories of the brain tissue (white and grey matter) and all cortical bones were evaluated.

For the strain-based assessment of the ribs, the probabilistic approach of Forman *et al.* (2012) described in Chapter 2.4.3 was also applied. The age was adjusted to the age of the bicyclist from the real-world case. The calculation was performed based on the maximum strain within one rib, using the maximum strain observed in one element (single element approach).

In addition to the strain-based assessment criteria, a kinematic-based assessment was performed for the head. The AIS 3+ and 4+ injury risk associated to the Head Injury Criterion (*HIC15*) and Brain Injury Criterion (*BrIC*) was calculated from the nodal history of a sensor located at the head CoG as described in Chapter 2.4.2.

6.2   Results

The results of the strain-based assessments of the simulated real-world accidents are presented case-by-case and are compared with the injuries from the real-world cases.

6.2.1   Case with Crossing Bicyclist

In the first analysed case, the driver of a Renault Megane was overtaking another vehicle while a bicyclist was crossing the road from the left side. The driver applied the brakes (with 6.5 m/s^2), but was not able to avoid the hitting the bicyclist (impact at 60 km/h). The bicyclist was riding at 10 km/h and was impacted close to the vehicle centreline. Figure 113 shows the reconstruction of the accident from the available PC-Crash file.

| t0 | 100 ms | 200ms | 400 ms |
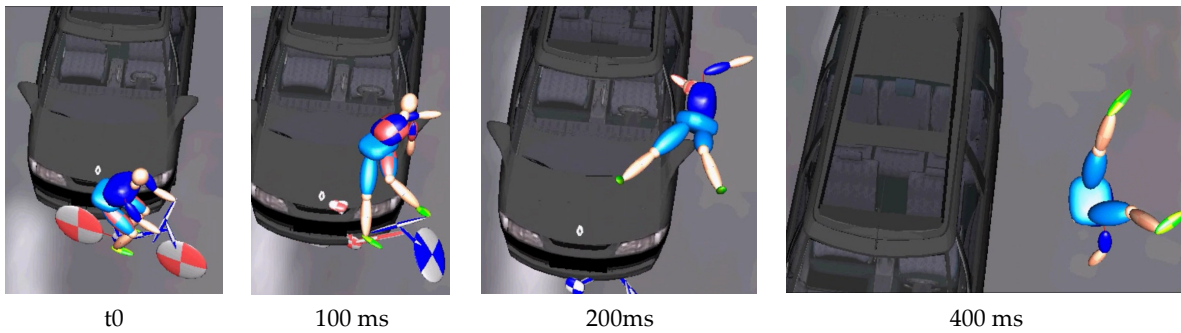
Figure 113: PC-Crash accident reconstruction of case with crossing bicyclists

The 65-yo female bicyclist sustained fatal injuries to the thorax and the head.

The following injuries were diagnosed:

- Head:
  - Subarachnoid bleeding
  - Cerebral bleeding
  - Multiple skull fractures
- Thorax:
  - Multiple rib fractures left (≥ three ribs)
  - Pneumothorax left

The damages on the involved car and bicycle from the real-world accident are shown in Figure 114 and Figure 115, respectively.

Figure 114: Car damage from real-world accident with crossing bicyclist

Figure 115: Damaged bicycle from real-world accident with crossing bicyclist

The kinematics of the simulation with the HBM impacted with the generic Renault Megane model are shown in Figure 116. The impact location of the hip and thigh of THUMS (Figure 116 – 50 ms) matches with the dents on the car shown in Figure 114. The damage to the bicycle model (Figure 116 -100 ms) was also comparable with the real-world damage shown in Figure 115. The head did not contact the vehicle. Once the left shoulder contacted the A-pillar at 100 ms (Figure 116), a rapid whiplash-like movement of the head was induced.

| t0 | t = 50 ms | t = 100 ms | t = 120 ms | t = 150 ms |
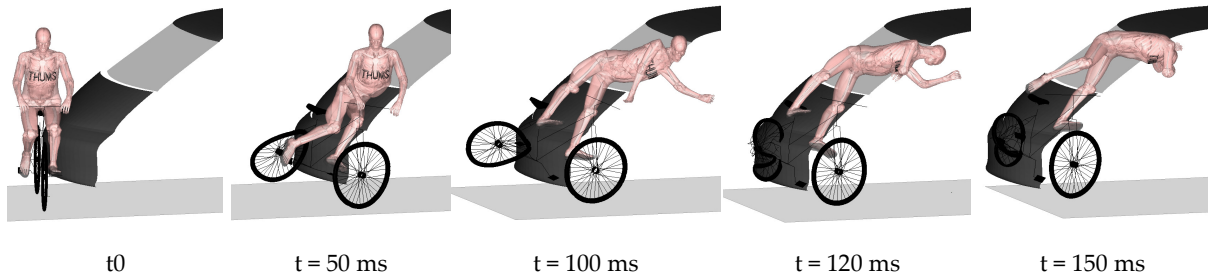
Figure 116: Accident simulation of crossing bicyclist with Human Body Model

Figure 117 and Figure 118 show the kinematic-based assessment for the head: the *HIC* indicated a moderate injury risk (Figure 117), while *BrIC* predicted a risk of 100% even for AIS 5 (Figure 118). In addition to the time independent evaluation of *BrIC*, the *BrIC* was also calculated at each time step using the current rotational velocities (bottom of Figure 118). The highest rotational velocity was 137 rad/s around the y-axis and was measured at 108 ms. The time of the maximal linear acceleration was observed slightly later at 115 ms, reaching a second peak when the head hits the shoulder at 140 ms.
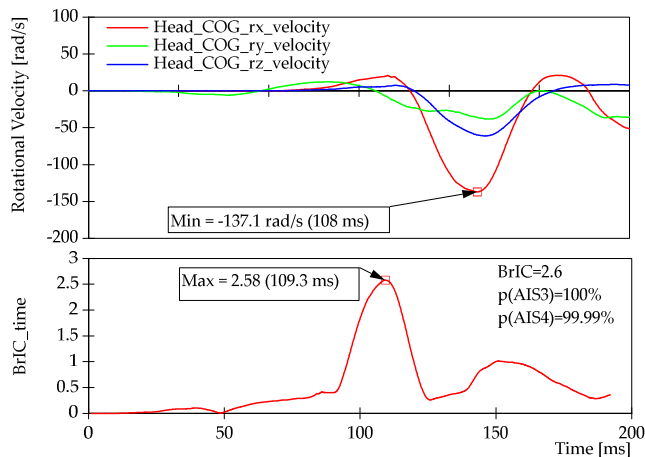
Figure 117: Rotational velocities and *BrIC* as a function of time for case with crossing bicyclist
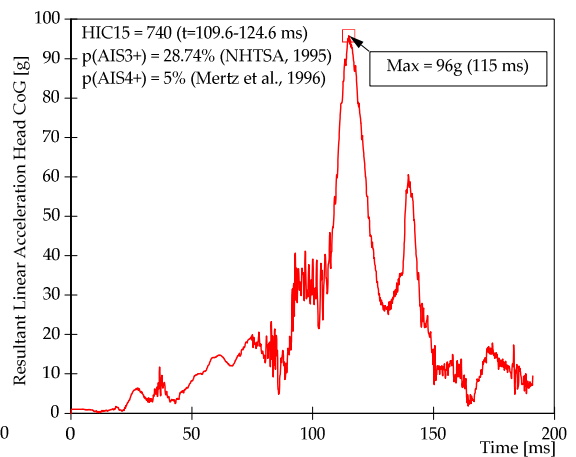
Figure 118: Resultant linear acceleration of the head CoG and *HIC* for case with crossing bicyclist

Table 9 shows the strain-based assessment for the head in numbers. All values exceeding the thresholds defined in Chapter 2.4.3 are highlighted in red. High strains in the brain were observed, exceeding the critical value of 0.3, which is indicative of brain tissue damage in the brain model of THUMS v4 (Watanabe *et al.*, 2011). No critical strain levels were reached within the skull (Table 9).

Table 9: Strain-based assessment for the head in the case with crossing bicyclist

	Brain	Skull
Total number of elements	15142	3324
Principal strain limit	0.30	0.015
Number of elements exceeding limit	3548	0
Time when max. number of elements exceeded threshold [ms]	122	-
95th percentile strain	0.45	0.00
99th percentile strain	0.63	0.00
MPS	0.89	0.01
CSDM (0.25)	42.98%	-

All elements of the brain tissue exceeding the critical principal strain of 0.3 are shown in red in Figure 119. In total, 43% of the brain volume experienced a strain in excess of 0.25 (Table 9), which is lower than the critical value of 54% (Watanabe *et al.*, 2011).
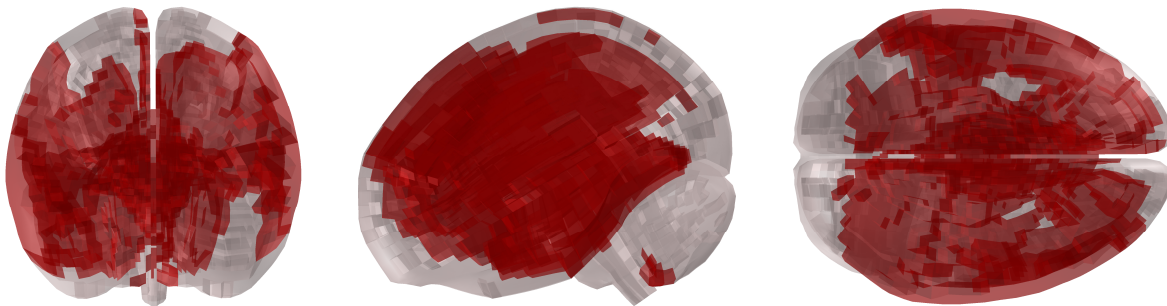
Figure 119: Visualisation of strain-based brain assesment of simulated case with crossing bicylist (strains > 0.3 shown in red)

Figure 120 shows the number of elements that exceeded the threshold as a function of time. The maximum number of elements exceeding a PS of 0.3 was reached at 122 ms. Figure 121 shows that the majority of elements experienced a maximum strain of around 0.2.
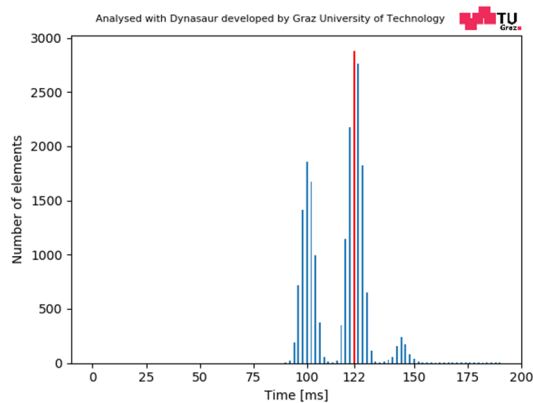
Figure 120: Number of brain elements exceeding a PS of 0.3 as a function of time for case with crossing bicyclist
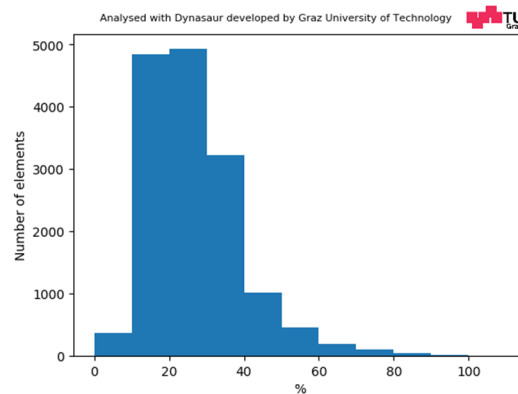
Figure 121: Distribution of maximum PS (100% = MPS = 0.89) within the brain tissue for case with crossing bicyclist

The probabilistic assessment of rib fractures in Table 10 shows that it is most probable that a 68-yo person (age of bicyclist involved in real-world case) will sustain three rib fractures in the simulated case. The strain analysis in Table 11 also indicates the presence of higher strain levels for the left than the right ribs. On the right side, only 41 elements of the total 6080 elements experienced a strain that exceeded 1.5%, and the 99th percentile principal strain was less than 1.5%.

Table 10: Probability of rib fractures of case with crossing bicyclist

Number of rib fractures	Probability of specific number of rib fractures for 68-yo person
0	0.0%
1	0.0%
2	17.0%
3	35.7%
4	29.8%
5	13.3%
6	3.6%
7	0.6%
8+	0.1%
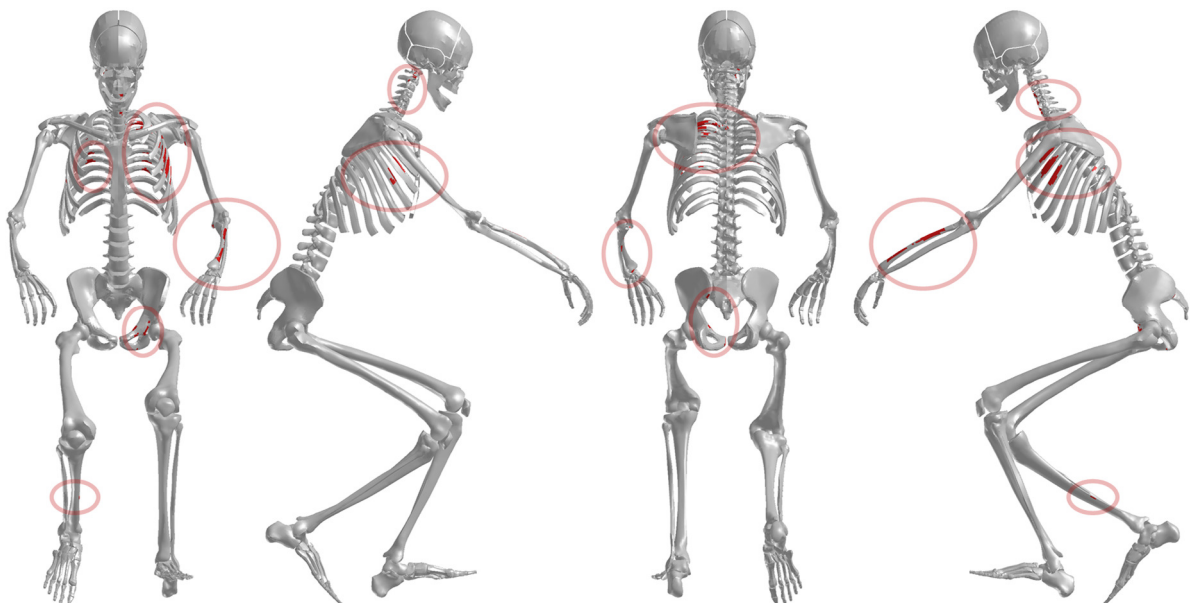
Figure 122: Visualisation of strain-based assessment for cortical bones of case with crossing bicyclist (elements with principal strain > 0.015 are shown in red)

The strain-based assessment of the cortical bone is visualised in Figure 122. The skeleton of the bicyclist in the initial posture is shown, and all elements that exceeded a critical strain of 0.015 (Wu *et al.*, 2017) are shown in red. The red circles mark the areas in which critical strains were found.

Table 11 shows the corresponding numbers for all relevant bones. The values exceeding a critical strain of 0.015 are again highlighted in red. The strains in the cortical bones of the vertebras C1-T3 exceeded a strain of 1.5%. The highest strains were observed in C6, which is, therefore, included in Table 11. For the humerus and tibia, only single elements exceeded the threshold.

Table 11: Strain-based assessment of cortical bones in the case with crossing bicyclist

	Total number of elements	Number of elements exceeding 1.5% strain	99th percentile strain	MPS	Fracture documented
Skull	3324	0	0.0028	0.0074	Yes
Ribs left	6080	494	0.0378	0.0893	Yes
Ribs right	6080	41	0.0144	0.0209	Yes
Humerus left	1323	7	0.0131	0.0192	No
Humerus right	1323	0	0.0094	0.0145	No
Pelvis	4464	79	0.0187	0.0483	No
Pelvis left	2232	77	0.0228	0.0483	No
Pelvis right	2232	2	0.0093	0.0169	No
Femur left	3060	0	0.0107	0.0143	No
Tibia left	2417	0	0.0113	0.0132	No
Femur right	3060	0	0.0062	0.0147	No
Tibia right	2417	3	0.0130	0.0160	No
C6	564	16	0.0248	0.0313	No

6.2.2 Case with Left-turning Bicyclist

In the second real-world case, the driver of a Renault Espace intended to overtake the bicyclist who was driving in the same direction. At the same time, the bicyclist was driving towards the middle of the road before turning to the left. The right side of the car front collided with the left-rear side of the bicycle. The PC-Crash reconstruction is shown in Figure 123.

| t0 | 100 ms | 200 ms | 400 ms | 800 ms |
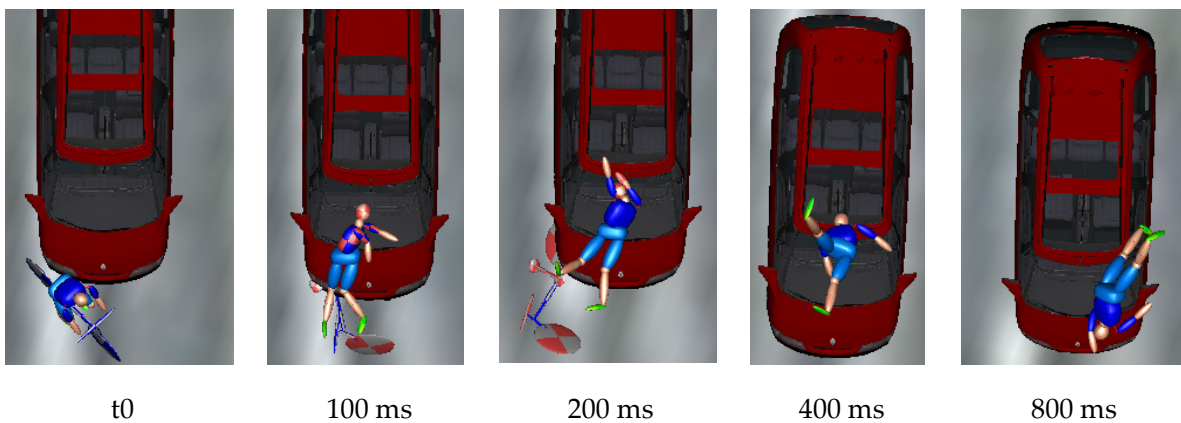
Figure 123: PC-Crash accident reconstruction of case with left turning bicyclist

Figure 124 and Figure 125 show the damages on the involved car and bicycle, respectively.

Figure 124: Damage to the car of the real-world case with left-turning bicyclist

Figure 125: Damages to the bicycle from real-world case with left-turning bicyclist

Several severe injuries were reported from the fatal injured bicyclist:

- Head:

  - Subdural bleeding (no intracerebral bleedings)

  - Nasal fracture

- Thorax:

  - Left lung contusion

  - Rupture of ascending aorta (4 cm)

  - Spleen haemorrhages

  - Multiple serial rib fracture on both sides (2-6)

- Spine:

  - Fracture of 6th cervical vertebra

- Extremities:

  - Haemorrhages in muscles of left shoulder

The kinematics from the HBM simulations of the case with the left-turning bicycle and the generic Renault Espace model are shown in Figure 126. The impact locations were plausible and fit to the deformations of the car from the pictures of the accident scene (Figure 124) and to the described injuries.

t0   50 ms   100 ms   150 ms
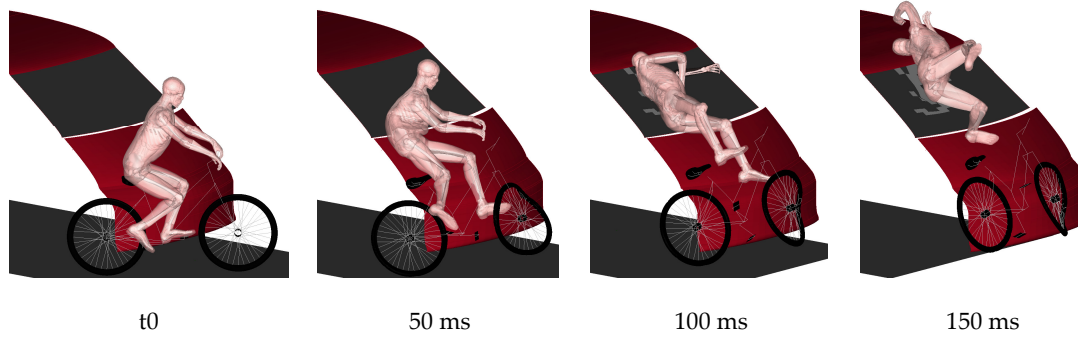
Figure 126: Accident simulation with Human Body Model of case with left-turning bicyclist

The left side of the thorax and the shoulder impacted the windscreen. The head impacted the upper edge of the windscreen and the roof leading to high accelerations at around 100 ms after t0 (Figure 128). At this time, the *HIC* and *BrIC* reached their maximum values. Both values were very high, indicating a head injury risk of 100%, which is shown in Figure 127 and Figure 128.
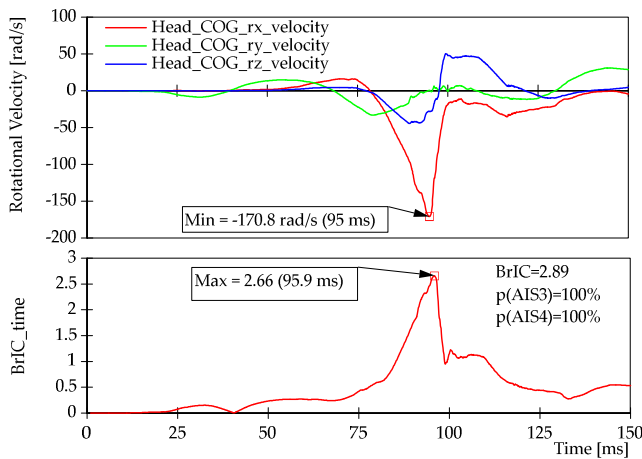
Figure 127: Rotational velocities and *BrIC* as a function of time in the case with left-turning bicyclist
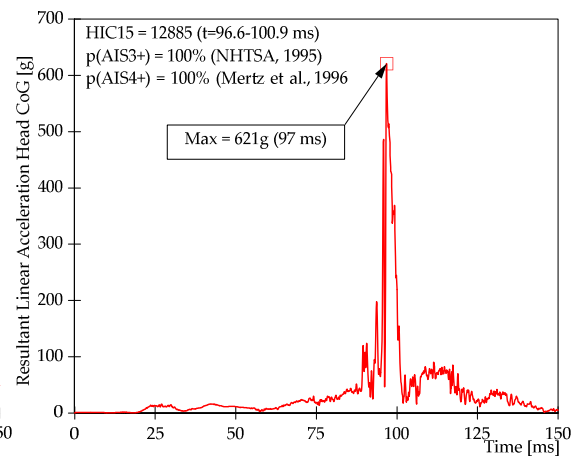
Figure 128: Resultant linear acceleration of the head CoG and *HIC* in the case with left-turning bicyclist

High levels of strain in the brain were observed, reaching a maximum of 1.4 (Table 12). All strain-based measures analysed within the cortical bone of the skull indicate a skull fracture.

Table 12: Strain-based assessment for the head in the case with the crossing bicyclist

	Brain	Skull
Total number of elements	15142	3324
Principal strain limit	0.30	0.015
Number of elements exceeding limit	12350	335
Time when max. number of elements exceeded threshold [ms]	101	99
95th percentile strain	0.76	0.03
99th percentile strain	0.96	0.06
MPS	1.43	0.16
CSDM (0.25)	92.82%	-

Figure 129 shows that elements exceeded the critical strain threshold of 0.3 in all areas of the brain (shown in red). 93% of the brain volume exceeded a PS of 0.25.
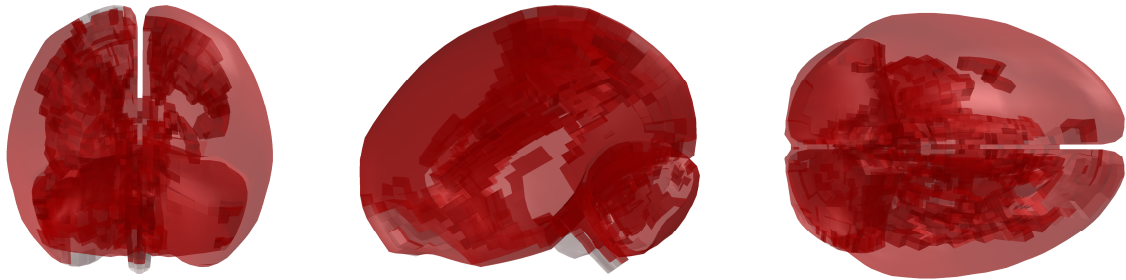
Figure 129: Visualisation of strain-based brain assesment in simulated case with left-turning bicyclist (strains > 0.3 shown in red)

The majority of elements exceeded the threshold 101 ms after t0 (Figure 130). Figure 131 shows that most of the elements experienced a strain between 30-40% of the MPS.
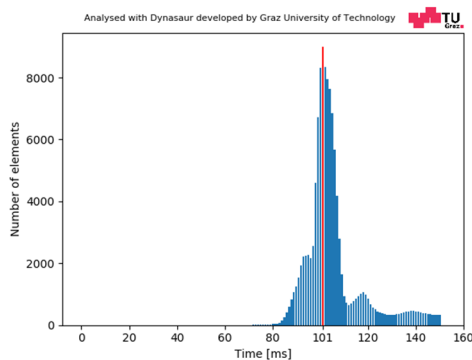
Figure 130: Number of brain elements exceeding a PS of 0.3 as a function of time in the case with left-turning bicyclist
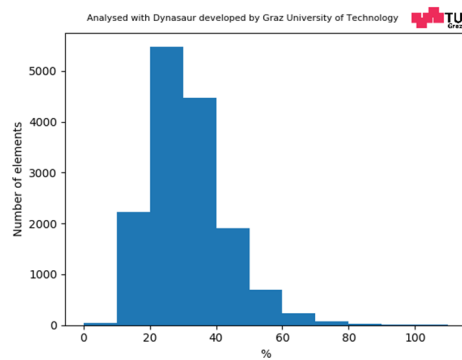
Figure 131: Distribution of maximum PS (100% = MPS = 1.43) in the case with left-turning bicyclist

A high thoracic injury risk is indicated by the strain-based probabilistic assessment results for a 59-yo person (Table 13). The probability of more than three rib fractures is 76%, with the highest probability of three rib fractures (31%).

Table 13: Probability of rib fractures in the case with the left-turning bicyclist

Number of rib fractures	Probability of specific number of rib fractures for 59-yo person
0	0.5%
1	5.1%
2	18.5%
3	31.4%
4	27.7%
5	13.0%
6	3.3%
7	0.5%
8+	0.0%

Figure 132 summarises the result of the strain-based assessment of the cortical bones. Most of the elements that exceeded a threshold of 0.015 were found in the skull and the ribs. Single elements of the pelvis and the right extremities also exceeded the critical strain. All values for the strain-based assessment are provided in Table 14.
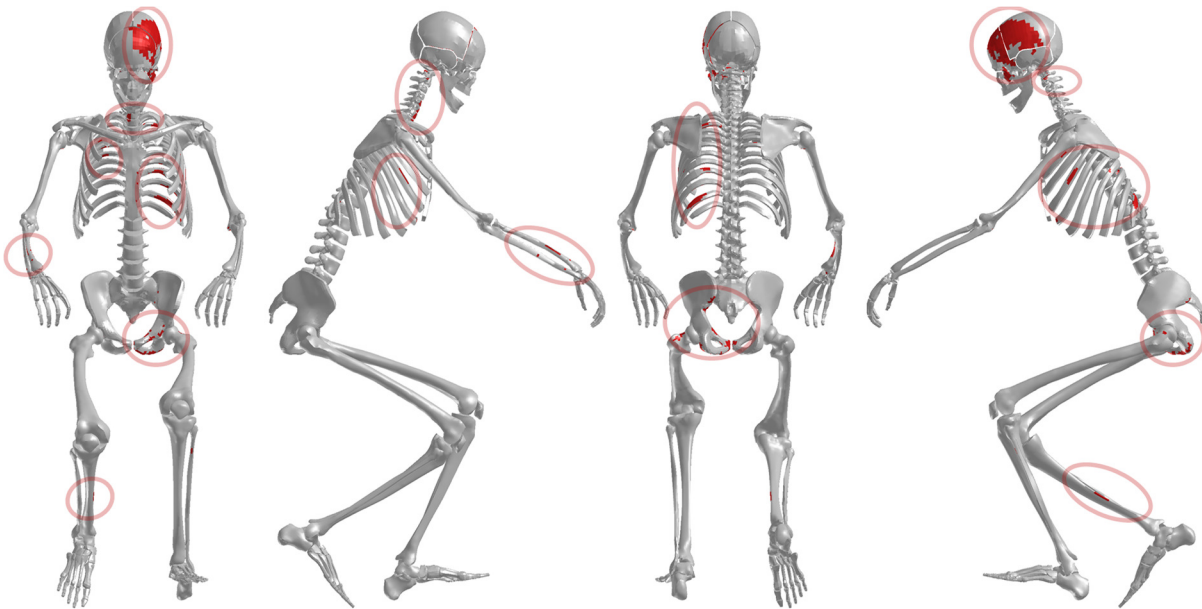
Figure 132: Visualisation of strain-based assessment for cortical bones in the case with left-turning bicyclist (elements with principal strain > 0.015 are shown in red)

In the spine, elements exceeding the threshold of 1.5% were observed in C1-T1 (Figure 132). The highest strains were observed in C6, in which 22 elements exceeded the threshold.

Table 14: Strain-based assessment of cortical bones in the case with left-turning bicyclist

	total # of elements	# of elements exceeding 1.5% strain	99th percentile strain	MPS	Fracture documented
Skull	3324	335	0.0561	0.1592	No
Ribs left	6080	269	0.0237	0.0453	Yes
Ribs right	6080	42	0.0144	0.0191	Yes
Humerus left	1323	7	0.0117	0.0212	No
Humerus right	1323	2	0.0091	0.0264	No
Pelvis	4464	164	0.0243	0.0639	No
Pelvis left	2232	148	0.0312	0.0639	No
Pelvis right	2232	16	0.0130	0.0339	No
Femur left	3060	20	0.0127	0.0246	No
Tibia left	2417	0	0.0090	0.0112	No
Femur right	3060	0	0.0070	0.0130	No
Tibia right	2417	16	0.0142	0.0175	No
C6	564	22	0.0316	0.0470	Yes

6.2.3   Case with Oncoming Bicyclist

In the third analysed case, the driver of a Skoda Fabia turned left at a crossing without recognising the oncoming bicyclist on the other side of the street, leading to a head-on collision.

The available accident reconstruction of the case is shown in Figure 133.

| t0 | 100 ms | 200 ms | 400 ms | 700 ms | 1100 ms |
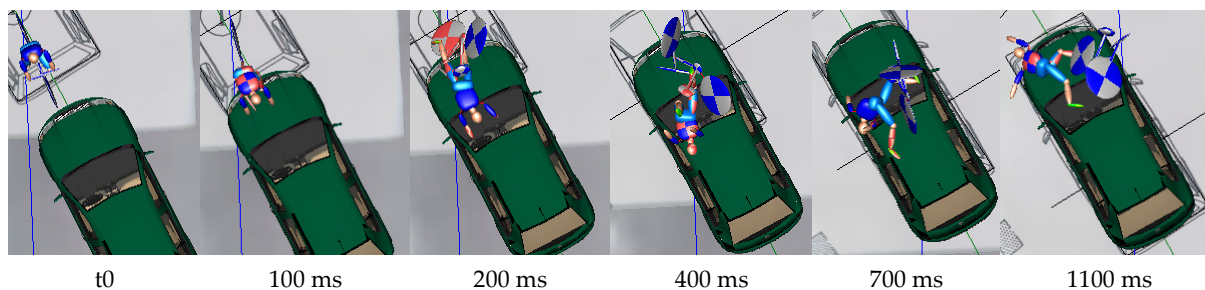
Figure 133: PC-Crash accident reconstruction in the case with oncoming bicyclist

The following injuries were reported from the autopsy of the fatally injured bicyclist:

- Head:
  - Round skin abrasions above right eyebrow and below malar bone
  - Skull fracture in the right forehead area
  - Bleedings under right pia mater
  - bleedings at frontal and occipital poles and at pons and spinal cord
- Neck:
  - Left side injured: large, deep, bleeding cut, muscles injured

- Thorax:
  - Large wound from neck to clavicle on the left side
  - Rib fracture of left ribs 1-8
- Upper Extremities:
  - Skin abrasions on left hand
- Lower Extremities:
  - Right leg: injuries on knee height – abnormal movability of right femur
  - Skin abrasions around left patella and right shin

The kinematics from the simulations with the HBM (Figure 135) matched the deformations of the car and bicycle shown in Figure 134.

Figure 134: Damages to the car and the bicycle in the case with oncoming bicyclist

| t0 | 100 ms | 250 ms |
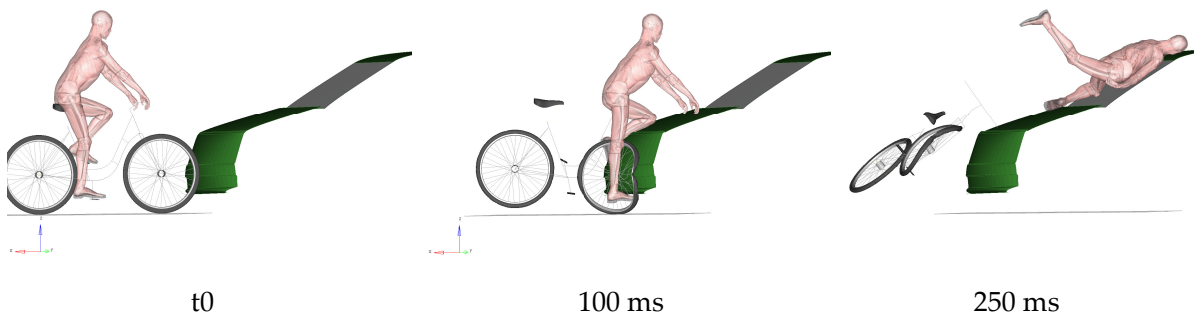
Figure 135: Accident simulation with Human Body Model in the case with oncoming bicyclist

High linear accelerations (Figure 137) and rotational velocities (Figure 136) were observed at around 215 ms, when the head impacted the upper frame and roof of the vehicle. A high injury risk is indicated by *BrIC* and a moderate risk by *HIC*.
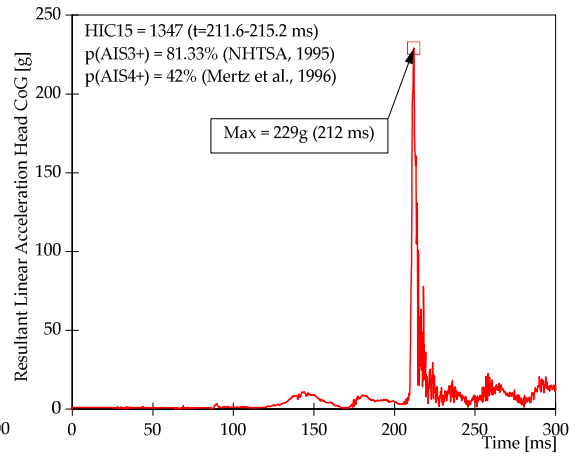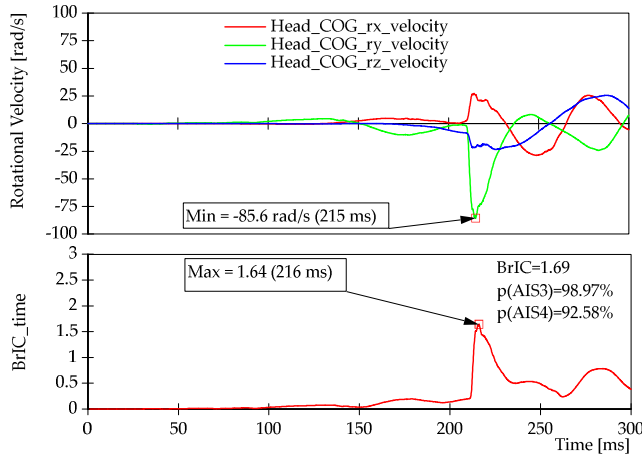
Figure 136: Rotational velocities and *BrIC* as a function of time in the case with oncoming bicyclist

Figure 137: Resultant linear acceleration of the head CoG and *HIC* in the case with oncoming bicyclist

The strain-based assessment showed high strains in the brain tissue. Nearly 4 000 of the 15 000 brain elements exceeded the critical strain of 0.3, which is shown in Figure 138. In total, 46% of the brain volume exceeded the threshold of 0.25 (Table 15). The maximum principal strain was 0.94, and the 95th percentile strain was 0.43. The maximum number of elements exceeded the PS limit of 0.3, 225 ms after t0.
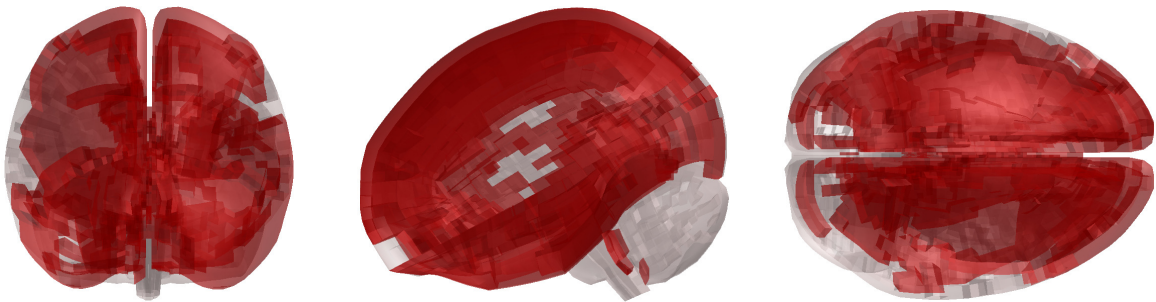
Figure 138: Visualisation of strain-based assessment of the brain in the simulated case with oncoming bicyclist (brain elements that exceeded a strain of 0.3 are shown in red)
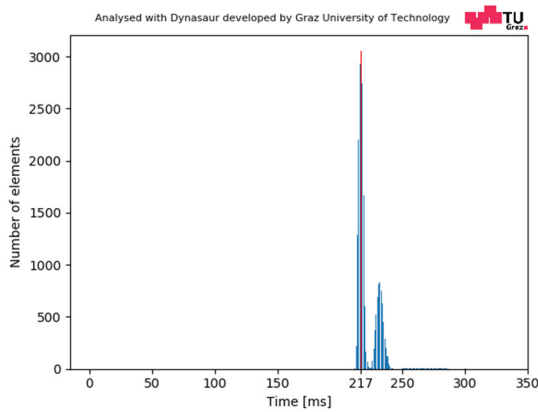
Figure 139: Number of brain elements exceeding a PS of 0.3 as a function of time in the case with oncoming bicyclist
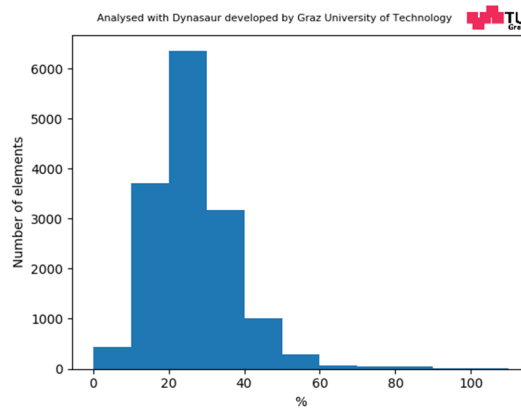
Figure 140: Distribution of maximum PS (100% = MPS = 0.94) in the case with oncoming bicyclist

The MPS observed within the skull was higher than 1.5%, but only 3 elements exceeded the limit. Therefore, the 99th PS was smaller than 1.5% (Table 15).

Table 15: Principal strains of brain and skull from in the case with oncoming bicyclist

	Brain	Skull
Total number of elements	15142	3324
Principal strain limit	0.3	0.015
Number of elements exceeding limit	3745	3
Time when max. number of elements exceeded threshold [ms]	217	212
95th percentile strain	0.432	0.004
99th percentile strain	0.599	0.007
MPS	0.942	0.025
CSDM (0.25)	45.8%	-

Only single elements of the right ribs exceeded the threshold strains. The probabilistic analysis (Forman *et al.*, 2012) of strains for a 73-yo person are shown in Table 16. A very small risk (8.6%) of one rib fracture was predicted during the primary impact.

Table 16: Probability of rib fractures in the case with an oncoming bicyclist

Number of rib fractures	Probability of specific number of rib fractures for 73-yo person
0	91.4%
1	8.6%
2	0.0%
3	0.0%
4	0.0%
5	0.0%
6	0.0%
7	0.0%
8+	0.0%

Table 17 gives an overview of the strains observed within the cortical bones. Strains in this impact were generally low, and only single elements exceeded the threshold of 1.5%. In the left and right

tibia, higher strains were observed. The highest strains within the spine were observed in T2, but only two elements exceeded a PS of 1.5%. The 99th percentile strain was smaller than 1.5%.

All elements of the cortical bone that exceeded a principal strain of 0.015 are shown in red in Figure 141.

Table 17: Strain-based assessment of cortical bones in the case with oncoming bicyclist

	total # of elements	# of elements exceeding 1.5% strain	99th percentile strain	MPS	Fracture documented
Skull.	3324	3	0.0069	0.0254	Yes
Ribs left	6080	0	0.0069	0.0107	Yes
Ribs right	6080	4	0.0094	0.0236	Yes
Humerus left	1323	1	0.0093	0.0155	No
Humerus right	1323	0	0.0087	0.0132	No
Pelvis	4464	0	0.0056	0.0103	
Pelvis left	2232	0	0.0036	0.0058	No
Pelvis right	2232	0	0.0065	0.0103	No
Femur left	3060	0	0.0088	0.0144	No
Tibia left	2417	18	0.0145	0.0222	No
Femur right	3060	0	0.0091	0.0104	No
Tibia right	2417	22	0.0149	0.0115	No
T2	738	2	0.0084	0.0315	No
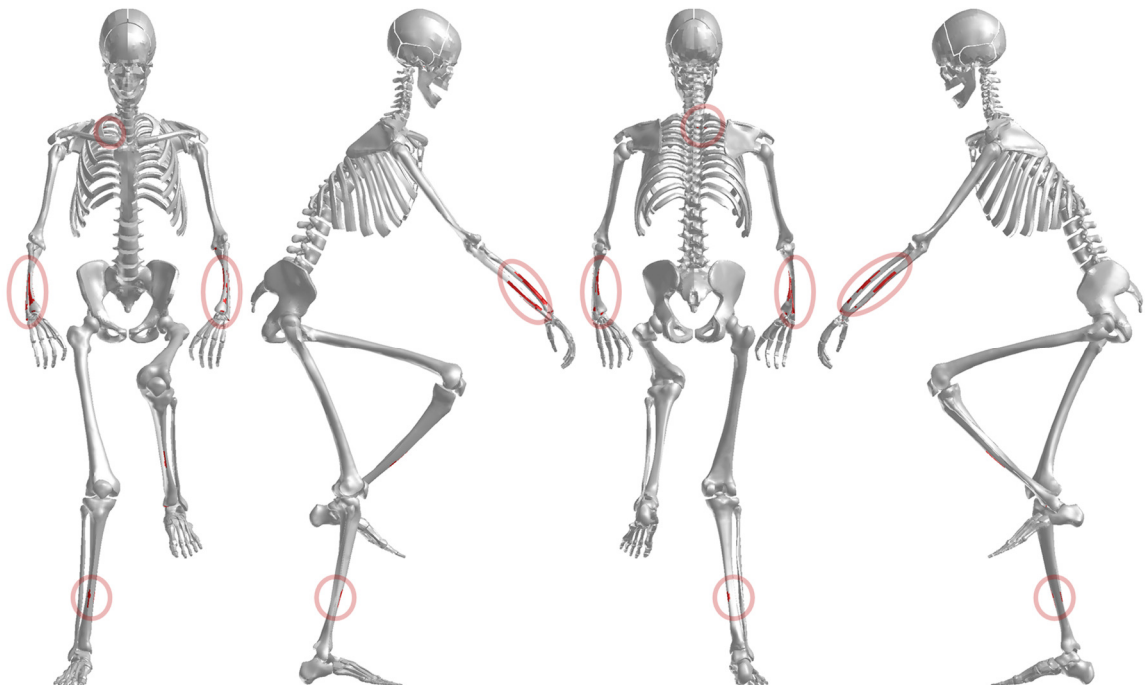
Figure 141: Visualisation of strain-based assessment of the simulated case with oncoming bicyclist

6.2.4 Case with Slightly Injured Bicyclist

In the fourth case, the driver of the car turned left into a parking lot on the other side of the street and collided with an oncoming bicyclist.

The PC-Crash reconstruction of the accident is shown in Figure 142.

| t0 | 200 ms | 400 ms | 800 ms | 1700 ms |
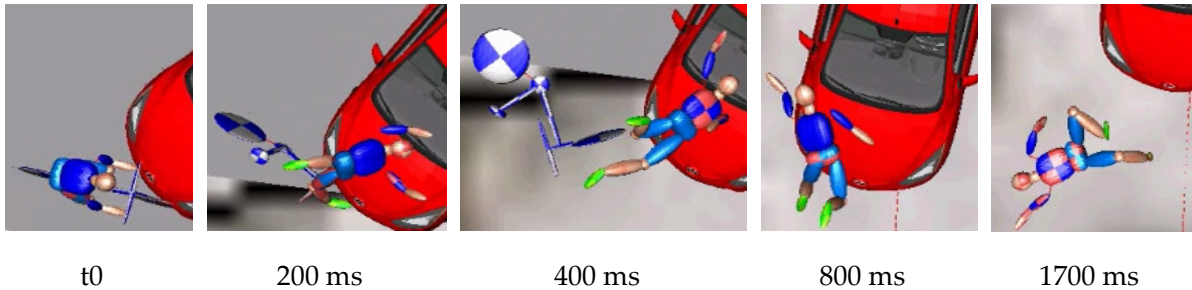
Figure 142: PC-Crash accident reconstruction of case with slightly injured bicyclist in PC-Crash

The damages to the car and bicycle from the accident scene are shown in Figure 143.

Figure 143: Damages to the car and the bicycle in the case with slightly injured bicyclist

Only minor injuries were reported from the real-world accident: The bicyclist suffered contusions on the left forehead, left shoulder and left knee (with skin abrasions).

Those reported injuries matched well with the impact locations shown in the simulations using the Human Body Model in Figure 144 and with the damages on the car (Figure 143). Due to the low collision speed, the bicyclist landed on the hood. Error termination due to negative volume of the shoulder flesh occurred at 250 ms when the bicyclists starts to slide downwards.

| t0 | 100 ms | 200 ms | 250 ms |
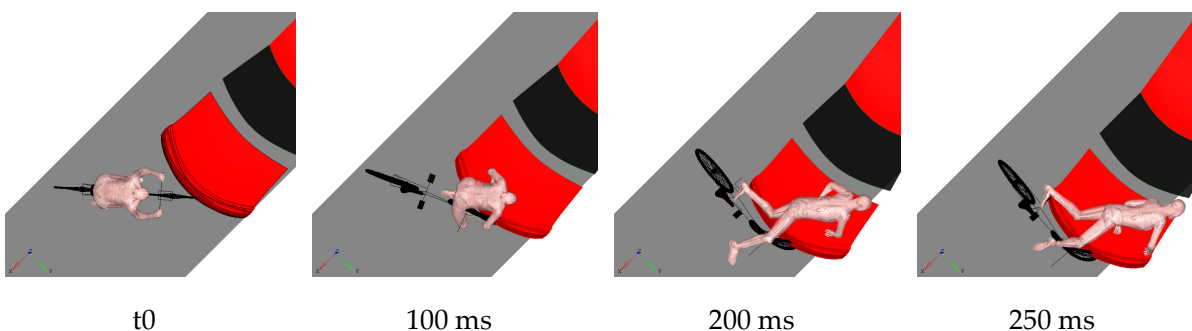
Figure 144: Accident simulation with Human Body Model of case with slightly injured bicyclist

The head did not contact the vehicle, which is why the linear accelerations shown in Figure 146 are only in the range of 10 g. The *BrIC* value based on the rotational velocities (Figure 145Figure 146) indicated a small brain injury risk.
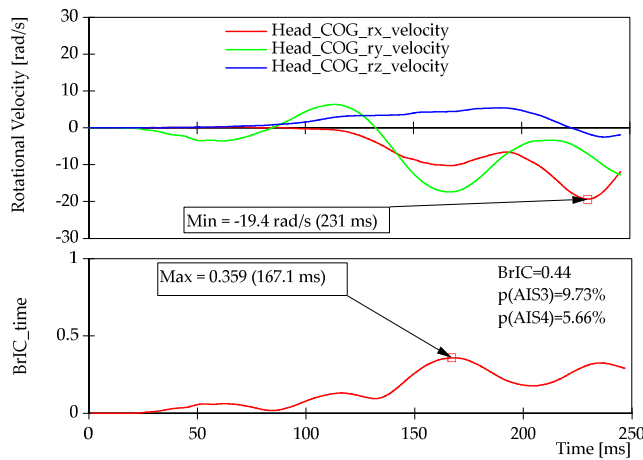
Figure 145: Rotational velocities and *BrIC* as a function of time in the case with slightly injured bicyclist
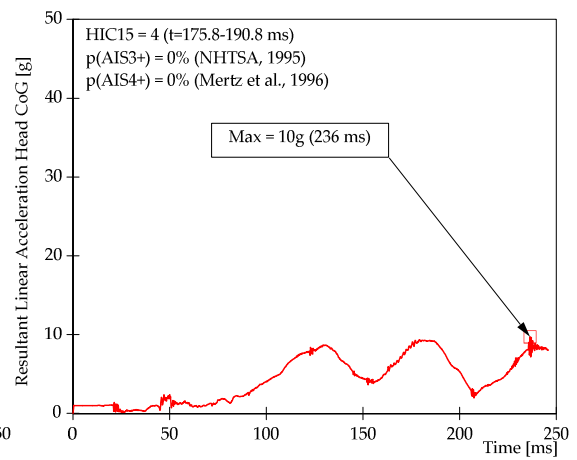
Figure 146: Resultant linear acceleration of the head CoG and *HIC* in the case with slightly injured bicyclist

The strain-based assessment of the head shown in Table 18 also indicates that the case was not critical for the brain or the skull.

Table 18: Strain-based assessment of the head in the case with slightly injured bicyclist

	Brain	**Skull**
Total number of elements	15142	3324
Principal strain limit	0.2	0.015
Number of elements exceeding limit	0	0
Time when max. number of elements exceeded threshold [ms]	-	-
95th percentile strain	-	-
99th percentile strain	0.034	0.00025
MPS	0.118	0.00061
CSDM (0.25)	0.00%	-

As shown in Table 19, no critical strain were observed in any cortical bone. Therefore, also no visualisation of the strain-based assessment is provided for this case.

Table 19: Strain-based assessment of cortical bones in the case with slightly injured bicyclist

	total # of elements	# of elements exceeding 1.5% strain	99th percentile strain	MPS	Fracture documented
Skull	3324	0	0.0003	0.0006	No
Ribs left	6080	0	0.0034	0.0044	No
Ribs right	6080	0	0.0040	0.0065	No
Humerus left	1323	0	0.0077	0.0121	No
Humerus right	1323	0	0.0058	0.0103	No
Pelvis	4464	0	0.0031	0.0062	No
Pelvis left	2232	0	0.0021	0.0035	No
Pelvis right	2232	0	0.0037	0.0062	No
Femur left	3060	0	0.0066	0.0074	No
Tibia left	2417	0	0.0096	0.0106	No
Femur right	3060	0	0.0076	0.0121	No
Tibia right	2417	0	0.0047	0.0079	No
Thoracic spine (T3)	692	0	0.0043	0.0048	No

6.2.5   Strain-Based Assessment Criteria

The results of the strain-based assessment for the cortical bones of the two analysed strain measures, 99th Percentile Principal Strain and Maximum Principal Strain of, were compared from all simulated cases in Figure 147. A significant difference between those two metrics is present. The 99th PS was sometime even less than half of the value of the MPS (below dashed line).

When applying MPS as strain-based assessment criterion, all circles out of the blue surface would predict and injury, while only those out of the green surface would indicate a fracture when applying 99th PS. Better correlation between predicted and real-world fractures was achieved when using 99th PS instead of MPS.
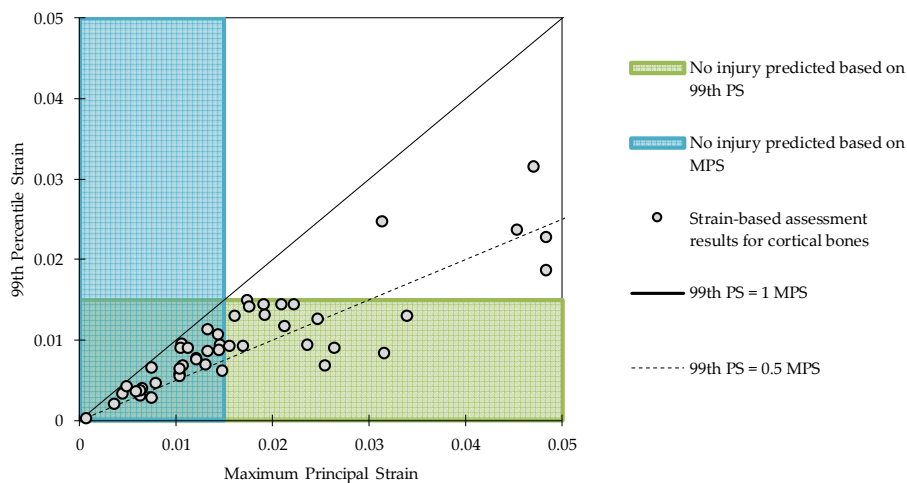
Figure 147: Comparison of 99th Percentile Strain and Maximum Principal Strain within cortical bones for all simulated bicycle accidents

6.3 Discussion

Within the research work presented in this thesis, a comparison of real-world injuries and predicted injuries was done for the first time for the whole body of a detailed HBM representing a bicyclist. Previous studies were focusing on the head only (Fahlstedt *et al.*, 2012; Fahlstedt *et al.*, 2016b; Fahlstedt *et al.*, 2015; Bourdet *et al.*, 2013) or were performed with multibody models, focusing on global kinematics (Serre *et al.*, 2007; Carter and Neal-Sturgess, 2009).

The applied methods in this study have several limitations:

- The structure of the applied GPV models was very simplified. Especially a realistic modelling of the windshield is challenging and can highly affect results. A non-local failure model was applied, which is, according to Alvarez and Kleiven (2016) the best state-of-the - art approach. However, errors up to 18% in terms of accelerations within head impacts for this modelling approach have been reported in the literature (Alvarez and Kleiven, 2016).

- Because the model of the bicyclist used in PC-Crash is very simplified, the initial conditions that matched the impact point from this reconstruction do not necessarily lead to the desired impact points in the HBM simulations. Small adjustments in the initial posture of the bicyclists were performed until the best correlations of impact points and damages to the vehicle were achieved.

- It was not possible to run the simulations until the ground impact, as error terminations occurred in all simulations during the free-flight phase. The robustness of the bicyclist model would have to be improved to manage to run longer simulations, which was beyond the scope of the present work.

- No muscle activity of the bicyclist was considered in these simulations. This activity can affect the stiffness of the flesh and the risk of lower leg injuries (Putra *et al.*, 2015; Iwamoto and Nakahira, 2014). Furthermore, no active reaction of the bicyclist can be replicated with the passive THUMS. In the real-world case the bicyclists might have reacted (e.g. turned the handlebar before the accident occurred or protected the face with the arms).

- The THUMS model has not been validated for any PMHS test representing a bicyclist. Only one PMHS test was found in the literature with limited information available, as the intention in the available study was to reconstruct an accident and not to provide validation data for HBMs (Serre *et al.*, 2007).

- No strain-based assessment of the internal organs or ligaments was performed.

6.3.1 Relevance of Selected Cases

The selected accidents cover three relevant categories of accident scenarios. Figure 148 shows the relevance of different accident scenarios for the bicyclist. Two of the analysed accidents represent accidents at junctions (left-turning bicyclist and oncoming bicyclist), which is the most relevant scenario. Accidents at junctions make up 43% of the light and 34% of the severe accidents. The case with slightly injured bicyclists was an accident that occurred in longitudinal traffic, where bicyclist

and vehicle were driving into the same direction. The accident with the crossing bicyclists represents the most relevant scenario in the category "other", contributing to 38% of the accidents of this category.

A relevant number of bicycle accidents (28% of fatal accidents) are single accidents where the bicyclists loses control the bicycle. No single accidents were reconstructed as part of the present study, as the focus was put on collisions with passenger cars.
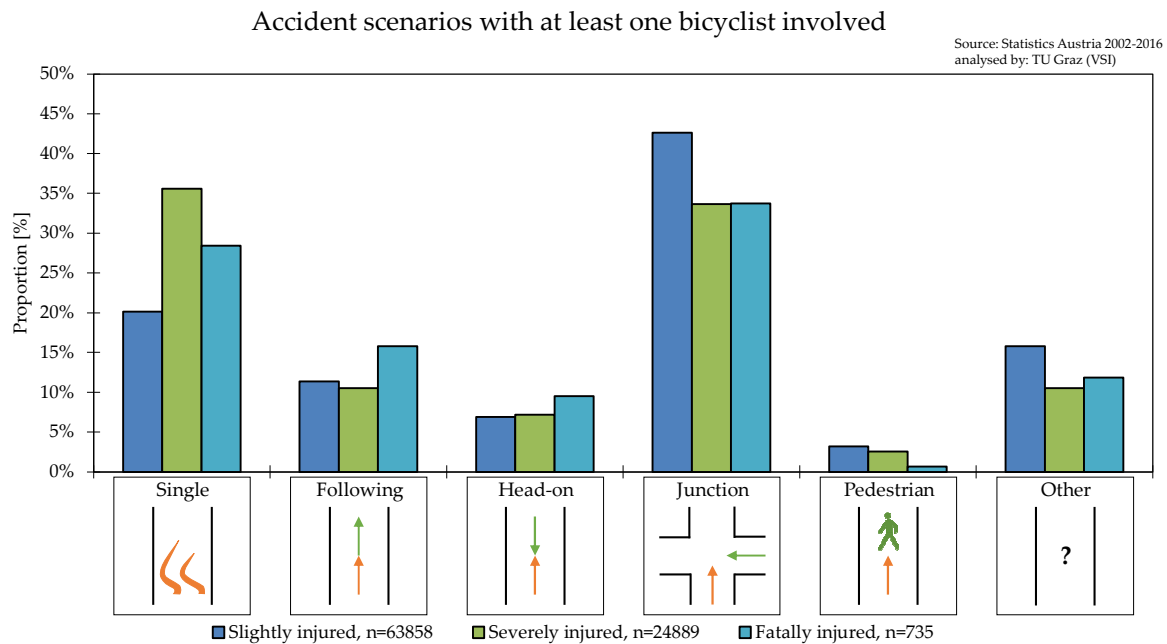
Figure 148: Accident scenarios involving bicyclists based on Austrian road traffic statistics from 2002-2016

Figure 149 shows the cumulative distribution of the collision speed of passenger cars in accidents involving at least one bicyclist. In the unbiased IGLAD dataset, the mean collision speed of passenger cars was 23.3 km/h for bicycle accidents (median value is 18.5 km/h). The red circles show the collision speeds of the discussed cases. The selected accidents represent a good sample: In 77% percent of the IGLAD cases, the collision speed was between 10 and 70 km/h, which is the range of the analysed real-world cases.
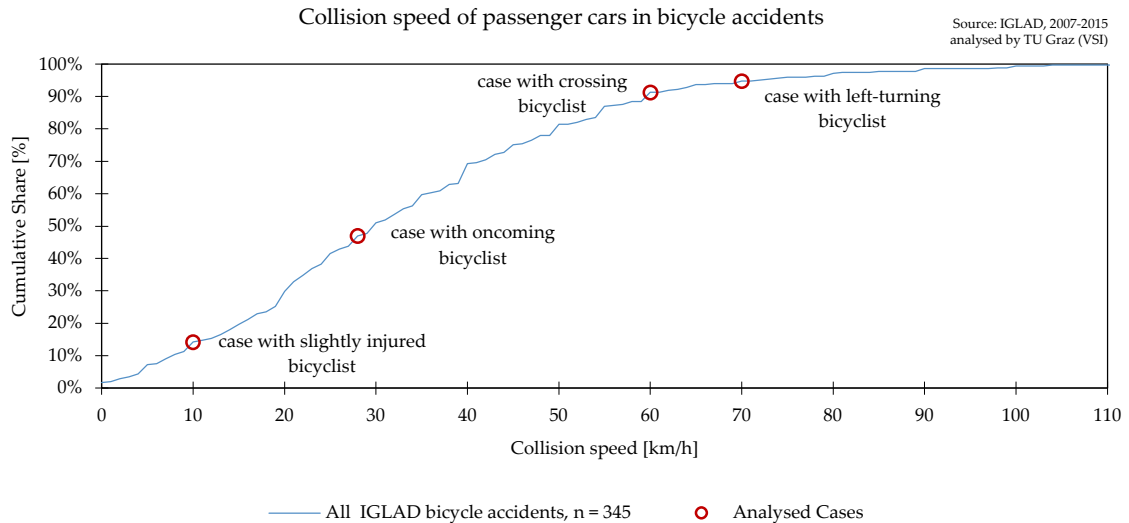
Figure 149: Collision speed of passenger cars at the first collision with bicyclists based on IGLAD data from 2007-2015 (n = 345)

6.3.2   Case with Crossing Bicyclist

The strain-based assessment predicted brain and thoracic injuries in accordance with the documented real-world cases. Some additional injuries were indicated that were not included in the injury report. In contrast to the strain-based assessment, no injuries to C6 and the pelvis were documented in the real-world case. As no autopsy protocol was available from this case, it is possible that these injuries might not have been identified or were not documented, because they are not as obvious as other severe injuries, such as a skull fracture. In general, fractures of C6 are plausible for severe bicycle accidents (Hackl *et al.*, 2001; Yoganandan *et al.*, 1989).

Regarding the pelvis, it also has to be considered that the simulations were performed with the male THUMS model, although the bicyclist was female in the real-world case. This was reasonable as the anthropometry was closer to the AM50 than to the AF05 model, but the geometry of the pelvis differs between males and females and was not adapted in the simulations.

Only single elements of the humerus and tibia exceeded the threshold, and 99th PS was below 1.5%, indicating a low probability of fracture.

The strain-based assessment of the ribs was in accordance with the documented injuries from the real-world accident. A minimum of three rib fractures was predicted, and the same information was provided in the accident report. In the report, a pneumothorax on the left side was also reported, which was cannot be directly predicted with the applied methods, but can be associated with the high number of predicted rib fractures.

No skull fracture was indicated by the strain-based assessment although reported in the real-world case. As there was also no visible deformation of the car in the real-world case that could be associated as a source of the fracture, it can be assumed that the skull fracture was caused by the ground impact.

No direct contact between the bicyclist's head and the vehicle was observed in the simulation or post-impact vehicle examination. In this case, one would expect that all head injuries were caused by the secondary impact. However, high strains in the brain were observed, although the head did not contact the vehicle. These findings are in accordance with those of PMHS tests, where rotational accelerations indicating a risk of TBI were also observed prior to the head impacts (Forman *et al.*, 2015b; Paas *et al.*, 2015a). This shows that injuries can be caused by the interaction of body parts, which highlights the need to properly replicate these effects and the benefit of the application of a biofidelic Human Body Model.

The case also shows the challenge of assigning injury sources in accident reconstructions. Brain injuries can be caused by a primary impact with the car, the free-flight phase, the secondary impact with the car, or the ground impact. This makes the validation of HBMs and assessment criteria based on the reconstruction of real-world accidents very challenging.

6.3.3 Case with the Left-turning Bicyclist

The strain-based assessment predicted all injuries reported in the real-world accident: The results of the strain analysis from the simulation showed the highest strains in the vertebral body of C6, at which a fracture was documented in the autopsy report. Furthermore, a high probability of at least three rib fractures was predicted, which matches the injuries from the real-world case.

In the real-world case, a rupture of the ascending aorta occurred. From the simulation, no strain-based assessment of the aorta was performed as no information on the validation of the aorta and applicable thresholds for THUMS v4 is available.

Pelvic and skull fractures were indicated by the strain-based assessment results that are not reported in the autopsy report.

In the real-world case, the bicyclist suffered several facial injuries. In the simulations, high amounts of strain on the skull were observed in the region of the right forehead. This indicated that the head impact condition on the windscreen was different in the simulations. Small changes in the impact location can lead to significant differences in the experienced loads, especially on the frame of the windscreen (Alvarez and Kleiven, 2016). This might be the reason why the strain-based assessment indicated the presences of a skull fracture that was not present in the real-world case.

If MPS would have been used as injury predictor, several additional, incorrect predictions would have been observed in the HBM simulations: No fractures were observed in the real-world cases for the humerus, femur and tibia. Applying the 99th percentile PS did not indicate injuries in these areas and, therefore, leads to better correlations with the real-world injuries.

6.3.4 Case with Oncoming Bicyclist

For Case 3, a systematic sensitivity study was performed to analyse the robustness of the results. As the baseline simulation led to an error termination just prior to the head impact due to negative volume, small adjustments in the initial conditions were performed, and the simulation that gave the best correlation between the impact points and the damages to the car was selected.

Table 20 gives an overview of the analysed variations that ran at least until the head impact.

The following variations were performed:

- It was observed in the baseline simulations that the femur was held back by the handlebar of the bicylce, leading to high degrees of deformation in the flesh of the upper leg. As no injuries were doucmented in the real-world case that would fit this mechanism, the contact was disabled within Run 002. This was found to be plausible, as in the real-world case, the bicyclist might turn the handlebar just before the impact, which cannot be simulated with the passive THUMS v4 model.
- The initial posture of the bicyclist was varied by adjusting the saddle height and the crank angle in Run 003 and Run 004, respectively.
- The initial orientation of the bicyclist was adjusted by 3° in both directions (Run 005 and Run 006).
- The GPV model of the Skoda Fabia was recalibrated to represent the maximum or minimum stiffness within the stiffness corridors for all contact areas (Appendix B). The windshield remained unchanged.
- In the baseline simulation, the brakes were induced at t0, causing the full acceleration of 7 m/s² to build up within the first 200 ms. In Run 009, the full deceleration had already been applied at t0.

Table 20: Overview sensitivity study for the case with an oncoming bicyclist

	Saddle height	Crank angle	Angle between bicyclist and GPV	Contact stiffness GPV	Contact bicycle - HBM	Braking	Termination time	Legend
Baseline	1000 mm	90°	177°	Mix	baseline	Baseline	200 ms	
Run 002	1000 mm	90°	177°		Handlebar excluded	Baseline	300 ms	
Run 003	850 mm	90°	177°	Mix	baseline	Baseline	255 ms	
Run 004	1000 mm	120°	177°	Mix	Baseline	Baseline	300 ms	
Run 005	1000 mm	90°	175°	Mix	Baseline	Baseline	300 ms	
Run 006	1000 mm	90°	179°	Mix	Baseline	Baseline	300 ms	
Run 007	1000 mm	90°	177°	Max	Baseline	Baseline	300 ms	
Run 008	1000 mm	90°	177°	Min	Baseline	Baseline	270 ms	
Run 009	1000 mm	90°	177°	Mix	Baseline	Full braking	300 ms	

Figure 150 shows the effect of the contact between the handlebar and bicyclist. The disabled contact (shown in green) led to a significantly higher head impact location than the baseline simulation (again in blue), which matches well with the docmented damages on the vehicle on the upper frame of the windshield. The simulation was, therefore, selected as the best estimate and is the one that was presented in the results section of this Chapter (6.2.3).
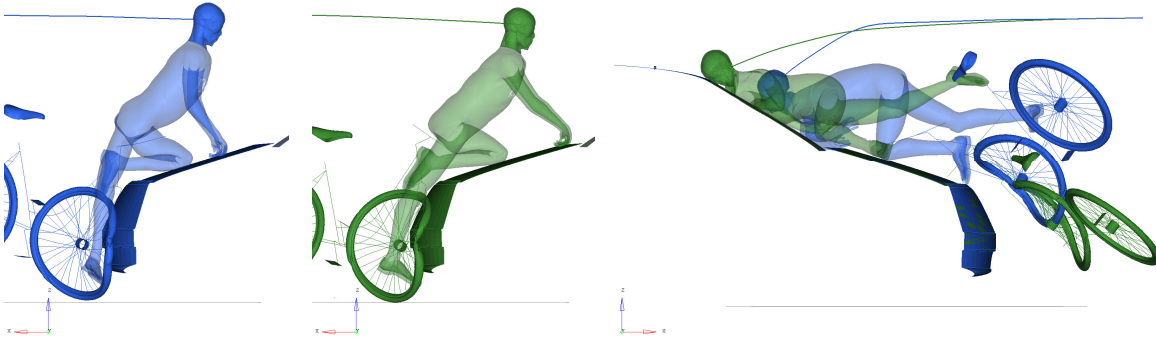
Figure 150: Effect of contact with handlebar on full-body kinematics for the case with an oncoming bicyclist

The differences in kinematics due to a 150 mm lower saddle height are shown in Figure 151. The blue bicyclist shows the baseline simulation just before the head impact occurred. The lines show the trajectory of the head CoG relative to the vehicle. The lower saddle height leads to a lower head impact location in the centre of the windshield.
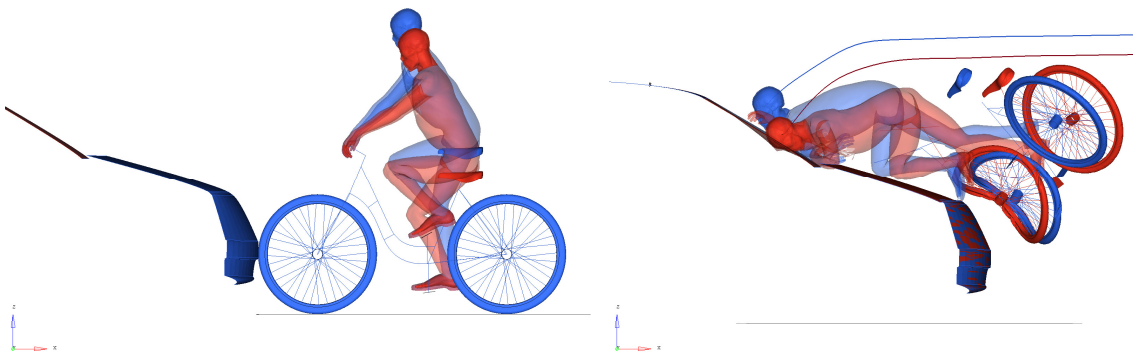
Figure 151: Effect of modified saddle height on full-body kinematics for the case with an oncoming bicyclist

Adjusting the crank angle and, therefore, the leg posture of the HBM led to a simulation with normal termination. The head trajectory and head impact point was slightly higher than in the baseline simulation. As shown in Figure 152, the kinematics of the torso and lower extremities were also affected.
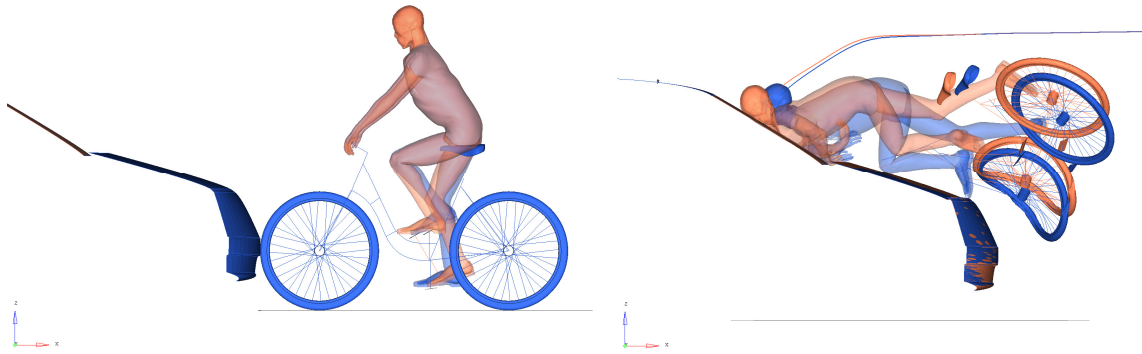
Figure 152: Effect of modified crank angle on full-body kinematics for the case with an oncoming bicyclist

The effects of changed initial orientation are shown in Figure 153. Changing the initial orientation of the bicyclist counter-clockwise led to a nearly perpendicular impact (shown in light violet). This variation led again to a slightly higher head impact location and differences in the head trajectory. Adjusting the initial orientation clockwise by three degrees did not lead to observable differences (dark violet) compared to the baseline simulation, but caused a normal termination of the simulation.
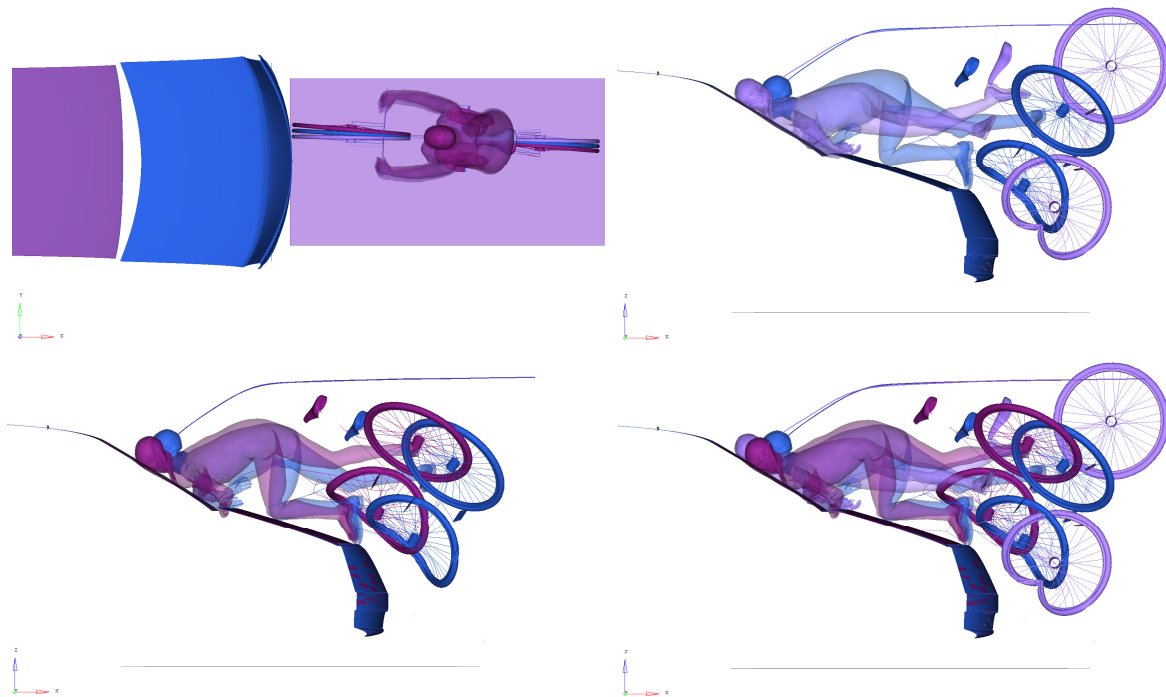
Figure 153: Effect of modified initial orientation of the bicyclist (±3°) on full-body kinematics for the case with an oncoming bicyclist

Adjusting the stiffness of the generic models of the Skoda Fabia led to differences in terms of inematics for the lower extremities and the torso, while the head trajectory and impact location remained nearly unaffected. On the left side of Figure 154 and Figure 155, the different postures of the left leg due to the adjusted stiffnesses are shown when the knee impacted the bonnet. While the higher stiffness (Figure 154) led to a higher location of the knee, the decreased stiffness (Figure 155) led to a lower position of the lower leg and foot.
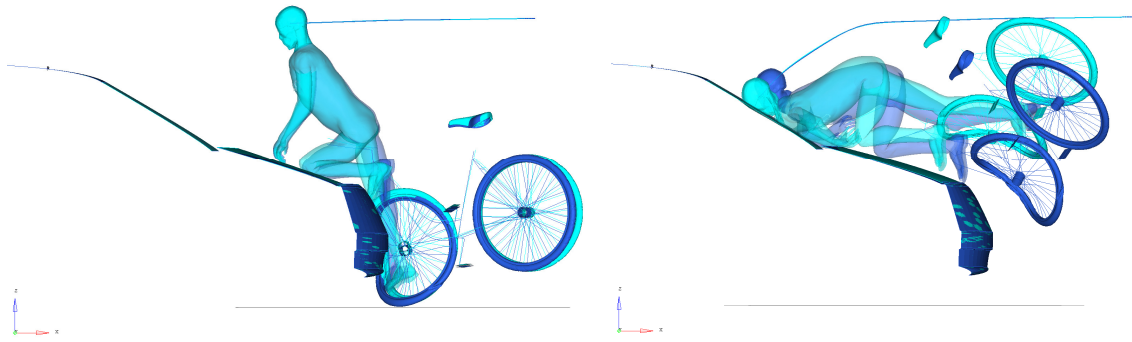
Figure 154: Effect of increased stiffness of the vehicle front and bonnet on full-body kinematics for the case with an oncoming bicyclist
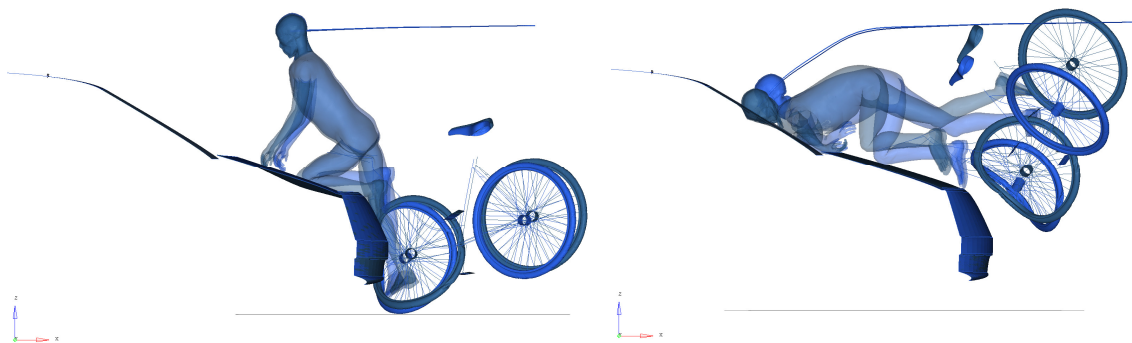
Figure 155: Effect of decreased stiffness of the vehicle front and bonnet on full-body kinematics for the case with an oncoming bicyclist

Because the vehicle braked earlier, the GPV model shown in grey in Figure 156 lagged behind the blue baseline vehicle in the left-hand pictures. This led to a later head impact with a slower impact structure. On the right side of Figure 156, the vehicle coordinate system was used as a reference, showing that the trajectories relative to the vehicle differed, and that the earlier braking led to a lower head impact location.
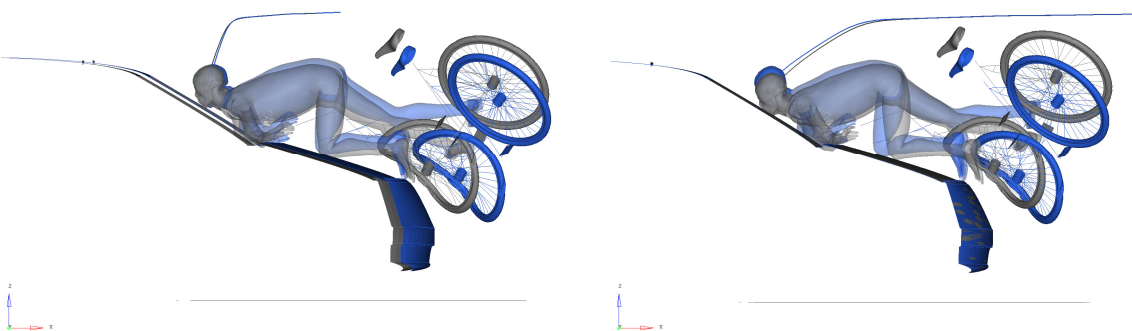
Figure 156: Effect of decreased stiffness of the vehicle front and bonnet on full-body kinematics for the case with an oncoming bicyclist

The strain-based assessment results of all previously shown variations are summarised in Figure 157. The 99th percentile principal strains are shown for the cortical bones of the skull and ribs as

well as for the brain tissue. As the baseline simulation ended prior to the head impact, strains were not comparable to those in the other simulations. Therefore, the bar is not filled in the graphs.

The strains inside the skull were generally lower than the critical value of 0.015 in all variations of the primary impact. The highest strains inside the skull were observed for the simulation with the GPV model with decreased stiffness of the vehicle front. The simulations with increased stiffness of the vehicle front, earlier braking and lower saddle height led to smaller strains than the other simulations.

When analysing the strains inside the brain, the simulation with lower saddle height and head impact location at the middle of the windscreen, showed significantly lower strains than the other simulations. The highest strains were observed in the simulation with changed leg posture due to a 30° adjusted crank angle.

The strain-based assessment of the ribs showed 99th percentile strains under the critical value for all variations. The selected simulation with disabled contact between the handlebar and bicyclist led to the highest strains. As the bicyclist with the 150 mm-lower saddle height hit the windshield more towards the centre and did not contact the stiff frame around it, those simulations showed the lowest strains in all areas. The simulations with earlier braking of the vehicles also generally showed smaller strains than most of the other variations, as the speed of the vehicle was 11% lower at the time of head impact (5.8 m/s instead of 6.5 m/s).
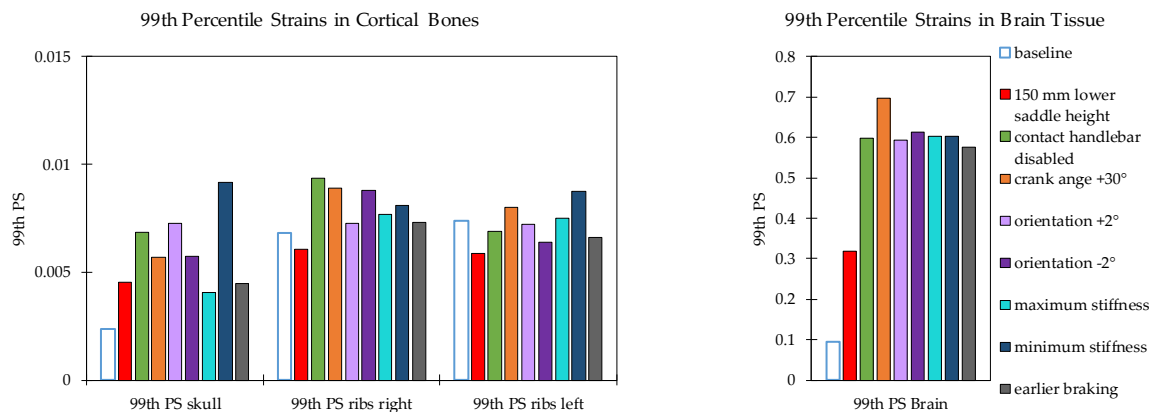
Figure 157: Comparison of strain-based assessment of the case with an oncoming bicyclist with varying boundary conditions

The sensitivity study showed that small changes in the unknown initial boundary conditions, such as varying the initial posture and position of the bicyclist, as well as varying the stiffness of the vehicle, led to differences in the kinematics, impact locations and strain-based assessment. This highlights the complexity of the assessment of VRU safety and the challenge of using real-world accident data for the validation of HBMs and assessment criteria. However, the general outcome of the assessment was the same in all of the shown variations: The 99th PS was smaller than the critical value of 0.015 for the skull and ribs in all variations and higher than the critical value of 0.3 for the brain in all simulations that ran up until the time of head impact.

Rib fractures and a skull fracture reported in the real-world case were not indicated by the strain-based assessment for this case in any variation. In the PC-Crash Simulation, the bicyclist impacted the vehicle several times. For this reason, those injuries might have occurred after the primary impact. As THUMS was not robust enough, it was not possible to simulate the whole in-crash phase and test this assumption.

6.3.5   Case with Slightly Injured Bicyclist

In the HBM simulations (Figure 144), the pelvis and torso hit the car more towards the vehicle centreline compared to the deformation of the vehicle from the pictures shown in Figure 143. Therefore, the impact angle and impact point slightly varied. However, no better agreement was achieved without a contact between head and windscreen, which did not happen in the real-world case. The presented simulation was found to be the best trade-off.

The strain-based assessment showed no critical strains in all body regions. This finding matches the minor real-world injuries.

The strain-based assessment could, therefore, be used to distinguish between severe and minor accidents in accordance with real-world injuries.

6.3.6   Strain-Based Assessment Criteria

The evaluation of strain-based assessment criteria is only possible with if detailed biofidelic HBMs are available and, therefore, represents one of the main advantages of HBM-based assessment. However, the validation of strain-based assessment criteria is still lacking. Furthermore, harmonised evaluation procedures and injury risk curves are missing.

In the latest validations of the THUMS v4 pedestrian model, deterministic strain-based assessment results were compared to injuries observed in PMHS tests (Chen *et al.*, 2018; Wu *et al.*, 2017). The results of these studies are summarised in Table 21. The strain-based assessment results from the simulations run with the morphed THUMS v4 model were compared with the fractures observed in the PMHS tests as reported by Chen *et al.* (2018) and Wu *et al.* (2017). The data presented in the table indicate that the strain-based assessment results are in accordance with the injuries from the PMHS tests for most of the analysed body regions (green fields). However, THUMS predicted tibia fractures in four out of five test cases, although they were not present in the PMHS (red fields). Cervical spine and thoracic spine fractures were not predicted by the HBM although they were present in the PMHS in two cases. For the pelvis and ribs, it was possible to predict generally whether a fracture was present or not, but the locations (diff. loc) and number of the rib fractures (lower nr.) differed between the prediction and PMHS in three out of five cases (yellow fields). (Chen *et al.*, 2018; Wu *et al.*, 2017). Chen *et al.* (2018) applied the MPS as a criterion (fracture indicated when above 0.015 for all cortical bones except the pelvis, where the threshold was set to 0.01). Wu *et al.* (2017) applied the same thresholds and analysed MPS for each element. Fractures were predicted from the simulation results, when the MPS of a minimum of four elements in a

cluster exceeded the threshold (Wu *et al.*, 2017). No further information is provided in either paper regarding how the principal strains were derived from the simulation results in detail.

Table 21: Comparison of predicted fractures from THUMS v4 simulation (Predict.) with those observed in PMHS tests (based on Chen *et al.*, 2018 and Wu *et al.*, 2017)

Body Region	PMHS-1 (Chen *et al.*, 2018)		PMHS-2 (Chen *et al.*, 2018)		V2370 (Wu *et al.*, 2017)		V2371 (Wu *et al.*, 2017)		V2374 (Wu *et al.*, 2017)	
	PMHS Injury	HBM Predict.	PMHS Injury	HBM Predict.	PMHS Injury	HBM Predict	PMHS Injury	HBM Predict	PMHS Injury	HBM Predict
Skull	No	No	No	No	No	No	No	No	No	No
Femur	No	No	No	No	No	No	No	No	No	No
Tibia	No	Yes	No	No	No	Yes	No	Yes	No	Yes
Pelvis	Yes	diff. loc.	Yes	diff. loc.	No	No	No	No	Yes	diff. loc.
Cervical Spine	Yes	No	No	No	Yes	diff. loc.	**Yes**	**Yes**	Yes	No
Thoracic Spine	Yes	No	Yes	diff. loc.	No	No	No	No	Yes	No
Ribs	**Yes**	**Yes**	Yes	diff. loc.	**Yes**	**Yes**	Yes	lower nr.	Yes	lower nr.

In Table 22, the results of the current study are shown. Injuries predicted by the strain-based assessment are compared to the injuries reported in the real-world bicycle accidents. Injuries were predicted when the 99th percentile strain exceeded the threshold (as defined in Chapter 2.4.3). Predicted and real-world injuries matched generally well. Incorrect predictions were observed for the skull, pelvis and cervical spine in two cases. No skull and rib fractures were predicted in two cases, although they were present in the real-world case. Fields are not coloured red, as the injury could have also occurred during the secondary impact, which makes it difficult to draw conclusions. In the case with the left-turning bicyclist, the bicyclist suffered a subdural haematoma, which could not be directly associated with strains experienced inside the brain. Therefore, this field is coloured yellow, as the prediction does not fully match the real-world injury.

The 99th percentile strain turned out to be more robust than the MPS. Applying the MPS would have led to an overprediction of injuries in several cases. This finding is in accordance with that of Peres *et al.* (2016), who focused on the prediction of pelvic fractures in side impacts.

Table 22: Comparison of real-world injuries and injuries predicted by strain-based assessment results from simulated bicycle accidents

Body Region	Crossing bicyclist		Left-turning bicyclist		Oncoming bicyclist		Minor injured bicyclist	
	Real-world Injury	HBM Predict.	Real-world Injury	HBM Predict.	Real-world Injury	HBM Predict.	Real-world Injury	HBM Predict.
Brain Injury	**Yes**	**Yes**	SDH	Yes	**Yes**	**Yes**	No	No
Skull	Yes	No	No	Yes	Yes	No	No	No
Lower Extr.	No	No	No	No	No	No	No	No
Humerus	No	No	No	No	No	No	No	No
Pelvis	No	Yes	No	Yes	No	No	No	No
Spine	No	Yes	**Yes**	**Yes**	No	No	No	No
Rib fract.	**Yes**	**Yes**	**Yes**	**Yes**	Yes	No	No	No

The current analysis as well as the analysis of results from the literature indicate that further research on strain-based assessment is needed. Further improvements are needed, especially for the pelvis and spine. Additional validations of the strain thresholds are needed for all body regions to strengthen the confidence in the results.

More research is also needed on strain-based, probabilistic assessment methods. This would allow HBM users to assess the risk of a specific injury, in terms of the severity of specific injuries, and cover human heterogeneity. A significant number of simulations of well-documented accident reconstructions in multiple scenarios will have to be carried out in the future to define reliable injury risk curves. The effect of uncertainties coming from unknown boundary conditions of the real-world accidents should be covered, as it was shown exemplary in Chapter 6.3.4. This means that, instead of single values for each accident, confidence intervals for the strain values could be considered. Furthermore, PMHS tests will be also needed to perform this task. The number of PMHS tests is limited, subjects usually only represent elderly people and tissue changes as well as the lack of fluid circulation can affect the observed injuries (Crandall *et al.*, 2011). On the other hand, they offer much clearer boundary conditions than those in real-world accidents, especially on the component level. Therefore, the advantages and disadvantages of both methods should be addressed by applying both data sources to derive and validate strain limits and injury risk functions.

For the time being, the 99th percentile strains turned out to be useful metrics to compare simulation results within parameter studies.

The postprocessing tool DYNASAUR, which was developed as part of the research described in this thesis, enables users to postprocess the big data files that result from the HBM simulations in a harmonised, time-efficient and stable way. The tool was made publicly available to advance

research on strain-based assessment criteria (Klug *et al.*, 2018c). An attempt to establish an international community that works on the validation of criteria for different body regions is being made. The open source approach of DYNASAUR allows researchers to easily implement new criteria and exchange knowledge among members of the scientific community.

The comparability of strain-based assessment results was not analysed in the present work. More research is needed for the single HBMs to validate the criteria and make strain-based assessment fully applicable. This challenge has to be tackled at first, before the comparability between models can be addressed.

6.4 Summary

- A harmonised postprocessing tool for the analysis of strain-based assessment criteria from HBMs was established, which should help users advance the harmonisation and make use of the full benefits of HBMs compared to other assessment methods.

- Real-world accidents were simulated with an HBM positioned on a bicycle. Results correlated well with the documentation from the real-world cases. It was possible to predict the majority of injuries from the real-world case. When simulating an accident with injuries of minor severity, no injuries were predicted by applying the strain-based assessment criteria.

- It was shown that the application of real-world accidents for the validation of assessment criteria is highly challenging. Many boundary conditions are unknown, the applied HBM was not robust enough to simulate ground impacts and the identification of injury sources is very challenging.

- Injuries can be caused during different phases of the impact. Brain injuries were predicted for one simulation without head contact. This makes the reconstruction of injuries and clear identification of injury sources without running detailed simulations highly challenging.

- Slight changes in the initial conditions and the stiffness of the vehicle affected the kinematics and strain-based assessment. Therefore, the validation of an HBM or an assessment criterion based on real-word injuries is extremely challenging. When deriving injury risk curves from real-world accidents, the uncertainties that arise from the unknown boundary conditions should be considered by applying confidence intervals of strain measures instead of single values from each accident reconstruction.

- It was shown that HBMs can also be used to replicate VRUs other than pedestrians: The real-world accidents included thoracic and spinal injuries, which cannot be assessed with state-of-the-art impactors. Those injuries were correctly predicted with the strain-based assessment method, which shows the potential of the application of HBMs for the assessment of protective measures for VRUs.

7 DISCUSSION

All parts of the presented solving approach have been discussed individually in the previous chapters.

In this chapter, a summary is provided. The requirements established in Chapter 1.3.8 are used to discuss if Human Body Models are an appropriate tool for the assessment of passive VRU safety. The fulfilment of each requirement prior and after the presented work is described, and an outlook on the work needed in the future is given.

7.1 Biofidelity

In the present thesis, the biofidelity of THUMS v4 and GHBMC PS were described in Chapter 2.3.1. For THUMS v4, several studies comparing the kinematics of the pedestrian model with different PMHS tests are available. Additional comparisons of the GHBMC PS model with full-scale PMHS tests should be performed in the future. No comparison of head impact times or contact forces of the model with PMHS tests is presently available. Both models offer good biofidelity, but further validations should be performed in the future.

Currently, HBMs are validated with varying load cases, and it is difficult to compare the degree of validation. The validation is usually performed by the HBM developers as continuous improvements of the models are needed. Whenever something changes in the models of FE software, all related validations have to be repeated. Detailed insight into the models is needed to perform proper validations. Validation load case are dependent on the intendent application of the HBM. Therefore, models have to be developed to answer specific questions and should be only applied within their specification (Cronin, 2011).

The harmonisation of HBM validation was not the purpose of this work. A harmonised validation catalogue for models applicable as VRUs has to be established to allow a fair comparison of the biofidelity of different HBMs. The THUMS user community is attempting to create such harmonised load cases (Fuchs and Peldschus, 2016; Fuchs and Peldschus, 2017). To properly evaluate the biofidelity, it is also important to consider the data quality of the PMHS tests. Uncertainties in the validation can also stem from the PMHS tests, and a high spread coming from the tests can lead to low validation requirements (Fuchs and Peldschus, 2017).

The comparison of the responses of the HBMs with those in full-scale PMHS pedestrian impact tests is of special importance for models mimicking VRUs, as it allows the evaluation of full-body kinematics in a load case representative for the intended final application. In such validation load cases, position vs. time and head impact time need to be evaluated instead of only analysing trajectories (z as a function of x).

Most of the PMHS full-scale studies were performed using modified serial vehicles as impact structures (Subit *et al.*, 2008; Schroeder *et al.*, 2000; Kerrigan *et al.*, 2009a; Kerrigan *et al.*, 2009b; Paas *et al.*, 2015b). The drawback of this approach is that the full FE serial vehicles are not publicly

available. Therefore, the test data cannot be virtually replicated by the whole scientific community for the validation of HBMs. Furthermore, inhomogeneities in the stiffness of the serial vehicles can lead to challenges in replicating them correctly in numerical vehicle models. Uncertainties related to the validation of the HBM can stem from the vehicle models.

Some recent studies have focused on the development of biofidelity corridors for dummies and HBMs, performing the impacts with generic vehicle bucks to allow the formation of well-defined and easily replicable boundary conditions (Song *et al.*, 2017a; Forman *et al.*, 2015b; Forman *et al.*, 2015a).

The development of biofidelity corridors requires scaling the responses from the PMHS anthropometry to an average size (Song *et al.*, 2017a; Forman *et al.*, 2015a; Kerrigan *et al.*, 2005b). Kerrigan *et al.* (2007) showed that it was not possible to sufficiently predict the response of a mid-sized PMHS from responses of PMHS with varying anthropometries by applying geometric scaling techniques. Yanaoka *et al.* (2016) found that scaling based on knee height led to the best results in terms of trajectories, but discrepancies were still observed, especially related to time histories. Therefore, the tests with the pedestrian bucks should be used to replicate each test (subject-wise) instead of scaling results and using the corridor approach. The HBM should be morphed to the anthropometry of the PMHS, especially considering the hip height relative to the ble (Paas *et al.*, 2015c). The full-scale PMHS tests published by Paas *et al.* (2015a) should be also considered for validation of pedestrian models, as these are the only tests with a more natural arm posture.

Furthermore, additional test data will be needed in the future to further improve the biofidelity of the models:

- More dynamic validation load cases for the validation of the flesh on the component level would be beneficial.

- A stronger focus should be placed on validation of the biofidelity of the spine, as it was shown in Chapter 5 that the spine kinematics are essential for the head impact kinematics.

- Tests with generic vehicle bucks that are representative for current vehicles are needed. The results of Chapter 3 can be used to design such bucks.

- More tests that replicate a natural arm posture and the interaction between upper extremities and bonnet are needed.

- Tests that enable tracking of kinematics until the ground impact are needed.

- Tests that replicate other groups of VRUs are needed. PMHS tests in postures that are representative for bicyclists or motorcyclists would allow researchers to assess the biofidelity of positioned PMHS. Especially the interaction of the legs and respective injury mechanisms would be of great interest because they differ from those of the pedestrian (Ito *et al.*, 2014).

- Tests with volunteers at low load levels would enable to study the effects of muscle activity on the VRU impact kinematics. Presently, only one study is available in which the neck stiffness was compared to volunteer tests in a test setup that was representative for VRU tests (Paas *et al.*, 2015a; Ono *et al.*, 2005). More research is needed in this field. The effect of muscle activity of the arm is currently unknown, and no active pedestrian model is available.

The application of real-world accident reconstructions for the validation of HBMs or validation of injury predictors is beneficial, as it leads to the creation of datasets that cover a wide range of the population and representative loads. It was shown in Chapter 7 that injury patterns from real-world accidents can be replicated with an HBM representing a bicyclist. However, there are many unknown boundary conditions which can affect the results strongly and therefore make validation very challenging. Traffic surveillance cameras or cameras used in NDS may deliver additional valuable input for the validation of kinematics, and especially for the secondary impact (Li *et al.*, 2018b; Han *et al.*, 2018).

General trends observed in real-world accidents should be compared to the trends observed in HBM simulations to prove whether the simulations lead to realistic conclusions. It would be beneficial to simulate a large number of accidents and analyse the total share of injuries in specific body regions instead of comparing single accidents. One real-world accident would result in several simulated cases, taking this approach, allowing users to address the uncertainties in the accident.

7.2 Appropriate Assessment Criteria

At the beginning point of this work, no harmonised guidelines for the interpretation of HBM results was available (Ghosh *et al.*, 2016). As part of the work described in this thesis, outputs for kinematic- and strain-based assessment were specified in detail. Guidelines for the postprocessing and interpretation of results are provided throughout the thesis. "DYNASAUR", a postprocessing tool for HBM simulations, was developed. This tool is now publicly available and procedures are clearly documented.

It was shown in Chapter 7 that the strain-based assessment has the potential to predict real-world injuries in several body regions that cannot be assessed with current state-of the art subsystem impactors. A good correlation between predicted rib fractures and those observed in the real-world accidents was observed. When simulating an accident with injuries of minor severity, no injuries were predicted by application of the strain-based assessment criteria. More research is needed to validate strain-based assessment criteria and link them with a risk of specific injuries, which is discussed in more detail in Chapter 6.3.6.

There are still only a few probabilistic approaches for strain-based assessment available (Peres *et al.*, 2016; Forman *et al.*, 2012). Attempts are being made to establish a community around "DYNASAUR" (Klug *et al.*, 2018c) and achieve more progress in this area with joint forces of the whole HBM community.

At this stage, the HBM can be used for kinematic-based assessment using the definitions provided in this thesis. However, the applied kinematic outputs can't be directly linked to human load limits. But, the output of the kinematic assessment can be used as input for subsystem tests, as is currently done by Euro NCAP for the assessment of deployable systems. Once the strain-based assessment has become more well-accepted and validated, the assessment could be performed directly with the HBM, and the tests with subsystems could be used for the validation of the numeric models of the impact structures.

7.3 Comparability

Due to the work described in this thesis, the comparability of the results gained with HBMs was significantly improved.

The first procedure that allows the objective comparison of kinematic-based assessment results of different HBMs in different FE software packages was developed. This procedure was applied to compare HITs, trajectories and contact forces in various pedestrian models and simulations performed by different institutions in four different FE software packages. Eventually, a certification procedure was derived that ensured the comparability of simulation results for the assessment of deployable systems within acceptable tolerance levels derived from reference simulations. The procedure allows users to identify inconsistent models, user errors and compatibility problems (with the settings or solver version).

Based on the research presented in this thesis in Chapter 4, the first detailed protocol for HBM simulations was developed by the author and implemented by Euro NCAP in January 2018 (Euro NCAP, 2017b, 2017a). Shortly afterwards, it was also adopted by Australasian NCAP (ANCAP, 2018). Boundary conditions are clearly described to improve comparability and harmonise pedestrian simulations. The protocol, consists of three main steps, for which consistent solver versions, contact and control settings have to be applied:

1. The generic vehicle models (described in Chapters 3 and 4) have to be impacted with the rigid cylindrical impactor at four different impact locations. Results are compared with the reference simulations. In this step, it has to be proven that the GV models show comparable performance in the specific environment in which they are used with the specific control settings that will be applied for the final assessment simulations (3). Incompatibilities between the GV model and the specific solver version or control settings can be identified and sorted out in this step.

2. The specific pedestrian model that is intended to be used for the assessment has to be certified. An comparison of the skeleton of the specific pedestrian model with the reference skeleton has to be provided together with a catalogue of measures to prove that the requested initial posture (established in Chapter 4.2.2) is fulfilled. The positioned model has to be impacted with the four GV models at the three different collision speeds. From these simulations, head impact time as well as trajectories of the head's centre of gravity, T12 and the centre of the *acetabuli* have to lie within the corridors and tolerances. A dossier

of the results for all twelve load cases has to be submitted to Euro NCAP in predefined templates including additional measures, such as contact forces, energies, added mass and additional tracking points. The plausibility and consistency of the results needs to be checked before the model is eventually certified, if it fulfils all requirements.

3. Once the certification process has been completed, the pedestrian model has to remain completely unchanged for the final assessment simulations in which the model is impacted by the full FE vehicle model to be assessed. The head impact time, wrap-around distance and defection due to the body loading are derived from these simulations.

The current tolerances should be narrowed down in the future to further improve comparability of results. Therefore, the harmonisation of HBMs has to progress. This may also require more harmonised anthropometries. Whenever the state of the art changes significantly (e.g. active pedestrian models, progress due to new methods within PMHS tests), the corridors will have to be adjusted. The certification procedure should not prevent HBM developers from improving the biofidelity of HBMs. However, it is important to capture the current state of the art in reference corridors and raise awareness that small changes in the HBM can cause significant differences of the output.

Additional requirements for pedestrian models of other statures will be needed. This is especially important for the child models, as there are no PMHS tests available, and material parameters and modelling approaches can differ from the adult models (Meng *et al.*, 2017). The definition of corridors and requirements for pedestrian models representing the stature of a 6-yo child is currently ongoing.

When additional metrics (e.g. head impact velocity, acceleration, strains) are assessed from HBM simulations in the future, additional outputs will have to be certified. The certifications have to cover the assessment criteria that are intended for application. Therefore, the certification procedures for the strain-based assessment might be also needed in the future. Load cases for specific body regions will have to be defined in which the outcomes of the strain-based assessment can be compared. A combination of PMHS tests (full-scale and component-level) and well-documented, real-world cases could be used as a starting point for this.

The use of open source Human Body Models would also allow users to further improve comparability and transparency, as everyone could use the same model or directly compare results or anthropometry with one baseline HBM. This is currently not feasible due to IP issues. Presently, only OS Child models (Peres, 2018; Shen *et al.*, 2015) are available that can be used to replicate VRUs. As the material parameters in OS models are completely open, this may also help ensure the comparability of strain-based assessments.

7.4 Human Variability

Human Body Models are available in different sizes and anthropometries and can be morphed (Zhang *et al.*, 2017a; Zhang *et al.*, 2017b; Schoell *et al.*, 2015; Huang *et al.*, 2018a; Giordano *et al.*, 2017). An open-source positioning and morphing tool was developed as part of the EU-funded Piper project and will help to make morphing easier applicable for everyone (Jolivet *et al.*, 2014).

It was shown in Chapter 5 that performing kinematic-based assessment with models of different sizes leads to reasonable results.

Currently, no 50th percentile female HBM is available, that can be used for the simulation of VRU accidents. The 5th percentile female is very small (151 cm and 49 kg) (Davis *et al.*, 2014) and needs extensive morphing before it could be used as 50th percentile female. Because of this issue, the 50th percentile male model was used in the bicycle accidents with female bicyclists, as the anthropometry was much more similar to this model than to the AF05.

In the future, more research will be needed to allow an age adjustment of HBMs in terms of material parameters and shape of body parts. This is of importance, as the results of real-world accident analyses have shown that specific injuries, such as pelvis injuries, are an issue especially for elderly females. (Klug *et al.*, 2015b)

7.5 Variability of Scenarios

As part of this research work, simulations of HBMs representing a pedestrian or bicyclist were performed. It was shown in Chapter 6 that HBMs are not only useful for simulating the interaction between pedestrians and impact structures, but can also be used to represent other vulnerable road users such as bicyclists. This chapter also included results that showed that scenarios from real-world accidents can be replicated. Reasonable results were obtained that were in accordance with documented damages to the vehicle. No simulations representing motorcyclists were performed as part of this work, although they also belong to the group of VRUs. The developed methods can also be applied to assess the protection of motorcyclists, but personal protection plays a larger role for this road user group. In an ongoing study, motorcycle accidents will also be reconstructed in the same manner as presented in Chapter 6 to cover this road user group.

No evaluation of ground impact was included in the present work, although a significant number of severe injuries can be also caused by the impact with objects in the environment. (Badea-Romero and Lenard, 2013; Shang *et al.*, 2018; Klug *et al.*, 2015b). It is possible to run HBM simulations until the VRU impacts the ground (Katsuhara *et al.*, 2014; Bastien *et al.*, 2017). However, no validation data is available and, therefore, the biofidelity of these simulations is unknown. Furthermore, in the simulation of the bicycle accident, stability issues were identified in the free-flight phase. The robustness of HBMs has to be considered and improved to allow simulations to run up until the ground impact. For this purpose, models with some simplifications, such as the GHBMC PS, might be more appropriate. From these simulations, kinematics could be assessed and phases of special

interest could be simulated with more detailed models. Conversion models could be used to identify phases and simulations of special interest.

Virtual testing with Human Body Models allows users to freely vary scenarios. The initial posture, velocity and impact points can be varied. Experiments must be properly designed to perform a limited number of simulations that enables users to capture the total performance of the impact structures. Li *et al.* (2016) concluded that about 120 cases have to be simulated to predict the AIS 2+ injury rate and distribution of pedestrian accidents (compared to GIDAS data). However, a homogenous stiffness of the impact structures has to be ensured to allow for the interpolation of results. Furthermore, numerical models of the structure have to be validated. For these purposes, physical tests with simple impactors on the real vehicle in randomly selected locations could be used.

8 CONCLUSIONS

Based on the research presented in this thesis, the following conclusions can be drawn with respect to the research questions stated at the beginning of the thesis:

Are assessment results comparable among different HBMs and among different institutions performing HBM simulations?

- To analyse the kinematic comparability of HBM simulation results, a new pedestrian simulation protocol was established which enables users to compare HBMs in specified reference load cases with properly defined boundary conditions which were derived from sensitivity studies. The importance of properly defined boundary conditions was shown, as the variation due to varied boundary conditions (all compliant with the 2017 Euro NCAP pedestrian testing protocol) was higher than variation between two HBMs in one code with fixed boundary conditions.

- When eighteen different results for the twelve reference load cases – performed by different institutions with different HBMs in different FE software packages – were obtained according to the protocol, outliers were identified. The relative amount of deviation among the kinematic-based assessment results was drastically reduced when these were eliminated.

- The newly developed certification procedure for HBMs limits the amount of variation allowed for the simulations in the reference load cases to the amount of variation that was observed within the consistent reference simulations (without outliers). The comparability of kinematic-based assessment results was, therefore, drastically improved. While, for example, the head impact times in the initial data set varied by up to 24%, the procedure limits the variation to a maximum of 10.5%. This means that the relative deviation of results was more than halved for this output, which is essential for the Euro NCAP assessment of deployable systems.

- Certification procedures were found to be important prerequisites that enable comparable virtual testing with HBMs for the assessment of VRU protection: Inconsistent pedestrian models, incompatibilities with control settings and user errors can be identified and sorted out. The certified HBMs showed comparable kinematic assessment results in a variety of load cases, including different shapes of passenger cars and different collision speeds.

- The comparability of strain-based assessment results was not investigated in the present research. However, the developed methods can be applied in the future to develop additional certification procedures that cover additional reference anthropometries, scenarios and additional criteria, such as strain-based assessment results.

- In general, the results of the presented research showed that it is feasible to gain comparable, kinematic-based assessment results among different institutions and different HBMs, when those who perform the simulations are guided effectively by a properly defined simulation protocol, and certification procedures are established.

Are Human Body Models useful for kinematic-based assessment of passive VRU safety?

- Further evidence was provided that the interactions between impact structures and the pedestrian are highly complex. The stiffness and geometry of the impact structure both affect the kinematic response. Increasing the vehicle stiffness affected the kinematics and led, depending on the vehicle shape, to higher or lower *HIT*s. At the same time, the results of the analysis of stiffnesses of vehicle fronts indicated a wide spread of results for the current vehicle fleet. This highlights the need for full-body and full-vehicle considerations for kinematic-based assessments with biofidelic HBMs.

- It was shown that Human Body Models are very useful for the assessment of passive VRU safety: Kinematic-based assessment results derived from HBM simulations were both beneficial and appropriate for the assessment of passive VRU safety, as additional meaningful outputs could be gained from the simulations that cannot be evaluated with other assessment methods. More research on the validation of comparable, kinematic-based assessment criteria that result directly from the HBM simulations is needed to enable associations to be made between HBM simulation results and human load limits or specific injury risks.

Are strain-based assessment criteria derived from HBM simulations appropriate for the assessment of passive VRU safety?

- The potential for strain-based assessment was shown: Good correlations between the strain-based assessment results and real-world injuries were observed for some body regions when bicycle accidents were simulated. However, the validation of strain-based assessment criteria for real-world accidents turned out to be highly challenging due to the many unknown boundary conditions. When injury risk curves are developed based on real-world accidents, the uncertainties that arise from small changes in the initial conditions should be considered (e.g. with confidence intervals).

- Strain-based assessment is not currently appropriate for the assessment of passive VRU safety. More work on the harmonisation of strain-based criteria and proof of validity is needed before this assessment can be fully applicable. An open-source, postprocessing tool (DYNASAUR) was established for the analysis of strain-based assessment criteria from HBMs, which should help establish a harmonized, strain-based assessment procedure.

Are Human Body Models appropriate tools for the assessment of passive VRU safety?

- Human Body Models clearly have a big potential for the assessment of VRU safety. More research is needed on the assessment criteria in general to allow for the full assessment with HBMs. In such future assessments, the impactor tests would be only needed for the validation of numeric models for the impact structures. For the time being, Human Body Models are appropriate for combined approaches to gain valuable additional kinematic-based assessment results. Impactors are still needed for the assessment of injury metrics, using the output from the HBM simulations as input for the physical tests.

- The research presented in this thesis addressed some of the challenges of virtual testing with HBMs. Several of these challenges are also relevant for the assessment of occupant protection. The author hopes to inspire researchers to address the remaining challenges and exploit the full potential of the assessment method, aiming to subsequently improve vehicle safety and, finally, save lives.

9 REFERENCES

ACEA (2018), "Average Vehicle Age", available at: https://www.acea.be/statistics/tag/category/average-vehicle-age (accessed 12 August 2018).

Akiyama, A., Okamoto, M. and Rangarajan, N. (2001), "Development and Application of the New Pedestrian Dummy", *The 17th ESV Conference Proceedings, Amsterdam, The Netherlands, 4.-7.6.2001*, NHTSA, pp. 1–12, available at: http://www-nrd.nhtsa.dot.gov/pdf/esv/esv17/proceed/00048.pdf.

Akiyama, A., Yoshida, S., Matsuhashi, T., Rangarajan, N., Shams, T., Ishikawa, H. and Konosu, A. (1999), "Development of Simulation Model and Pedestrian Dummy", *International Congress & Exposition, Detroit, Michigan, 1.-4.3.1999*, SAE International.

Alvarez, V.S. and Kleiven, S. (2016), "Importance of Windscreen Modelling Approach for Head Injury Prediction", *2016 IRCOBI Conference Proceedings, Malaga, Spain, 14.-16.9.2016*, IRCOBI, pp. 813–830, available at: http://www.ircobi.org/wordpress/downloads/irc16/pdf-files/100.pdf.

ANCAP (2018), *Pedestrian Protection v8.4*, 8.4.th ed., available at: https://s3.amazonaws.com/cdn.ancap.com.au/app/public/assets/3e1d2890f2fa101e4a652eef193afd97a57391be/original.pdf?1513577963.

Asanuma, H. and Takahashi, Y. (2015), "Improvement and Validation of the Lower Limb and the Pelvis for a Pedestrian Dummy", *SAE 2015 World Congress & Exhibition, 24.4.2015*, SAE International.

Badea-Romero, A. and Lenard, J. (2013), "Source of head injury for pedestrians and pedal cyclists. Striking vehicle or road?", *Accident; analysis and prevention*, Vol. 50, pp. 1140–1150. doi: 10.1016/j.aap.2012.09.024.

Bakker, J., Jeppson, H., Hannawald, L., Spitzhüttl, F., Longton, A. and Tomasch, E. (2017), "IGLAD - International Harmonized In-Depth Accident Data", *The 25th ESV Conference Proceedings, Michigan, USA, 5.-8.6.2017*, NHTSA, available at: http://indexsmart.mirasmart.com/25esv/PDFfiles/25ESV-000248.pdf.

Barbat, S., Fu, Y., Zhan, Z., Yang, R.-J. and Gehre, C. (2013), "Objective Rating Metric for Dynamic Systems", *The 23rd ESV Conference Proceedings, Seoul, Republic of Korea, 27.-30.5.2013*, NHTSA, pp. 1–10, available at: https://www-esv.nhtsa.dot.gov/Proceedings/23/files/23ESV-000448.PDF.

Barry, F. and Simms, C. (2016), "Assessment of Head-Ground Impact Patterns in Real World Pedestrian-Vehicle Collisions", *2016 IRCOBI Conference Proceedings, Malaga, Spain, 14.-16.9.2016*, IRCOBI, pp. 509–511, available at: http://www.ircobi.org/wordpress/downloads/irc16/pdf-files/70.pdf.

Bastien, C., Orlowski, M. and Bhagwani, M. (2017), "Validation of Finite Element Human Model Throw Distance in Pedestrian Accident Scenarios", paper presented at 11th European LS-DYNA Conference, 9.-11.5.2017, available at: https://www.dynalook.com/11th-european-ls-dyna-conference/pedestrian-safety-head-impact/validation-of-thums-human-model-throw-distance-in-pedestrian-accident-scenarios.

Belytschko, T., Liu, W.K. and Moran, B. (2013), *Nonlinear finite elements for continua and structures*, Second edition. ISBN: 9781306069397.

Bhattacharjee, S.S., Mane, S., Kusnoorkar, H., Hwang, S. and Niesluchowski, M. (2017), "Pedestrian Head Impact Time Estimate based on Vehicle Geometric Parameters", *SAE World Congress Proceedings, Detroit, USA, 4.-6.4.2017*, SAE International.

Bose, D., Bhalla, K., Rooij, L., Millington, S., Studley, A. and Crandall, J. (2004), "Response of the knee joint to the pedestrian impact loading environment", *SAE International*. doi: 10.4271/2004-01-1608.

Bose, D., Bhalla, K.S., Untaroiu, C.D., Ivarsson, B.J., Crandall, J.R. and Hurwitz, S. (2008), "Injury Tolerance and Moment Response of the Knee Joint to Combined Valgus Bending and Shear Loading", *Journal of Biomechanical Engineering*, Vol. 130 No. 3, pp. 1–8. doi: 10.1115/1.2907767.

Bose, D., Subit, D., Ivarsson, B.J., Crandall, J.R., Takahashi, Y., Kikuchi, Y. and Akiyama, A. (2007), "Biofidelity Improvements to the Polar-II Pedestrian Dummy Lower Extremity", *SAE 2007 World Congress Proceedings, 16.4.2007*, SAE International.

Bourdet, N., Deck, C., Carreira, R.P. and Willinger, R. (2012), "Head impact conditions in the case of cyclist falls", *Proceedings of the Institution of Mechanical Engineers, Part P: Journal of Sports Engineering and Technology*, Vol. 226 No. 3-4, pp. 282–289. doi: 10.1177/1754337112442326.

Bourdet, N., Deck, C., Serre, T., Perrin, C., Llari, M. and Willinger, R. (2013), "In-depth real-world bicycle accident reconstructions", *International Journal of Crashworthiness*, Vol. 19 No. 3, pp. 222–232. doi: 10.1080/13588265.2013.805293.

Bourdet, N., Luttenberger, P., Teibinger, A., Mayer, C. and Willinger, R. (2014), "Pedestrian and bicyclists head impact conditions against small electric vehicle", *2014 IRCOBI Conference Proceedings, Berlin, Germany, 10.-12.9.2014*, IRCOBI, pp. 685–696, available at: http://www.ircobi.org/wordpress/downloads/irc14/pdf_files/77.pdf.

Bourdet, N., Mojumder, S., Piantini, S., Deck, C., Pierini, M. and Willinger, R. (2016), "Proposal of a new motorcycle helmet test method for tangential impact", *2016 IRCOBI Conference Proceedings, Malaga, Spain, 14.-16.9.2016*, IRCOBI, pp. 479–489, available at: http://www.ircobi.org/wordpress/downloads/irc16/pdf-files/65.pdf.

Bovenkerk, J. and Zander, O. (2009), *Evaluation of the extended scope for FlexPLI obtained by adding an upper body mass*.

Brun-Cassan, F., Vincent, J.C., Tarriere, C., Fayon, A., Cesari, D., Cavallero, C. and Mauron, G. (1984), "Comparison of Experimental Car-Pedestrian Collisions Performed with Various Modified Side-Impact Dummies and Cadavers", *28th Stapp Car Crash Conference, Chicago, USA, 6.11.1984*, SAE International, available at: http://papers.sae.org/841664/.

Brunner, Horst, Krettek, Christian, Otte, Dietmar, Zwipp and Hans (2003), "Scientific Approach and Methodology of a New In-depth Investigation Study in Germany so called GIDAS", paper presented at International Technical Conference on the Enhanced Safety of Vehicles, 19.-22.5.2003, Nagoya, Japan.

Carter, E.L. and Neal-Sturgess, C.E. (2009), "MADYMO reconstruction of a real-world collision between a vehicle and cyclist", *International Journal of Crashworthiness*, Vol. 14 No. 4, pp. 379–390. doi: 10.1080/13588260902823999.

Cesari, D. (1998), *Pedestrian protection - synthesis of experimental and simulation researches performed in France.*

Chen, H. (2017), "Evaluating Pedestrian Head Sub-system Test Procedure against Full-scale Vehicle-Pedestrian Impact Using Numerical Models", Dissertation, School of Engineering and Applied Science, University of Virginia, Charlottesville, May 2017.

Chen, H., Poulard, D., Crandall, J.R. and Panzer, M.B. (2015a), "Pedestrian Response with Different Initial Positions During Impact with a Mid-Sized Sedan", *The 24th ESV Conference Proceedings, Gothenburg, Sweden, 8.-11.6.2015*, NHTSA, pp. 1–12, available at: https://www-esv.nhtsa.dot.gov/proceedings/24/files/24ESV-000391.PDF.

Chen, H., Poulard, D., Forman, J., Crandall, J. and Panzer, M.B. (2018), "Evaluation of geometrically personalized THUMS pedestrian model response against sedan-pedestrian PMHS impact test data", *Traffic injury prevention*, pp. 1–7. doi: 10.1080/15389588.2018.1450979.

Chen, Q., Lin, M., Dai, B. and Chen, J. (2015b), "Typical Pedestrian Accident Scenarios in China and Crash Severity Mitigation by Autonomous Emergency Braking Systems", *SAE 2015 World Congress Proceedings, 24.4.2015*, SAE International.

Coley, G., Lange, R. de, Oliveira, P. de, Neal-Sturgess, C.E. and Happee, R. (2001), "Pedestrian human body validation using detailed real-world accidents", *2001 IRCOBI Conference Proceedings, Isle of Man, UK, 10.-12.10.2001*, IRCOBI, available at: http://www.ircobi.org/wordpress/downloads/irc0111/2001/Session2/2.2.pdf.

Combest, J.C. (2016), "Current status and future plans of the GHBMC (Global Human Body Models Consortium)", paper presented at 6th International Symposium: Human Modeling and Simulation in Automotive Engineering, 20.10.-21.10.2016, Heidelberg, Germany.

Coulongeat, F., Roth, F., Schenk, T. and Seibert, D. (2014), "Simulation of a real accident with a pedestrian using a FE human model: potential from the view of Integrated Safety", *2014 IRCOBI Conference Proceedings, Berlin, Germany, 10.-12.9.2014*, IRCOBI, pp. 712–713, available at: http://www.ircobi.org/wordpress/downloads/irc14/pdf_files/79.pdf.

Courant, R., Friedrichs, K. and Lewy, H. (1967), "On the Partial Difference Equations of Mathematical Physics", *IBM Journal of Research and Development*, Vol. 11 No. 2, pp. 215–234. doi: 10.1147/rd.112.0215.

Crandall, J., Wiley, K., Longhitano, D. and Akiyama, A. (2005), "Development of performance specifications for a pedestrian research dummy", *The 19th ESV Conference Proceedings, Washington, D.C., USA, 6.-9.6.2005*, NHTSA.

Crandall, J.R. (1994), "The preservation of human surrogates for biomechanical studies", PhD Thesis, Department of Mechanical and Aerospace Engineering, University of Virginia, Virginia, USA, 1994.

Crandall, J.R., Bose, D., Forman, J., Untaroiu, C.D., Arregui-Dalmases, C., Shaw, C.G. and Kerrigan, J.R. (2011), "Human surrogates for injury biomechanics research", *Clinical anatomy (New York, N.Y.)*, Vol. 24 No. 3, pp. 362–371. doi: 10.1002/ca.21152.

Crandall, J.R., Lessley, D.J., Kerrigan, J.R. and Ivarsson, B.J. (2006), "Thoracic deformation response of pedestrians resulting from vehicle impact", *International Journal of Crashworthiness*, Vol. 11 No. 6, pp. 529–539. doi: 10.1533/ijcr.2006.0146.

Crisfield, M.A. and Borst, R.d. (2012), *Non-linear finite element analysis of solids and structures, Wiley series in computational mechanics,* 2nd ed., Wiley, Chichester, West Sussex, U.K.

Crocetta, G., Piantini, S., Pierini, M. and Simms, C. (2015), "The influence of vehicle front-end design on pedestrian ground impact", *Accident Analysis & Prevention*, Vol. 79, pp. 56–69. doi: 10.1016/j.aap.2015.03.009.

Cronin, D.S. (2011), "Explicit Finite Element Method Applied to Impact Biomechanics Problems", *2011 IRCOBI Conference Proceedings, Krakow (Poland), 14.-16.9.2011*, IRCOBI, pp. 240–254, available at: http://www.ircobi.org/wordpress/downloads/irc0111/2011/KeynoteLecture/2.pdf.

Davis, M.L., Allen, B.C., Geer, C.P., Stitzel, J.D. and Gayzik, F.S. (2014), "A Multi-Modality Image Set for the Development of a 5th Percentile Female Finite Element Model", *2014 IRCOBI Conference Proceedings, Berlin, Germany, 10.-12.9.2014*, IRCOBI, pp. 461–475, available at: http://www.ircobi.org/wordpress/downloads/irc14/pdf_files/54.pdf.

Deck, C., Bourdet, N., Halldin, P., DeBruyne, G. and Willinger, R. (2017), "Protection capability of bicycle helmets under oblique impact assessed with two separate brain FE models", *2017 IRCOBI Conference Proceedings, Antwerp, Brussels, 13.-15.9.2017*, IRCOBI, pp. 190–200, available at: http://www.ircobi.org/wordpress/downloads/irc17/pdf-files/32.pdf.

del Pozo de Dios, E., Ferrer, A., Hill, J., Fagerlind, H., Giustiniani, G. and Persia, L. (2013), "Towards a Global and Harmonized Database for In–Depth Accident Investigation in Europe: The Dacota Project", *The 23rd ESV Conference Proceedings, Seoul, Republic of Korea, 27.-30.5.2013*, NHTSA, pp. 1–9, available at: https://www-esv.nhtsa.dot.gov/Proceedings/23/isv7/main.htm.

Demetropoulos, C.K., Yang, K.H., Grimm, M.J., Khalil, T.B. and King, A.I. (1998), "Mechanical Properties of the Cadaveric and Hybrid III Lumbar Spines", *42nd Stapp Car Crash Conference Proceedings, Tempa, AZ, 02.-04.11.*, SAE International.

Department of Transport (2013), "Road accident in-depth studies (RAIDS)", available at: https://www.gov.uk/government/publications/road-accident-investigation-road-accident-in-depth-studies/road-accident-in-depth-studies-raids#further-information (accessed 13 August 2018).

Depriester, J.P., Perrin, C., Serre, T. and Chalandon, S. (2005), "Comparison of Several Methods for Real Pedestrian Accident Reconstruction", *The 19th ESV Conference Proceedings, Washington, D.C., USA, 6.-9.6.2005*, NHTSA, pp. 1–14, available at: https://www-esv.nhtsa.dot.gov/Proceedings/19/05-0333-O.pdf.

Detwiller, M. and Gabler, H.C. (2017), "Potential Reduction in Pedestrian Collisions with an Autonomous Vehicle", *The 25th ESV Conference Proceedings, Michigan, USA, 5.-8.6.2017*, NHTSA, pp. 1–8, available at: https://www-esv.nhtsa.dot.gov/Proceedings/25/25ESV-000404.pdf.

Edwards, M., Nathanson, A., Carroll, J., Wisch, M., Zander, O. and Lubbe, N. (2015), "Assessment of Integrated Pedestrian Protection Systems with Autonomous Emergency Braking (AEB) and Passive Safety Components", *Traffic injury prevention*, 16 Suppl 1, S2-S11. doi: 10.1080/15389588.2014.1003154.

Eggers, A., Schwedhelm, H., Zander, O., Puppini, R., Puleo, G., Mayer, C., Kumar, N., Jacob, C. and Beaugonin, M. (2012), *Analysis of new simulation technologies for pedestrian safety. Potential of VT to fully substitute RT for this purpose: imviter D6.1, imviter*.

Elliott, J., Lyons, M., Kerrigan, J., Wood, D. and Simms, C. (2012a), "Predictive capabilities of the MADYMO multibody pedestrian model. Three-dimensional head translation and rotation, head impact time and head impact velocity", *Proceedings of the Institution of Mechanical Engineers, Part K: Journal of Multi-body Dynamics*, Vol. 226 No. 3, pp. 266–277. doi: 10.1177/1464419311430176.

Elliott, J.R., Simms, C.K. and Wood, D.P. (2012b), "Pedestrian head translation, rotation and impact velocity. The influence of vehicle speed, pedestrian speed and pedestrian gait", *Accident Analysis & Prevention*, Vol. 45 No. 0, pp. 342–353. doi: 10.1016/j.aap.2011.07.022.

Erhart, T. (2011), "Review of Solid Element Formulations in LS-DYNA Properties, Limits, Advantages, Disadvantages", *LS-DYNA Forum 2011, Stuttgart, Germany, 12.10.2011*, DYNAmore, available at: https://www.dynamore.de/de/download/papers/forum11/entwicklerforum-2011/erhart.pdf.

ERTRAC Working Group on Road Transport Safety and Security (2011), *European Roadmap Safe Road Transport*.

Euro NCAP (2000), "Official Skoda Fabia 2000 safety rating", available at: https://www.euroncap.com/en/results/skoda/fabia/15528 (accessed 1 September 2018).

Euro NCAP (2007), "Official Mazda 2 2007 safety rating", available at: https://www.euroncap.com/en/results/mazda/2/15729 (accessed 22 October 2018).

Euro NCAP (2015a), *AEB VRU systems*, 1.0.1st ed.

Euro NCAP (2015b), *Pedestrian CAE Models & Codes* No. 13, 1.5th ed., available at: http://euroncap.blob.core.windows.net/media/21510/tb-013-pedestrian-cae-models-v15.pdf.

Euro NCAP (2016), *Euro NCAP Pedestrian Testing Protocol* No. 8.3, available at: http://euroncap.blob.core.windows.net/media/25840/euro-ncap-pedestrian-testing-protocol-v83-december-2016.pdf (accessed 22 February 2017).

Euro NCAP (2017a), *Euro NCAP Pedestrian Testing Protocol* No. 8.4, available at: https://cdn.euroncap.com/media/32288/euro-ncap-pedestrian-testing-protocol-v84.pdf (accessed 4 June 2018).

Euro NCAP (2017b), *Pedestrian Human Model Certification* No. 024, v1.01, available at: https://cdn.euroncap.com/media/34544/tb-024-pedestrian-human-model-certification-v101.pdf.

Euro NCAP (2018), "Timeline", available at: https://www.euroncap.com/en/about-euro-ncap/timeline/ (accessed 12 August 2018).

European Commission (2016), "Statistics – accidents data - Mobility and transport - European Commission", available at: https://ec.europa.eu/transport/road_safety/specialist/statistics_en# (accessed 26 June 2018).

Fahlstedt, M., Baeck, K., Halldin, P., Vander Sloten, J., Goffin, J., Depreitere, B. and Kleiven, S. (2012), "Influence of Impact Velocity and Angle in a Detailed Reconstruction of a Bicycle

Accident", *2012 IRCOBI Conference Proceedings, Dublin, Ireland, 12.-14.09.2012*, IRCOBI, pp. 787–799, available at: http://www.ircobi.org/wordpress/downloads/irc12/pdf_files/84.pdf.

Fahlstedt, M., Depreitere, B., Halldin, P., Vander Sloten, J. and Kleiven, S. (2015), "Correlation between Injury Pattern and Finite Element Analysis in Biomechanical Reconstructions of Traumatic Brain Injuries", *Journal of Biomechanics*, Vol. 48 No. 7, pp. 1331–1335. doi: 10.1016/j.jbiomech.2015.02.057.

Fahlstedt, M., Halldin, P. and Kleiven, S. (2016a), "Comparison of multibody and finite element human body models in pedestrian accidents with the focus on head kinematics", *Traffic injury prevention*, Vol. 17 No. 3, pp. 320–327. doi: 10.1080/15389588.2015.1067803.

Fahlstedt, M., Halldin, P. and Kleiven, S. (2016b), "The protective effect of a helmet in three bicycle accidents—A finite element study", *Accident Analysis & Prevention*, pp. 135–143. doi: 10.1016/j.aap.2016.02.025.

Feist, F. (2016), *Generic Parameterisable Vehicle Model: 3rd Generation of GV Models*.

Feist, F., Gugler, J., Arregui-Dalmases, C., del Pozo de Dios, E., López-Valdés, F., Deck, C. and Willinger, R. (2009), "Pedestrian Collisions with Flat-Fronted Vehicles: Injury Patterns and Importance of Rotational Accelerations as A Predictor for Traumatic Brain Injury (TBI)", *The 21st ESV Conference Proceedings, Stuttgart, Germany, 15.-18.6.2009*, NHTSA.

Feist, F. and Klug, C. (2016), "A Numerical Study on the Influence of the Upper Body and Neck on Head Kinematics in Tangential Bicycle Helmet Impact", *2016 IRCOBI Conference Proceedings, Malaga, Spain, 14.-16.9.2016*, IRCOBI, pp. 162–184, available at: http://www.ircobi.org/wordpress/downloads/irc16/pdf-files/28.pdf.

Feist, F. and Klug, C. (2017), "Verletzungen des Beckens und der Oberschenkel in Fußgängerunfällen mit PKWs", paper presented at Safety Update, 26.-27.9.2017, Graz.

Ferenczi, I., Helmer, T., Wimmer, P. and Kates, R. (2015), "Recent Advances in Effectiveness Analysis and Virtual Design of Integrated Safety Systems", *The 24th ESV Conference Proceedings, Gothenburg, Sweden, 8.-11.6.2015*, NHTSA, pp. 1–11, available at: https://www-esv.nhtsa.dot.gov/Proceedings/24/isv7/main.htm.

Forman, J., Joodaki, H., Forghani, A., O Riley, P., Bollapragada, V., Lessley, D., Overby, B., Heltzel, S. and Crandall, J. (2015a), "Biofidelity Corridors for Whole-Body Pedestrian Impact with a Generic Buck", *2015 IRCOBI Conference Proceedings, Lyon, France, 9.-11.9.2015*, IRCOBI, pp. 356–372, available at: http://www.ircobi.org/wordpress/downloads/irc15/pdf_files/49.pdf.

Forman, J.L., Joodaki, H., Forghani, A., Riley, P.O., Bollapragada, V., Lessley, D.J., Overby, B., Heltzel, S., Kerrigan, J.R., Crandall, J.R., Yarboro, S. and Weiss, D.B. (2015b), "Whole-body Response for Pedestrian Impact with a Generic Sedan Buck", *Stapp Car Crash Journal*, Vol. 59, pp. 401–444.

Forman, J.L., Kent, R.W., Mroz, K., Pipkorn, B., Bostrom, O. and Segui-Gomez, M. (2012), "Predicting Rib Fracture Risk with Whole-Body Finite Element Models: Development and Preliminary Evaluation of a Probabilistic Analytical Framework", *Annals of Advances in Automotive Medicine*, Vol. 56, pp. 109–124.

Fredriksson, R., Dahlgren, M., van Schijndel, M., Hair, S. de and van Montfort, S. (2014), "A real-life based evaluation method of deployable vulnerable road user protection systems", *Traffic injury prevention*, 15 Suppl 1, S183-9. doi: 10.1080/15389588.2014.928930.

Fredriksson, R. and Rosen, E. (2012), "Priorities for Bicyclist Protection in Car Impacts—a Real life Study of Severe Injuries and Car Sources", *2012 IRCOBI Conference Proceedings, Dublin, Ireland, 12.-14.09.2012*, IRCOBI, pp. 779–786, available at: http://www.ircobi.org/downloads/irc12/pdf_files/83.pdf.

Fredriksson, R., Shin, J. and Untaroiu, C.D. (2011), "Potential of pedestrian protection systems - a parameter study using finite element models of pedestrian dummy and generic passenger vehicles", *Traffic injury prevention*, Vol. 12 No. 4, pp. 398–411. doi: 10.1080/15389588.2011.566655.

Fredriksson, R. and Sui, B. (2015), "Fatal Powered Two-Wheeler (PTW) crashes in Germany – an in-depth study of the events, injuries and injury sources", *2015 IRCOBI Conference Proceedings, Lyon, France, 9.-11.9.2015*, IRCOBI, available at: http://www.ircobi.org/wordpress/downloads/irc15/pdf_files/12.pdf.

Fuchs, T., Fressmann, D., Mayer, C., Pipkorn, B., Segura, R., Weber, J., Yasuki, T. and Peldschus, S. (2014), "Challenges in Using a Finite Element Human Body Model in Different Crash Codes", *2014 IRCOBI Conference Proceedings, Berlin, Germany, 10.-12.9.2014*, IRCOBI, pp. 1–2, available at: http://www.ircobi.org/wordpress/downloads/irc14/pdf_files/59.pdf.

Fuchs, T. and Peldschus, S. (2016), "Towards a More Standardized Application of Human Body Models", paper presented at 6th International Symposium: Human Modeling and Simulation in Automotive Engineering, 20.10.-21.10.2016, Heidelberg, Germany.

Fuchs, T. and Peldschus, S. (2017), "Qualifying FE Human Body Models for Specific Load Cases: Assessing Uncertainties during the Validation Proces", *2017 IRCOBI Conference Proceedings, Antwerp, Belgium, 13.-15.9.2017*, IRCOBI, pp. 531–532, available at: http://www.ircobi.org/wordpress/downloads/irc17/pdf-files/65.pdf.

Funk, J.R., Kerrigan, J.R. and Crandall, J.R. (2004), "Dynamic Bending Tolerance and Elastic-Plastic Material Properties of the Human Femur", *Annu Proc Assoc Adv Automot Med*, Vol. 48, pp. 215–233.

García, J., Bueno, P., Seibert, D., Narbona, A. and Cordero, R. (2012), *D 4.3. Conclusions/Recommendations for VT in homologation/regulation procedures, Deliverable*.

Gayzik, F.S., Moreno, D.P., Geer, C.P., Wuertzer, S.D., Martin, R.S. and Stitzel, J.D. (2011), "Development of a full body CAD dataset for computational modeling. A multi-modality approach", *Annals of biomedical engineering*, Vol. 39 No. 10, pp. 2568–2583. doi: 10.1007/s10439-011-0359-5.

Gehre, C., Gades, H. and Wernicke, P. (2009), "Objective Rating of Signals Using Test and Simulation Responses", *The 21st ESV Conference Proceedings, Stuttgart, Germany, 15.-18.6.2009*, NHTSA, pp. 1–8, available at: https://www-esv.nhtsa.dot.gov/Proceedings/21/09-0407.pdf.

GHBMC (2016), "Global Human Body Models Consortium", available at: https://www.ghbmc.com/ (accessed 17 August 2018).

Ghosh, P., Mayer, C., Deck, C., Bourdet, N., Meyer, F., Willinger, R., Bensler, H. and Weber, J. (2016), "Head Injury Risk Assessment in Pedestrian Impacts on Small Electric Vehicles using Coupled SUFEHM-THUMS Human Body Models Running in Different Crash Codes", *2016 IRCOBI Conference Proceedings, Malaga, Spain, 14.-16.9.2016*, IRCOBI, pp. 490–502, available at: http://www.ircobi.org/wordpress/downloads/irc16/pdf-files/66.pdf.

Giordano, C., Li, X. and Kleiven, S. (2017), "Performances of the PIPER scalable child human body model in accident reconstruction", *PloS one*, Vol. 12 No. 11, e0187916. doi: 10.1371/journal.pone.0187916.

Golman, A.J., Danelson, K.A., Gaewsky, J.P. and Stitzel, J.D. (2015), "Implementation and validation of thoracic side impact injury prediction metrics in a human body model", *Computer methods in biomechanics and biomedical engineering*, Vol. 18 No. 10, pp. 1044–1055. doi: 10.1080/10255842.2013.869319.

Golman, A.J., Danelson, K.A., Miller, L.E. and Stitzel, J.D. (2014), "Injury prediction in a side impact crash using human body model simulation", *Accident Analysis & Prevention*, Vol. 64, pp. 1–8. doi: 10.1016/j.aap.2013.10.026.

Gross, D., Ehlers, W. and Wriggers, P. (2005), *Formeln und Aufgaben zur Technischen Mechanik 3: Kinetik, Hydrodynamik, Springer-Lehrbuch*, 7., aktualisierte Aufl., Springer, Berlin. ISBN: 3-540-24025-X.

Guillemot, H., Got, C., Besnault, B., Le Coz, Y, J., Robin, S., Lavaste, F. and Lassau, J. (1997), "Pelvic injuries in side impact collisions: a field accident analysis and dynamic tests on isolated pelvic bones", *41st Stapp Car Crash Conference Proceedings, Lake Buena Vista, Florida, USA, 13.-14.11.*, SAE International.

Hackl, W., Hausberger, K., Sailer, R., Ulmer, H. and Gassner, R. (2001), "Prevalence of cervical spine injuries in patients with facial trauma", *Oral surgery, oral medicine, oral pathology, oral radiology, and endodontics*, Vol. 92 No. 4, pp. 370–376. doi: 10.1067/moe.2001.116894.

Hainisch, T. (2015), "Erstellung von FE Fahrradmodellen zum Abbilden unterschiedlicher Rahmen-Geometrien und -Größen für Crashsimulationen", Bachelorarbeit, Institut für Fahrzeugsicherheit, TU Graz, Graz, 18 June.

Hamdane, H., Serre, T., Masson, C. and Anderson, R. (2015), "Issues and challenges for pedestrian active safety systems based on real world accidents", *Accident Analysis & Prevention*, Vol. 82, pp. 53–60. doi: 10.1016/j.aap.2015.05.014.

Hammad, A., Kalra, A., Khandelwal, P., Jin, X. and Yang, K.H. (2017), "Development of Upper Extremity Finite Element Model for Elderly Female. Validated Against Dynamic Loading Conditions", *Proceedings of the ASME International Mechanical Engineering Congress and Exposition - 2017, Tampa, Florida, USA, 3.11.2017*, The American Society of Mechanical Engineers, New York, N.Y., V012T16A006.

Han, Y., Li, Q., He, W., Wan, F., Wamg, B. and Mizuno, K. (2017), "Analysis of Vulnerable Road User Kinematics Before/During/After Vehicle Collisions Based on Video Records", *2017 IRCOBI Conference Proceedings, Antwerp, Brussels, 13.-15.9.2017*, IRCOBI, pp. 151–165, available at: http://www.ircobi.org/wordpress/downloads/irc17/pdf-files/26.pdf.

Han, Y., Li, Q., Wang, F., Wang, B., Mizuno, K. and Zhou, Q. (2018), "Analysis of pedestrian kinematics and ground impact in traffic accidents using video records", *International Journal of Crashworthiness*, Vol. 1 No. 2, pp. 1–10. doi: 10.1080/13588265.2018.1429520.

Hansen, K., Dau, N., Feist, F., Deck, C., Willinger, R., Madey, S.M. and Bottlang, M. (2013), "Angular Impact Mitigation system for bicycle helmets to reduce head acceleration and risk of traumatic brain injury", *Accident Analysis & Prevention*, Vol. 59, pp. 109–117. doi: 10.1016/j.aap.2013.05.019.

Hardy, R. (2009), *APROSYS - Final report for the work on "Pedestrian and Pedal Cyclist Accidents" (SP3)*.

Hardy, W.N., Foster, C.D., Mason, M.J., Yang, K.H., King, A.I. and Tashman, S. (2001), "Investigation of Head Injury Mechanisms Using Neutral Density Technology and High-Speed Biplanar X-ray", *Stapp Car Crash Journal*, Vol. 45, pp. 337–368.

Hering, A.M. and Derler, S. (2000), "Motorcycle helmet drop tests using a Hybrid III dummy", *2000 IRCOBI Conference Proceedings, Montpellier (France), 20.-22.9.2000*, IRCOBI, pp. 307–321, available at: http://www.ircobi.org/wordpress/downloads/irc2000/pdf_files/2000_23.pdf.

Huang, J., Long, Y., Yan, Y. and Hu, L. (2018a), "Development and Validation of an Age-Specific Lower Extremity Finite Element Model for Simulating Pedestrian Accidents", *Applied bionics and biomechanics*, Vol. 2018, p. 5906987. doi: 10.1155/2018/5906987.

Huang, J., Peng, Y., Yang, J., Otte, D. and Wang, B. (2018b), "A study on correlation of pedestrian head injuries with physical parameters using in-depth traffic accident data and mathematical models", *Accident Analysis & Prevention*, Vol. 119, pp. 91–103. doi: 10.1016/j.aap.2018.07.012.

Hummel, T., Kühn, M., Bende, J. and Lang, A. (2011), *Advanced Driver Assistance Systems: An investigation of their potential safety benefits based on an analysis of insurance claims in Germany*, Forschungsbericht / Gesamtverband der Deutschen Versicherungswirtschaft e.V FS, Fahrzeugsicherheit / Unfallforschung der Versicherer, Vol. 03, GDV, Berlin. ISBN: 978-3-939163-37-4.

Hutchinson, T.P., Anderson, R.W.G. and Searson, D.J. (2012), "Pedestrian headform testing. Inferring performance at impact speeds and for headform masses not tested, and estimating average performance in a range of real-world conditions", *Traffic injury prevention*, Vol. 13 No. 4, pp. 402–411. doi: 10.1080/15389588.2012.660252.

Hynčík, L., Bońkowski, T. and Vychytil, J. (2017), "Virtual hybrid human body model for PTW safety assessment", *Applied and Computational Mechanics*, Vol. 11 No. 2. doi: 10.24132/acm.2017.389.

Ishikawa, H., Kajzer, J. and Schroeder, G. (1993), "Computer Simulation of Impact Response of the Human Body in Car-Pedestrian Accidents", *37th Stapp Car Crash Conference Proceedings, San Antonio, TX, 7.-8.11.1993*, SAE International.

Isshiki, T., Antona-Makoshi, J. and Konosu, A. (2017), "Optimal specifications for the Advanced Pedestrian Legform Impactor", *Stapp Car Crash Journal*, Vol. 61, pp. 1–24.

Isshiki, T., Antona-Makoshi, J., Konosu, A. and Takahashi, Y. (2018), "Simplifying the Structural Design of the Advanced Pedestrian Legform Impactor for Use in Standardized Testing", *SAE World Congress Proceedings, 10.4.2018*, SAE International.

Isshiki, T., Konosu, A. and Takahashi, Y. (2014), "Development of an Appropriate Pedestrian Legform Impact Test Method which can be used for all Types of Vehicles including High

Bumper Vehicles. Development of a Simplified Upper Body Part (SUBP) FE Model", *2014 IRCOBI Conference Proceedings, Berlin, Germany, 10.-12.9.2014*, IRCOBI, pp. 759–784, available at: http://www.ircobi.org/wordpress/downloads/irc14/pdf_files/85.pdf.

Isshiki, T., Konosu, A. and Takahashi, Y. (2016a), "Development and Evaluation of the Advanced Pedestrian Legform Impactor Prototype which can be Applicable to All Types of Vehicles Regardless of Bumper Height - Part 1: Finite Element Model", *2016 IRCOBI Conference Proceedings, Malaga, Spain, 14.-16.9.2016*, IRCOBI, pp. 770–785, available at: http://www.ircobi.org/wordpress/downloads/irc16/pdf-files/98a.pdf.

Isshiki, T., Konosu, A. and Takahashi, Y. (2016b), "Development and Evaluation of the Advanced Pedestrian Legform Impactor Prototype which can be Applicable to All Types of Vehicles Regardless of Bumper Height -Part 2: Actual Test Tool", *2016 IRCOBI Conference Proceedings, Malaga, Spain, 14.-16.9.2016*, IRCOBI, pp. 786–799, available at: http://www.ircobi.org/wordpress/downloads/irc16/pdf-files/98b.pdf.

Ito, D., Yamada, H., Oida, K. and Mizuno, K. (2014), "Finite element analysis of kinematic behavior of cyclist and performance of cyclist helmet for human head injury in vehicle-to-cyclist collision", *2014 IRCOBI Conference Proceedings, Berlin, Germany, 10.-12.9.2014*, IRCOBI, pp. 119–131, available at: http://www.ircobi.org/wordpress/downloads/irc14/pdf_files/21.pdf.

Iwamoto, M. and Nakahira, Y. (2014), "A Preliminary Study to Investigate Muscular Effects for Pedestrian Kinematics and Injuries Using Active THUMS", *2014 IRCOBI Conference Proceedings, Berlin, Germany, 10.-12.9.2014*, IRCOBI, pp. 444–460, available at: http://www.ircobi.org/wordpress/downloads/irc14/pdf_files/53.pdf.

Ji, S. and Zhao, W. (2015), "A Pre-computed Brain Response Atlas for Instantaneous Strain Estimation in Contact Sports", *Annals of biomedical engineering*, Vol. 43 No. 8, pp. 1877–1895. doi: 10.1007/s10439-014-1193-3.

John O. Hallquist (2006), *LS-DYNA Theory Manual*.

Jolivet, E., Petit, P., Janak, T., Lemaire, T., Peres, J., Chhabra, A., Paruchuri, S., Singh, S., Faure, F., Chawla, A. and Beillas, P. (2014), "PIPER: Open source software to position and personalize Human Body models for crash applications", *5th International Symposium: Human Modeling and Simulation in Automotive Engineering, Munich, Germany, 16.-17.10.2014*, carhs.

JSOL Corporation (2018), "THUMS", available at: https://cae.jsol.co.jp/en/product/structure/thums/feature/ (accessed 17 August 2018).

Kajzer, J., Schroeder, G., Ishikawa, H., Matsui, Y. and Bosch, U. (1997), "Shearing and Bending Effects at the Knee Joint at High Speed Lateral Loading", *41st Stapp Car Crash Conference Proceedings, Lake Buena Vista, Florida, USA, 13.-14.11.*, SAE International.

Kam, C.Y., Kerrigan, J., Meissner, M., Drinkwater, C., Murphy, D., Bolton, J., Arregui, C., Kendall, R., Ivarsson, J., Crandall, J., Deng, B., Wang, J.T., Kerkeling, C. and Hahn, W. (2005), "Design of a Full-Scale Impact System for Analysis of Vehicle Pedestrian Collisions", *SAE 2005 World Congress & Exhibition, Detroit, USA, 11.4.2005*, SAE International.

Katsuhara, T., Miyazaki, H., Kitagawa, Y. and Yasuki, T. (2014), "Impact Kinematics of Cyclist and Head Injury Mechanism in Car-to-Bicycle Collision", *2014 IRCOBI Conference Proceedings,*

Berlin, Germany, 10.-12.9.2014, IRCOBI, pp. 670–685, available at: http://www.ircobi.org/wordpress/downloads/irc14/pdf_files/76.pdf.

Kerrigan, J., Arregui, C. and Crandall, J. (2009a), "Pedestrian Head Impact Dynamics: Comparison of Dummy and PMHS in Small Sedan and large SUV Impacts", *The 21st ESV Conference Proceedings, Stuttgart, Germany, 15.-18.6.2009*, NHTSA, pp. 1–15, available at: http://www-nrd.nhtsa.dot.gov/pdf/esv/esv21/09-0127.pdf.

Kerrigan, J., Arregui-Dalmases, C. and Crandall, J. (2012a), "Assessment of pedestrian head impact dynamics in small sedan and large SUV collisions", *International Journal of Crashworthiness*, Vol. 17 No. 3, pp. 243–258. doi: 10.1080/13588265.2011.648517.

Kerrigan, J., Kam, C., Drinkwater, C., Murphy, D., Bose, D., Ivarsson, J. and Crandall, J. (2005a), "Kinematic comparison of the POLAR-II and PMHS in pedestrian impact tests with a sport-utility vehicle", *2005 IRCOBI Conference Proceedings, Prague, Czech Republic, 21.-23.9. 2005*, IRCOBI, pp. 159–174, available at: http://www.ircobi.org/wordpress/downloads/irc0111/2005/Session3/31.pdf.

Kerrigan, J., Subit, D., Untaroiu, C., Crandall, J. and Rudd, R. (2009b), "Pedestrian Lower Extremity Response and Injury. A Small Sedan vs. A Large Sport Utility Vehicle", *SAE International Journal of Passenger Cars - Mechanical Systems*, Vol. 1 No. 1, pp. 985–1002. doi: 10.4271/2008-01-1245.

Kerrigan, J.R., Arregui-Dalmases, C., Foster, J., Crandall, J.R. and Rizzo, A. (2012b), "Pedestrian Injury Analysis: Field Data vs. Laboratory Experiments", *2012 IRCOBI Conference Proceedings, Dublin, Ireland, 12.-14.09.2012*, IRCOBI, pp. 672–689, available at: http://www.ircobi.org/wordpress/downloads/irc12/pdf_files/75.pdf.

Kerrigan, J.R., Crandall, J.R. and Deng, B. (2007), "Pedestrian kinematic response to mid-sized vehicle impact", *International Journal of Vehicle Safety*, Vol. 2 No. 3, pp. 221–240. doi: 10.1504/IJVS.2007.015541.

Kerrigan, J.R., Crandall, J.R. and Deng, B. (2008), "A comparative analysis of the pedestrian injury risk predicted by mechanical impactors and post mortem human surrogates", *Stapp Car Crash Journal*, Vol. 52, pp. 527–567.

Kerrigan, J.R., Murphy, D., Drinkwater, D.C., Kam, C., Bose, D. and Crandall, J.R. (2005b), "Kinematic corridors for PMHS tested in full-scale pedestrian impact tests", *The 19th ESV Conference Proceedings, Washington, D.C., USA, 6.-9.6.2005*, NHTSA, pp. 1–18.

Khandelwal, P., Kalra, A., Jiang, B., Hammad, A., Jin, X. and Yang, K.H. (2017), "Development and Validation of a Finite Element Lower Limb Model for Elderly Females", *Proceedings of the ASME International Mechanical Engineering Congress and Exposition - 2017, Tampa, Florida, USA, 3.11.2017*, The American Society of Mechanical Engineers, New York, N.Y., V012T16A007.

Kimpara, H. and Iwamoto, M. (2012), "Mild traumatic brain injury predictors based on angular accelerations during impacts", *Annals of biomedical engineering*, Vol. 40 No. 1, pp. 114–126. doi: 10.1007/s10439-011-0414-2.

Kimpara, H., Nakahira, Y., Iwamoto, M., Miki, K., Ichihara, K., Kawano, S. and Taguchi, T. (2006), "Investigation of anteroposterior head-neck responses during severe frontal impacts using a brain-spinal cord complex FE model", *Stapp Car Crash Journal*, Vol. 50, pp. 509–544.

Kitagawa, Y. and Yasuki, T. (2014), "Development and Application of THUMS Version 4", *5th International Symposium: Human Modeling and Simulation in Automotive Engineering, Munich, Germany, 16.-17.10.2014*, carhs.

Kleiven, S. and Hardy, W.N. (2002), "Correlation of an FE Model of the Human Head with Local Brain Motion--Consequences for Injury Prediction", *Stapp Car Crash Journal*, Vol. 46, pp. 123–144.

Klug, C., Feist, F., Raffler, M., Sinz, W., Petit, P., Ellway, J. and van Ratingen, M. (2017), "Development of a Procedure to Compare Kinematics of Human Body Models for Pedestrian Simulations", *2017 IRCOBI Conference Proceedings, Antwerp, Belgium, 13.-15.9.2017*, IRCOBI, pp. 509–530, available at: http://www.ircobi.org/wordpress/downloads/irc17/pdf-files/64.pdf.

Klug, C., Feist, F., Raffler, M., Sinz, W. and van Ratingen, M. (2016), "Methodology for kinematic comparison of human body models for pedestrian simulations", paper presented at 6th International Symposium: Human Modeling and Simulation in Automotive Engineering, 20.10.-21.10.2016, Heidelberg, Germany.

Klug, C., Feist, F., Sinz, W., Ellway, J. and van Ratingen, M. (2018a), "A procedure to compare kinematics of Human Body Models for pedestrian assessments", paper presented at SAE Government Industry Meeting 2018, 24.-26.1.2018, Washington, D.C., USA.

Klug, C., Feist, F. and Tomasch, E. (2015a), "Testing of bicycle helmets for preadolescents", *2015 IRCOBI Conference Proceedings, Lyon, France, 9.-11.9.2015*, IRCOBI, pp. 136–155, available at: http://www.ircobi.org/wordpress/downloads/irc15/pdf_files/24.pdf.

Klug, C., Feist, F. and Wimmer, P. (2018b), "Simulation of a Selected Real World Car to Bicyclist Accident using a Detailed Human Body Model", *2018 IRCOBI Conference Proceedings, Athens, Greece, 12.-14.9.2018*, IRCOBI, pp. 182–183, available at: http://www.ircobi.org/wordpress/downloads/irc18/pdf-files/27.pdf.

Klug, C., Luttenberger, P., Schachner, M., Micorek, J., Greimel, R. and Sinz, W. (2018c), "Postprocessing of Human Body Model Results – Introduction of the Open Source Tool DYNASAUR", paper presented at 7th International Symposium: Human Modeling and Simulation in Automotive Engineering, 18.-19.10.2018, Berlin, Germany.

Klug, C., Weinberger, M., Tomasch, E., Feist, F., Sinz, W., Steffan, H., Kinsky, T., Roth, F., Praxl, N. and Buenger, B. (2015b), "Pelvic and femoral injuries in car-to-pedestrian accidents", *2015 IRCOBI Conference Proceedings, Lyon, France, 9.-11.9.2015*, IRCOBI, pp. 49–63, available at: http://www.ircobi.org/wordpress/downloads/irc15/pdf_files/15.pdf.

Kühn, M., Fröming, R. and Schindler, V. (2006), *Fußgängerschutz: Unfallgeschehen, Fahrzeuggestaltung, Testverfahren*, Springer. ISBN: 978-3-540-34302-8.

Kunitomi, S., Yamamoto, Y., Kato, R., Antona-Makoshi, J., Konosu, A., Dokko, Y. and Yasuki, T. (2017), "The Development of the Lower Extremity of a Human FE Model and the Influence of Anatomical Detailed Modelling in Vehicle-to-Pedestrian Impacts", *2017 IRCOBI Conference Proceedings, Antwerp, Belgium, 13.-15.9.2017*, IRCOBI, available at: http://www.ircobi.org/wordpress/downloads/irc17/pdf-files/62.pdf.

Leglatin, N., Blundell, M.V. and Blount, G.N. (2006), "The simulation of pedestrian impact with a combined multibody finite elements system model", *Journal of Engineering Design*, Vol. 17 No. 5, pp. 463–477. doi: 10.1080/09544820600664622.

Lenard, J., Badea-Romero, A. and Danton, R. (2014), "Typical pedestrian accident scenarios for the development of autonomous emergency braking test protocols", *Accident; analysis and prevention*, Vol. 73, pp. 73–80. doi: 10.1016/j.aap.2014.08.012.

Lenard, J., Morris, A., Tomasch, E., Nehmzow, D., Otte, D., Cant, L., Haddak, M., Vallet, G., Ebbinger, H., Barnes, J., Vries, Y. de, van Kampen, B. and Paez, J. (2006), "PENDANT: A European Crash Injury Database", *2nd International Conference on ESAR "Expert Symposium on Accident Research", Hanover, Germany, 1.-2.9.2006*, ESAR, available at: https://dspace.lboro.ac.uk/dspace-jspui/bitstream/2134/2635/1/PUB460.pdf.

Li, G., Lyons, M., Wang, B., Yang, J., Otte, D. and Simms, C. (2017a), "The influence of passenger car front shape on pedestrian injury risk observed from German in-depth accident data", *Accident Analysis & Prevention*, Vol. 101, pp. 11–21. doi: 10.1016/j.aap.2017.01.012.

Li, G., Otte, D., Yang, J. and Simms, C. (2016), "Can a Small Number of Pedestrian Impact Scenarios Represent the Range of Real-world Pedestrian Injuries?", *2016 IRCOBI Conference Proceedings, Malaga, Spain, 14.-16.9.2016*, IRCOBI, pp. 20–34, available at: http://www.ircobi.org/wordpress/downloads/irc16/pdf-files/12.pdf.

Li, G., Wang, F., Otte, D., Cai, Z. and Simms, C. (2018a), "Have pedestrian subsystem tests improved passenger car front shape?", *Accident Analysis & Prevention*, Vol. 115, pp. 143–150. doi: 10.1016/j.aap.2018.03.014.

Li, G., Yang, J. and Simms, C. (2015), "The influence of gait stance on pedestrian lower limb injury risk", *Accident Analysis & Prevention*, Vol. 85, pp. 83–92. doi: 10.1016/j.aap.2015.07.012.

Li, G., Yang, J. and Simms, C. (2017b), "Safer passenger car front shapes for pedestrians: A computational approach to reduce overall pedestrian injury risk in realistic impact scenarios", *Accident Analysis & Prevention*, Vol. 100, pp. 97–110. doi: 10.1016/j.aap.2017.01.006.

Li, Q., Han, Y. and Mizuno, K. (2018b), "Ground Landing Mechanisms in Vehicle-To-Pedestrian Impacts Based on Accident Video Records", *SAE World Congress Proceedings, 10.4.2018*, SAE International.

Lindman, M., Jakobsson, L. and Jonsson, S. (2011), "Pedestrians interacting with a passenger car; a study of real world accidents", *2011 IRCOBI Conference Proceedings, Krakow (Poland), 14.-16.9.2011*, IRCOBI, pp. 255–264, available at: http://www.ircobi.org/wordpress/downloads/irc0111/2011/Session6/61.pdf.

Lindman, M., Jonsson, S., Jakobsson, L., Karlsson, T., Gustafson, D. and Fredriksson, A. (2015), "Cyclists interacting with passenger cars; a study of real world crashes", *2015 IRCOBI Conference Proceedings, Lyon, France, 9.-11.9.2015*, IRCOBI, pp. 1–12, available at: http://www.ircobi.org/wordpress/downloads/irc15/pdf_files/10.pdf.

Livermore Software Technology Corporation (2014a), *LS-DYNA Keyword User's Manual: Volume II, Material Models*, LS-DYNA R7.1, Livermore, California.

Livermore Software Technology Corporation (2014b), *LS-DYNA Keyword User's Manual: Volume I*, LS-DYNA R7.1, *revision 5471*, Livermore, California.

Lubbe, N., Hikichi, H., Takahashi, H. and Davidsson, J. (2011), "Review of the EURO NCAP Upper Leg Test", *The 22nd ESV Conference Proceedings, Washington, D.C., USA, 13.-16.6.2011*, NHTSA, available at: http://publications.lib.chalmers.se/publication/151221-review-of-the-euro-ncap-upper-leg-test.

Luttenberger, P., Tomasch, E., Willinger, R., Mayer, C., Bakker, J., Bourdet, N., Ewald, C. and Sinz, W. (2014), "Method for future pedestrian accident scenario prediction", in *Transport Research Arena*.

Mallory, A., Fredriksson, R., Rosen, E. and Donnelly, B. (2012), "Pedestrian Injuries by Source: Serious and Disabling Injuries in US and European Cases", *Annals of Advances in Automotive Medicine, Seattle, USA, 14-17.10. 2012*, AAAM, pp. 13–24, available at: http://www.ncbi.nlm.nih.gov/pmc/articles/PMC3503427/.

Mao, H., Zhang, L., Jiang, B., Genthikatti, V.V., Jin, X., Zhu, F., Makwana, R., Gill, A., Jandir, G., Singh, A. and Yang, K.H. (2013), "Development of a finite element human head model partially validated with thirty five experimental cases", *Journal of Biomechanical Engineering*, Vol. 135 No. 11, 111002-1-15. doi: 10.1115/1.4025101.

Martinez, L., Guerra, L.J., Ferichola, G., Garcia, A. and Yang, J. (2007), "Stiffness corridors of the European fleet for pedestrian simulation", *The 20th ESV Conference Proceedings, Lyon, France, 18.-21.6.2007*, NHTSA, available at: http://www-nrd.nhtsa.dot.gov/pdf/esv/esv20/07-0267-W.pdf.

Martínez, F., Páez, J., Furones, A. and Sánchez, S. (2016), "Pedestrian-Vehicle Accidents Reconstruction with PC-Crash®. Sensibility Analysis of Factors Variation", *Transportation Research Procedia*, Vol. 18, pp. 115–121. doi: 10.1016/j.trpro.2016.12.016.

Masson, C., Serre, T. and Cesari, D. (2007), "Pedestrian-Vehicle Accident: Analysis of 4 Full Scale Tests with PMHS", *The 20th ESV Conference Proceedings, Lyon, France, 18.-21.6.2007*, NHTSA, available at: https://www-esv.nhtsa.dot.gov/Proceedings/20/07-0428-W.pdf.

McNally, D.S. and Whitehead, S. (2013), "A computational simulation study of the influence of helmet wearing on head injury risk in adult cyclists", *Accident Analysis & Prevention*, Vol. 60, pp. 15–23. doi: 10.1016/j.aap.2013.07.011.

Meng, Y., Pak, W., Guleyupoglu, B., Koya, B., Gayzik, F.S. and Untaroiu, C.D. (2017), "A finite element model of a six-year-old child for simulating pedestrian accidents", *Accident Analysis & Prevention*, Vol. 98, pp. 206–213. doi: 10.1016/j.aap.2016.10.002.

Mertz, H.J., Prasad, P. and Nusholtz, G. (1996), "Head Injury Risk Assessment for Forehead Impacts", *International Congress & Exposition, 26.2.1996*, SAE International.

Mizuno, Y. and Ishikawa, H. (2001), "Summary of IHRA Pedestrian Safety WG Activities – Proposed Test Methods to Evaluate Pedestrian Protection Aforded by Passenger Cars", *The 17th ESV Conference Proceedings, Amsterdam, The Netherlands, 4.-7.6.2001*, NHTSA.

Mohan, P., Marzougui, D. and Kan, C.-D. (2009), "Development and Validation of Hybrid III Crash Test Dummy", *SAE World Congress Proceedings, APR. 20, 2009*, SAE International.

Moser, A., Steffan, H., Hoschopf, H. and Kasanický, G. (2000), "Validation of the PC-Crash Pedestrian Model", *SAE technical papers*, Vol. 109 No. 6, pp. 1316–1339.

Mueller, B., MacAlister, A., Nolan, J. and Zuby, D. (2015), "Comparison of HIC and BRIC head injury risk in IIHS frontal crash tests to real-world head injuries", *The 24th ESV Conference Proceedings, Gothenburg, Sweden, 8.-11.6.2015*, NHTSA, available at: https://www-esv.nhtsa.dot.gov/proceedings/24/files/24ESV-000272.PDF.

Nahum, A.M., Smith, R. and Ward, C.C. (1977), "Intracranial Pressure Dynamics During Head Impact", *21st Stapp Car Crash Conference Proceedings, New Orleans, LA, 19.10.1977*, SAE International.

Nasdala, L. (2010), *FEM-Formelsammlung Statik und Dynamik*, Vieweg+Teubner, Wiesbaden. ISBN: 978-3-8348-0980-3.

NHTSA (2018a), "National Automotive Sampling System (NASS)", available at: https://www.nhtsa.gov/research-data/national-automotive-sampling-system-nass (accessed 13 August 2018).

NHTSA (2018b), *Traffic Safety Facts - Pedestrians: 2016 Data*, Washington, D.C., USA.

Nightingale, R.W., McElhaney, J.H., Camacho, D.L., Kleinberger, M., Winkelstein, B.A. and Myers, B.S. (1997), "The Dynamic Responses of the Cervical Spine: Buckling, End Conditions, and Tolerance in Compressive Impacts", *41st Stapp Car Crash Conference Proceedings, Lake Buena Vista, Florida, USA, 13.-14.11.*, SAE International.

Ono, K., Ejima, S., Kaneoka, K., Fukushima, M., Yamada, S., Ujihashi, S. and Compigne, S. (2005), "Biomechanical Responses of Head/Neck/Torso to Lateral Impact Loading on Shoulders of Male and Female Volunteers", *2005 IRCOBI Conference Proceedings, Prague, Czech Republic, 21.-23.9. 2005*, IRCOBI, pp. 383–396, available at: http://www.ircobi.org/wordpress/downloads/irc0111/2005/Session6/66.pdf.

Ott, K.A., Wiechel, J.F., Guenther, D.A., Stammen, J. and Mallory, A.E. (2012), "Assessment of the Simulated Injury Monitor (SIMon) in Analyzing Head Injuries in Pedestrian Crashes", *SAE International Journal of Passenger Cars - Mechanical Systems*, Vol. 5 No. 1, pp. 487–505. doi: 10.4271/2012-01-0569.

Otte, D., Jänsch, M. and Haasper, C. (2012), "Injury protection and accident causation parameters for vulnerable road users based on German In-Depth Accident Study GIDAS", *Accident Analysis & Prevention*, Vol. 44 No. 1, pp. 149–153. doi: 10.1016/j.aap.2010.12.006.

Paas, R. (2015), "Head kinematics in car-pedestrian crashes", Dissertation, Chalmers tekniska högskola, 2015.

Paas, R., Davidsson, J. and Brolin, K. (2015a), "Head Kinematics and Shoulder Biomechanics in Shoulder Impacts Similar to Pedestrian Crashes — A THUMS Study", *Traffic injury prevention*, Vol. 16 No. 5, pp. 498–506. doi: 10.1080/15389588.2014.968778.

Paas, R., Davidsson, J., Masson, C., Sander, U., Brolin, K. and Yang, J. (2012), "Pedestrian Shoulder and Spine Kinematics in Full-Scale PMHS Tests for Human Body Model Evaluation", *2012 IRCOBI Conference Proceedings, Dublin, Ireland, 12.-14.09.2012*, IRCOBI, pp. 730–750, available at: http://www.ircobi.org/wordpress/downloads/irc12/pdf_files/79.pdf.

Paas, R., Masson, C. and Davidsson, J. (2015b), "Head boundary conditions in pedestrian crashes with passenger cars. Six-degrees-of-freedom post-mortem human subject responses",

International Journal of Crashworthiness, Vol. 20 No. 6, pp. 547–559. doi: 10.1080/13588265.2015.1060731.

Paas, R., Östh, J. and Davidsson, J. (2015c), "Which Pragmatic Finite Element Human Body Model Scaling Technique Can Most Accurately Predict Head Impact Conditions in Pedestrian-Car Crashes?", *2015 IRCOBI Conference Proceedings, Lyon, France, 9.-11.9.2015*, IRCOBI, pp. 546–576, available at: http://www.ircobi.org/wordpress/downloads/irc15/pdf_files/64.pdf.

Pak, W. and Untaroiu, C.D. (2016), "Development and Validation of a 95 th Percentile Male Pedestrian Finite Element Model", 12.-14.6.2016, Detroit, USA, available at: https://www.dynalook.com/14th-international-ls-dyna-conference/occupantsafety/development-and-validation-of-a-95-th-percentile-male-pedestrian-finite-element-model/view.

Pal, C., Okabe, T., Vimalathithan, K., Manoharan, J., Muthanandam, M. and Narayanan, S. (2014), "Estimation of Pelvis Injuries and Head Impact Time using Different Pedestrian Human FE Models", *SAE 2014 World Congress & Exhibition, 8.4.2014*, SAE International.

Pal, C., Tomosaburo, O., Muthanandam, M. and Narayanan, S. (2013), "Human FE model to estimate head contact time for pedestrian Protection", *The 23rd ESV Conference Proceedings, Seoul, Republic of Korea, 27.-30.5.2013*, NHTSA, pp. 1–9, available at: https://www-esv.nhtsa.dot.gov/Proceedings/23/files/23ESV-000376.PDF.

Pastor, C. (2013), "Correlation between pedestrian injury severity in real-life crashes and Euro NCAP pedestrian test results", *The 23rd ESV Conference Proceedings, Seoul, Republic of Korea, 27.-30.5.2013*, NHTSA, pp. 1–9, available at: https://www-esv.nhtsa.dot.gov/Proceedings/23/files/23ESV-000308.PDF.

Peng, Y., Chen, Y., Yang, J., Otte, D. and Willinger, R. (2012a), "A study of pedestrian and bicyclist exposure to head injury in passenger car collisions based on accident data and simulations", *Safety Science*, Vol. 50 No. 9, pp. 1749–1759. doi: 10.1016/j.ssci.2012.03.005.

Peng, Y., Deck, C., Yang, J., Otte, D. and Willinger, R. (2012b), "A study of adult pedestrian head impact conditions and injury risks in passenger car collisions based on real world accident data", *Traffic injury prevention*, Vol. 14 No. 6, pp. 639–646. doi: 10.1080/15389588.2012.733841.

Peres, J. (2018), "A Pedestrian Version of the Piper 6 Year Old Child Model", *2018 IRCOBI Conference Proceedings, Athens, Greece, 12.-14.9.2018*, IRCOBI, pp. 247–248, available at: http://www.ircobi.org/wordpress/downloads/irc18/pdf-files/38.pdf.

Peres, J., Auer, S. and Praxl, N. (2016), "Development and comparison of different injury risk functions predicting pelvic fracturesin side impact for a Human Body Model", *2016 IRCOBI Conference Proceedings, Malaga, Spain, 14.-16.9.2016*, IRCOBI, available at: http://www.ircobi.org/wordpress/downloads/irc16/pdf-files/87.pdf.

Perry, J. (1992), *Gait analysis: Normal and pathological function*, Slack Incorporated. ISBN: 1556427662.

Piantini, S., Mangini, M., Baldanzini, N., Pierini, M., Franci, A. and Peris, A. (2017), "Prediction of motorcyclist serious injury in powered two-wheeler to other vehicle urban crash", *2017 IRCOBI Conference Proceedings, Antwerp, Brussels, 13.-15.9.2017*, IRCOBI, pp. 54–62, available at: http://www.ircobi.org/wordpress/downloads/irc17/pdf-files/16.pdf.

Pipkorn, B., Forsberg, C., Takahashi, Y., Ikeda, M., Fredriksson, R., Svensson, C. and Thesleff, A. (2014), "Development and component validation of a generic vehicle front buck for pedestrian impact evaluation.", *2014 IRCOBI Conference Proceedings, Berlin, Germany, 10.-12.9.2014*, IRCOBI, pp. 718–729.

Poulard, D., Chen, H. and Panzer, M. (2016), "Geometrical Personalization of Pedestrian Finite Element Models Using Morphing Increases the Biofidelity of Their Impact Kinematics", *SAE 2016 World Congress Proceedings, 12.4.2016*, SAE International.

Prasad, P. and Mertz, H.J. (1985), "The Position of the United States Delegation to the ISO Working Group 6 on the Use of HIC in the Automotive Environment", *Government/Industry Meeting & Exposition, 20.5.1985*, SAE International.

Putra, I., Carmai, J., Koetniyom, S. and Markert, B. (2015), "The Effects of Active Muscle Contracion into Pedestrian Kinematics and Injury During Vehicle-Pedestrian Collision", paper presented at LS-DYNA Conference, 15.-17.6.2015, Würzburg, Germany.

Pyttel, T., Liebertz, H. and Cai, J. (2011), "Failure criterion for laminated glass under impact loading and its application in finite element simulation", *International Journal of Impact Engineering*, Vol. 38 No. 4, pp. 252–263. doi: 10.1016/j.ijimpeng.2010.10.035.

Rohlmann, A., Neller, S., Claes, L., Bergmann, G. and Wilke, H.J. (2001), "Influence of a follower load on intradiscal pressure and intersegmental rotation of the lumbar spine", *Spine*, Vol. 26 No. 24, pp. 557–561.

Rosén, E. and Sander, U. (2009), "Pedestrian fatality risk as a function of car impact speed", *Accident Analysis & Prevention*, Vol. 41 No. 3, pp. 536–542. doi: 10.1016/j.aap.2009.02.002.

Roseveare, A.J., Plant, D.J. and Ghajari, M. (2016), "A New Helmet-liner Design for Improved Survivability", *2016 IRCOBI Conference Proceedings, Malaga, Spain, 14.-16.9.2016*, IRCOBI, pp. 388–389, available at: http://www.ircobi.org/wordpress/downloads/irc16/pdf-files/52.pdf.

Ross, R., Thomas, P., Sexton, B., Otte, D., Koßmann, I., Vallet, G., Martin, J., Laumon, B. and Lejeune, P. (1998), "An Approach to the Standardisation of Accident and Injury Registration Systems (STAIRS) in Europe", *The 16th ESV Conference Proceedings, Ontario, Canada, 31.5.-4.6.1998*, NHTSA, p. 1298-305, available at: https://www-nrd.nhtsa.dot.gov/pdf/esv/esv16/98s6p16.pdf.

SAE International (2010a), *Pedestrian Dummy Full Scale Test Results and Resource Materials* No. J2868, 201010th ed., USA.

SAE International (2010b), *Performance Specifications for a Midsize Male Pedestrian Research Dummy* No. J2782, 201010th ed., SAE International, USA, available at: https://saemobilus.sae.org/content/J2782_201010.

Sanchez-Molina, D., Velazquez-Ameijide, J., Arregui-Dalmases, C., Crandall, JR and Untaroiu, C.D. (2012), "Minimization of analytical injury metrics for head impact injuries", *Traffic injury prevention*, Vol. 13 No. 3, pp. 278–285. doi: 10.1080/15389588.2011.650803.

Schachner, M., Micorek, J., Luttenberger, P., Greimel, R. and Klug, C. (2018), "Dynasaur", available at: https://gitlab.com/VSI-TUGraz/Dynasaur.

Schmitt, K.-U., Niederer, P.F., Cronin, D.S., Muser, M.H. and Walz, F. (2014), *Trauma Biomechanics: An Introduction to Injury Biomechanics,* 4th ed. 2014, Springer Berlin Heidelberg, Berlin, Heidelberg, s.l. ISBN: 9783642539190.

Schmitt, K.-U., Niederer, P.F. and Walz, F. (2004), *Trauma Biomechanics: Introduction to Accidental Injury*, Springer Berlin Heidelberg, Berlin, Heidelberg, s.l. ISBN: 978-3-662-05448-2.

Schoell, S.L., Weaver, A.A., Urban, J.E., Jones, D.A., Stitzel, J.D., Hwang, E., Reed, M.P., Rupp, J.D. and Hu, J. (2015), "Development and Validation of an Older Occupant Finite Element Model of a Mid-Sized Male for Investigation of Age-related Injury Risk", *Stapp Car Crash Journal*, Vol. 59, pp. 359–383.

Schreiber, P., Crandall, J., Hurwitz, S. and Nusholtz, G.S. (1998), "Static and dynamic bending strength of the leg", *International Journal of Crashworthiness*, Vol. 3 No. 3, pp. 295–308. doi: 10.1533/cras.1998.0077.

Schroeder, G., Fukuyama, K., Yamazaki, K., Kamiji, K. and Yasuki, T. (2008), "Injury mechanism of pedestrians impact test with a sport-utility vehicle and mini-van", *2008 IRCOBI Conference Proceedings, Bern, Switzerland*, IRCOBI, pp. 259–273, available at: http://www.ircobi.org/wordpress/downloads/irc0111/2008/Session5/5_3.pdf.

Schroeder, G., Konosu, A., Ishikawa, H. and Kajzer, J. (2000), "Injury Mechanism of Pedestrians during a Front- End Collision with a Late Model Car", *Spring Forum for Pedestrian Protection, Yokohama, Japan*, JSAE.

Serre, T., Masson, C., Perrin, C., Chalandon, S., Llari, M., Py, M., Cavallero, C. and Cesari, D. (2007), "Real accidents involving vulnerable road users: in-depth investigation, numerical simulation and experimental reconstitution with PMHS", *International Journal of Crashworthiness*, Vol. 12 No. 3, pp. 227–234. doi: 10.1080/13588260701441050.

Shang, S., Otte, D., Li, G. and Simms, C. (2018), "Detailed assessment of pedestrian ground contact injuries observed from in-depth accident data", *Accident Analysis & Prevention*, Vol. 110, pp. 9–17. doi: 10.1016/j.aap.2017.10.011.

Shang, S., Otte, D. and Simms, C.K. (2017), "Pedestrian-ground contact injuries observed from German in-depth accident data", *2017 IRCOBI Conference Proceedings, Antwerp, Brussels, 13.-15.9.2017*, IRCOBI, pp. 166–167, available at: http://www.ircobi.org/wordpress/downloads/irc17/pdf-files/27.pdf.

Shaw, J.M., Herriott, R.G., McFadden, J.D., Donnelly, B.R. and Bolte, J.H. (2006), "Oblique and lateral impact response of the PMHS thorax", *Stapp Car Crash Journal*, Vol. 50, pp. 147–167.

Shen, M., Mao, H., Jiang, B., Zhu, F., Jin, X., Dong, L., Ham, S.J., Palaniappan, P., Chou, C. and Yang, K. (2016), "Introduction of Two New Pediatric Finite Element Models for Pedestrian and Occupant Protections", *SAE 2016 World Congress Proceedings, APR. 12, 2016*, SAE International.

Shen, M., Zhu, F., Jiang, B., Sanghavi, V., Fan, H., Cai, Y., Wang, Z., Kalra, A., Jin, X., Chou, C.C. and Yang, K.H. (2015), "Development and a Limited Validation of a Whole-Body Finite Element Pedestrian and Occupant Models of a 10-Year-Old Child", *2015 IRCOBI Conference Proceedings, Lyon, France, 9.-11.9.2015*, IRCOBI, pp. 672–688, available at: http://www.ircobi.org/wordpress/downloads/irc15/pdf_files/73.pdf.

Shigeta, K., Kitagawa, Y. and Yasuki, T. (2009), "Development of next generation human FE model capable of organ injury prediction", *The 21st ESV Conference Proceedings, Stuttgart, Germany, 15.-18.6.2009*, NHTSA, pp. 9–111, available at: http://www-nrd.nhtsa.dot.gov/pdf/esv/esv21/09-0111.pdf.

Siegkas, P. and Ghajari, M. (2017), "Computational modelling of oblique impactson helmets with a new add-on lining system", *2017 IRCOBI Conference Proceedings, Antwerp, Brussels, 13.-15.9.2017*, IRCOBI, pp. 705–706, available at: http://www.ircobi.org/wordpress/downloads/irc17/pdf-files/98.pdf.

Simms, C. and Wood, D. (2009), *Pedestrian and Cyclist Impact: A Biomechanical Perspective, Solid Mechanics and Its Applications*, Vol. 166, Springer Netherlands, Dordrecht. ISBN: 978-90-481-2742-9.

Simms, C. and Wood, D.P. (2006), "Pedestrian Risk from Cars and Sport Utility Vehicles - A Comparative Analytical Study", *Proceedings of the Institution of Mechanical Engineers, Part D: Journal of Automobile Engineering*, Vol. 220 No. 8, pp. 1085–1100. doi: 10.1243/09544070JAUTO319.

Snedeker, J.G., Muser, M.H. and Walz, F.H. (2003), "Assessment of pelvis and upper leg injury risk in car-pedestrian collisions: comparison of accident statistics, impactor tests and a human body finite element model", *Stapp Car Crash Journal*, Vol. 47, pp. 437–457.

Snedeker, J.G., Walz, F.H., Muser, M.H., Lanz, C. and Schroeder, G. (2005), "Assessing femur and pelvis injury risk in car-pedestrian collisions: comparison of full body PMTO impacts, and a human body finite element model", *The 19th ESV Conference Proceedings, Washington, D.C., USA, 6.-9.6.2005*, NHTSA, pp. 5–103, available at: http://www-nrd.nhtsa.dot.gov/pdf/esv/esv19/05-0103-O.pdf.

Song, E., Petit, P., Trosseille, X., Uriot, J., Potier, P., Dubois, D. and Douard, R. (2017a), "New Reference PMHS Tests to Assess Whole-Body Pedestrian Impact Using a Simplified Generic Vehicle Front-End", *Stapp Car Crash Journal*, Vol. 61, pp. 299–354.

Song, E., Uriot, J., Potier, P., Dubois, D., Petit, P., Trosseille, X. and Douard, R. (2017b), "Reference PMHS Tests to Assess Whole-Body Pedestrian Impact Using a Simplified Generic Vehicle Front-End", *2017 IRCOBI Conference Proceedings, Antwerp, Brussels, 13.-15.9.2017*, IRCOBI, pp. 133–150, available at: http://www.ircobi.org/wordpress/downloads/irc17/pdf-files/25.pdf.

Soni, A., Robert, T. and Beillas, P. (2013a), "Effects of pedestrian pre-crash reactions on crash outcomes during multi-body simulations", *2013 IRCOBI Conference Proceedings, Gothenburg, Sweden, 11.-13.9.2013*, IRCOBI, available at: http://www.ircobi.org/wordpress/downloads/irc13/pdf_files/92.pdf.

Soni, A., Robert, T., Rongieras, F. and Beillas, P. (2013b), "Observations on pedestrian pre-crash reactions during simulated accidents", *Stapp Car Crash Journal*, Vol. 57, pp. 157–183.

Stander, N., Roux, W., Basudhar, A., Eggleston, T., Goel, T. and Craig, K. (2015), *LS-OPT® User's Manual: Version 5.2*.

Statistik Austria (2000), *Statistik der Straßenverkehrsunfälle: Unfalltypen Katalog (Gültig ab 2000)*.

Statistik Austria (2010), *Standard-Dokumentation Metainformationen (Definitionen, Erläuterungen, Methoden, Qualität) zur Statistik der Straßenverkehrsunfälle*.

Statistik Austria (2017), *Information zur Statistik der Straßenverkehrsunfälle mit Personenschaden ab dem Berichtsjahr 2012*.

Stemper, B.D., Yoganandan, N. and Pintar, F.A. (2004), "Response Corridors of the Human Head-Neck Complex in Rear Impact", *Annual Proceedings / Association for the Advancement of Automotive Medicine*, Vol. 48, pp. 149–163.

StGB § 84 (1) (2016), *Strafgesetzbuch: StGB*.

Strandroth, J., Nilsson, P., Sternlund, S., Rizzi, M. and Krafft, M. (2016), "Characteristics of future crashes in Sweden – identifying road safety challenges in 2020 and 2030", *2016 IRCOBI Conference Proceedings, Malaga, Spain, 14.-16.9.2016*, IRCOBI, pp. 47–60, available at: http://www.ircobi.org/wordpress/downloads/irc16/pdf-files/15.pdf.

Strandroth, J., Rizzi, M., Sternlund, S., Lie, A. and Tingvall, C. (2011), "The correlation between pedestrian injury severity in real-life crashes and Euro NCAP pedestrian test results", *Traffic injury prevention*, Vol. 12 No. 6, pp. 604–613. doi: 10.1080/15389588.2011.607198.

Subit, D., Ivarsson, J., Crandall, J., Kikuchi, Y. and Takahashi, Y. (2006), "The Influence of Pelvis Design on the Lateral Pelvic Impact Response of the Polar-II Pedestrian Dummy", *SAE 2006 World Congress Proceedings, 3.4.2006*, SAE International.

Subit, D., Kerrigan, J., Crandall, J., Fukuyama, K., Yamazaki, K., Kamiji, K. and Yasuki, T. (2008), "Pedestrian-vehicle interaction: Kinematics and injury analysis of four full-scale tests", *2008 IRCOBI Conference Proceedings, Bern, Switzerland*, IRCOBI, pp. 275–294, available at: http://www.ircobi.org/wordpress/downloads/irc0111/2008/Session5/5_4.pdf.

Svensson, M., D'Addetta, G.A., Carlsson, A., Ewald, C., Luttenberger, P., Mayer, C., Strandroth, J., Tomasch, E., Gutsche, A.J. and Wismans, J. (2014), "Future Accident Scenarios involving Small Electric Vehicles", *2014 IRCOBI Conference Proceedings, Berlin, Germany, 10.-12.9.2014*, IRCOBI, pp. 51–52, available at: http://www.ircobi.org/wordpress/downloads/irc14/pdf_files/13.pdf.

Takahashi, Y., Asanuma, H. and Yanaoka, T. (2015), "Development of a Full-Body Human FE Model for Pedestrian Crash Reconstructions", *2015 IRCOBI Conference Proceedings, Lyon, France, 9.-11.9.2015*, IRCOBI, pp. 530–545, available at: http://www.ircobi.org/wordpress/downloads/irc15/pdf_files/63.pdf.

Takahashi, Y., Matsuoka, F., Okuyama, H. and Imaizumi, I. (2012), "Development of Injury Probability Functions for the Flexible Pedestrian Legform Impactor", *SAE International Journal of Passenger Cars - Mechanical Systems*, Vol. 5 No. 1, pp. 242–252. doi: 10.4271/2012-01-0277.

Takhounts, E.G., Craig, M.J., Moorhouse, K., McFadden, J. and Hasija, V. (2013), "Development of brain injury criteria (BrIC)", *Stapp Car Crash Journal*, Vol. 57, pp. 243–266.

Takhounts, E.G., Eppinger, R.H., Campbell, J.Q., Tannous, R.E., Power, E.D. and Shook, L.S. (2003), "On the Development of the SIMon Finite Element Head Model", *Stapp Car Crash Journal*, Vol. 47, pp. 107–133.

Takhounts, E.G., Hasija, V., Ridella, S.A., Rowson, S. and Duma, S.M. (2011), "Kinematic rotational brain injury criterion (BRIC)", *The 22nd ESV Conference Proceedings, Washington, D.C., USA, 13.-16.6.2011*, NHTSA, available at: https://www-esv.nhtsa.dot.gov/Proceedings/22/files/22ESV-000263.pdf.

Tang, J., Zhou, Q., Nie, B., Yasuki, T. and Kitagawa, Y. (2016), "Influence of Pre-impact Pedestrian Posture on Lower Extremity Kinematics in Vehicle Collisions", *SAE International Journal of Transportation Safety*, Vol. 4 No. 2, pp. 278–288. doi: 10.4271/2016-01-1507.

TASS International BV (2017), *MADYMO Human Body Models Manual*.

Timmel, M., Kolling, S., Osterrieder, P. and Du Bois, P.A. (2007), "A finite element model for impact simulation with laminated glass", *International Journal of Impact Engineering*, Vol. 34 No. 8, pp. 1465–1478. doi: 10.1016/j.ijimpeng.2006.07.008.

Tomasch, E. and Steffan, H. (2006), "ZEDATU - Zentrale Datenbank tödlicher Unfälle in Österreich - A Central Database of Fatalities in Austria", *2nd International Conference on ESAR "Expert Symposium on Accident Research", Hanover, Germany, 1.-2.9.2006*, ESAR.

Untaroiu, C., Kerrigan, J., Kam, C., Crandall, J., Yamazaki, K., Fukuyama, K., Kamiji, K., Yasuki, T. and Funk, J. (2007), "Correlation of strain and loads measured in the long bones with observed kinematics of the lower limb during vehicle-pedestrian impacts", *Stapp Car Crash Journal*, Vol. 51, pp. 433–466.

Untaroiu, C.D., Ivarsson, J., Genovese, D.R., Bose, D. and Crandall, J.R. (2008a), "Biomechanical injury response of leg subjected to combined axial compressive and bending loading", *Biomedical sciences instrumentation*, Vol. 44, pp. 141–146.

Untaroiu, C.D., Meissner, M.U., Crandall, J.R., Takahashi, Y., Okamoto, M. and Ito, O. (2009), "Crash reconstruction of pedestrian accidents using optimization techniques", *International Journal of Impact Engineering*, Vol. 36 No. 2, pp. 210–219. doi: 10.1016/j.ijimpeng.2008.01.012.

Untaroiu, C.D., Pak, W., Meng, Y., Schap, J., Koya, B. and Gayzik, S. (2018), "A Finite Element Model of a Midsize Male for Simulating Pedestrian Accidents", *Journal of Biomechanical Engineering*, Vol. 140 No. 1. doi: 10.1115/1.4037854.

Untaroiu, C.D., Putnam, J.B., Schap, J., Davis, M.L. and Gayzik, F.S. (2015), "Development and Preliminary Validation of a 50th Percentile Pedestrian Finite Element Model", paper presented at IDETC/CIE 2015, 2.-5.8.2015, Boston, Massachusetts, USA.

Untaroiu, C.D., Shin, J., Crandall, J.R., Fredriksson, R., Bostrom, O., Takahashi, Y., Akiyama, A., Okamoto, M. and Kikuchi, Y. (2010), "Development and validation of pedestrian sedan bucks using finite-element simulations. A numerical investigation of the influence of vehicle automatic braking on the kinematics of the pedestrian involved in vehicle collisions", *International Journal of Crashworthiness*, Vol. 15 No. 5, pp. 491–503. doi: 10.1080/13588265.2010.484189.

Untaroiu, C.D., Shin, J., Ivarsson, J., Crandall, J.R., Subit, D., Takahashi, Y., Akiyama, A. and Kikuchi, Y. (2008b), "A study of the pedestrian impact kinematics using finite element dummy models: the corridors and dimensional analysis scaling of upper-body trajectories", *International Journal of Crashworthiness*, Vol. 13 No. 5, pp. 469–478. doi: 10.1080/13588260802055387.

Untaroiu, C.D., Yue, N. and Shin, J. (2013), "A finite element model of the lower limb for simulating automotive impacts", *Ann Biomed Eng*, Vol. 41 No. 3, pp. 513–526. doi: 10.1007/s10439-012-0687-0.

van Hoof, J., Lange, R. de and Wismans, J.S.H.M. (2003), "Improving pedestrian safety using numerical human models", *Stapp Car Crash Journal*, Vol. 47, pp. 401–436.

van Schijndel, M., Hair, S. de, Rodarius, C. and Fredriksson, R. (2012), "Cyclist kinematics in car impacts reconstructed in simulations and full scale testing with Polar dummy", *2012 IRCOBI Conference Proceedings, Dublin, Ireland, 12.-14.09.2012*, IRCOBI, pp. 800–812, available at: http://www.ircobi.org/wordpress/downloads/irc12/pdf_files/85.pdf.

Vehicle Safety Institute (2018), "CEDATU. Central Database for In-Depth Accident Study", available at: https://www.tugraz.at/institute/vsi/unfalldatenbank-zedatu/allgemeine-informationen/ (accessed 15 June 2018).

Versace, J. (1971), "A Review of the Severity Index", *15th Stapp Car Crash Conference Proceedings, Coronado, CA, 17.11.1971*, SAE International.

Vertal, P. and Steffan, H. (2016), "Evaluation of the Effectiveness of Volvo's Pedestrian Detection System Based on Selected Real-Life Fatal Pedestrian Accidents", *SAE 2016 World Congress Proceedings, 12.4.2016*, SAE International.

Viano, D.C. (1989), "Biomechanical Responses and Injuries in Blunt Lateral Impact", *33rd Stapp Car Crash Conference Proceedings, 4.10.1989*, SAE International.

Wallentowitz, H., Bovenkerk, J., Sahr, C., Kalliske, I., Porstmann, M. and Zander, O. (2009), "Challenge and approach to real-world pedestrian protection – investigated by Polar-II pedestrian dummy", *International Journal of Crashworthiness*, Vol. 14 No. 5, pp. 457–467. doi: 10.1080/13588260902826497.

Watanabe, R., Miyazaki, H., Kitagawa, Y. and Yasuki, T. (2011), "Research of the Relationship of Pedestrian Injury to Collision Speed, Car-type, Impact Location and Pedestrian Sizes Using Human FE Model (THUMS Version 4)", *The 22nd ESV Conference Proceedings, Washington, D.C., USA, 13.-16.6.2011*, NHTSA, pp. 1–13, available at: https://www-esv.nhtsa.dot.gov/Proceedings/22/files/22ESV-000043.pdf.

Watson, J.W. (2010), "Investigation of Cyclist and Pedestrian Impacts with Motor Vehicles using Experimentation and Simulation", PhD Thesis, Februar 2010.

Wen, L., Bastien, C., Blundell, M., Neal-Sturgess, C. and Kayvantash, K. (2015), "Stability and sensitivity of THUMS pedestrian model and its trauma response to a real life accident", paper presented at LS-DYNA Conference, 15.-17.6.2015, Würzburg, Germany.

WHO (2015), *Global status report on road safety 2015*, World Health Organization, Geneva, Switzerland. ISBN: 9789241565066.

WHO (2016), "Road traffic mortality rate, 2013", available at: http://gamapserver.who.int/mapLibrary/Files/Maps/Global_RoadTraffic_Mortality_2013.png.

Wimmer, P., Benedikt, M., Huber, P. and Ferenczi, I. (2015), "Fast calculating surrogate models for leg and head impact in vehicle-pedestrian collision simulations", *Traffic injury prevention*, 16 Suppl 1, S84-90. doi: 10.1080/15389588.2015.1014902.

Wisch, M., Lerner, M., Vukovic, E., Hynd, D., Fiorentino, A. and Fornells, A. (2017), "Injury Patterns of Older Car Occupants, Older Pedestrians or Cyclists in Road Traffic Crashes with Passenger Cars in Europe – Results from SENIORS", *2017 IRCOBI Conference Proceedings,*

Antwerp,   Brussels,   13.-15.9.2017,   IRCOBI,   pp.   63–78,   available   at: http://www.ircobi.org/wordpress/downloads/irc17/pdf-files/17.pdf.

Wood, D.P., Simms, C. and Walsh, D.G. (2005), "Vehicle-pedestrian collisions. Validated models for pedestrian impact and projection", *Proceedings of the Institution of Mechanical Engineers, Part D: Journal of Automobile Engineering*, Vol. 219 No. 2, pp. 183–195. doi: 10.1243/095440705X6703.

Wu, G. and Cavanagh, P.R. (1995), "ISB recommendations for standardization in the reporting of kinematic data", *Journal of biomechanics*, Vol. 28 No. 10, pp. 1257–1261. doi: 10.1016/0021-9290(95)00017-C.

Wu, G., Siegler, S., Allard, P., Kirtley, C., Leardini, A., Rosenbaum, D., Whittle, M., D'Lima, D.D., Cristofolini, L., Witte, H., Schmid, O. and Stokes, I. (2002), "ISB recommendation on definitions of joint coordinate system of various joints for the reporting of human joint motion—part I: ankle, hip, and spine", *Journal of biomechanics*, Vol. 35 No. 4, pp. 543–548. doi: 10.1016/S0021-9290(01)00222-6.

Wu, G., van der Helm, Frans C.T., Veeger, H.E.J., Makhsous, M., van Roy, P., Anglin, C., Nagels, J., Karduna, A.R., McQuade, K., Wang, X., Werner, F.W. and Buchholz, B. (2005), "ISB recommendation on definitions of joint coordinate systems of various joints for the reporting of human joint motion—Part II. Shoulder, elbow, wrist and hand", *Journal of biomechanics*, Vol. 38 No. 5, pp. 981–992. doi: 10.1016/j.jbiomech.2004.05.042.

Wu, S.R. and Gu, L. (2012), *Introduction to the explicit finite element method for nonlinear transient dynamics*, Wiley, Hoboken NJ.

Wu, T., Kim, T., Bollapragada, V., Poulard, D., Chen, H., Panzer, M.B., Forman, J.L., Crandall, J.R. and Pipkorn, B. (2017), "Evaluation of biofidelity of THUMS pedestrian model under a whole-body impact conditions with a generic sedan buck", *Traffic injury prevention*, Vol. 18 No. 1, 148-154. doi: 10.1080/15389588.2017.1318435.

Yamada, H. and Evans, F.G. (1970), *Strength of biological materials*, Williams & Wilkins, USA. ISBN: 0683093231.

Yanaoka, T., Torikai, K. and Takahashi, Y. (2016), "Investigation of the Effect of the Height Alignment on the Validity of the Scaled Whole Body Trajectories in Car-to-pedestrian Collisions", *International Journal of Automotive Engineering*, No. 7, 45-41.

Yang, J.K., Lövsund, P., Cavallero, C. and Bonnoit, J. (2000), "A Human-Body 3D Mathematical Model for Simulation of Car-Pedestrian Impacts", *Journal of Crash Prevention and Injury Control*, Vol. 2 No. 2, pp. 131–149. doi: 10.1080/10286580008902559.

Yang, K.H., Hu, J., White, N.A., King, A.I., Chou, C.C. and Prasad, P. (2006), "Development of numerical models for injury biomechanics research: a review of 50 years of publications in the Stapp Car Crash Conference", *Stapp Car Crash Journal*, No. 50, pp. 429–490.

Yang, K.-H. (2018), *Basic Finite Element Method as Applied to Injury Biomechanics*, Elsevier. ISBN: 9780128098318.

Yoganandan, N., Maiman, D.J., Pintar, F.A. and Sances, A. (1989), "Cervical spine injuries from motor vehicle accidents", *Images of the Twenty-First Century. Proceedings of the Annual International Engineering in Medicine and Biology Society, Seattle, WA, USA, 9.-12.11.1989*, IEEE, p. 808.

Yoganandan, N., Nahum, A.M. and Melvin, J. (Eds.) (2015), *Accidental injury: Biomechanics and prevention*, Third edition, Springer, New York.

Yoganandan, N., Pintar, F.A., Sances, A., JR, Walsh, P.R., Ewing, C.L., Thomas, D.J. and Snyder, R.G. (1995), "Biomechanics of skull fracture", *Journal of neurotrauma*, Vol. 12 No. 4, pp. 659–668. doi: 10.1089/neu.1995.12.659.

Yoganandan, N., Zhang, J. and Pintar, F. (2004), "Force and acceleration corridors from lateral head impact", *Traffic injury prevention*, Vol. 5 No. 4, pp. 368–373. doi: 10.1080/15389580490510336.

Zander, O., Gehring, D.-U. and Leßmann, P. (2011), "Improved assessment methods of lower extremity injuries in vehicle-to-pedestrian accidents using impactor tests and full-scale dummy tests", *The 22nd ESV Conference Proceedings, Washington, D.C., USA, 13.-16.6.2011*, NHTSA, available at: https://www-esv.nhtsa.dot.gov/Proceedings/22/files/22ESV-000079.pdf.

Zander, O., Gehring, D.-U. and Leßmann, P. (2013), "Improved Safety of Bicyclists in the Event of a Collision with Motor Vehicles and During Single Accidents", *The 23rd ESV Conference Proceedings, Seoul, Republic of Korea, 27.-30.5.2013*, NHTSA, available at: https://www-esv.nhtsa.dot.gov/Proceedings/23/files/23ESV-000180.PDF.

Zander, O., Gehring, D.-U., Leßmann, P. and Bovenkerk, J. (2009), "Evaluation of a Flexible Pedestrian Legform Impactor (FlexPLI) for the implementation within legislation on pedestrian protection", *The 21st ESV Conference Proceedings, Stuttgart, Germany, 15.-18.6.2009*, NHTSA, available at: http://bast.opus.hbz-nrw.de/frontdoor.php?source_opus=718&la=en.

Zander, O., Gehring, D.-U. and van Ratingen, M. (2015), "Beyond Safety Legislation: Contribution of Consumer Information Programmes to Enhanced Injury Mitigation of Pedestrians during Accidents with Motor Vehicles", *The 24th ESV Conference Proceedings, Gothenburg, Sweden, 8.-11.6.2015*, NHTSA, pp. 1–14, available at: https://www-esv.nhtsa.dot.gov/Proceedings/24/files/24ESV-000258.PDF.

Zhang, K., Cao, L., Fanta, A., Reed, M.P., Neal, M.O., Wang, J.-T., Lin, C.-H. and Hu, J. (2017a), "An automated method to morph finite element whole-body human models with a wide range of stature and body shape for both men and women", *Journal of biomechanics*, Vol. 60, pp. 253–260. doi: 10.1016/j.jbiomech.2017.06.015.

Zhang, K., Cao, L., Wang, Y., Hwang, E., Reed, M.P., Forman, J. and Hu, J. (2017b), "Impact Response Comparison Between Parametric Human Models and Postmortem Human Subjects with a Wide Range of Obesity Levels", *Obesity (Silver Spring, Md.)*, Vol. 25 No. 10, pp. 1786–1794. doi: 10.1002/oby.21947.

Zhao, W., Kuo, C., Wu, L., Camarillo, D.B. and Ji, S. (2017), "Performance Evaluation of a Pre-computed Brain Response Atlas in Dummy Head Impacts", *Annals of biomedical engineering*, Vol. 45 No. 10, pp. 2437–2450. doi: 10.1007/s10439-017-1888-3.

10 LIST OF FIGURES

11 LIST OF TABLES

TABLES APPENDIX

12 APPENDIX

A. State of the Art

Table Appendix A-1: PMHS tests in the context of VRU protection

	PMHS	Impact Structure	Main Purpose of the Study
Ishikawa *et al.*, 1993	1 female and 9 males; 17-74 yo; 166-192 cm; 54-90 kg; Tied wrists, SSL forward;	2 different medium-sizes car bodies on sled with varying bumper stiffnesses; impacts at 25, 32 and 40 km/h	PMHS tests for validation of a GEBOD multibody pedestrian model
Cesari, 1998 (EEVC WG17)	1 female and 4 males; 75-94 YO; 53.5-70 kg; 161-175 cm	2 large family cars; impacts at 32-40 km/h	Original document not available; Information from (van Hoof *et al.*, 2003) Tests were performed for the EEVC WG17; one production vehicle and one optimised for Euro NCAP pedestrian rating was tested
Yang *et al.*, 2000	3 males; 72-84 yo; 167-185 cm; 60-78 kg;	Small experimental car; impacts at 25, 32 and 39 km/h	Validation of GEBOD/MADYMO multibody pedestrian model
Schroeder *et al.*, 2000	5 males; 53-78 yo; 167-182 cm; 63-84 kg; SSL backwards	late car model and car constructed before 1990; impacts at 30 and 40 km/h	Original document not available – information obtained from Kerrigan *et al.* (2012b)
Snedeker *et al.*, 2005	2 females and 3 males; 32-78 yo; 160-180 cm; 50-75 kg; SSL forward	Bucks representing 2 sedans and 2 vans with differing ble radius; impacts at 40 km/h	Understanding of pelvis and upper leg injuries and comparison with subsystem tests and accident statistics
Kerrigan *et al.*, 2005a	1 female and 1 male; 53-75 yo; 168-171 cm; 46.7-104 kg; SSL forward	SUV; impacts at 40 km/h	Comparison of kinematics of Polar II dummy and PMHS
Kerrigan *et al.*, 2005b	1 female and 2 males; 61-70 yo; 170-175 cm; 54.4-81.6 kg; SSL backwards; Wrists tied	Small sedan; impacts at 40 km/h	Biofidelity corridors for the kinematic response were developed

	PMHS	Impact Structure	Main Purpose of the Study
Crandall *et al.*, **2006**	2 females and 3 males; 53-75 yo; 168-173 cm; 46.7-104.2 kg; SSL backwards; Wrists tied	Midsized sedan and SUV 40 km/h	Analysis of thoracic deformations
Kerrigan *et al.*, **2007**	5 females and 2 males; 32-71 yo; 163-184 cm; 63.5-92.9 kg; SSL backwards; Wrists tied	Small sedan; impacts at 40 km/h	Evaluation of the ability of a geometric scaling technique to predict the response of a mid-sized pedestrian from the responses of pedestrians of other statures.
Masson *et al.*, **2007**	4 males; 74-88 yo; 161-185 cm; 44-89 kg; Different initial postures, Natural arm posture	Small and big sedan 29.7-39.7 km/h	Examine the pedestrian kinematics in real-world conditions: Two tests were performed in standard configuration and two based on reconstruction of real-world accidents.
Serre *et al.*, **2007**	Pedestrian: 64 yo; 65 kg; 160 cm Bicyclist: Female, 65 yo, 52 kg; 160 cm	Pedestrian: Renault Twingo; 40 km/h Bicyclist: Peugeot 205; 42.2 km/h	Two real-world accidents were reconstructed
Untaroiu *et al.*, **2007**	4 males; 62-67 yo; 46.3-114.3 kg; 154-183 cm; Tied wrists; SSL backwards	Small MPV and large sedan 40 km/h	Determine the loads in the long bones of the lower extremities during vehicle-pedestrian impact tests and correlate load data with observed kinematics
Kerrigan *et al.*, **2008**	5 females and 2 males; 32-71 yo; 163-184 cm; 63.5-92.9 kg; SSL backwards; Wrists tied	Small sedan; impacts at 40 km/h	Comparison of the injury risk to pedestrians of PMHS and EEVC impactors
Schroeder *et al.*, **2008**	4 males; 60-85 yo; 165-181 cm; 60-85 kg; SSL forwards; Wrists tied	SUV and Minivan; impacts at 40 km/h	Analysis of the differences of injury that might be caused by different car-front shapes; Comparison with previous tests with Sedan
Subit *et al.*, **2008**	4 males; 62-67 yo; 154-183 cm; 46.3-114 kg; SSL backwards;	Mid-sized sedan; small city car; impacts at 40 km/h	Analysis of the kinematics and injuries of a pedestrian hit by a vehicle with PMHS of differing anthropometry and two different cars shapes

	PMHS	Impact Structure	Main Purpose of the Study
	Wrists tied		
Kerrigan *et al.*, 2009a	2 females and 3 males; 53-75 yo; 176-187 cm; 46.7-104.2 kg; SSL backwards; Wrists tied	Small sedan and large SUV; impacts at 40 km/h	The study compares head impact dynamics between PMHS and the Polar-II pedestrian crash dummy in vehicle-pedestrian impacts
Kerrigan *et al.*, 2009b	2 females and 4 males; 53-75 yo; 176-187 cm; 46.7-104.2 kg; SSL backwards; Wrists tied	Small sedan and large SUV; impacts at 40 km/h	Analysis of differences of injuries of the lower extremities between impacts with SUV or sedan
Kerrigan *et al.*, 2012a	2 females and 3 males; 53-75 yo; 168-173 cm; 46.7-104.2 kg; SSL backwards; Wrists tied	Midsized sedan and SUV; impacts at 40 km/h	Comparison of dummy and PMHS head kinematics
Paas *et al.*, 2012	1 PMHS; 72 yo; 69 kg; SSL slightly forward; Natural arm posture	Small sedan; impacts at 40 km/h	Investigate shoulder and spine response by analysing new and existing PMHS tests; Loading conditions of the PMHS tests were compared to existing component tests and representative of real-life accidents
Paas *et al.*, 2015b	1 female; 5 males; 47-88 yo; 154-179 cm; 47-88 kg; SSL forward; Natural arm posture	Small sedan; impacts at 40 km/h	Analysis of the influence of anthropometry, upper body and arm kinematics on head linear and angular kinematics
Forman *et al.*, 2015a	3 males; 54-73 yo; 73-82 kg; 178-187 cm; Tied wrists; SSL backwards	Generic sedan buck (SAE); impacts at 40 km/h	Development of biofidelity corridors for pedestrian dummies for trajectories
Forman *et al.*, 2015b	3 males; 54-73 yo; 73-82 kg; 178-187 cm; Tied wrists; SSL backwards	Generic sedan buck (SAE); impacts at 40 km/h	Analysis of head velocities, body accelerations, angular velocities, interface forces and injuries

	PMHS	Impact Structure	Main Purpose of the Study
Song et al., 2017a	11 males; 62-87 yo; 58-87 kg; 156-173 cm; Tied wrists; SSL backwards	Generic bucks representing Sedan, Van and SUV; impacts at 40 km/h	Development of biofidelity corridors based on simple, easily reproducible test conditions, for whole-body pedestrian impact
Song et al., 2017b	4 males; 71-87 yo; 171-178 cm; 60-88 kg; Tied wrists; SSL backwards	Generic buck representing mid-size sedan (no bonnet); impacts at 28,8 km/h (8 m/s)	Provide reference PMHS tests, which are easily reproducible to assess biofidelity of dummies or computational models; focus on lower extremities

Table Appendix A-2: Recent studies applying HBM for research on injury mechanisms of bicyclists and pedestrian

	HBM	Main Research Purpose	Result
Watanabe et al., 2011	THUMS v4 AM50	The likelihood of injuries to the head and thorax for SUV impacts was investigated	Injuries were observed in the simulations with the THUMS v4 model at Impact Velocities of 40 km/h or higher.
Pal et al., 2013	JAMA model AM50 and 6-yo	Analysis of factors affecting head impact time	The higher the ratio of pedestrian height with respect to the height of the bonnet leading edge, the higher *HIT*s were observed due to increased inertia. The initial posture affects *HIT* as the degree of constraint and the timing of the shoulder restraint on the hood affects the rotational movement of the head. Impacts at the bumper corner resulted in more sliding compared to the centreline and lower-head impact velocities. *HIT* was shortest at the vehicle centreline and greatly depended on the impact velocity (no linear dependency).
Coulongeat et al., 2014	THUMS v3 scaled	Reconstruction of a real-world pedestrian accident to understand injury mechanisms and potential of an AEB system	Deformations of the vehicle in the simulations and fractures predicted by the HBM (skull, lower extremities, pelvis) were consistent with the real-world accident, but pelvic fractures were overestimated. Due to decreased impact velocity with AEB, no skull fractures were observed in the HBM simulations.

	HBM	Main Research Purpose	Result
Ito *et al.*, 2014	THUMS v3 AM50	Comparison of impact kinematics and body loads of pedestrian and cyclists	Different loading pattern of the lower extremities were observed as leg of the bicyclist was fixed between the car front and the bicycle frame. Simulations of the bicyclist with helmet led to a reduction in kinematic and strain-based injury predictors.
Katsuhara *et al.*, 2014	THUMS v4 AM50	Analysis of head injury sources for bicyclists in crashes with a SUV and sedan	High CSDM values were associated to the upper part of the A-pillar for SUVs and sedans. In the sedan, critical HIC values showed up mainly when the A-pillar was hit, while for the SUV cases, the rear end of the hood was also very relevant. In general, critical HIC values were reached more often than critical CSDM values. 40% of the injuries were predicted at ground impacts.
Pal *et al.*, 2014	Combination of JAMA model and GHBMC – scaled to AF05 and AF50	Study the effect of height, age, gender and pelvis shape on pelvic injuries	It was found that the hip/ble height ratio had a significant influence on pelvic injuries. The gender-based pelvis shape also affected the pelvis injury risk. Simulation of pelvic fracture had only very small effect on *HIT* (slightly longer *HIT* for model with fracture option).
Chen *et al.*, 2015a	THUMS v4 AM50	Analysis of the influence of initial pedestrian posture and orientation on impact kinematics and injury indicators	Due to the differing initial conditions (3 different postures and varying orientation), *HIVel* varied between 10.7-15.3 m/s, *HIT* between 111-139 ms and *WAD* from 1900 to 2100 mm.
Li *et al.*, 2015	THUMS v4 AM50	Analysis of the effect of differing leg postures on the injury risk of lower extremities for impacts with a sedan and a SUV	Von-Mises stresses in the femur und tibia cortical bones and the lateral knee bending angle were strongly affected by differing initial postures. It was concluded that it is, therefore, important to take differing gait stances into account when assessing injuries of lower extremities.
Ghosh *et al.*, 2016	THUMS-D and VW in LS-DYNA and VPS	Assessment of head injury risks for impacts with small electric vehicles in two different FE codes	The overall kinematics were comparable in both codes, but the difference in terms of *HIT* was 3 ms (3%). Differences of the impact location and contact force led to significant differences in the prediction of Subdural Haematoma were observed. The need for harmonised HBMs was underlined.
Bhattacharjee *et al.*, 2017	GHBMC family	Analysis of effect of vehicle geometry on *HIT* for a sedan, a mid-size SUV and a pick-up truck	Regression analysis was performed and the following expression was formulated for estimation of *HIT*: *HIT* = -32.1-0.0518 *bleh + 0.11106*WAD

B. Generic Vehicle Models

Geometry:

In Table Appendix B-1, the main geometric parameters of the four different vehicle shapes are compared. The median parameters of the Bezier curves (methodology explained in Chapter 2.5.1) that were used to derive the median shapes are shown per vehicle category in Table Appendix B-2 to Table Appendix B-5.

Table Appendix B-1: Parameters of Median Geometries

Parameter		FCR	MPV	RDS	SUV
LBRH [mm]	Lower Bumper Reference Height	395.7	426.6	367.65	458.6
UBRH [mm]	Upper Bumper Reference Height	526.9	553.2	486.95	593.8
bleh [mm]	Bonnet Leading Edge Height	739.6	788.9	657.05	904.1
LSRH [mm]	Lower Spoiler Reference Height	252.5	259.4	198.95	339.3
bmplead [mm]	Bumper Lead	85.7	111.0	50	61.3
A4Bx [mm]	Bonnet length	1202.3	905.0	1258.1	1198.1
Width [mm]	Vehicle width (limited to bumper corners)	1174.0	946.5	1079.825	1388.0
m [kg]	Vehicle mass	1540.0	1433.0	1312.5	1625.0

Table Appendix B-2: Parameters of Bezier Curves for Median FCR Geometry

	sp1	sp2	bp1	bp2	bp3	bl1	bl2	grl	bnt	wsh
LdMx	-13.3	-24.2	-24.1	-1.3	-4.0	-62.5	-85.7	-19.5	-147.6	-1227.7
LdMz	224.8	252.5	386.2	395.7	507.0	701.2	739.6	546.7	770.9	927.8
LdMt	28.1	89.5	1.0	91.1	92.0	115.0	140.0	95.0	150.1	148.5
LdMu	-2.0	-2.0	-2.0	-2.0	-2.0	-2.0	-2.0	-2.0	-2.0	-2.0
LdEx	-116.1	-127.0	-130.1	-107.3	-110.0	-262.5	-285.7	-125.5	-347.6	-1413.5
LdEy	587.0	587.0	587.0	587.0	587.0	587.0	587.0	587.0	587.0	729.0
LdEu	-60.0	-60.0	-60.0	-60.0	-60.0	-60.0	-58.0	-60.0	-56.0	157.0
TrMx	-24.2	-24.1	-1.3	-4.0	-19.5	-85.7	-147.6	-62.5	-1202.3	-1938.0
TrMz	252.5	386.2	395.7	507.0	546.7	739.6	770.9	701.2	975.0	1333.1
TrMt	158.8	41.2	90.5	92.0	0.0	140.0	155.0	115.0	174.0	155.7
TrMu	-2.0	-2.0	-2.0	-2.0	-2.0	-2.0	-2.0	-2.0	0.0	0.0
TrEx	-127.0	-130.1	-107.3	-110.0	-125.5	-285.7	-347.6	-262.5	-1388.1	-2013.8
TrEy	587.0	587.0	587.0	587.0	587.0	587.0	587.0	587.0	731.0	573.1
TrEu	-60.0	-60.0	-60.0	-60.0	-60.0	-58.0	-56.0	-60.0	157.0	163.7

Table Appendix B-3: Parameters of Bezier Curves for Median MPV Geometry

	sp1	sp2	bp1	bp2	bp3	bl1	bl2	grl	bnt	wsh
LdMx	-21.5	0.0	-5.6	0.0	0.0	-90.0	-111.0	-20.0	-170.0	-956.8
LdMz	243.0	281.1	400.5	426.6	553.2	764.0	791.0	587.0	841.0	1028.9
LdMt	0.0	0.0	0.0	90.1	93.0	124.1	140.0	90.0	147.5	147.0
LdMu	-2.0	-2.0	-2.0	-2.0	-2.0	-2.0	-2.0	-2.0	-2.0	-2.0
LdEx	-147.9	-126.4	-73.6	-68.0	-68.0	-199.1	-220.1	-88.0	-279.1	-1142.5
LdEy	473.3	473.3	473.3	473.3	473.3	473.3	473.3	473.3	473.3	731.3
LdEu	-60.0	-60.0	-60.0	-60.0	-60.0	-60.0	-58.0	-60.0	-56.0	-40.0
TrMx	0.0	-5.6	0.0	0.0	-20.0	-111.0	-170.0	-90.0	-905.0	-1763.5
TrMz	281.1	400.5	426.6	553.2	587.0	791.0	841.0	764.0	1029.0	1494.4
TrMt	93.0	90.1	90.0	90.0	0.0	140.0	147.5	124.1	171.0	156.0
TrMu	-2.0	-2.0	-2.0	-2.0	-2.0	-2.0	-2.0	-2.0	0.0	0.0
TrEx	-126.4	-73.6	-68.0	-68.0	-88.0	-220.1	-279.1	-199.1	-1090.7	-1858.4
TrEy	473.3	473.3	473.3	473.3	473.3	473.3	473.3	473.3	731.3	593.1
TrEu	-60.0	-60.0	-60.0	-60.0	-60.0	-58.0	-56.0	-60.0	-40.0	163.7

Table Appendix B-4: Parameters of Bezier Curves for Median RDS Geometry

	sp1	sp2	bp1	bp2	bp3	bl1	bl2	grl	bnt	wsh
LdMx	-19.8	-41.5	-31.1	-13.0	-9.7	-38.8	-54.0	-10.5	-130.5	-1292.9
LdMz	193.2	215.0	360.1	373.5	465.7	636.2	657.1	502.5	715.1	871.3
LdMt	23.8	89.0	10.5	101.6	87.3	127.0	132.5	87.0	153.5	146.0
LdMu	-2.0	-2.0	-2.0	-2.0	-2.0	-2.0	-2.0	-2.0	-2.0	-2.0
LdEx	-129.3	-151.1	-127.2	-109.1	-105.8	-176.6	-191.8	-106.6	-268.3	-1557.1
LdEy	539.9	539.9	539.9	539.9	539.9	539.9	539.9	539.9	539.9	720.9
LdEu	-60.0	-60.0	-60.0	-60.0	-60.0	-60.0	-58.0	-60.0	-56.0	95.2
TrMx	-41.5	-31.1	-13.0	-9.7	-10.5	-54.0	-130.5	-38.8	-1258.1	-2005.7
TrMz	215.0	360.1	373.5	465.7	502.5	657.1	715.1	636.2	915.8	1239.8
TrMt	175.0	2.0	86.0	87.2	0.0	132.5	153.5	127.0	176.5	158.7
TrMu	-2.0	-2.0	-2.0	-2.0	-2.0	-2.0	-2.0	-2.0	0.0	0.0
TrEx	-151.1	-127.2	-109.1	-105.8	-106.6	-191.8	-268.3	-176.6	-1522.3	-2064.9
TrEy	539.9	539.9	539.9	539.9	539.9	539.9	539.9	539.9	720.9	574.5
TrEu	-60.0	-60.0	-60.0	-60.0	-60.0	-58.0	-56.0	-60.0	95.2	92.8

Table Appendix B-5: Parameters of Bezier Curves for Median SUV Geometry

	sp1	sp2	bp1	bp2	bp3	bl1	bl2	grl	bnt	wsh
LdMx	-27.2	-46.4	-26.1	0.0	-2.6	-52.1	-67.7	-40.6	-118.8	-1267.0
LdMz	289.1	351.5	450.7	465.9	587.3	875.8	904.1	603.6	935.0	1087.5
LdMt	31.0	79.0	4.0	91.6	109.0	119.9	140.0	87.0	154.0	145.5
LdMu	-2.0	-2.0	-2.0	-2.0	-2.0	-2.0	-2.0	-2.0	-2.0	0.0
LdEx	-122.8	-141.9	-163.1	-137.0	-139.6	-246.7	-262.2	-177.6	-313.4	-1419.2
LdEy	694.0	694.0	694.0	694.0	694.0	694.0	694.0	694.0	694.0	761.3
LdEu	-60.0	-60.0	-60.0	-60.0	-60.0	-60.0	-60.0	-60.0	-60.0	148.9
TrMx	-46.4	-26.1	0.0	-2.6	-40.6	-67.7	-118.8	-52.1	-1210.2	-1998.5
TrMz	351.5	450.7	465.9	587.3	603.6	904.1	935.0	875.8	1126.2	1538.6
TrMt	162.5	51.0	91.5	92.9	2.0	140.0	154.0	119.9	175.6	154.5
TrMu	-2.0	-2.0	-2.0	-2.0	-2.0	-2.0	-2.0	-2.0	0.0	0.0
TrEx	-141.9	-163.1	-137.0	-139.6	-177.6	-262.2	-313.4	-246.7	-1362.4	-2063.7
TrEy	694.0	694.0	694.0	694.0	694.0	694.0	694.0	694.0	761.3	598.0
TrEu	-60.0	-60.0	-60.0	-60.0	-60.0	-60.0	-60.0	-60.0	148.9	160.0

Stiffness of GV models

The Generic Vehicle (GV) model structure used for the simulations shown in the Chapters 4 and 5 is shown in Figure Appendix B-1. It was assumed that the structural response under the loads of a pedestrian impact could be modelled through an outer shell surface, an interface layer (for modelling the vehicles fascia) and a generic foam, with the foam layer, resting on a rigid skeletal vehicle structure, as the bottom layer. The compaction layer emulates hard structures and works as an end stop, as a contact with the interface layer is defined. The foam is intended to replicate a variety of unknown base structures, such as, for example, ribs, collapsible cones, buckling structures and foams, i.e., structures which absorb energy. It features piecewise-linear behaviour, defined energy absorption, negligible expansion under compression and no strain rate dependency. In LS-Dyna, the Mat_Fu_Chang_Foam with log-log interpolation was used (with one unloading curve and two equivalent loading curves). To avoid any issues associated with spurious modes (hourglassing) and issues with volume-locking, the foam layer was assigned selective-reduced integration (SRI) hexahedral elements. The surface of the foam was covered by an interface layer, which provided a realistic mass of the contact interface and, thus, inertial effects upon impact and realistic structural mechanical characteristics (Young's modulus, tangential modulus, yield stress of steel for the bonnet and plastic for the other parts). The stiffness characteristics and a cross-section of the model are shown in Figure Appendix B-2. The final material parameters applied within the simulations after the calibration are listed in Table Appendix B-6.

A rigid surface was used to model the windscreen and the roof, as these areas were not relevant for the kinematic assessment.

The developed GV models are applied within the Euro NPCA TB 024 and are available in LS-DYNA, VPS, Radioss and Abaqus as part of the certification pack at https://www.euroncap.com/en/for-engineers/supporting-information/
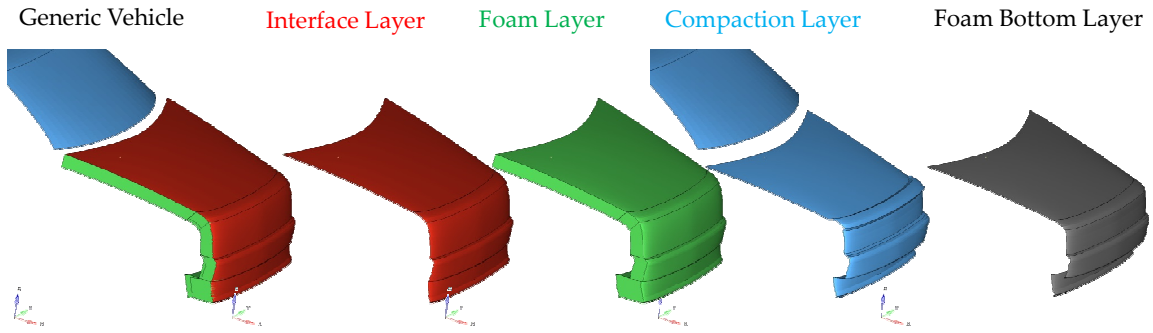
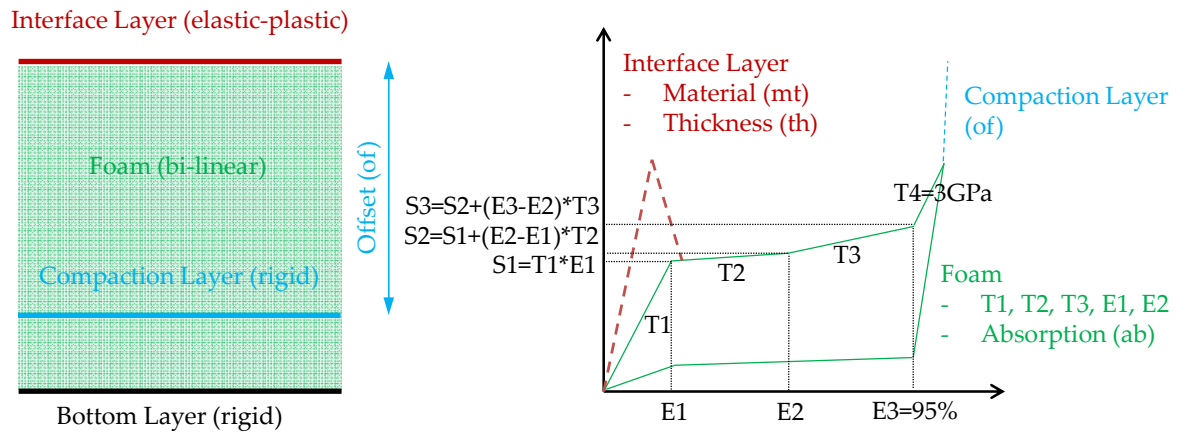Figure Appendix B-1: Layers forming the GV models (Feist, 2016)

Figure Appendix B-2: Stiffness Characteristic of GV Models (Feist, 2016)

Table Appendix B-6: Material Parameters of GV Models

Parameter	Abbr.	Spoiler	Bumper	Grill	Bonnet lead	Bonnet
Density foam	*RO*	7.000E-08	7.000E-08	7.000E-08	7.000E-08	2.000E-09
Thickness interface layer	*TH*	1.680E+00	1.860E+00	1.990E+00	1.000E+00	1.300E+00
Thickness of the wrapping rear interface layer	*RTH*	1.700E+00	-	-	1.400E-01	-
Thickness of the wrapping front interface layer	*FTH*	1.000E+00	-	-	-	2.000E-01
Thickness of the wrapping side interface layer	*STH*	-	-	-	-	4.000E-01
Material ID interface layer	*MT*	9900004	9900004		9900004	9900002
Primary stiffness	*T1*	2.899E-05	6.337E-05	3.270E-06	8.000E-03	1.225E-09
Secondary stiffness	*T2*	1.382E-05	7.743E-05	3.646E-03	1.000E-17	1.225E-09
Tertiary stiffness	*T3*	2.997E-02	5.127E-04	1.466E-03	1.000E-17	1.225E-09
(Yield) Strain at transition between primary and secondary stiffness	*E1*	1.002E-04	2.999E-01	3.203E-01	1.000E-02	2.986E-01
Transition stiffness between yield and compaction stiffness	*E2*	4.877E-01	8.497E-01	8.221E-01	5.100E-01	8.000E-01
Energy absorption	*AB*	9.500E-01	9.500E-01	9.500E-01	9.500E-01	9.500E-01
Offset between interface and compaction layer	*OF*	198	99	99	99	99 (RDS = 64)
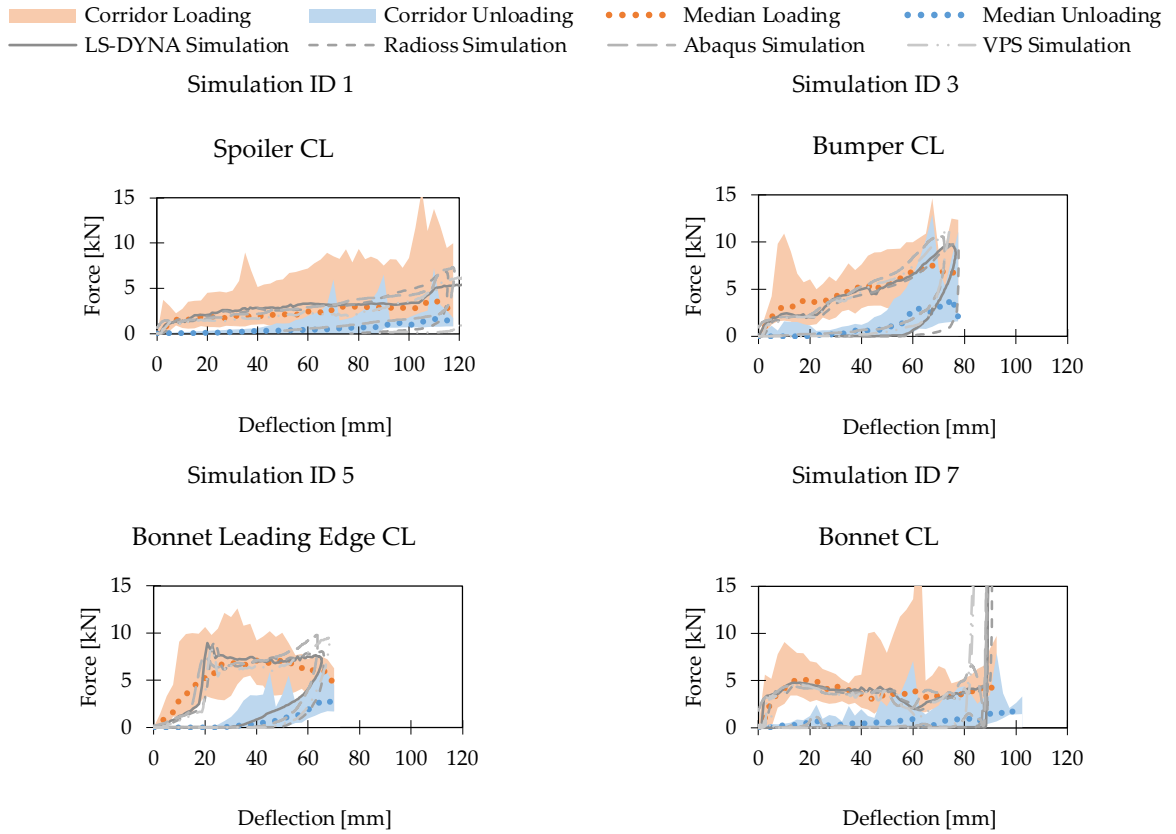
Figure Appendix B-3: Responses of generic FCR models
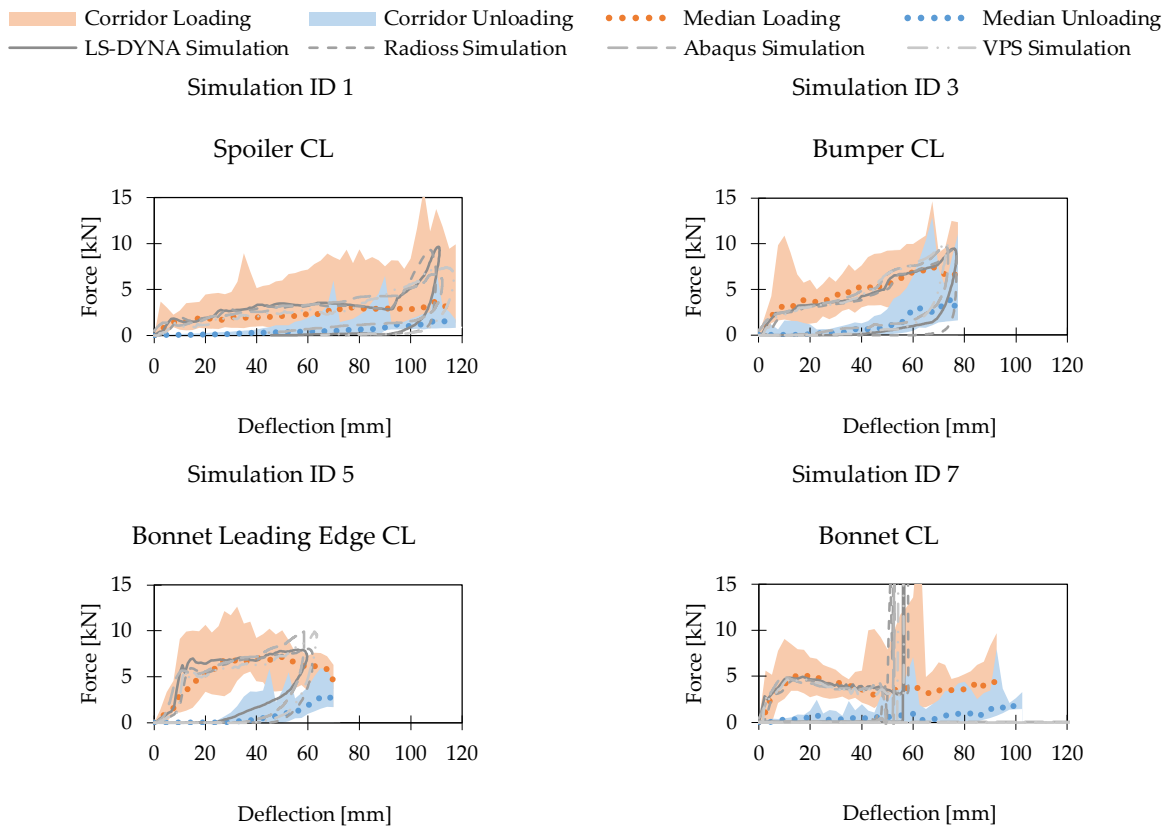
Figure Appendix B-4: Responses of generic RDS models
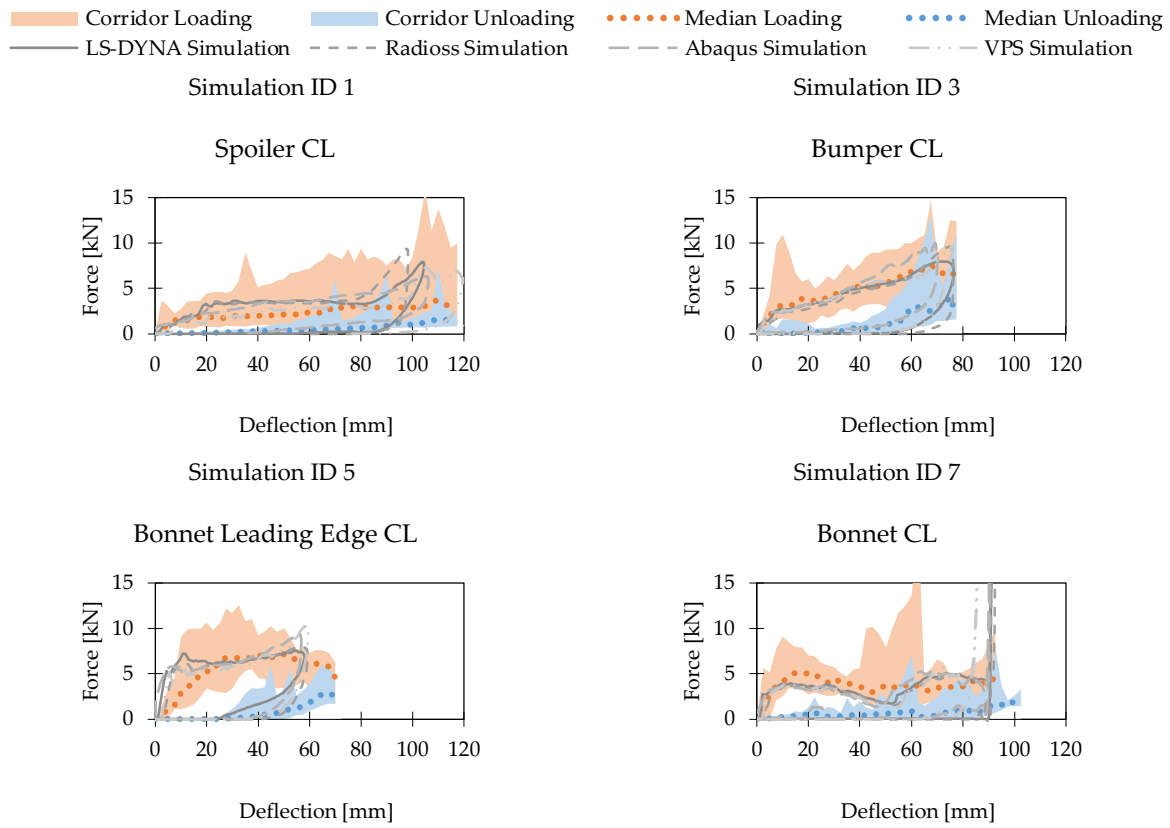
Figure Appendix B-5: Responses of generic MPV models
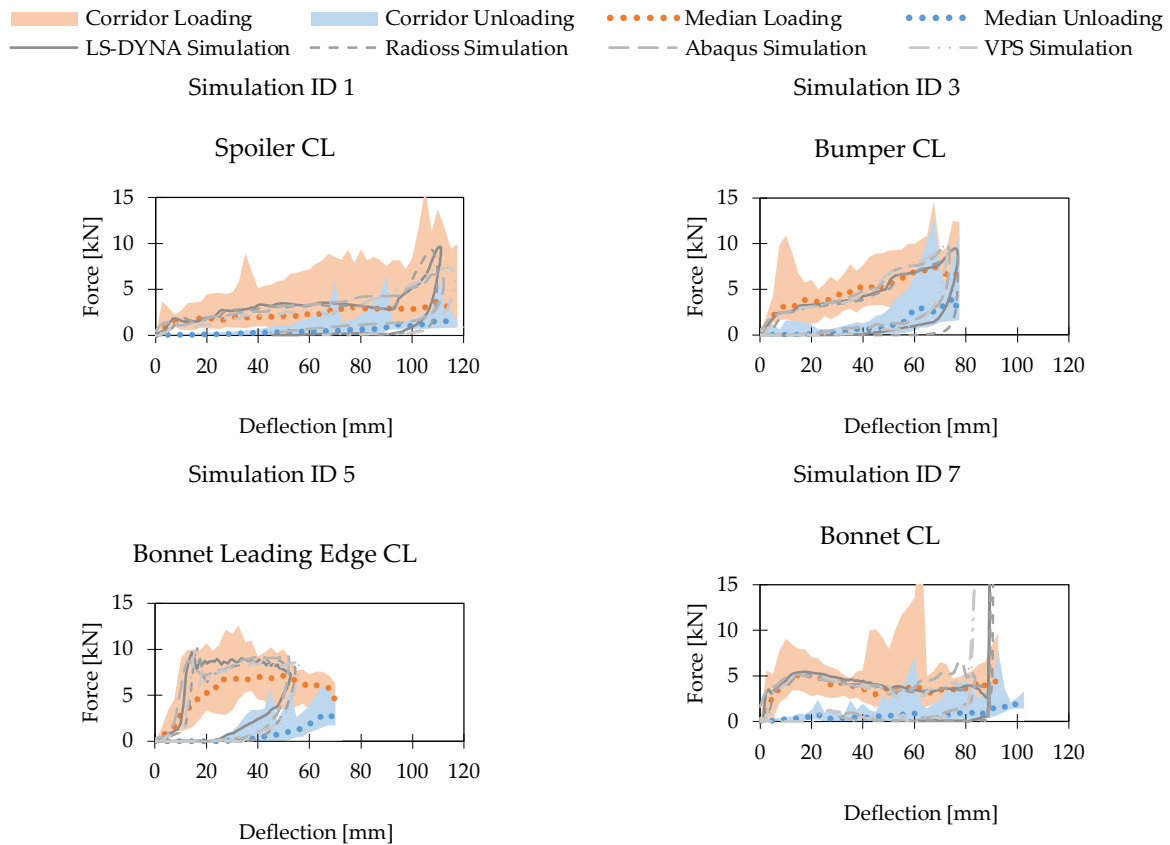
Figure Appendix B-6: Responses of generic SUV models

Generic Parameterisable Vehicle Models for Accident Reconstruction in Chapter 6:
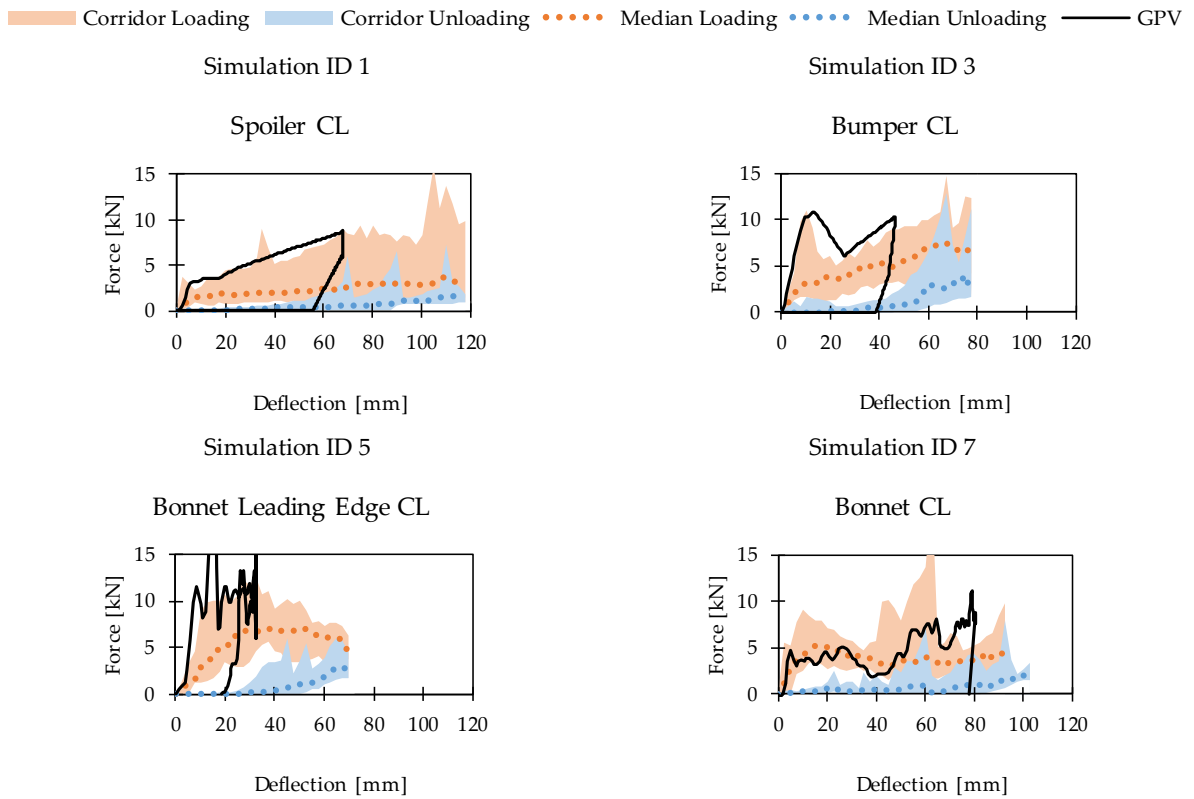
Figure Appendix B-7: Calibrated stiffness of GPV model representing the Skoda Fabia from the real-world accident with an oncoming bicyclist
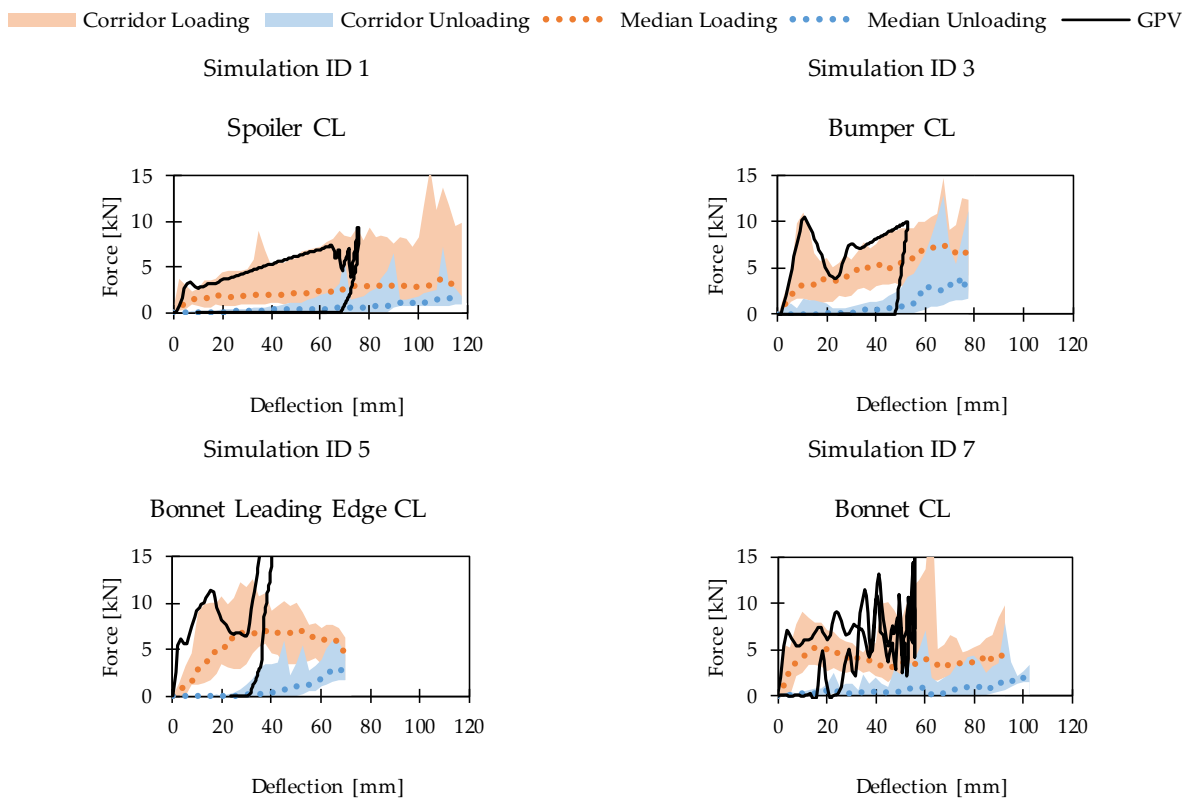
Figure Appendix B-8: Calibrated stiffness of GPV model representing the Mazda 2 from the real-world accident with minor injuries

C.   Reference Points and Positioning Protocol for Human Body Models

Table Appendix C-1: Definition of Reference Points

Abbreviation	Long Name	Definition
HC	Head Centre of Gravity	CoG of all parts of skull, scalp, face, brain, intracranial space, scalp) connected to all nodes of inner cranium (at least 100 nodes)
C1	Centre of first cervical vertebrae	Centre* (averaged coordinates) of all nodes of vertebral body of C1 connected to all nodes of C1 (Figure Appendix C-1)
C7	Centre of seventh cervical vertebrae	Centre* of all nodes of vertebral body (as defined in Figure Appendix C-2) of C7; connected to all nodes of vertebral body of C7
T8	Centre of eighth thoracic vertebrae	Centre* of all nodes of vertebral body (as defined in Figure Appendix C-2) T8; connected to all nodes of vertebral body (as shown in Figure Appendix C-2) of T8
T12	Centre of twelfth thoracic vertebrae	Centre* of all nodes of vertebral body (as defined in Figure Appendix C-2) T12; connected to all nodes of vertebral body of T12
ACr	Centre of the right *acetabulum*	Centre* of all nodes within the concave surface of the right acetabulum as shown in Figure Appendix C-3, connected with all nodes inside. The sharp edge where the bone changes curvature is selected as boundary, and all nodes inside are picked
ACl	Centre of the left *acetabulum*	As ACr, but for the right *acetabulum*
AC	midpoint of the right and left *acetabulum* centres	The midpoint of the left and right *acetabulum* centres (ACr and ACl) connected to all nodes of the right and left *acetabulum.*
Fr	Right Midpoint of *femoral epicondyle*	Midpoint of lateral and medial right femoral epicondyle. It is connected to its surrounding nodes (all nodes of the elements around FEM and FEL on the femur). The procedure shown in Figure Appendix C-5 can be applied: The femur has to be positioned such that the lateral and medial epicondyle overlay one another as much as possible. A section cut normal to the view plan should be created. Create a circle from the contour of femoral condyle. The midpoint of the circle can be used as reference for FEM and FEL which should be placed with an offset normal to the view plane. Turn the femoral bone 90 degrees around and identify the most lateral and the most medial point in line with the centre of the circle created at the previous step.
Fl	Left Midpoint of *femoral epicondyle*	Same as Fr, but for left side
Mr	*Inter-malleolar* point right	Midpoint of the tip of the *medial malleolus* (MM) and tip of the lateral malleolus (LM). It should be connected to its surrounding nodes (all nodes of the elements around mm and LM of the tibia and fibula as shown in Figure Appendix C-4)
Ml	*Inter-malleolar* point left	Same definition as Mr, but for left *malleolar*
HMr	Midpoint of right *humoral epicondyles*	Midpoint (HM) of EL (the most caudal-lateral point on lateral epicondyle) and EM (the most caudal-medial point on medial epicondyle), as shown in Figure Appendix C-6

Abbreviation	Long Name	Definition
HMl	Midpoint of left *humoral epicondyles*	Same definition as HMr, but for the left humerus
SCr	*Scapula* reference point right	Midpoint of AA (the most laterodorsal point of the *Angulus Acromialis*) and PC (the most ventral point of *processus coracoideus*) as shown in Figure Appendix C-7
SCl	*Scapula* reference point left	Same definition as SCr, but for left scapula
USr	*Ulnar Styloid* right	Most *caudal-medial* point on the right *ulnar styloid* connected to the nodes of the surrounding elements, as shown in Figure Appendix C-8
USl	*Ulnar Styloid* left	Same definition as USr, but for left ulna

* Centre always refers to the node with the averaged coordinates of the nodes that were selected to derive the centre as described in Equation (29).

$$x_c = \sum_{i=1}^{n} \frac{x_i}{n} \qquad y_c = \sum_{i=1}^{n} \frac{y_i}{n} \qquad z_c = \sum_{i=1}^{n} \frac{z_i}{n} \tag{29}$$
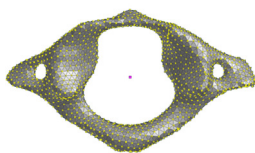
Figure Appendix C-1: Nodes to derive centre of C1
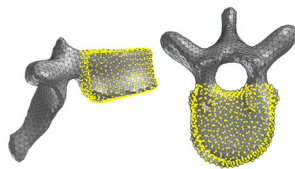
Figure Appendix C-2: Definition of vertebral body
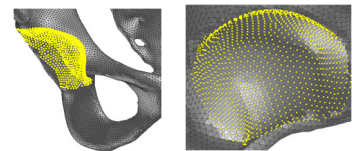
Figure Appendix C-3: Nodes to derive centre of *acetabulum*
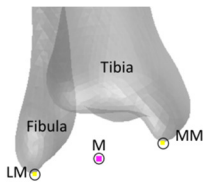
Figure Appendix C-4: Definition of *inter-malleolar point*
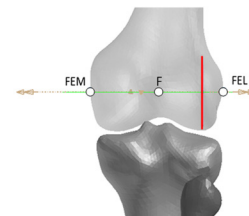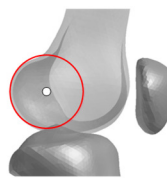
Figure Appendix C-5: Definition of *femoral epicondyle*
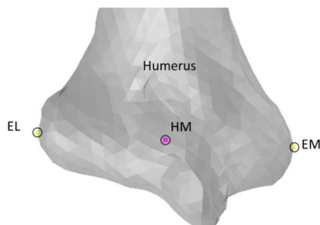
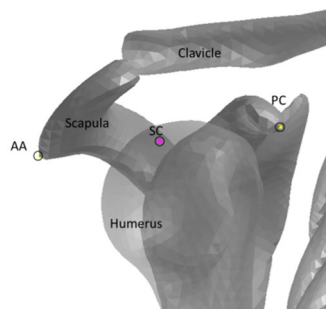Figure Appendix C-6: Midpoint of *humoral epicondyle*

Figure Appendix C-7: Definition of *scapula* reference point for shoulder joint
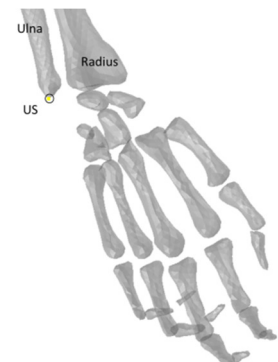

Figure Appendix C-8: Definition of *ulnar styloid*

The HBM reference coordinate system is defined as:

- The local HBM x-axis is the sagittal axis, facing anterior.

- The y-axis is the defined as the frontal axis and

- the z-direction is defined as the vertical axis, facing in the inferior direction.

The reference axis for the skeleton is based on the recommendations of the international society of biomechanics (ISB) using anatomic landmarks (Wu *et al.*, 2005; Wu *et al.*, 2002; Wu and Cavanagh, 1995). All axes describing the initial posture with the corresponding landmarks are shown in Figure Appendix C-9 (small capital refers to the right and l, to the left side of the body)
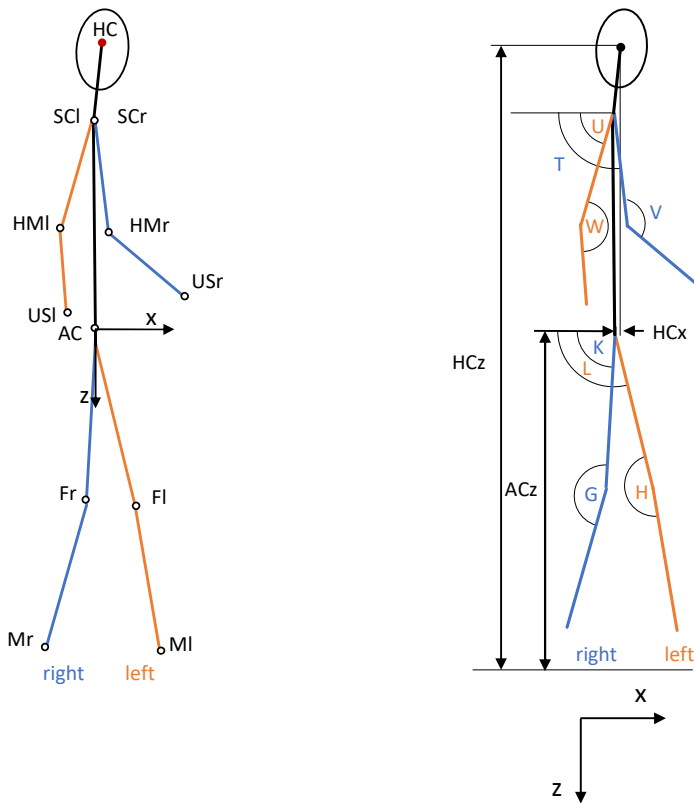
Figure Appendix C-9: Reference axis for Human Body Models used to measure angles of initial posture

Table Appendix C-2: Initial Postures Used in Sensitivity Study

Measure	Unit	THUMS											GHBMC		
		Pos 1	Pos 2	Pos 3	Pos 4	Pos 5	Pos 6	Pos 7	Pos 8	Pos 9	Pos 10	Pos 11	Pos 1	Pos 2	Pos 3
Heel-to-heel distance (x)	mm	316	316	316	313	316	316	326	333	311	316	316	314	314	314
Height of AC relative to the ground level	mm	931	931	931	931	931	931	**946**	**946**	931	931	931	956	956	956
Right Upper Leg Angle (Y with respect to horizontal)	°	87	87	87	85	87	87	87	87	85	87	87	87	87	87
Left Upper Leg Angle (Y with respect to horizontal)	°	103	103	103	109	103	103	103	103	108	103	103	103	103	103
Right Knee Flexion Angle	°	166	166	166	168	166	166	166	166	168	166	166	166	166	166
Left Knee Flexion Angle	°	177	177	177	161	177	177	177	177	162	177	177	177	177	177
Distance between right heel and AC (X)	mm	216	216	216	239	216	216	216	223	242	216	216	215	215	215
Right Upper Arm Angle (Y with respect to horizontal)	°	97	**106**	**98**	**108**	106	106	106	98	96	100	106	95	**109**	**98**
Left Upper Arm Angle (Y with respect to horizontal)	°	96	**65**	**70**	**62**	65	65	65	70	74	60	64	85	**59**	**69**
Right Elbow Flexion Angle	°	129	**152**	**144**	**177**	152	152	152	144	141	145	152	116	**152**	**136**
Left Elbow Flexion Angle Left	°	137	**151**	**162**	**152**	151	151	151	162	170	148	151	125	**155**	**166**
x-Position of HC relative to AC	mm	48	47	48	**15**	**58**	42	47	48	**15**	98	99	41	41	41
Height of HC relative to the ground level	mm	1680	1681	1681	1681	**1678**	1682	**1696**	**1696**	1681	**1678**	**1665**	1685	1685	1685
x-Position of C7 relative to AC	mm	6	5	6	**20**	6	5	5	6	**20**	**46**	8	7	7	7

Table Appendix C-3: Specifications for initial posture for AM50 and 6yo models

Abbrev.	Measure	Ref. Value AM50 Model	Ref. Value 6yo Model	Tolerance (+/-)
Px	Heel-to-heel distance longitudinal	310 mm	199 mm	5.0%
Py	Heel to heel distance lateral	185 mm	152 mm	15.0%
ACz	Height of AC relative to the ground level	949 mm	640 mm	2.0%
K	Right Upper Leg Angle (around y w.r.t. horizontal)	89°	89°	3°
L	Left Upper Leg Angle (around y w.r.t. the horizontal)	106°	106°	5°
G	Right Knee Flexion Angle (around y)	164°	164°	3°
H	Left Knee Flexion Angle (around y)	175°	175°	5°
T_y	Right Upper Arm Angle (around y w.r.t. horizontal)	98°	98°	3°
U_y	Left Upper Arm Angle (around y w.r.t. horizontal)	70°	70°	3°
T_x	Right Upper Arm Angle (around x w.r.t. horizontal)	100°	100°	5°
U_x	Left Upper Arm Angle (around x w.r.t. horizontal)	100°	100°	5°
V	Right Elbow Flexion Angle	140°	140°	5°
W	Left Elbow Flexion Angle Left	160°	160°	10°
HCx	x-Position of HC relative to AC	44 mm	6.5 mm	15 mm
HCz	Height of HC relative to the ground level	1692 mm	1117 mm	1.0%

Table Appendix C-4: Keywords for connection of sensor nodes to surrounding structure

Code	Keyword	Recommended Parameters
LS-DYNA	*CONSTRAINED_INTERPOLATE	DDOF = 123456, CIDD = 0, ITYP = 1, IDOF = 123, TWGHTi = RWHGTi = 0
VPS	OTMCO_/	DOFCOD = 111000, IMETH = 0, IELM = 1, ITYP = 0, RADIUS = 0, WTFAC = 1
RADIOSS	/RBE3	I_MODIF = 2 or 3, WTi = 1, TRAROT_REFi = 111111, TRAROT_Mi = 111000
ABAQUS	*MPC	BEAM, NSET1, NSET2

D. Comparison of THUMS v4 and GHBMC PS Results in LS-DYNA

FCR 30 km/h

FCR 40 km/h

FCR 50 km/h
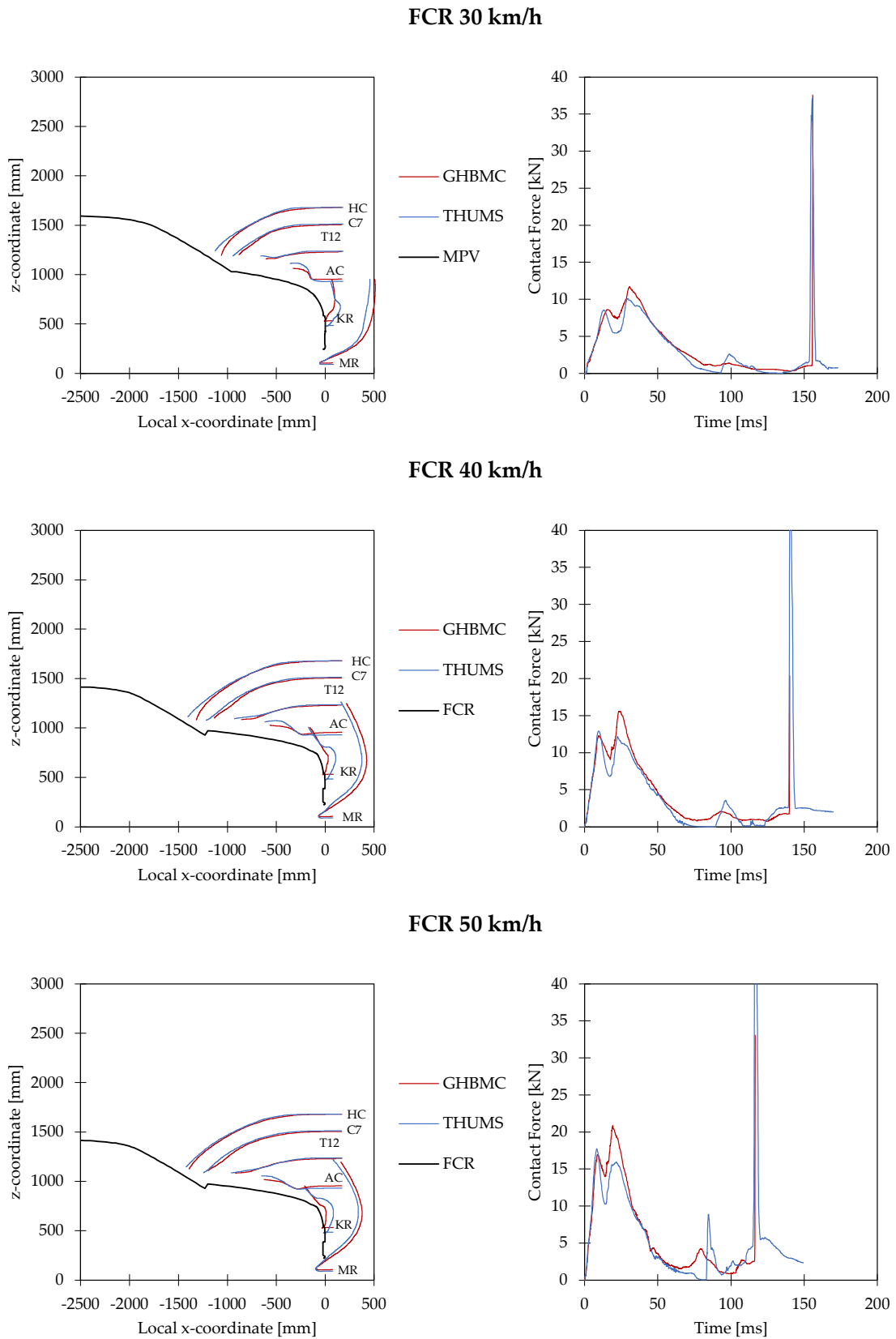
Figure Appendix D-1: Comparison of response of THUMS and GHBMC pedestrian model for impacts with generic FCR model
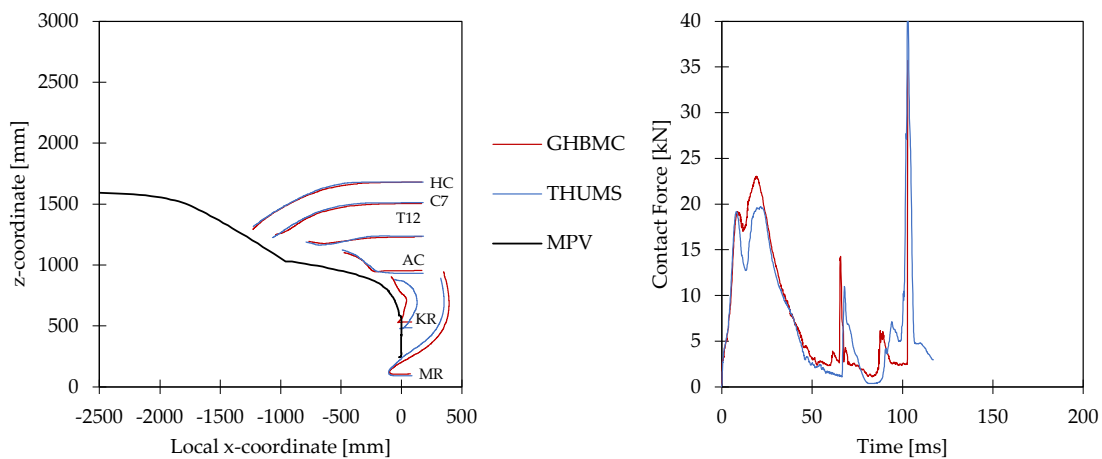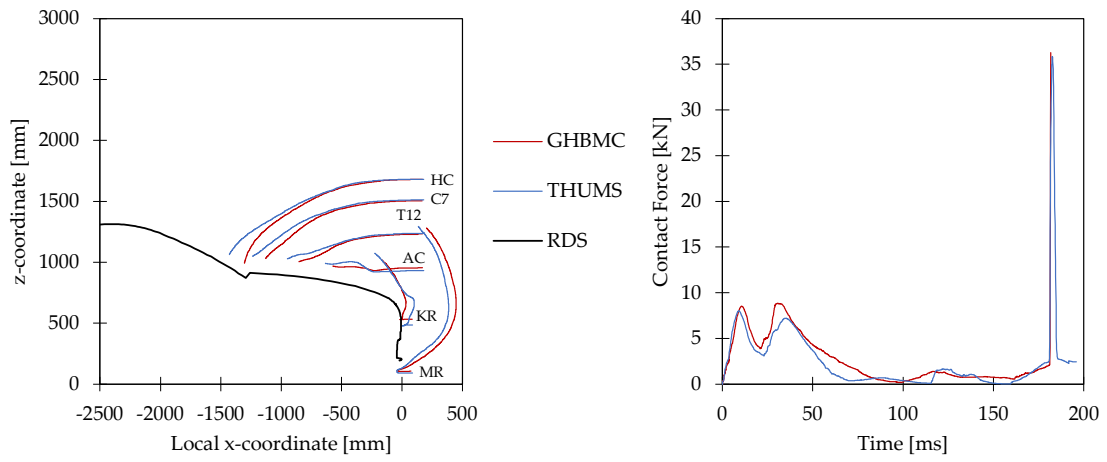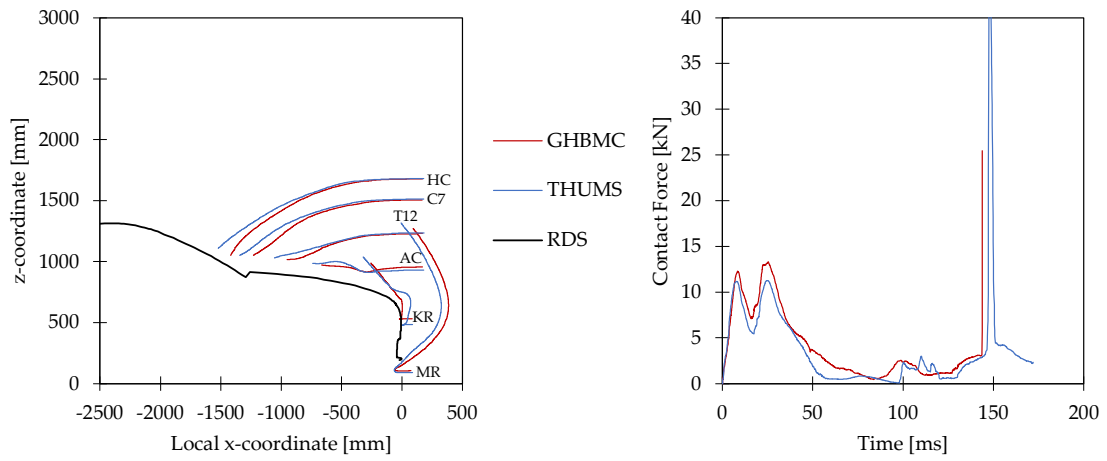
MPV 30 km/h
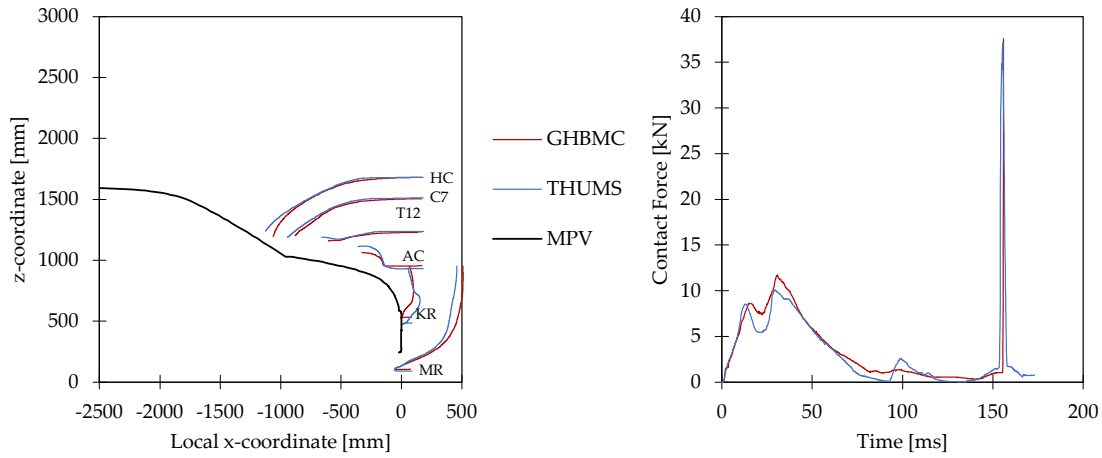
MPV 40 km/h
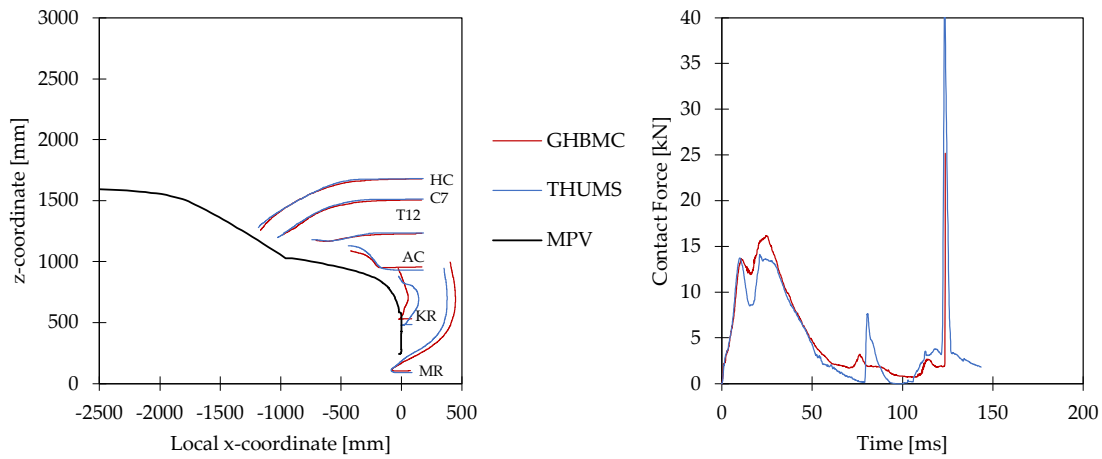
MPV 50 km/h

Figure Appendix D-2: Comparison of response of THUMS and GHBMC pedestrian model for impacts with generic MPV model
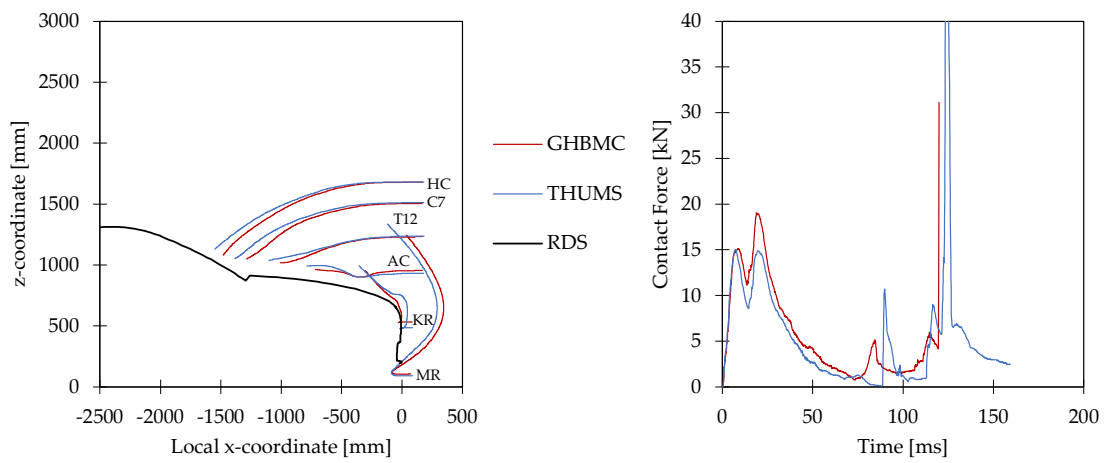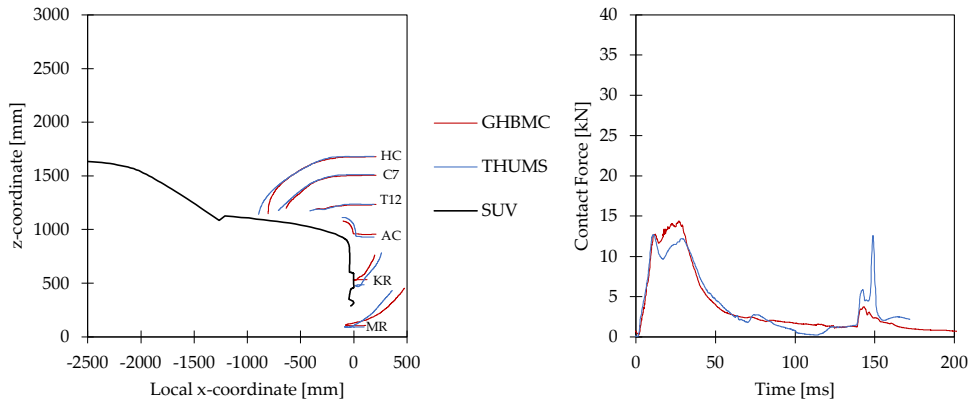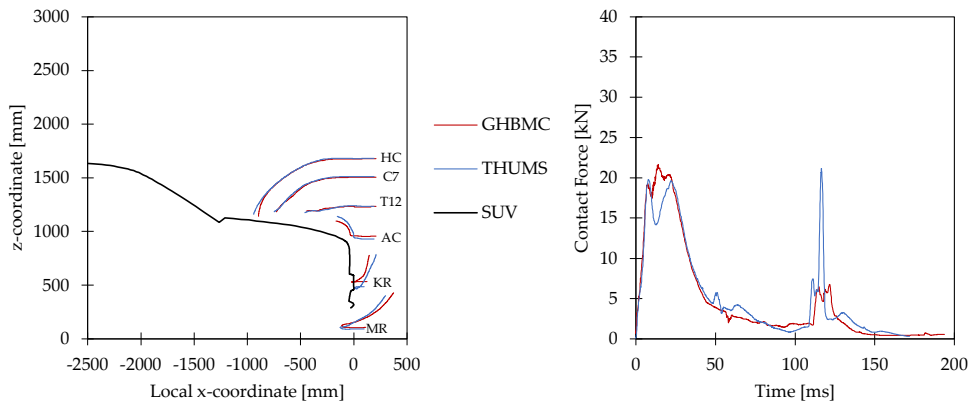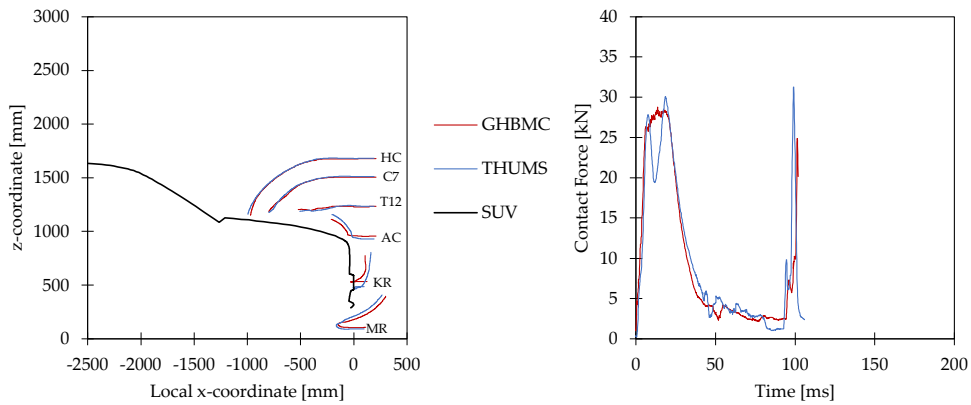
RDS 30 km/h

RDS 40 km/h

RDS 50 km/h

Figure Appendix D-3: Comparison of response of THUMS and GHBMC pedestrian model for impacts with generic RDS model

SUV 30 km/h

SUV 40 km/h

SUV 50 km/h

Figure Appendix D-4: Comparison of response of THUMS and GHBMC pedestrian model for impacts with generic SUV model

E. Corridors for Certification Procedure for Pedestrian Models

The numeric values for the corridors are available within the Excel templates from the certification pack for TB024 via: https://www.euroncap.com/en/for-engineers/supporting-information/

Corridors for Family Car

The following figures show the corridors for pedestrian impact simulations with the generic FCR model at 30, 40 and 50 kph, respectively, based on the set of consistent reference simulations.

FCR 30 km/h
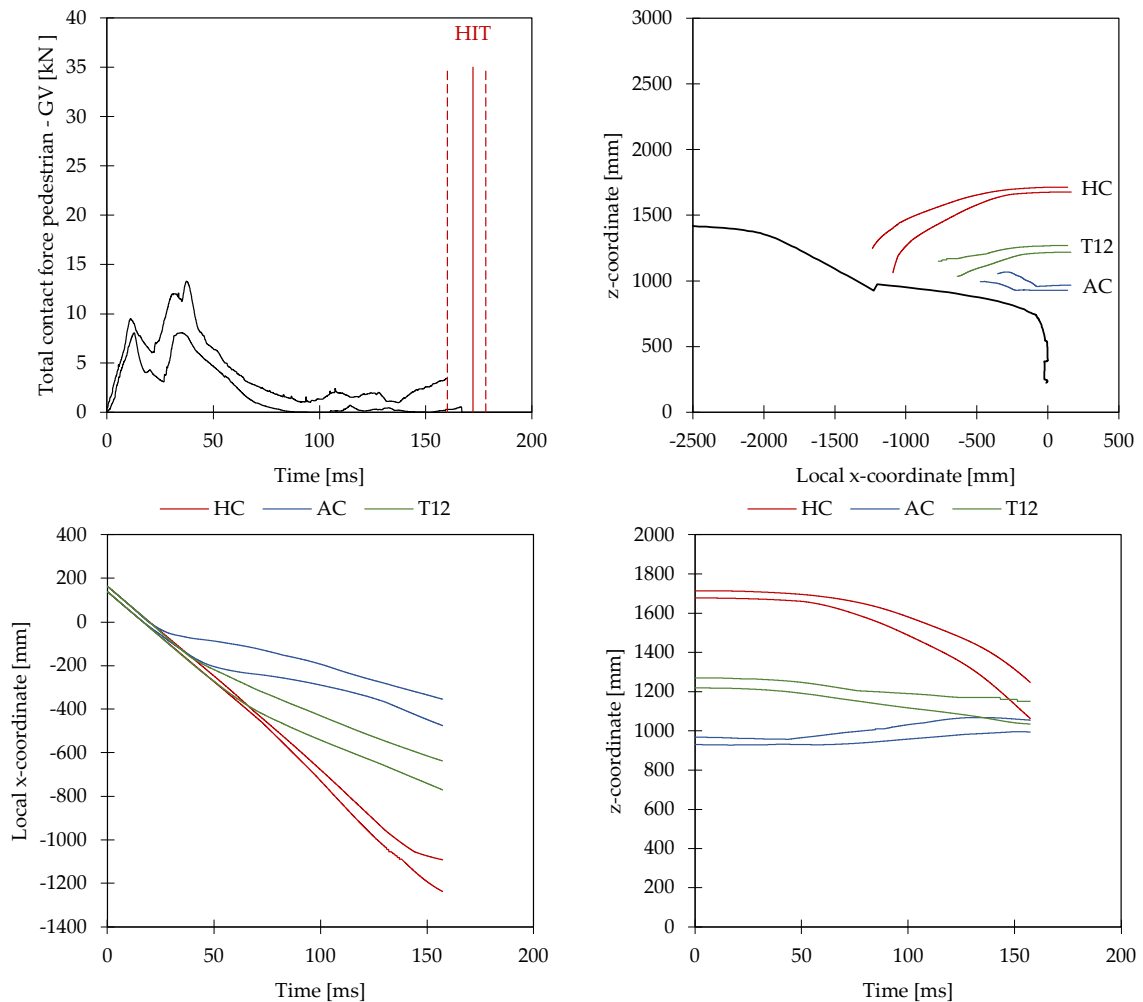
Figure Appendix E-1: Corridors for impact with generic FCR model at 30 km/h – Reference *HIT* = 172.3 ms

FCR 40 km/h
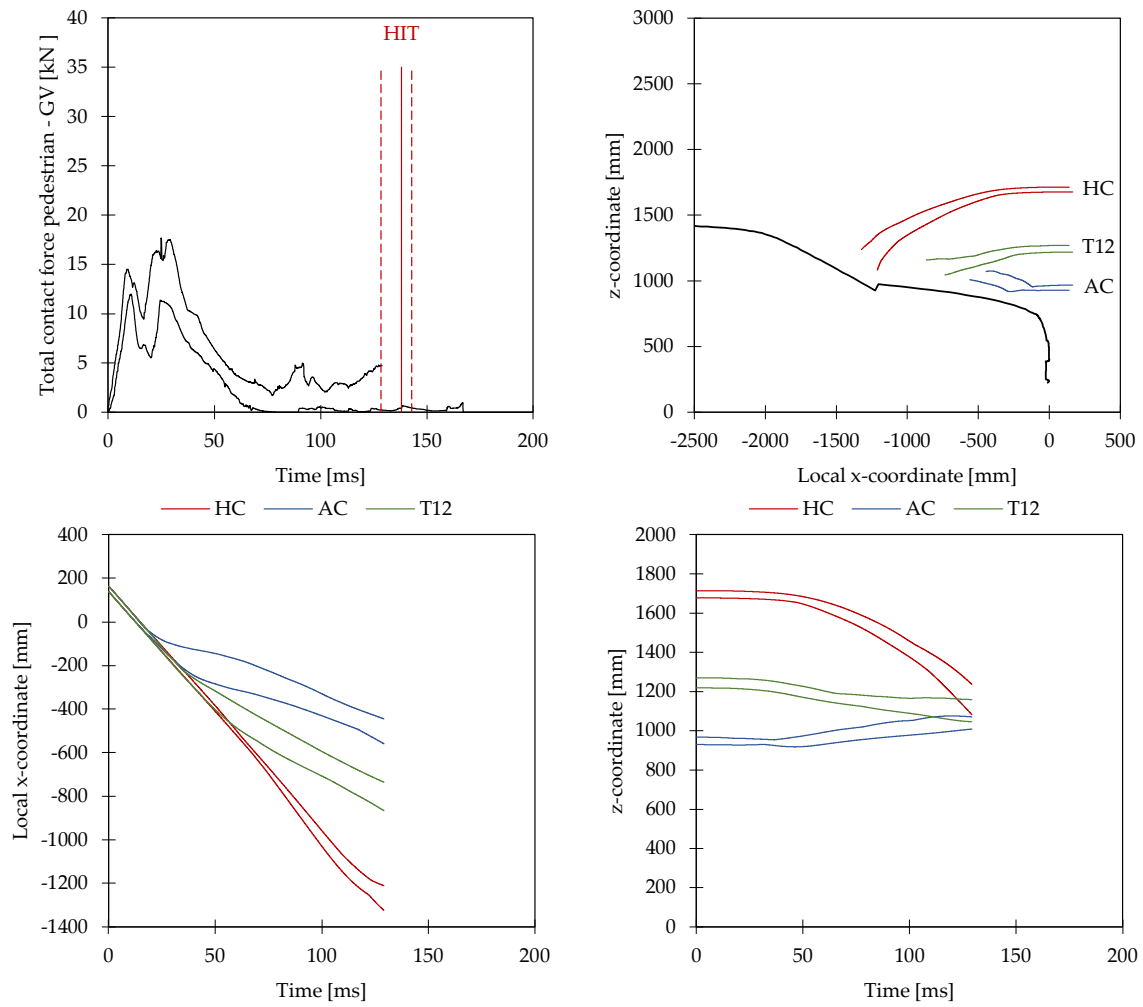
Figure Appendix E-2: Corridors for impact with generic FCR model at 40 km/h – Reference *HIT* = 138.1 ms
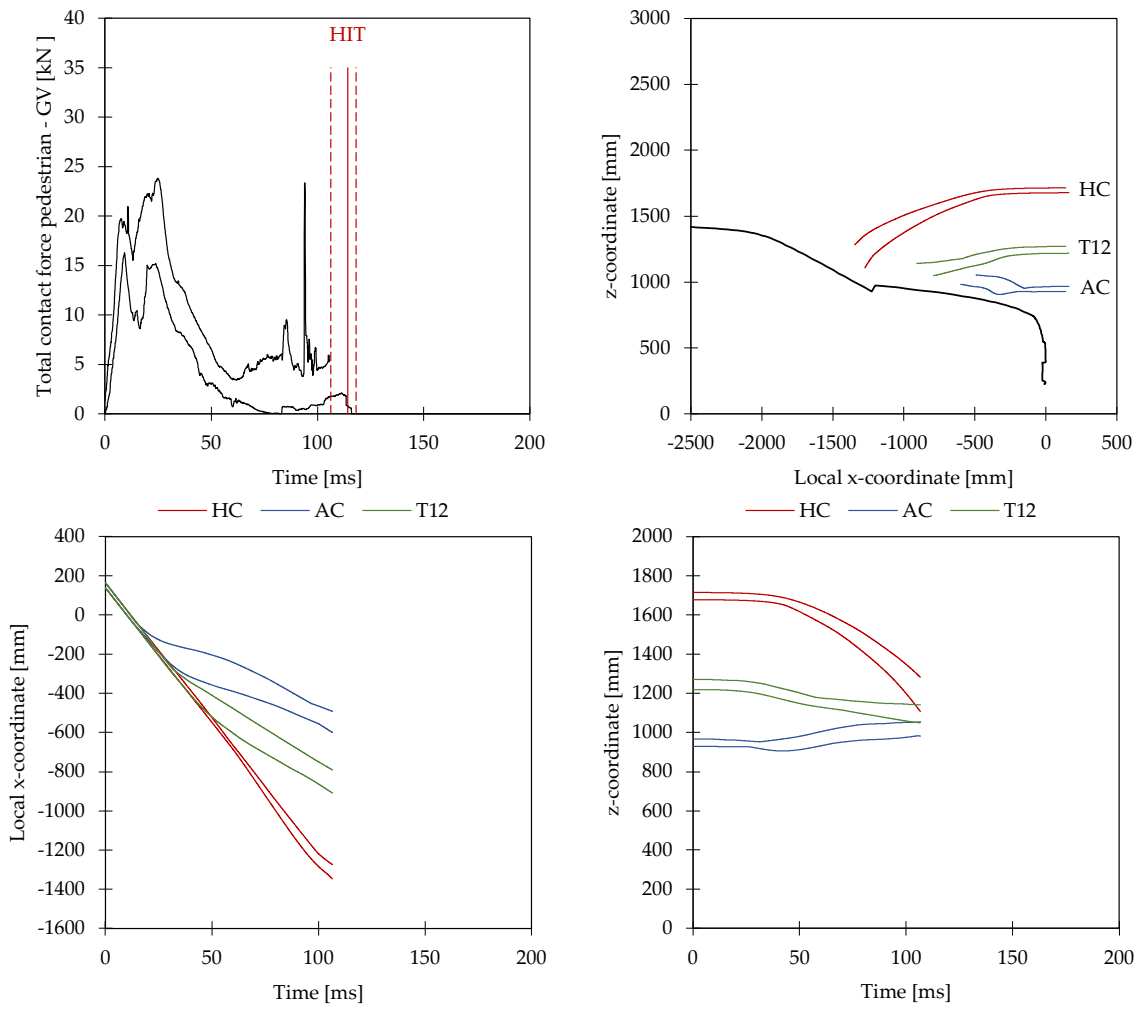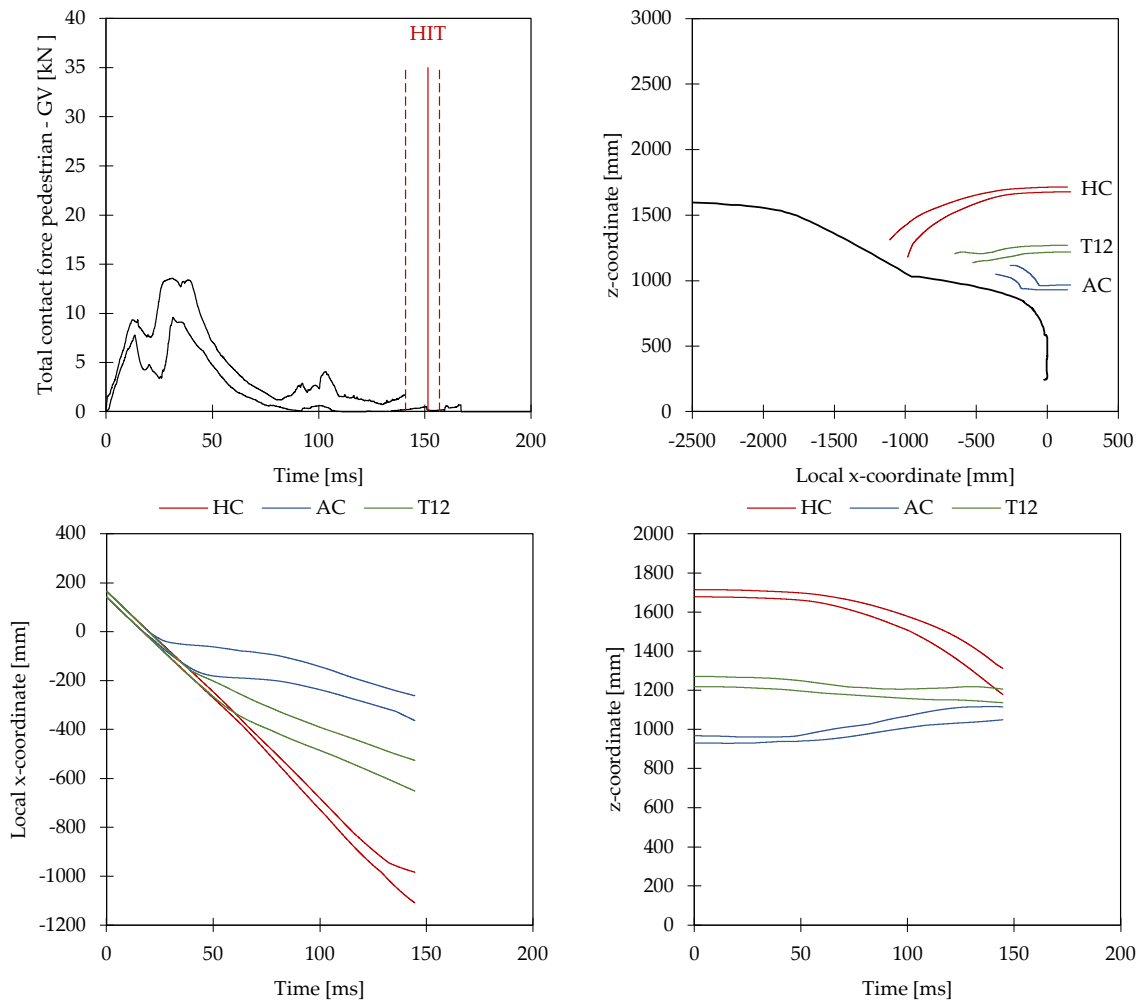
FCR 50 km/h

Figure Appendix E-3: Corridors for impact with generic FCR model at 50 km/h – Reference *HIT* = 114.3 ms

Corridors for MPV

The following figures show the corridors for pedestrian impact simulations with the generic MPV model at 30, 40 and 50 kph, respectively, based on the set of consistent reference simulations.

MPV 30 km/h

Figure Appendix E-4: Corridors for impact with generic MPV model at 30 km/h – Reference *HIT* = 151.5 ms
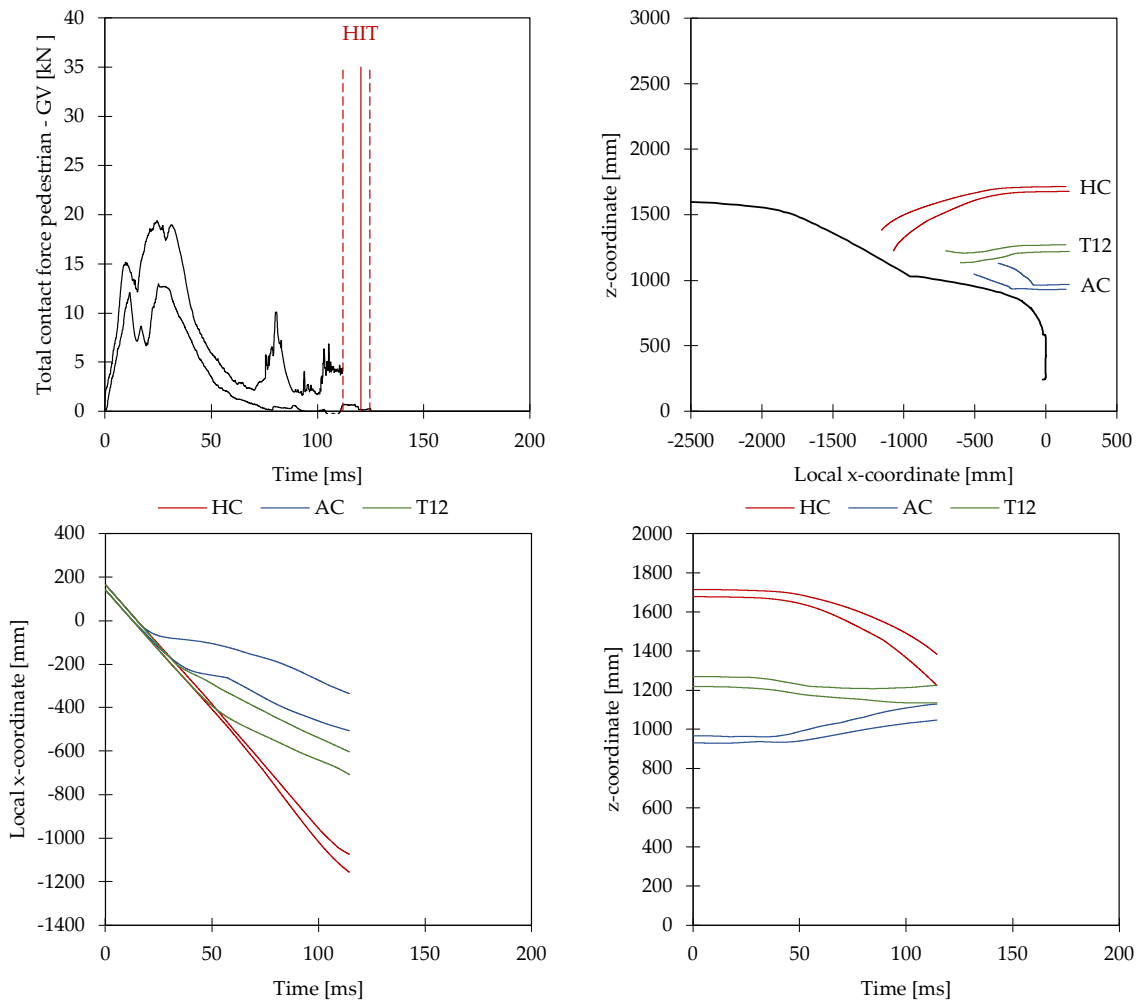
MPV 40 km/h

Figure Appendix E-5: Corridors for impact with generic MPV model at 40 km/h – Reference *HIT* = 120.4 ms
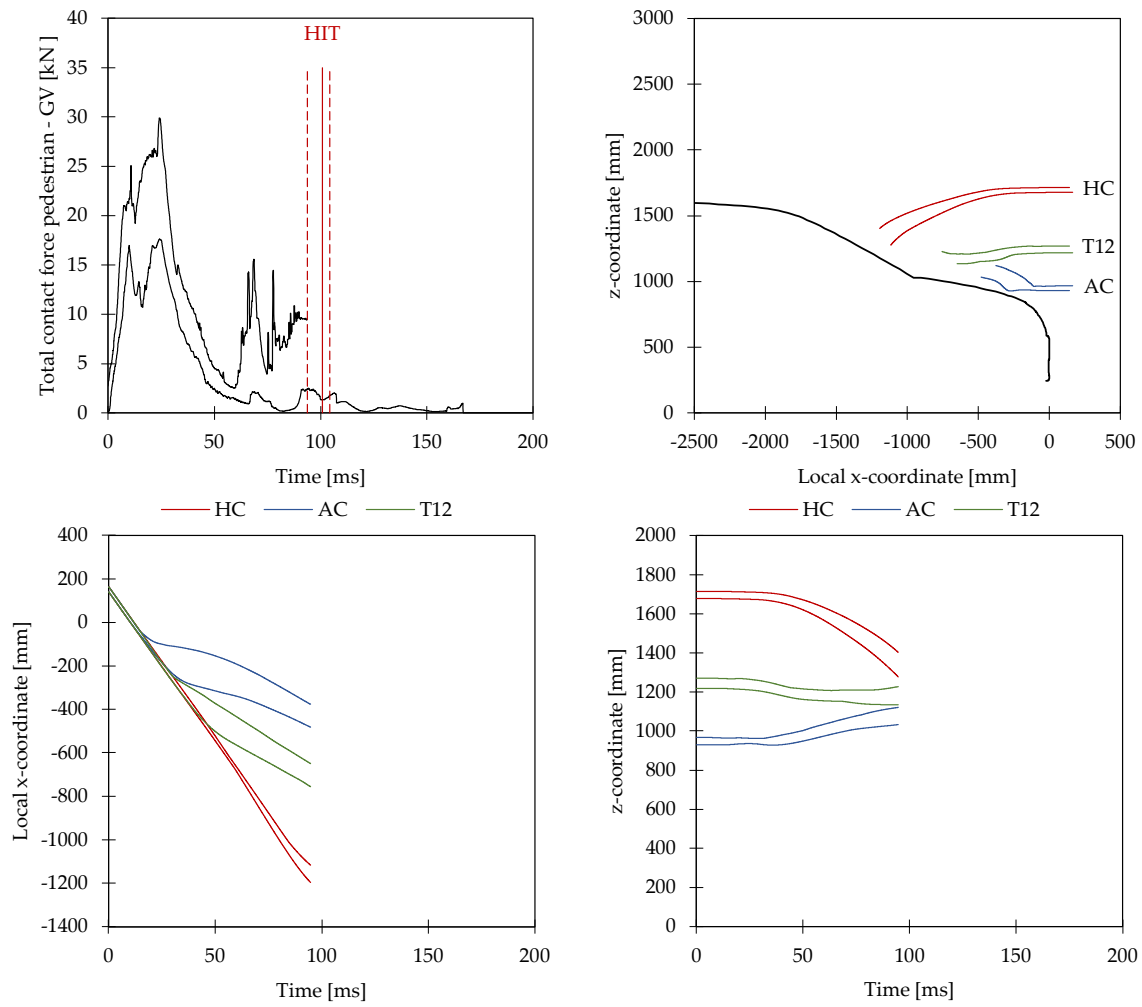
MPV 50 km/h

Figure Appendix E-6: Corridors for impact with generic MPV model at 50 km/h – Reference *HIT* = 100.8 ms

Corridors for Roadster

The following figures show the corridors for pedestrian impact simulations with the generic RDS model at 30, 40 and 50 kph, respectively, based on the set of consistent reference simulations.
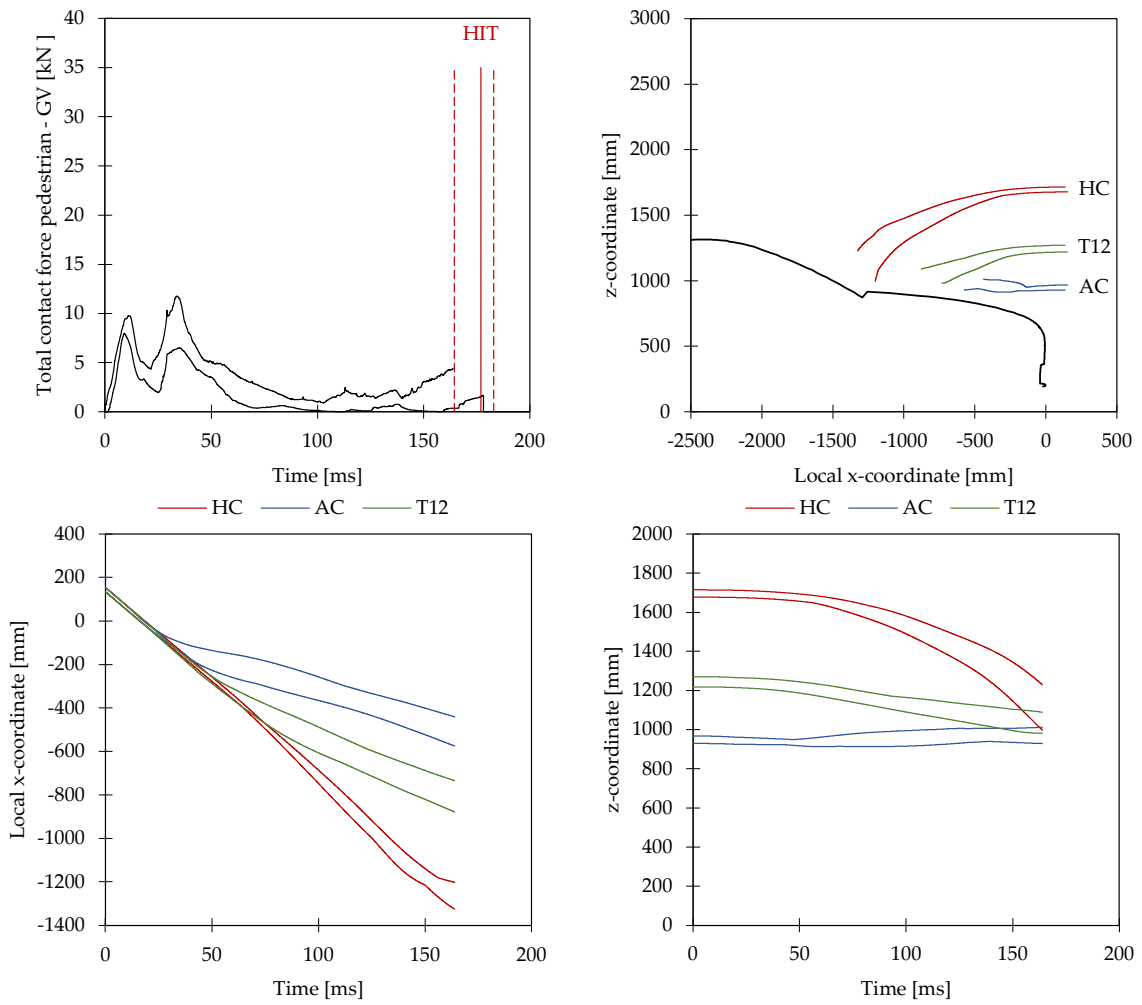
RDS 30 km/h

Figure Appendix E-7: Corridors for impact with generic RDS model at 30 km/h – Reference *HIT* = 176.9 ms
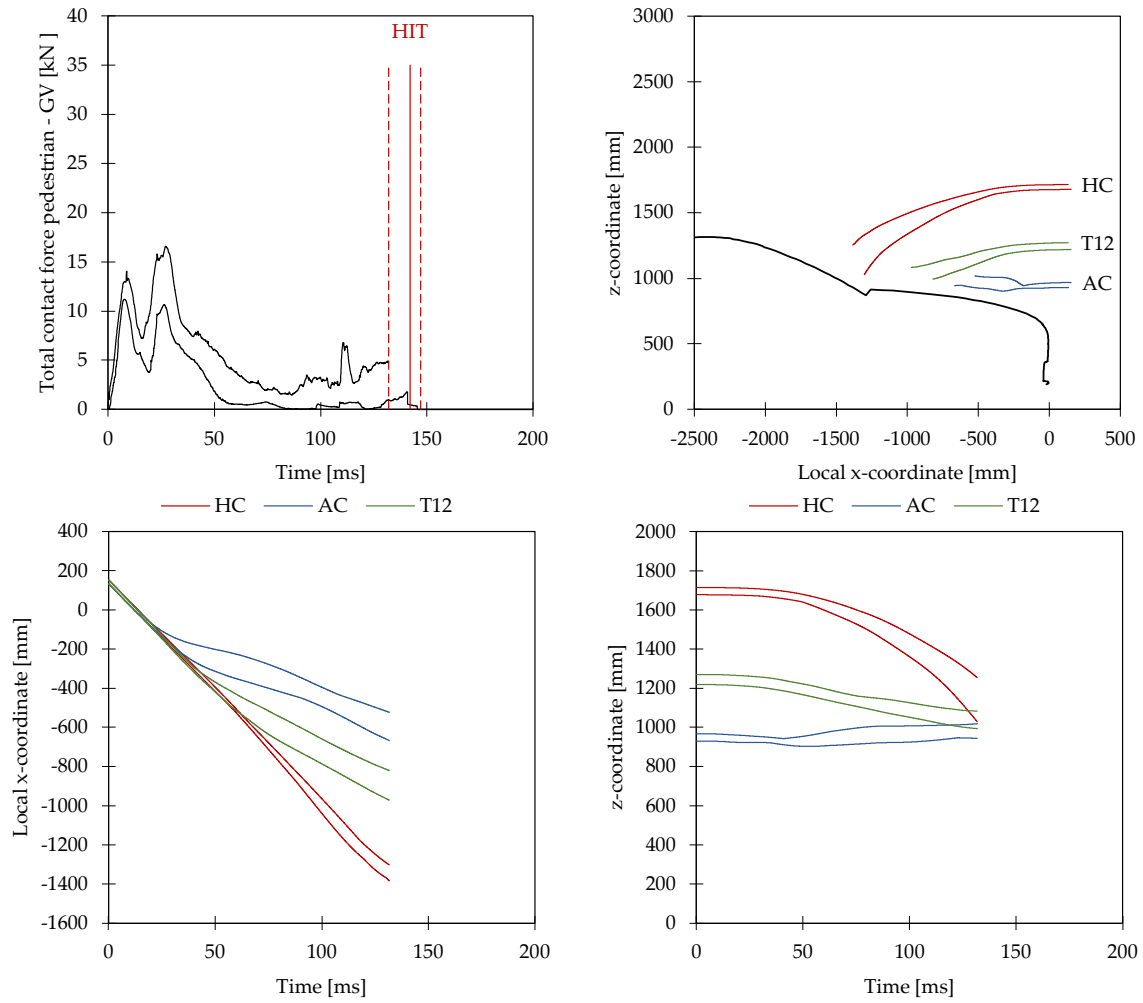
RDS 40 km/h

Figure Appendix E-8: Corridors for impact with generic RDS model at 40 km/h – Reference *HIT* = 142.1 ms
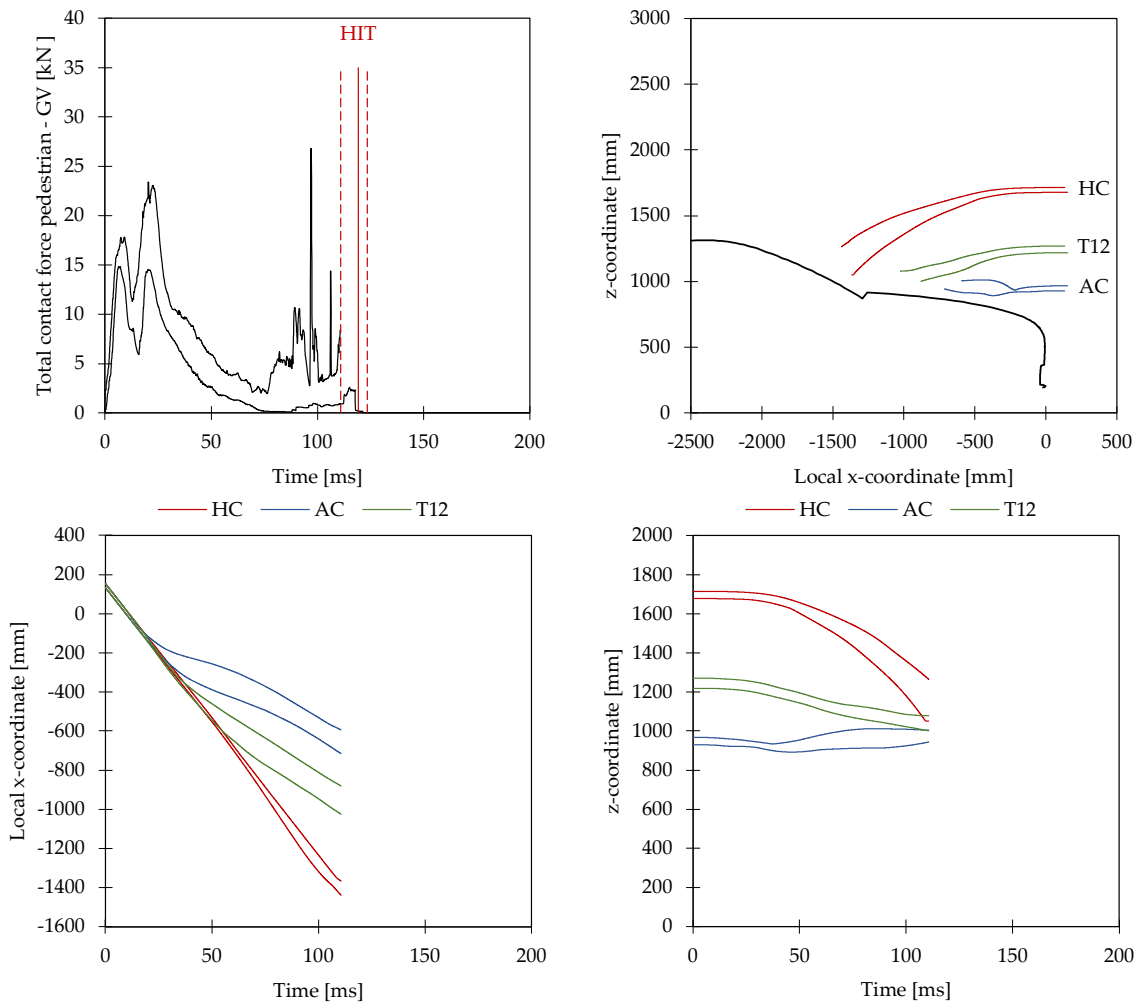
RDS 50 km/h

Figure Appendix E-9: Corridors for impact with generic RDS model at 50 km/h – Reference *HIT* = 119.3 ms

Corridors for SUV

Figures 8a-c show the corridors for the generic SUV model at 30, 40 and 50 kph, respectively.
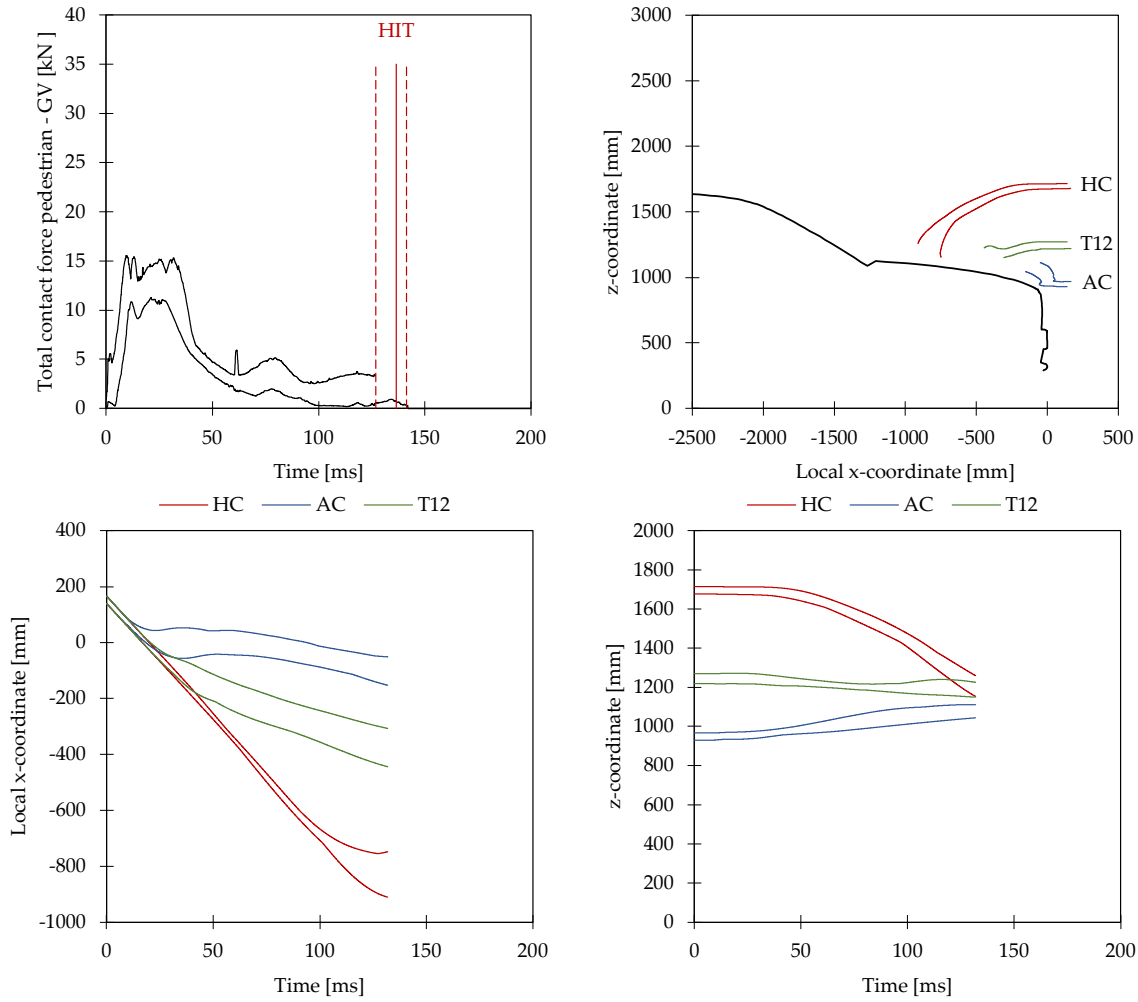
SUV 30 km/h

Figure Appendix E-10: Corridors for impact with generic SUV model at 30 km/h – Reference *HIT* = 136.5 ms
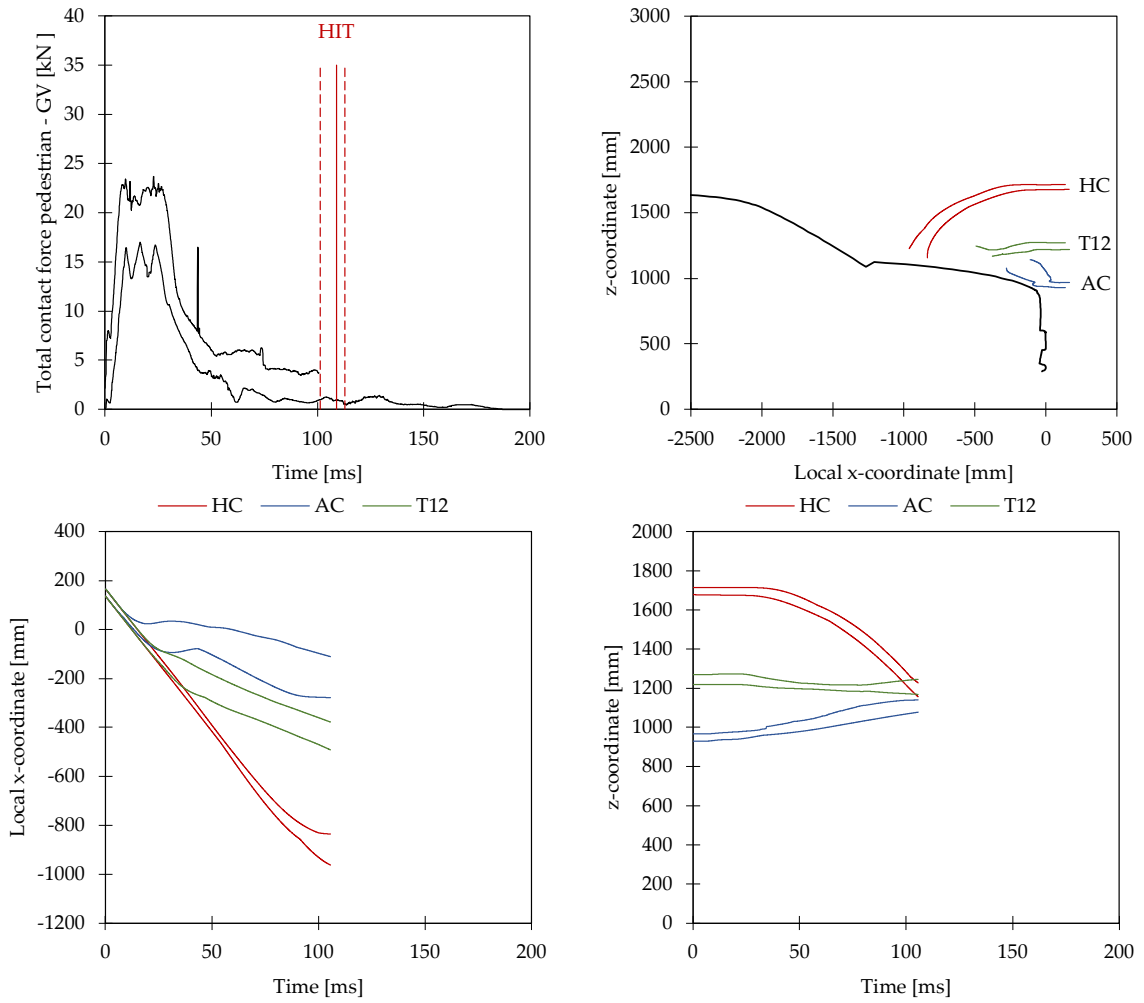
SUV 40 km/h

Figure Appendix E-11: Corridors for impact with generic SUV model at 40 km/h – Reference *HIT* = 109.0 ms
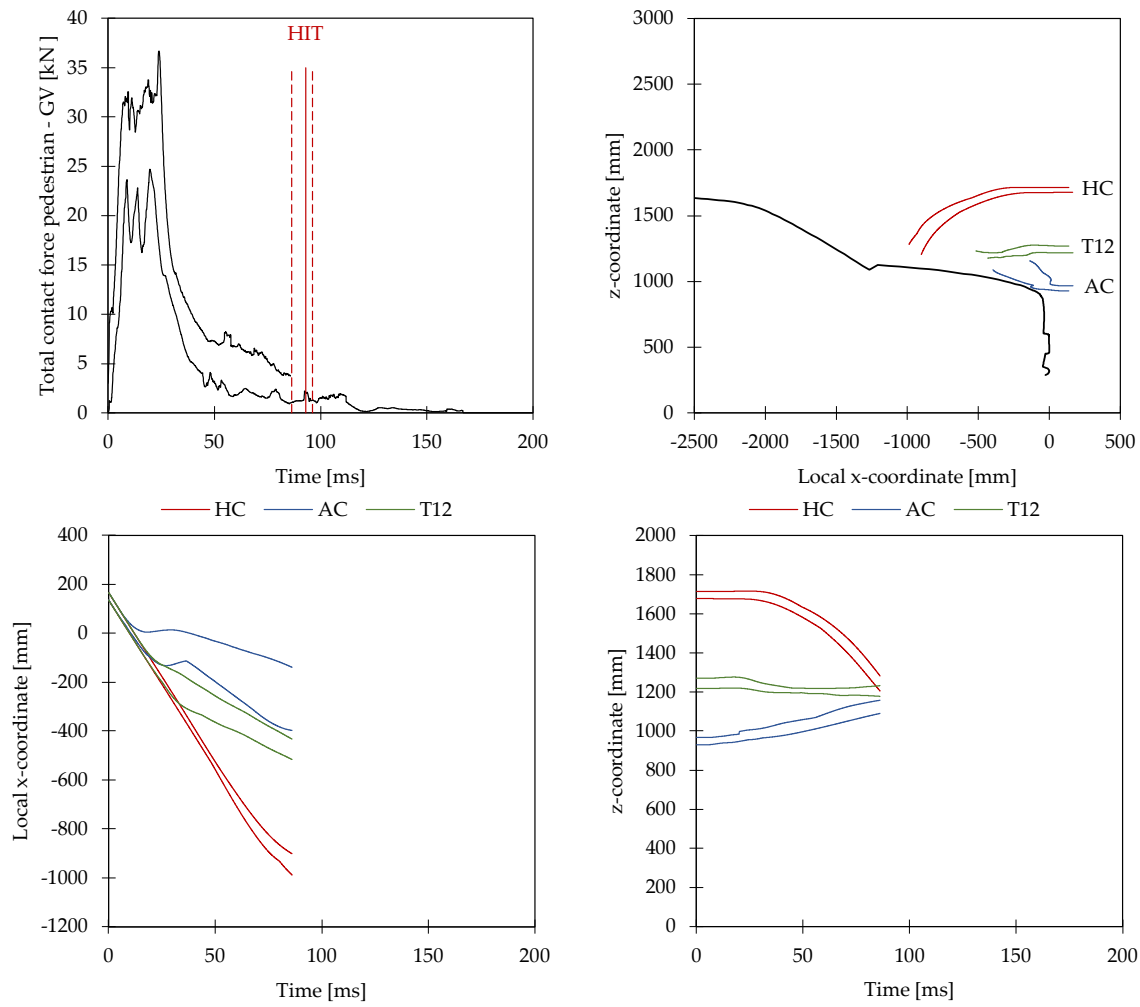
SUV 50 km/h

Figure Appendix E-12: Corridors for impact with generic SUV model at 50 km/h – Reference *HIT* = 92.9 ms

F. Division of Work for Related Publications

Peer Reviewed Publications:

- <u>Klug, C.</u>, Feist, F. and Wimmer, P. (2018), "Simulation of a Selected Real World Car to Bicyclist Accident using a Detailed Human Body Model", *2018 IRCOBI Conference Proceedings*:
  The study was designed by Corina Klug (CK) under supervision of Florian Feist (FF) with contribution of Peter Wimmer (PW). The positioning tool for the bicyclist and the Generic Parameterisable Vehicles were developed by FF. CK performed and analysed all related simulations and wrote the manuscript, which was reviewed by the co-authors.

- <u>Klug, C.</u>, Feist, F., Raffler, M., Sinz, W., Petit, P., Ellway, J. and van Ratingen, M. (2017), "Development of a Procedure to Compare Kinematics of Human Body Models for Pedestrian Simulations", *2017 IRCOBI Conference Proceedings:*
  The study was designed by Corina Klug (CK) in collaboration with of the co-authors FF, Wolfgang Sinz (WS), Philippe Petit (PP), James Ellway (JE) and Michiel van Ratingen (MR), who initiated the study. Marco Raffler (MR) performed the calibrations of the generic vehicle models supervised by CK. FF developed the concept of the GV models. All analysis and simulations were performed by CK. CK wrote the manuscript, which was critically reviewed by all co-authors.

- Feist, F. and <u>Klug, C.</u> (2016), "A Numerical Study on the Influence of the Upper Body and Neck on Head Kinematics in Tangential Bicycle Helmet Impact", *2016 IRCOBI Conference Proceedings:*
  The study was designed by FF with contribution of CK. FF generated the data and was responsible for writing the manuscript. CK performed the analysis of injury criteria and critically reviewed the manuscript.

- <u>Klug, C.</u>, Feist, F. and Tomasch, E. (2015), "Testing of bicycle helmets for preadolescents", *2015 IRCOBI Conference Proceedings:*
  The study was designed by CK under the supervision of FF and Ernst Tomasch (ET). FF performed the simulations with the FE helmet model. CK was responsible for the physical tests and carried out the analysis of injury criteria and simulations with the THUMS head model. CK was responsible for writing the manuscript, that was critically reviewed by FF and ET.

- <u>Klug, C.</u>, Weinberger, M., Tomasch, E., Feist, F., Sinz, W., Steffan, H., Kinsky, T., Roth, F., Praxl, N. and Buenger, B. (2015), "Pelvic and femoral injuries in car-to-pedestrian accidents", *2015 IRCOBI Conference Proceedings:*
  The study was designed by CK under supervision of FF, ET and WS in collaboration with the other co-authors. Martin Weinberger (MW) and CK together analysed the data of the accident databases under supervision of ET. Franz Roth (FR) provided the case-by-case study of GIDAS cases. CK wrote the manuscript, which was critically reviewed by all co-authors.

- <u>Klug, C.</u>, Sinz, W., Brenn, G. and Feist, F. (2013), "Experimental sphere-in-sphere testing for the validation of a numerical cerebrospinal fluid model", *2013 IRCOBI Conference Proceedings*: The study was designed by FF. CK was responsible for the experimental tests under the supervision of FF and WS. The FE simulations were carried out and analysed by CK under supervision of FF. The analytical approach was developed by Günter Brenn and compared with the experiments by CK. CK was responsible for writing the manuscript, which was critically reviewed by all co-authors.

Other Scientific Contributions:

- <u>Klug, C.</u>, Luttenberger, P., Schachner, M., Micorek, J., Greimel, R. and Sinz, W. (2018), "Postprocessing of Human Body Model Results – Introduction of the Open Source Tool DYNASAUR", presented at 7th International Symposium: Human Modeling and Simulation in Automotive Engineering:
  The software DYNASAUR was designed by Peter Luttenberger (PL) and CK. The original version of the software was programmed mainly by Robert Greimel, which was later significantly revised by Jakub Micorek and Martin Schachner. The presented analysis were performed by CK.

- <u>Klug, C.</u>, Feist, F., Sinz, W., Ellway, J. and van Ratingen, M. (2018), "A procedure to compare kinematics of Human Body Models for pedestrian assessments", presented at SAE Government Industry Meeting:
  The study was designed by Corina Klug (CK) in collaboration with of the co-authors FF, Wolfgang Sinz (WS), James Ellway (JE) and Michiel van Ratingen (MR), who initiated the study. FF developed the concept of the GV models. All analysis and simulations were performed by CK. CK prepared the presentation, which was reviewed by the co-authors.

- Feist, F. and <u>Klug, C.</u> (2017), "Verletzungen des Beckens und der Oberschenkel in Fußgängerunfällen mit PKWs", presented at Safety Update, 26.-27.9, Graz.
  The presented study consisted of two parts: CK was responsible for the accident analysis and FF for the HBM pedestrian simulations against Generic Parameterisable Vehicle Models.

- <u>Klug, C.</u>, Feist, F., Raffler, M., Sinz, W. and van Ratingen, M. (2016), "Methodology for kinematic comparison of human body models for pedestrian simulations", presented at 6th International Symposium: Human Modeling and Simulation in Automotive Engineering:
  The study was designed by Corina Klug (CK) in collaboration with of the co-authors FF, Wolfgang Sinz (WS), James Ellway (JE) and Michiel van Ratingen (MR), who initiated the study. FF developed the concept of the GV models. All analysis and simulations were performed by CK. CK prepared the presentation, which was reviewed by the co-authors.